UNIVERSITY OF CALIFORNIA
RIVERSIDE

Synthesis, Characterization, and Activity of Well-Defined Lewis Acids on Metal Oxides

A Dissertation submitted in partial satisfaction
of the requirements for the degree of

Doctor of Philosophy

in

Chemistry

by

Kavyasripriya K. Samudrala

December 2023

Dissertation Committee:
Dr. Matthew P. Conley Chairperson
Dr. Boniface Fokwa
Dr. Francisco Zaera

The Dissertation of Kavyasripriya K. Samudrala is approved:

_____

_____

_____

Committee Chairperson

University of California, Riverside

Acknowledgements

I would like to thank my mentor and advisor, Matt Conley. He has been patient and guided me when I needed it, and also given me the time and space to figure things out on my own when I needed to pick myself up. His guidance and insight has pushed me to be a better scientist, and tangentially, has been formative in me becoming a more confident person. I'll work on the apologizing, but I appreciate the patience with me as I fumbled through ideas and experiments more than I can say.

I would like to give my thanks to Dr. Lingchao Zhu for his time and insight with all things NMR throughout my Ph.D. He has been a wealth of information, and his patience with my every question made it possible for me to learn so much.

I have had the pleasure of working with some amazing labmates throughout my doctorate. Damien, Jessica, and Winn were incredibly patient with me as a very timid first-year graduate student, and their guidance was invaluable as I learned about synthetic chemistry techniques. The conversations and laughs with Yutthana Lakliang, Josh Richardson, Marc Groves, and Max Kling made getting through graduate school a little easier. I'd like to thank Jiaxin Gao, especially, for being my pandemic buddy and confidante throughout graduate school. You helped me get through tough days in the lab, and you taught me more than you realize. Thank you for always being my buddy through some very harebrained plans, and more importantly, for laughing with me through them. We're both pretty funny, but I honestly think you might be the funnier one.

My family means the world to me, and I'm blessed to have quite a world of them. To my parents, Krishna and Srimathi, I cannot find the words to tell you how much you

mean to me, but everything, all of this, is for you guys. You are the smartest people I know, and your sacrifices have made me who I am. I hope I can make you proud. To my Paati, Vathsala, I love you and I miss you. Your strength has been a model for me. Seshu Babai and Latha Pinni, you have been my parents here in Riverside. I love you guys, and I cannot thank you enough for making me feel safe and loved, always. Thank you to all of my babais, pinnis, attas, mamas, mamaiyyas, peddammas, and peddanannas, I would not have had the confidence to go through this program without your endless support and love.

My siblings and cousins: Srikar, Shriya, Ramya, Vishnu Anna, Vaishnavi, Sri Charan, Subhashini, Shravani, Srinivas, Subha Akka, Pratyusha Akka, Mike Anna, Sulakshana, Soumitri, Seenu Anna, Shravani Akka, Sasidhar Anna, Kutty (Ph.D.), Aditya, Sri Hari, Tharun Anna, Sowji, Vini, Shini (and others). I love you guys. You have gotten me through graduate school by listening patiently, but more importantly, by making fun of me pretty mercilessly. Thank you all for reminding me to not take things so seriously. Srikar, Shriya, Ramya, you guys are my day one crew, and I love you.

I have amazing friends who have been cheerleaders for me throughout my many anxious and indecisive moments. Friends who have pushed me on in every way, and have been amazing sounding boards in times of confusion. I could not have done this without them. Thank you, Kim, Krishna, Elizabeth, Sheel, Katie, Samira, Tanmai, Shane, Alexis, Caroline, Sandra, Monique. Given how scatterbrained I can be, these people have had the patience of saints and have reminded me that I’m me, regardless of a Ph.D.

The text, figures, and schemes for the following chapters have been reproduced from the following manuscripts.

Chapter 1:

Samudrala, K. K.; Conley, M. P. Effects of Surface Acidity on the Structure of Organometallics Supported on Oxide Surfaces. *Chem. Commun.* **2023**, *59* (28), 4115–4127. https://doi.org/10.1039/d3cc00047h.

Chapter 2:

Samudrala, K. K.; Huynh, W.; Dorn, R. W.; Rossini, A. J.; Conley, M. P. Formation of a Strong Heterogeneous Aluminum Lewis Acid on Silica. *Angew. Chemie - Int. Ed.* **2022**, *61* (40). https://doi.org/10.1002/anie.202205745.

Chapter 3:

Samudrala, K. K.; Conley, M. P. A Supported Ziegler-Type Organohafnium Site Metabolizes Polypropylene. *J. Am. Chem. Soc.* **2023**, 0–4. https://doi.org/10.1021/jacs.3c05940.

Chapter 4:

Samudrala, K. K.; Akram, M. O.; Martin, C. D.; Conley, M. P. Formation of Strong Boron Lewis Acid Sites on Silica. *Submitted*.

The co-author (Matthew P. Conley) listed in the above publications directed and supervised the research which forms the basis for this dissertation.

ABSTRACT OF THE DISSERTATION

Synthesis, Characterization, and Activity of Well-Defined Lewis Acids on Metal Oxides

by

Kavyasripriya K. Samudrala

Doctor of Philosophy, Graduate Program in Chemistry
University of California, Riverside, December 2023
Dr. Matthew P. Conley, Chairperson

Heterogenous catalysts often contain complex mixtures of dormant and active sites. Selective deposition of reactive organometallic or inorganic fragments using surface organometallic methods can be used to study structure-property relationships in these materials. The most common reaction pathway using surface organometallic methods involves the reaction of a surface hydroxyl on a metal oxide with an organometallic. A less common pathway involves reaction with strong Lewis acid sites, which is critically important to form ion-pairs for olefin polymerization catalysis. These Lewis sites are usually present in low concentrations on metal oxides, making the study of these ion-pairs a challenge. Surface organometallic methods can be used to develop model systems that mirror the activity of these highly reactive Lewis sites with higher surface coverage.

This work describes the reactivity of dehydroxylated silica with homogeneous Lewis acids to develop novel derivatized supports that maintain well-defined Lewis acidic properties. The first part of this work discusses the reactivity of a Lewis superacid, $Al(OC(CF_3)_3)(PhF)$, with the silanol -OH sites on silica to form the well-defined support $\equiv SiOAl(OC(CF_3)_3)_2(O(Si\equiv)_2)$. Fluoride ion affinity (FIA) calculations, along with experimental trends observed through Guttman-Beckett studies, show that this well-defined aluminum site is a stronger Lewis acid than $B(C_6F_5)_3$ and $Al(OC(CF_3)_3)(PhF)$. This catalyst exhibits characteristic reactivity patterns of Lewis acids, such as methide abstraction of $Cp_2Zr(CH_3)_2$ to generate organometallic ion-pairs that are active in olefin polymerization. Characterization of these supports by solid state NMR further confirms structural insights. The next part of this thesis examines the reaction of $Cp_2Hf(CH_3)_2$ with the aluminum site to form cationic $Cp_2Hf(CH_3)^+$ sites. These sites react with polypropylene and H_2 to form oils with moderate molecular weights. These results demonstrate that Ziegler-Natta-type active sites are compatible with polyolefin upcycling. The final part of this thesis examines the reactivity of a Lewis acidic carboranyl borane with isolated silanols to generate a well-defined Lewis site ($^{Me}oCb_2B)(OSi\equiv)$. The three-coordinate boron site isolated on the support maintains strong Lewis acidity, and reactions of this support with $Cp_2Hf(CH_3)_2$ show that the Lewis sites also demonstrate methide abstraction, but with low efficiency, likely due to the steric environment of the carborane.

Table of Contents

List of Figures

List of Schemes

List of Tables

General Experimental Considerations

All manipulations were performed under an inert atmosphere of dinitrogen or argon using standard Schlenk or glovebox techniques. Solvents including pentane, diethyl ether, toluene, and THF were dried by passing through a J.C. Meyer solvent system containing two activated alumina columns, then following drying procedures mentioned below as appropriate per solvent. Hydrocarbon solvents and ethereal solvents were dried over sodium/benzophenone, degassed by freeze-pump-thaw cycles, distilled under vacuum, and stored in an inert atmosphere glovebox. Halogenated solvents, including fluorobenzene, were dried over CaH_2, degassed, and vacuum distilled prior to use. The primary metal oxide used in this thesis was $SiO_{2\text{-}700}$, which was purchased as Aerosil-200 silica and partially dehydroxylated at 700˚C, following a procedure previously reported.[1] Gases such as vinyl chloride and deuterium were stored over activated BASF Cu catalyst and 4Å molecular sieves for at least 24h to remove O_2 and H_2O. High pressure experiments for hydrogenolysis used ultra high purity hydrogen purchased from Airgas passed through oxygen/water trap (CRS, ZPure H_2O/O_2) immediately before use.

References

1. Copéret, C.; Comas-Vives, A.; Conley, M. P.; Estes, D. P.; Fedorov, A.; Mougel, V.; Nagae, H.; Núnez-Zarur, F.; Zhizhko, P. A. Surface Organometallic and Coordination Chemistry toward Single-Site Heterogeneous Catalysts: Strategies, Methods, Structures, and Activities. *Chem. Rev.* **2016**, *116* (2), 323–421. https://doi.org/10.1021/acs.chemrev.5b00373.

Chapter 1. Introduction to the Dissertation

Abstract

Well-defined organometallics supported on high surface area oxides are promising heterogeneous catalysts. An important design factor in these materials is how the metal interacts with the functionalities on an oxide support, where the metal can either form a covalent M–O bond or form an electrostatic $M^{+}\cdots{}^{-}O$ ion-pair, which impacts how well-defined organometallics will interact with substrates in catalytic reactions. A less common reaction pathway involves the reaction of a Lewis site on the oxide with the organometallic, resulting in abstraction to form an ion-pair, which is relevant to industrial olefin polymerization catalysts.

Introduction

Chemical industry overwhelmingly prefers the use of heterogeneous catalysts due to the ease of separation and scalability, among other reasons. The mixtures that compose these heterogenous catalysts can be complex and generate a variety of active sites, making it challenging to parse structure-property relationships in these systems. These well-defined heterogeneous systems are typically generated using a high surface area metal oxide and an organometallic species. The Brønsted acidic -OH site on the metal oxide and the organometallic M-R can react to form either a covalent M-O bond or form an M^{+}---O^{-} ion-pair. The organometallic can also react with Lewis sites on the metal

oxide support, which results in abstraction to form an ion-pair. This pathway is relevant to olefin polymerization catalysts, which have been of high interest to both industrial and academic research for decades.

This chapter explores the reactivity patterns between an organometallic and a metal oxide support through Brønsted and Lewis acidity on surface sites. This draws on homogeneous chemistry studies, which have been observed to form reactive ion-pairs. The applications of well-defined surface sites are far reaching, given the ubiquity of heterogeneous catalyzed industrial processes. Developing an understanding of the topography of these materials, and the ways that key concepts in chemistry such as Brønsted and Lewis acidity can factor into the activity observed in these catalysts, is critical from an academic and industrial perspective.

Brønsted and Lewis acidity are two of the most deeply ingrained concepts in all of chemistry. For example, manipulation of Bronsted acid strength using acid dissociation constants (*i.e.* pK_a) is a part of the general chemistry curriculum and is one of the clearest examples of a structure-property relationship. We suspect that nearly all the readers of this work would be able to rank Bronsted acid strength in the order HCl < H_2SO_4 < HSO_3CF_3.

Common pK_a or Hammett acidity scales for liquid acids include significant solvation energies that ultimately drive acid dissociation in solution. The Haber-Born cycle shown in Figure 1.1 for aqueous HCl illustrates this point. Heterolytic cleavage of HCl to form H^+ and Cl^- is endothermic, which is characteristic of all HX acids, and is usually measured as the deprotonation energy (DPE = -E_{pa}; E_{pa} = proton affinity). The

driving force for HCl dissociation in aqueous media is entirely driven by ΔH_{hyd} for H^+ and Cl^-. This also explains why acidity trends often change when moving from water to polar aprotic MeCN. HCl acts as a weaker acid in MeCN (pK_a (MeCN) = 10.4) than it does in H_2O (pK_a (H_2O) = -8);[1] ΔH_{diss} decreases to -34.7 kJ mol^{-1} driven mostly by the decrease in ΔH_{MeCN} for Cl^- (347.7 kJ mol^{-1}, ΔH_{MeCN} for H^+ = -1100 kJ mol^{-1}). [2-4]

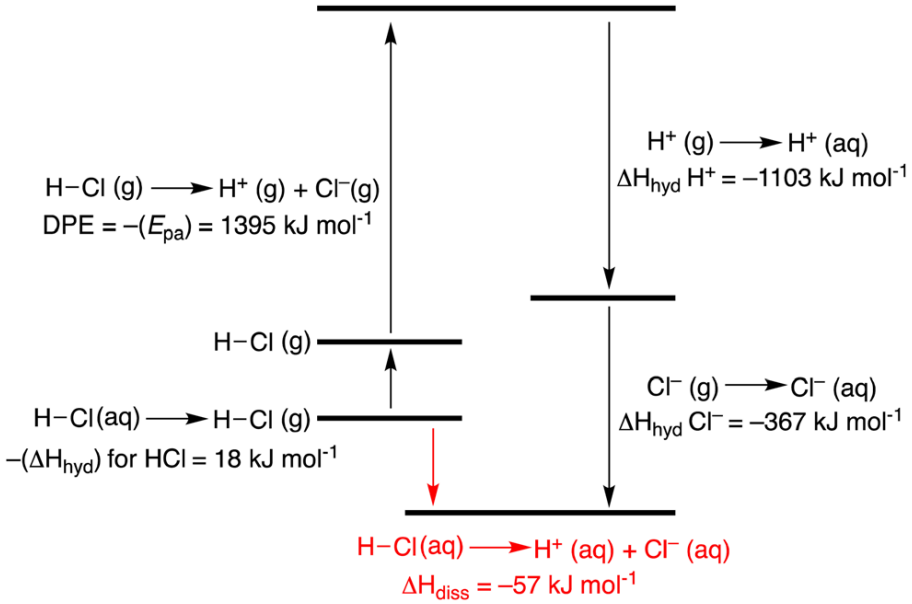

Figure 1.1. Haber–Born cycle giving the energetics for HCl dissolution in water. Values in the figure and cited in the text are taken from ref. 2 and 3. ΔH_{hyd} is taken from ref. 4.

Measuring the Bronsted strength of solid acids is challenging. For example, acidic oxides react with bases (*e.g.* pyridine, NH_3, PR_3, *etc*.) to form ion-pairs, Figure 1.2. [5-7] Experimentally, adsorption/ desorption techniques give ΔH_{abs}, but these values do not typically scale with acid strength as expected for Hammett acids.[8,9] Indeed, the thermodynamic cycle shown in Figure 1.2 shows that DPE and E_{pa} of the base are

included in ΔH_{abs}, but a third $\Delta H_{ion\text{-}pair}$ is also necessary in a 1 : 1 adduct. In essence, the solvation terms driving the dissociation of HX in solution are absent on an oxide surface.

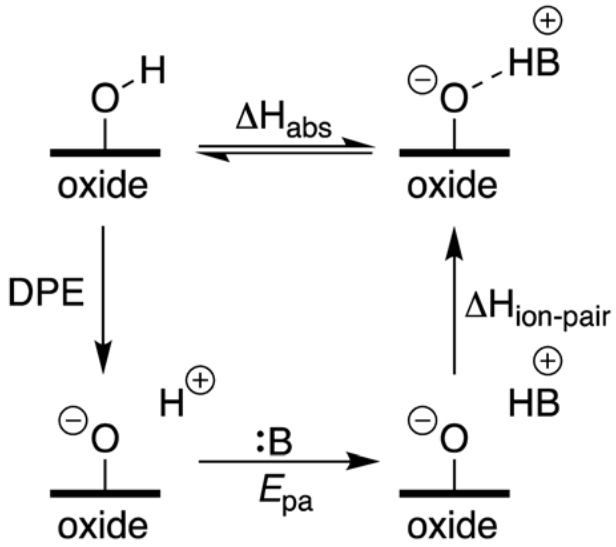

Figure 1.2. Thermodynamic steps involved in the adsorption of a base onto an acidic support.

This challenge is not unique to oxides. Solid carborane acids are the strongest known Bronsted acids. [10, 11] These acids react with even the most inert solvents (*e.g.* liquid SO_2, alkanes, *etc*.), contrasting these Bronsted acids from more typical liquid superacids containing mixtures of HX and Lewis acids.[12] Reed described a clever strategy to assess Bronsted acid strength by measuring $\nu_{N\text{-}H}$ of $[Oct_3N\text{-}H][X]$ in CCl_4 solution. [13] The apolar solvent promotes contact ion-pair formation, thus the $\nu_{N\text{-}H}$ value correlates with ion-pair strength; weaker ion-pairs will have high $\nu_{N\text{-}H}$ values and correlate with stronger acidity. Indeed, there is a linear correlation between $\nu_{N\text{-}H}$ of $[Oct_3N\text{–}H][X]$ and DPE from DFT calculations across a wide range of anions, though calorimetry data that would deliver $\Delta H_{ion\text{-}pair}$ was not reported.

However, the challenge becomes more complex because many oxides containing Brønsted acidic –OH groups also contain Lewis sites that react with common bases used to probe these surfaces. [14] Indeed, strong Lewis acid sites are common on oxide surfaces and have important roles as heterogeneous catalysts. [15,16] and are known to activate inert C–H bonds.[17–23]

Acidity is also practically important when reacting organometallics with oxides to form well-defined heterogenous catalysts. [23–28] Predicting which of the three structures would form in Figure 1.3 is straightforward, only if the types of reactive sites on an oxides are known. Oxides containing weak Brønsted acid –OH sites will react with L_nM–R to form **A** while strong Brønsted acid –OH sites will form **B**. Alkyl or hydride abstraction reactions occur in reactions of organometallics and oxides containing a significant quantity of Lewis sites to form **C**. Though less common, this reaction is an important method to generate ion-pairs on surfaces. [29]

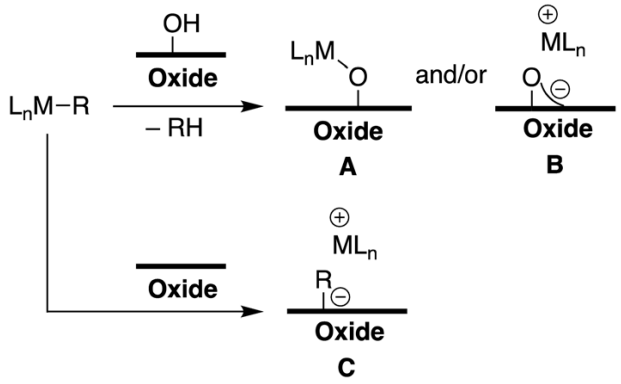

Figure 1.3. Reactions of LnM–R with an oxide can form neutral **A** or ion-paired **B** or **C**.

This article describes how Brønsted and Lewis acidity on surfaces affects the speciation shown in Figure 1.3, with an emphasis on generation of ion-pairs. We begin

with a short description of molecular olefin polymerization catalysts because the activity of these complexes often depends on strong Brønsted and Lewis acid activators that form weakly coordinating anions that are critical for activity in this class of catalyst. [30] Using this reaction as motivation we also describe methods to generate well-defined strong Brønsted and Lewis acids on oxide surfaces that function as weakly coordinating oxides, which are an emerging class of supports that can have impact on well-defined catalysts beyond olefin polymerization catalysis. An ever-present challenge in these studies is the characterization of the active site at the molecular level. This usually requires a combination of experimental spectroscopies. For example, rich molecular information is available using solid-state NMR spectroscopy, [31] and the advent of dynamic nuclear polarization (DNP) [32,33] overcomes the low inherent sensitivity of NMR spectroscopy. When used in combination with computational studies [34] that correlate structure with the trends in NMR properties excellent structural resolution is possible. X-ray absorption spectroscopy is also commonly used to characterize these types of materials, [35] but care must be taken to correlate XAS properties with a library of carefully chosen molecular precursors. [36]

The importance of acidity on surfaces in heterogeneous olefin polymerization catalysts

Catalysts that generate polyolefin plastics, extremely versatile materials produced on massive scales, are some of the most efficient and selective examples of catalysts in organometallic chemistry. This is in no small part due to the detailed mechanistic

understanding of how these catalysts form and function in solution. The preceding decades saw tremendous advances in the design of transition metal catalysts for the polymerization of olefins, [30,37–45] which continue to advance to address key challenges associated with the synthesis of state-of-the-art plastics. [46] These success stories are certainly related to systematic modification of simplified structural models to achieve a target property, Figure 1.4(a).

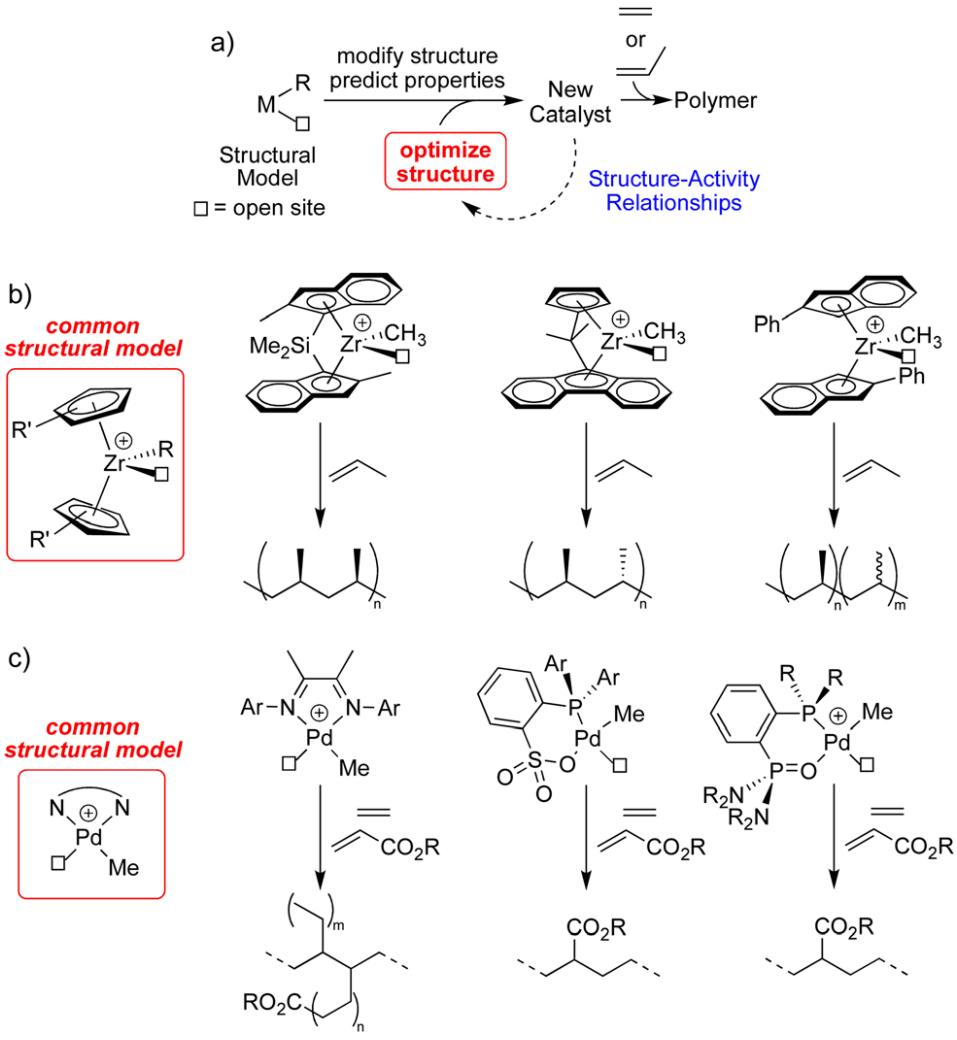

Figure 1.4. The structure activity relationship in olefin polymerization catalysts (a). Examples showing how the common Cp_2Zr–R+ motif can be extended to complex structures that exert diastereocontrol in polypropylene synthesis (b). A related (N^N)Pd–

Me+ (N^N = bidentate nitrogen containing ligand) structural model that results in polar monomer incorporation (c).

In the most basic form, an active catalyst for olefin polymerization contains an empty coordination site *cis* to a metal-alkyl (or metal-hydride) of a (usually) cationic organometallic complex. The open coordination site and/or charge is installed using activators that suit either the early metal catalysts shown in Figure 1.4(b) or the late metal catalysts shown in Figure 1.4(c). The vast majority of polymers generated industrially use Group IV organometallic cations, usually formed *in situ* using organoaluminum activators, in the presence of strong Lewis acid (e.g. $B(C_5F_5)_3$, oxide, methaluminoxane).[30,47] One exquisite set of examples showing how discrete control of the stereochemical environment of the active Zr–R+ site result in different polypropylene products is shown in Figure 1.4(b),[38] and relies on the formation of an ion-pair containing a weakly coordinating anion (e.g. $[MeB(C_6F_5)_3]$, $[B(C_6F_5)_4]$, [MeAlOX], etc.) for catalytic activity.

Late transition metal catalysts are often activated by solvated ether acid ($[HOEt_2][BAr_4]$, Ar = C_6F_5 [48] or 3,5-$(CF_3)_2$–C_6H_4 [49]). The organopalladium catalysts shown in Figure 1.4(c) follow a similar structural model, but engage in different structure property trends because palladium catalysts can incorporate polar monomers into polyethylene chains. The a-diimine palladium catalysts reported by Brookhart and co-workers polymerize mixtures of ethylene and acrylate esters to incorporate the polar monomer into chain ends,[50] and manipulation of the aryl group on the ligand can modulate branching in the polymer.[51] However, the neutral phosphine–sulfonate

palladium catalyst incorporates acrylate esters in-chain because these catalysts undergo slow chainwalking processes that creates branches.[40] The cationic phosphine-phosphine oxide catalyst essentially combines these two design strategies to form an electron rich palladium cation that produces linear copolymers that incorporate polar monomer in the PE chain.[52]

How do these trends apply to heterogeneous catalysts? The structure–property trend shown in Figure 1.5(a), from a molecular chemist's point of view, is essentially broken for heterogeneous catalysts because of the challenges in assessing active site structure in these very complicated materials (**Figure 5(a)**). Indeed, a proposed intermediate for the ''classic'' Ziegler–Natta catalyst ($TiCl_4/AlR_3/MgCl_2$) was only recently detected using advanced EPR methods, **Figure 5(b).**[53] More modern heterogeneous catalysts rely on mixtures of zirconocenes, alkylaluminums (or methaluminoxane[47]) and an oxide.[54] Based on the clear evidence from solution catalysts shown above, these likely form organometallic zirconocenium ionpairs, **Figure 5(c).** Applying a similar strategy to heterogeneous Pd catalysts for olefin polymerization is not practical because common organoaluminum compounds are incompatible with most palladium precursors. [55]

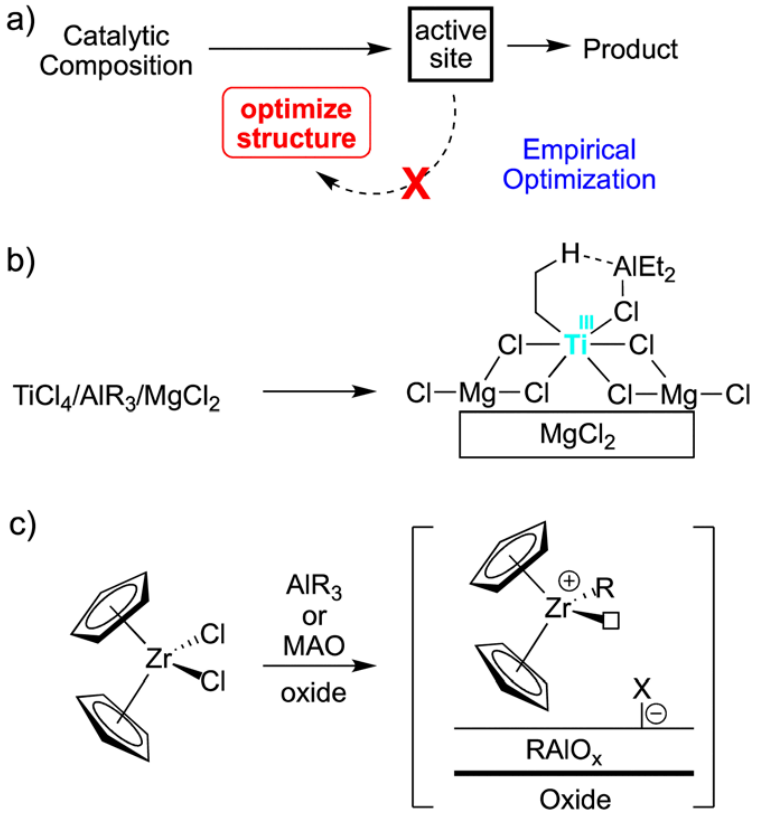

Figure 1.5. Empirical optimization for heterogeneous olefin polymerization catalysts resulting from poor structural knowledge of the active site (a). A plausible intermediate in classic Ziegler–Natta polymerization catalysts detected by EPR spectroscopy (b). Common mixtures used industrially that likely form $Cp_2Zr–R+$ species on AlR_3 functionalized supports.

This is where acidity of surfaces emerges as an important factor in active site formation. We studied a model for industrial catalysts containing $Cp^b{}_2ZrCl2$ (Cp_b = 1-butylcyclopentadienyl) in the presence of excess $AliBu_3$ and g-alumina partially dehydroxylated at 600 ˚C.[56] The complex reactivity of this mixture shown in Figure 1.6 is required for self-assembly of the active site, and hinges on the promiscuity of the excess $AliBu_3$ in this mixture. First, $AliBu_3$ reacts with accessible –OH sites present on the g-alumina surface. This reaction is critical because $AliBu_3$ also rapidly reacts with

$Cp^b_2ZrCl_2$ to form mixtures of $Cp^b_2Zr(\mu\text{-}H)_3(AliBu_2)AliBu_3$ and $Cp^b_2Zr(\mu\text{-}H)_3(AliBu_2)3(\mu\text{-}Cl)_2$ that would undoubtedly react with –OH sites on alumina to form inactive zirconium species. The latter reaction of $AliBu_3$ and unbridged zirconocenes appears general, but Zr(II) intermediates form with ansa-metallocenes resulting in complex speciation in solution.[57] After $AliBu_3$ performs these necessary tasks only $Cp^b_2Zr(\mu\text{-}H)_3(AliBu_2)AliBu_3$ reacts with residual Lewis sites on the passivated γ-alumina surface to form $[Cp^b_2ZrH][HAlOX]$ ion-pairs. This reactivity is akin to the well-known reactions of Cp_2ZrMe_2 with the strong Lewis acid $B(C_6F_5)_3$ to form $[Cp_2ZrMe][MeB(C_6F_5)_3]$ ion-pairs in solution,[30] and related to classic examples describing how organometallics react with γ-alumina surfaces.[29,58]

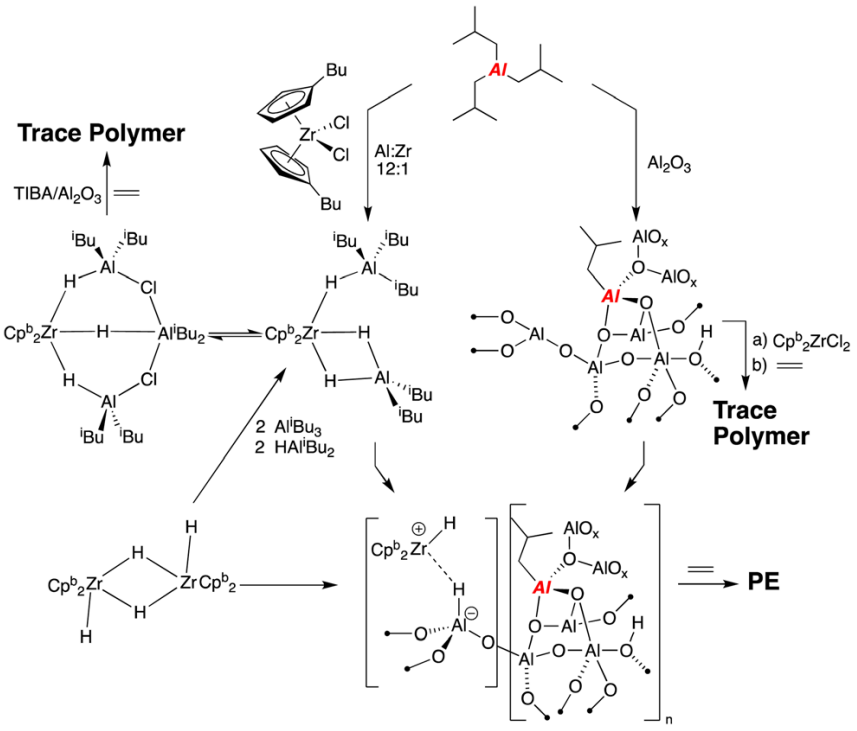

Figure 1.6. The network of reactions that occur to form active Cp^b_2Zr–H+ sites on $AliBu_3/Al_2O_3$ surfaces.

Similar reactivity is not possible on Al^iBu_3/silica[54,59] because this support lacks sufficient Lewis acidity to activate the in situ generated $Cp^b_2Zr(m\text{-}H)_3(Al^iBu_2)Al^iBu_3$. However, relating the reactivity in Figure 1.6 to any Cp_2ZrCl_2/AlR_3/oxide combination should be taken with extreme caution. Though $Cp^b_2ZrCl_2/Al^iBu_3$/silica is not an active catalyst, zirconocene dichlorides with methaluminoxane and silica (or alumina[60]) are another common mixture for active olefin polymerization catalysts. Determining structure in the latter combination are exceptionally challenging because of the complexities associated with the behavior of methaluminoxane in solution and on oxide surfaces.

Installing an aluminum Lewis site on silica

The reactivity in Figure 1.6 clearly implicates that Al^iBu_3/alumina contains strong Lewis acid sites and that the $[H–AlO_X]$ anion behaves as a weakly coordinating anion.[61] Installing a strong Lewis site on an oxide to form a well-defined site is a surprising challenge. Partially dehydroxylated silica nearly always reacts with AlR_3[59,62–64] or GaR_3[65–67] to form mixtures of surface species. $B(C_6F_5)_3$ shows complicated reactivity with silica supports, Figure 1.7(a). Reactions with silica pre-treated at 700 ˚C ($SiO_{2\text{-}700}$, B1 – OH nm^2) form unstable adducts with isolated silanols and the borane, which can be deprotonated with aniline bases to form $[PhNHMe_2][RSiOB(C_6F_5)_3]$.[68–70] However, silica pre-treated at 500 ˚C ($SiO_{2\text{-}500}$) reacts with $B(C_6F_5)_3$ through a series of steps to form pairs of $RSiOB(C_6F_5)_2$ sites that are not capable of activating Cp_2ZrMe_2.[71]

We investigated the reaction of $Al(OC(CF_3)_3)(PhF)$[72] with $SiO_{2\text{-}700}$.[73] The choice of this particular combination was driven by two complementary rationales. First, $Al(OC(CF_3)_3)(PhF)$ is a significantly stronger Lewis acid than $B(C_6F_5)_3$ based on fluoride ion affinity calculations.[74,75] Second, the Al–O in $Al(OC(CF_3)_3)(PhF)$ should be more reactive to the isolated silanols than the B–C in $B(C_6F_5)_3$. In both cases the Lewis acid coordinates to the silanol to form a bridging silanol intermediate (Figure. 1.7(b)), which is certainly plausible for $B(C_6F_5)_3$ based on the reactivity shown in Figure. 1.7(a) (top reaction) and was fully characterized in reactions of $SiO_{2\text{-}700}$ and $Al(OC(CF_3)_3)(PhF)$,[76] which will be described in more detail in the section describing Brønsted acidity. In the transition state that results in grafting onto $SiO_{2\text{-}700}$ the acidic proton is either transferred to the B–C to form $RSiOB(C_6F_5)_2$ and C_6F_5H, which is evidently high barrier, or to the Al–O to form $RSiOAl(OC(CF_3)_3)_2(O(SiR)_2)$ and $HOC(CF_3)_3$. The fact that $RSiOAl(OC(CF_3)_3)_2(O(SiR)_2)$ forms and $RSiOB(C_6F_5)_2$ does not is similar to results showing that $Zr(OtBu)_4$ reacts with silica faster than $Zr(CH_3{}^tBu)_4$ despite the obvious thermodynamic driving force for the latter.[77]

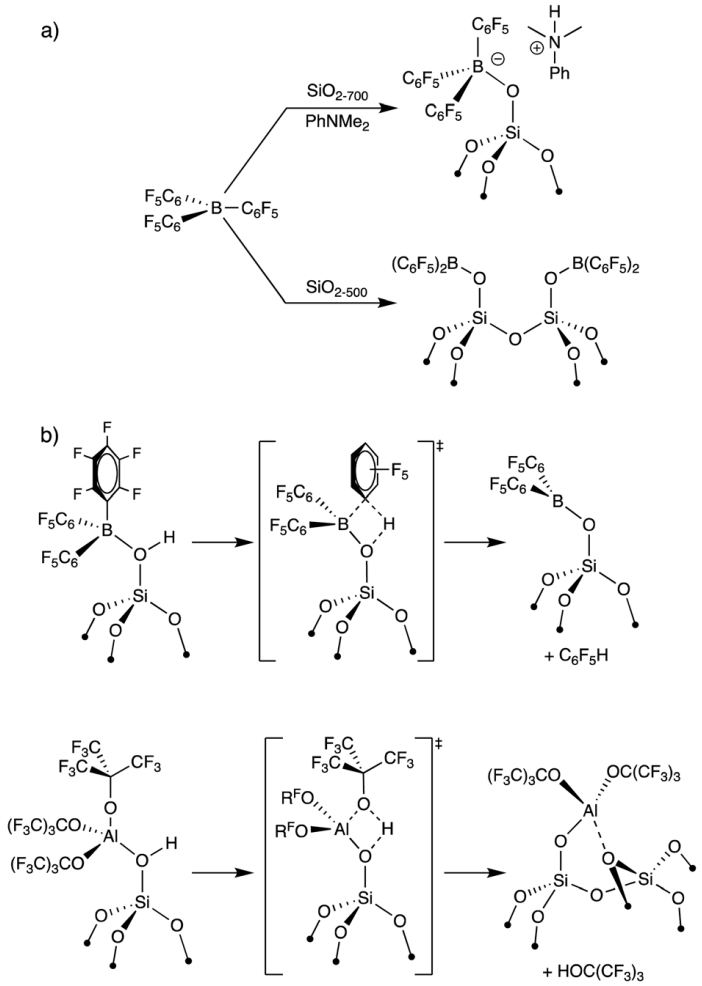

Figure 1.7. Reactions of $B(C_6F_5)_3$ with SiO_2 (a). Differences in transition state structure for the reaction of $B(C_6F_5)_3$ or $Al(OC(CF_3)_3)$ with SiO_2 (b).

The 27Al MAS NMR spectrum of $RSiOAl(OC(CF_3)_3)_2(O(SiR)_2)$ acquired at 18.8 T shown in Figure. 1.8(a) contains a signal at 74 ppm with a quadrupolar coupling constant (C_Q) of 18.0 MHz, consistent with a distorted trigonal bipyramidal Al environment (t = 0.63) that is reproduced using the small cluster model shown in Figure. 1.8(b). Fluoride ion affinity (FIA) calculations using typical isodesmic reactions[74,75] show that $RSiOAl(OC(CF_3)_3)_2(O(SiR)_2)$ has a FIA of 528 kJ mol^{-1}. This value is significantly

larger than the calculated FIA for $B(C_6F_5)_3$ (448 kJ mol^{-1}) and slightly larger than isolable $Al(OC(CF_3)_3)(PhF)$ (514 kJ mol^{-1}), but less than a hypothetical free $^{i}Pr_3Si^+$ (1073 kJ mol^{-1}).[78]

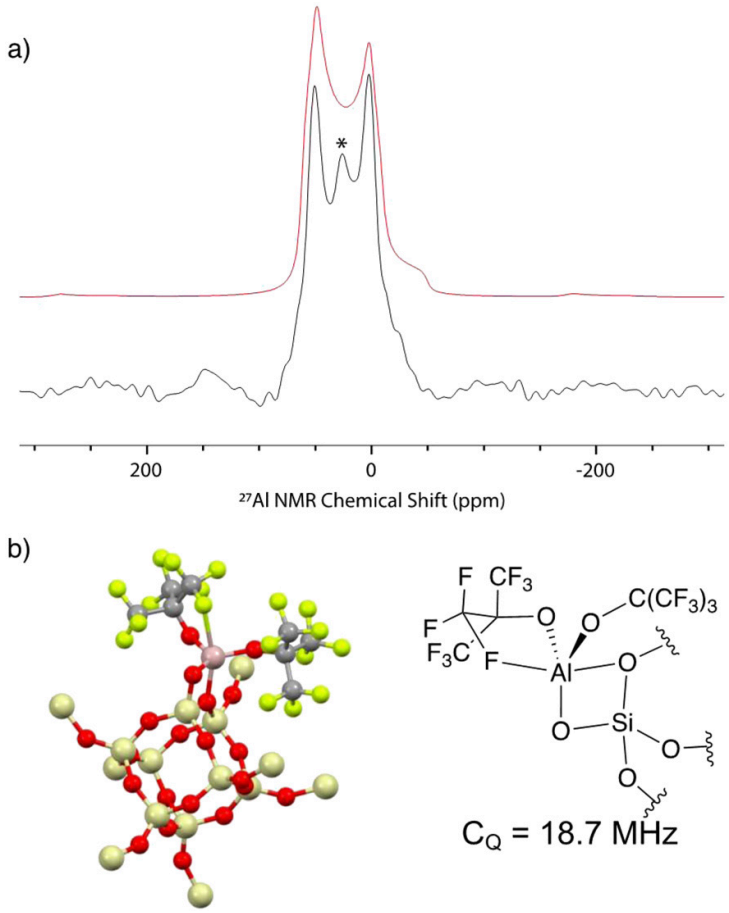

Figure 1.8. $^{27}Al\{^1H\}$ MAS NMR spectrum of $RSiOAl(OC(CF_3)_3)_2(O(SiR)_2)$ at 18.8 T (a, experimental in black simulation in red, n_{rot} = 18.87 kHz, * = probe background); calculated structures approximating $RSiOAl(OC(CF_3)_3)_2(O(SiR)_2)$ using a silsesquioxane cluster (b).[79] A structure showing the coordination environment around Al and the calculated ^{27}Al C_Q is given next to the calculated structure. Reproduced from ref. 76 with permission from WileyVCG GmbH, copyright 2022.

Cp_2ZrMe_2 reacts with $RSiOAl(OC(CF_3)_3)_2(O(SiR)_2)$ to form $[Cp_2ZrCH_3][SiOAl(OC(CF_3)_3)_2(CH_3)]$ as a major product, which is indicative of methide

abstraction. Thus this material behaves similarly to $B(C_6F_5)_3$ in solution or solid Al^iBu_3/Al_2O_3, Figure. 1.9. Unlike Al^iBu_3/Al_2O_3, which contains a very small quantity of Lewis sites (~1.8 mmol g^{-1} based on active Zr–H^+ quantification), the surface coverage of Lewis acidic Al in $RSiOAl(OC(CF_3)_3)_2(O(SiR)_2)$ is 240 mmol g^{-1}. This advantage will likely facilitate synthesis and characterization of other organometallic ion-pairs on this well-defined strong Lewis acid containing oxide.

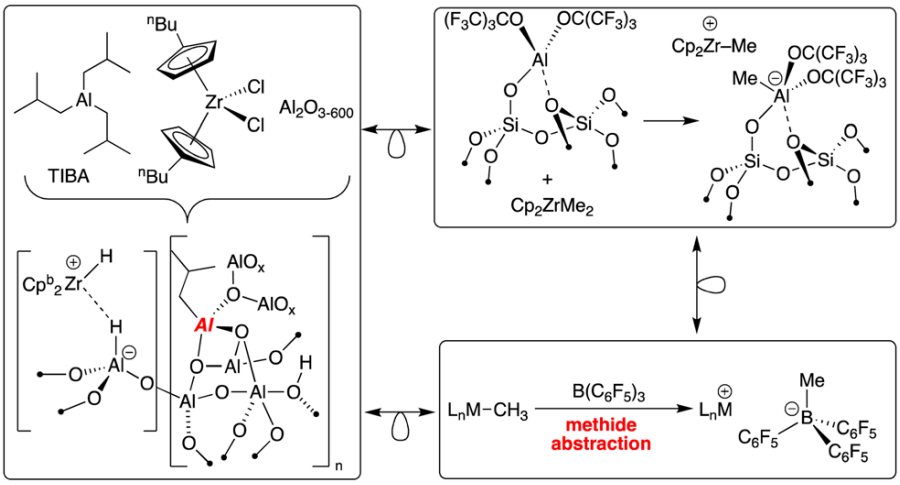

Figure 1.9. The connections between Cp^bZrCl_2/Al^iBu_3/alumina, $B(C_6F_5)_3$ and $RSiOAl(OC(CF_3)_3)_2(O(SiR)_2)$ to form type C species.

Towards weakly coordinating supports: the importance of Brønsted acidity

Brønsted acidic –OH sites, such as those present on sulfated oxides, form weakly coordinating ion pairs with organometallics.80 The reactivity of Cp*ZrMe3 with SiO2 and sulfated aluminum oxide (SAO) serves as a representative example that distinguishes between type A and type B surface species, Figure. 1.10. When supported on SiO2 the organozirconium species formed, Cp*ZrMe2(OSiR), is unreactive to ethylene

polymerization because the necessary coordination site is ‘‘blocked’’ by the OSiR ligand.81 However, SAO reacts with Cp*ZrMe3 to form the [Cp*ZrMe2][SZO] ion-pair that is active for ethylene polymerization and arene hydrogenation reactions.82,83

Though the results in Figure. 1.10 clearly implicate that SAO is a stronger Brønsted acid than SiO2, the acid strength of sulfated oxides as a family of materials is controversial. For example, sulfated zirconium oxide (SZO) was reported to isomerize n-butane to isobutane at lower temperatures than 100% H2SO4, which was interpreted as evidence for superacidic –OH sites on the ZrO2 surface.84 Subsequent colorimetric studies performed by adsorption of Hammett bases with known basicity onto SZO also suggested that the OH sites on this support have H_0 values less than 16.04, suggesting that SZO is at least 4 orders of magnitude more acidic than 100% H_2SO_4 ($H_0 = 12$).[85] As noted in the introduction, solid acids cannot be treated with similar methods as liquid acids, and colorimetric methods are not reliable measures of acid strength of solid acids.[86,87] Indeed, related studies suggest that the Brønsted acid site has little, if any, influence on alkane isomerization chemistry of SZO.[88,89]

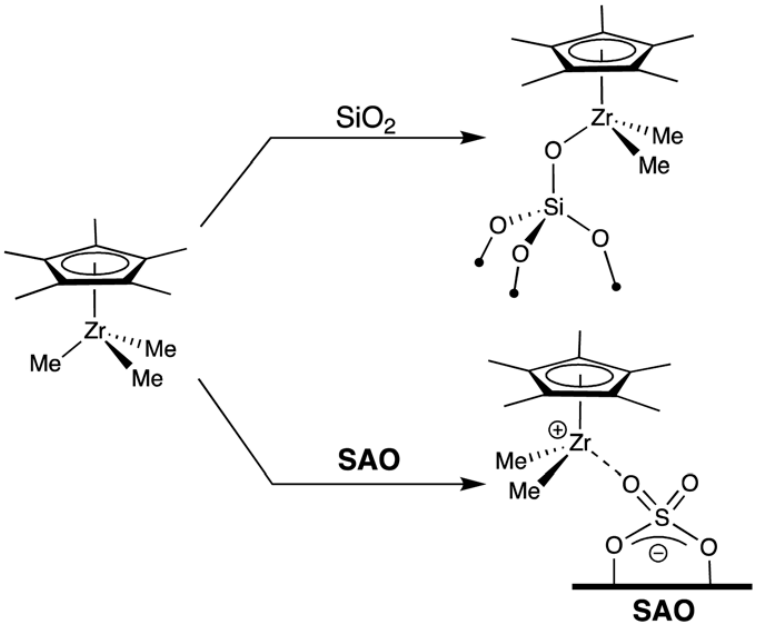

Figure 1.10. Reaction of Cp^*ZrMe_3 with SiO_2 to generate $Cp^*ZrMe_2(OSiR)$ or sulfated aluminum oxide (SAO) to generate $[Cp^*_2ZrMe][SZO]$.

The SZO surface is complex and contains Brønsted,[90] Lewis,[91] and pyrosulfate sites;[92] selection of a probe molecule to evaluate only acidity of –OH sites is a challenge. We found that SZO partially dehydroxylated at 300 ˚C reacts with P^tBu_3 at 25 ˚C in Et_2O to form only $[HP^tBu_3][SZO]$.[93] This result prompted us to systematically study the reaction of substituted $^tBu_2PAr$ with SZO in MeCN to determine how electronics at phosphorus affect the formation of $[(^tBu)_2ArPH][SZO]$, Figure 1.11(a). In all cases the adsorption equilibria follow classic Langmuir binding isotherms that allow for extraction of K_a for the range of $[(^tBu)_2ArPH][SZO]$ generated in this study. Binding to SZO (19000 o K_a o 74000 in MeCN) systematically decreases as the pK_a of $[(^tBu)_2ArPH][BF_4]$ increases over almost four orders of magnitude (12.6 o pK_a o 16.4 in MeCN). A Hammett plot of s, derived from the pK_a of the $[(^tBu)_2ArPH][BF_4]$,[94] versus K_a is linear, Figure

1.11(b). This particular result shows that Hammett behavior is possible for a solid acid once solvation is introduced. This behavior is inconsistent with superacidic behavior. First, MeCN reacts with superacids to form [H(MeCN)n] solvates,12 which is expected to result in significantly higher Ka values. Second, weaker bases like PPh3 (pKa(HPPh3) = 7.6 in MeCN) have very low affinity for SZO (Ka B 3 M1), and p-nitroaniline (pKa(anilinium) = 6.22 in MeCN)95 does not react to form an ammonium on the SZO surface.

a)

X	σ	pK_a [1H][BF_4]	K_a (x10^4 M^{-1})
OMe	-1.6	16.4	7.4
^{t}Bu	-1	5.5	15.8
Me	-0.9	5.5	15.7
TMS	-0.1	4.7	14.9
H	0	4.3	14.7
F	0.8	3.0	14.0
CF_3	1.9	2.6	12.9
CN	2.2	1.9	12.6

b)

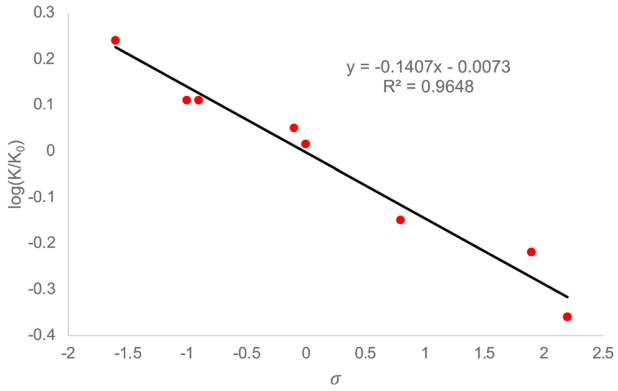

Figure 1.11. Reactions of ^{t}Bu$_2$PAr with SZO to form [(^{t}Bu)$_2$ArPH][SZO] in MeCN slurry (a). s, pK_a of [(^{t}Bu)$_2$ArPH][BF_4], and K_a for each substituent tested is given in the table below the equation. Hammett plot for the binding of tBu$_2$PAr to SZO (b).

This study shows that the –OH sites on SZO are, in fact, a rather weak Brønsted acids. Indeed, DFT calculations show that sulfuric acid adsorbs onto ZrO_2 surfaces to form tripodal sulfate sites with the proton laying on nearby Zr–O–Zr bridges.[96] The calculated DPE of the protonated Zr–O–Zr bridges ranges from 1339–1548 kJ mol^{1}, significantly higher than the DPE of H_2SO_4 (1306 kJ mol^{1}). This collection of results is satisfying because ZrO_2 is a mild proton acceptor (i.e. a Brønsted base), and it is not expected that the reaction of a strong acid and a weak base would result in a superacid.

Until recently, sulfated oxides were the only weakly coordinating support available to form ion-pairs with organometallics. This is a significant limitation considering the structural diversity and range of ion-pairing characteristics widely available to the community that uses weakly coordinating anions in solution.[97,98] We approached this challenge by generating a very strong Brønsted acid site on an oxide. The Brønsted site in zeolites and silica alumina are silanols coordinated to a nearby Lewis acidic aluminum in the material framework, simplified in Figure 1.12(a). We viewed this as a solid Lewis acid activated Brønsted acids that have extensive precedent in the synthetic organic chemistry community.[99] Selection of an appropriately strong Lewis acid should result in formation of a well-defined strong Brønsted acid site that when deprotonated should behave as a weakly coordinating anion.[100]

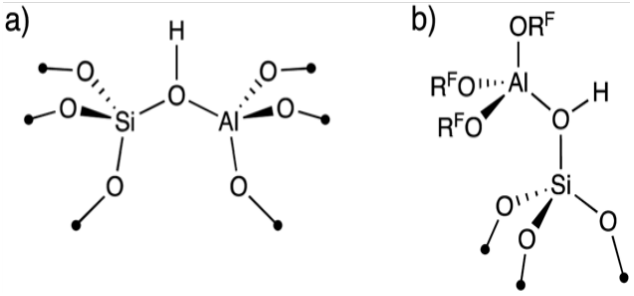

Figure 1.12. The acidic bridging silanol in a silica alumina (a) and in $Al(OC(CF_3)_3)(PhF)$ reacted with $SiO_{2\text{-}700}$ to form $RSi–OHAl(OR^F)_3$ (b).

The reaction of $Al(OC(CF_3)_3)(PhF)$ with $SiO_{2\text{-}700}$ results in solvent specific reactivity. In PhF with mild heating $RSiOAl(OC(CF_3)_3)_2(O(SiR)_2)$ forms as discussed above.[73] In perfluorohexanes at 25 ˚C $Al(OC(CF_3)_3)(PhF)$ reacts with $SiO_{2\text{-}700}$ to form the bridging silanol $RSi–OHAl(OR^F)_3$, Figure 1.12(b).[76] $Al(OC(CF_3)_3)$ coordinated to an isolated silanol on a small cluster model reproduces ν_{OH} (exp = 3550 cm^{-1}, calc = 3542 cm^{-1}), 1H NMR chemical shift (exp = 5.0 ppm, calc = 5.1 ppm), Al NMR properties (exp C_Q = 14.6 MHz, calc C_Q = 15.3 MHz), and H–Al distance (exp = 2.4–2.5 Å, calc = 2.46 Å). The excellent agreement between experiment and theory provides foundation for the calculated DPE using this model, which was 1099 kJ mol^{-1}. At the same level of theory the DPE of HSO_3CF_3 is 1233 kJ mol^{-1} (exp = 1240 kJ mol^{-1}). Though $RSi–OHAl(OR^F)_3$ is a strong Brønsted acid it is still far weaker than $H[Al(OR^F)_4]$ (calc = 1041 kJ mol^{-1})[101] and $H[CHB_{1\text{-}C}l_{11}]$ (calc = 1000 kJ mol^{-1}).[13]

The strong Brønsted acidity of $RSi–OHAl(OR^F)_3$ implies weakly coordinating behavior when deprotonated. The reaction of $RSi–OHAl(OR^F)_3$ with $NOct_3$ forms $[HNOct_3][RSiO– Al(OR^F)_3]$, which has a ν_{NH} at 3070 cm^{-1}. This value is higher than

[ClO_4] (3049 cm^{-1}), [FSO_3] (2953 cm^{-1}), and [CF_3SO_3] (2939 cm^{-1}); but lower than [$CHB_{1^-}Cl_{11}$] (3163 cm^{-11}) and [$B(C_6F_5)_4$] (3223 cm^{-1}). These results indicate that [RSiO–$Al(OR^F)_3$] is more weakly coordinated to the ammonium than first generation anions, but less weakly coordinated than state-of-the-art borane and carborane anions.

The relationship between ^{29}Si NMR chemical shift and Brønsted acidity: an emerging scale for solid-state acidity?

The power of pK_a or Hammett acidity parameters are obvious. These values provide a direct method to compare a key thermodynamic driving force that predicts reactivity. A similar ‘‘singlepoint’’ measurement or parameter that predicts the Brønsted acidity of a solid acid would be similarly beneficial. From the discussion above, we tend to focus on calculated DPE as a reliable measure of acidity for solids because this is the only parameter that gives a measure for the thermochemical driving force for the heterolytic cleavage of an –OH to H^+ and –O. The drawback of this approach is that values obtained from these calculations depend on how accurately the model represents reality, which can be difficult when modelling surface species.

One of the most common methods to obtain information about acidity on a surface is to adsorb a probe that has a spectroscopic readout. The classic example is adsorption of pyridine onto an oxide, which has a characteristic n_CQ_C stretch that is used to quantify Brønsted and Lewis site surface coverage.[6,102] Solid-state NMR spectroscopy of oxides contacted with probe molecules is another promising method to obtain information about acidity. Drago showed that adsorption of triethylphosphine oxide

(TEPO) onto an oxide results in changes in ^{31}P MAS NMR chemical shift that correlates to some degree with Brønsted or Lewis acidity of surface sites.[103] The $^{31}P\{^{1}H\}$ NMR chemical shift of TEPO coordinated to a Lewis acid is also an excellent probe to measure Lewis acid strength.[104] Indeed, phosphorous probes are very useful probes for acidity because they are both Brønsted and Lewis bases, and the high sensitivity 31P NMR nucleus allows for rapid signal acquisition. [5, 105]

The ^{29}Si NMR chemical shift of R_3Si-capped oxides is emerging as another single-point measurement that provides information about Brønsted acidity of –OH sites on oxides. The origin of deshielding in ^{29}Si NMR is related to the structure of $R_3Si–X$ or $[R_3Si][X]$.[106] For a planar ‘‘free’’ $^{i}Pr_3Si^{+}$, which has resisted isolation even with the most weakly coordinating anions,[107,108] DFT calculations predict a ^{29}Si NMR chemical shift of 343 ppm. The ^{29}Si NMR chemical shift of $[^{i}Pr_3Si][CH_6B_{11}Br_6]$ is 110 ppm, and data from single crystal X-ray diffraction studies show that the Si is pyramidal ($S_{C–Si–C}$ = 350.91) because a Br from the carborane anion is in close contact to the Lewis acidic silicon.[109] DFT reproduces this structure and ^{29}Si NMR chemical shift, and broadly reproduces these parameters for a wide range of $R_3Si–X$ or $[R_3Si][X]$. [29]

Si NMR chemical shift deshielding is related to the paramagnetic term (s^{p}) of the isotropic chemical shift (s^{iso}). The magnitude of s^{p} is proportional to the coupling between the ground state wavefunction (j_0) and an excited state wave- function (j_n) through the angular momentum operator ($\hat{}L_{ki}$, where ki = element of the shielding tensor, eqn (1)). The denominator in eqn (1) shows that large s^{p} contributions are expected when j_0 and j_n are close in energy, which is maximized at the HOMO– LUMO gap. This effect is largest

for the s_{11} component of the chemical shift tensor, which is reliably calculated using DFT methods, and has found broad application to predict structure and reactivity in organometallic compounds,[110–112] organic molecules,[113] and aryllithium reagents.[114]

$$\sigma_{ij}^{p} \propto \frac{\langle \varphi_0 | \hat{L}_{ki} | \varphi_n \rangle \langle \varphi_n \left| \frac{\hat{L}_{kNj}}{r_{kN^3}} \right| \varphi_0 \rangle}{\Delta E_{n-0}} \qquad (1)$$

Figure 1.13 shows the surface of the chemical shift tensor (CST), the orientation of the CST, and the orbitals involved in s^p for planar iPr_3Si^+ and pyramidal $[iPr_3Si][CH_6B_{11}Br_6]$. In both cases the HOMO is the $s_{Si–C}$ and the LUMO is the formally empty p-orbital on silicon. In anion-free $^iPr_3Si^+$ the planar silicon places the $s_{Si–C}$ perpendicular to the LUMO, which results in strong paramagnetic deshielding and large s^p. Approach of the weak $[CH_6B_{11}Br_6]$ nucleophile results in pyramidalization at silicon, which reduces s^p and results in a less deshielded ^{29}Si NMR nucleus.

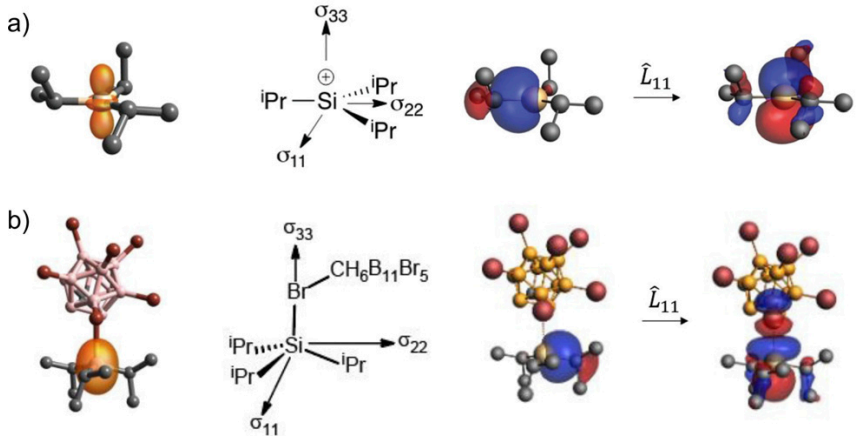

Figure 1.13. Surface of the CST using TensorView,115 orientation of the CST, and orbitals involved in sp of the most deshielded (s11) term of the CST that result in the downfield chemical shift for iPr3Si+ (a) and [iPr3Si][CH6B11Br6] (b). Reproduced from ref. 106 with permission from the Royal Society of Chemistry, copyright 2020.

There is a reasonable correlation between DPE and ^{29}Si NMR chemical shift, Figure 1.14(a). This trend is related to the pyramidalization at silicon and not charge, the latter of which is not expected to affect chemical shift.[116] Importantly, this correlation is applicable over a broad range of DPE for both molecular HX and small clusters that approximate the chemical environment of R_3Si-capped surfaces. The three small clusters shown in Figure 13(b) approximate the isolated silanol on silica (DPE = 1503 kJ mol^{-1}),[117] the acidic bridging silanol in RSi– $OHAl(OR^F)_3$, and the –OH on SZO (DPE = 1188 kJ mol^{-1}). The acidic RSi–$OHAl(OR^F)_3$ and SZO supports react with allyltriisopropylsilane to form the corresponding [^{i}Pr$_3$Si][oxide] ion-pairs.[76,118]

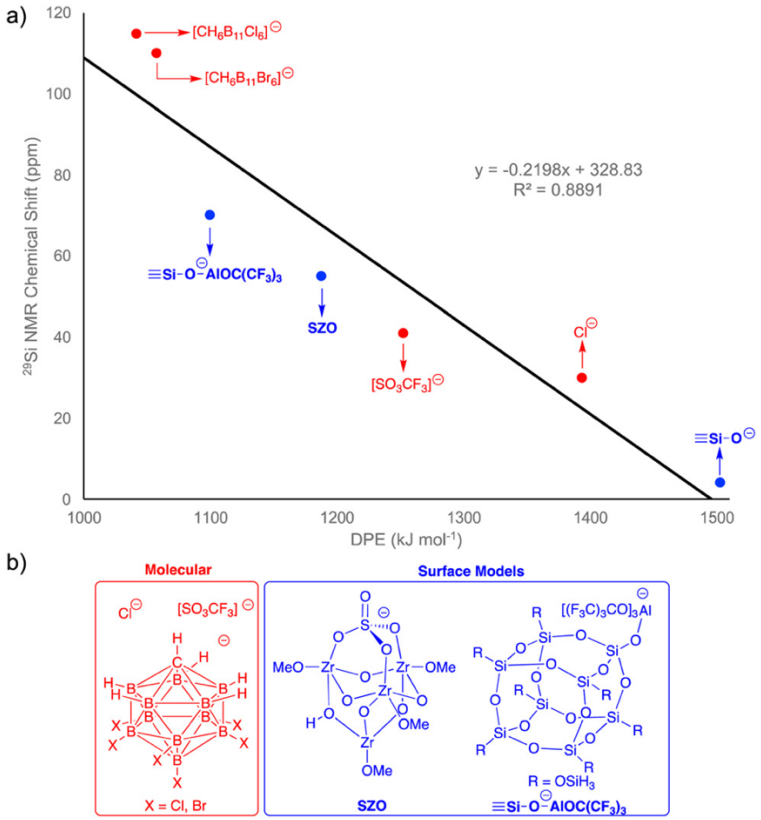

Figure 1.14. Plot of DPE of HX versus 29Si NMR chemical shift (a). Structures of the anions (b).

The four molecular anions shown in Figure 1.14 span B350 kJ mol[1] in DPE. As the anion becomes less basic (i.e., HX becomes more acidic) the ^{29}Si NMR chemical shift appears more downfield. Silanols on silica are weak acids. Thus, the shielded ^{29}Si chemical shift values for R_3Si-supported on silica appear (~4 ppm)[119–121] as expected. As the DPE of the –OH group on the support decreases the 29 Si NMR chemical shift also increases. These trends are very similar to those found by Reed in studies that resulted in the ν_{NH} scale with $[Oct_3NH][X]$.[13]

To our knowledge H-Beta treated with $PhSiMe_3$ is the only example of a Me_3Si-functionalized zeolite, which has a ^{29}Si NMR signal at 17 ppm for the organosilane.[122] This result would seem to break the line shown in Figure 1.14 because zeolites should behave as strong Brønsted acids. However, it is not clear which –OH groups in H-Beta react with $PhSiMe_3$, and the strong Brønsted acid bridging silanol in micropores may not be accessible to $PhSiMe_3$.

Weakly coordinating oxides in olefin polymerization reactions

As noted in Figure 1.5, the most common mixture to generate heterogeneous catalysts for olefin polymerization contains a metallocene, an alkylaluminum (or MAO), and an oxide. This method is broadly applicable to group IV metals, but less so for late transition metal olefin polymerization catalysts. Figure 1.15 shows examples of heterogeneous (a-diimine)Ni catalysts. Combinations of (a-diimine)$NiBr_2$ containing a pendant –OH group on the ligand, SiO_2/MAO, and exogenous $Et_3Al_2Cl_3$, are active in

ethylene polymerization but the broad molecular weight polymer formed in this reaction is a hallmark of ill-defined active sites.[123] Well defined catalysts containing (α-diimine)Ni(CH_2SiMe_3)$_2$ grafted onto $SiO_{2\text{-}700}$ show modest activity in the presence of BF_3.[124]

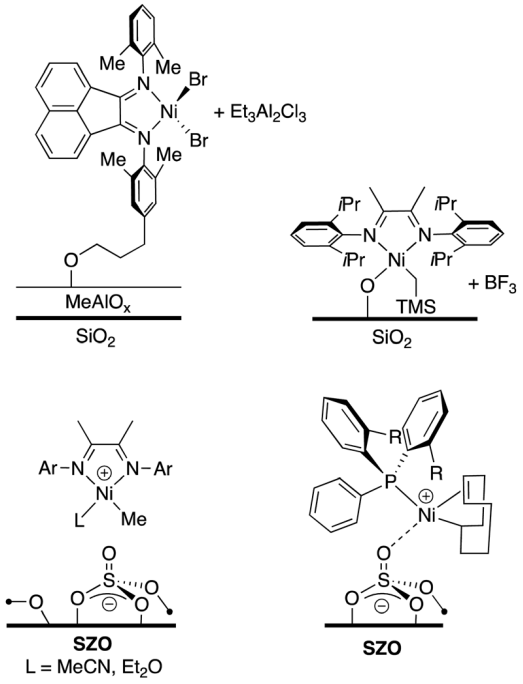

Figure 1.15. Heterogeneous Ni complexes for olefin polymerization.

Sulfated oxides are ideal candidates to form well-defined heterogeneous catalysts for olefin polymerization because these are sufficiently weakly coordinating to form the requisite organometallic ion-pair that fulfills the requirements for the basic structural model shown in Figure 1.4. Reactions of an (a-diimine)$NiMe_2$ with SZO generate well-defined Ni–Me^+ sites, all of which are active in olefin insertion reactions, which produce narrow molecular weight polymers and can tolerate polar monomers.[125] Active catalysts are also available containing organozirconium[126] or organohafnium[127] complexes

supported on sulfated oxides, showing that this strategy is general for reactions of M–R with sulfated oxides to form polymerization complexes. [$HPAr_3$][SZO] prepared similarly to those discussed above react with $Ni(cod)_2$ to form [$Ni(PAr_3)(codH)$][SZO] that are also reactive in olefin polymerization reactions,[128] showing that complex catalyst architectures are likely possible on sulfated oxides.

However, even general reactions have pitfalls. The reaction of the bulky (α-diimine)$PdMe_2$[129,130] shown in Figure 1.16 reacts with SZO to form a well-defined Pd–Me^+ site.[131] This reaction is also accompanied by significantly more CH_4 than expected, indicating that some Pd sites lack the alkyl group necessary for polymerization. Indeed, active site counting shows that only ~9% of the Pd is active in polymerization reactions. Accessing heterogeneous Pd catalysts for olefin polymerization is generally difficult because of incompatibilities with AlR_3, preventing use of common mixtures for catalyst generation, and for the undesirable reactivity shown in Figure 1.16 between (α-diimine)$PdMe_2$ and SZO. The other known examples involve supported phosphine sulfonate Pd species,[132] or anilinonapthoquinone Pd-complexes adsorbed onto silica.[133]

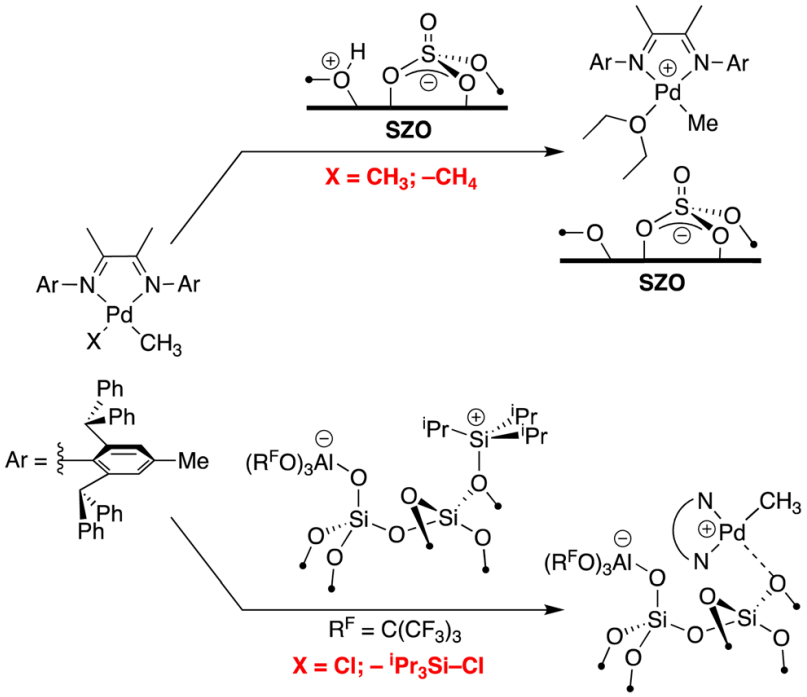

Figure 1.16. Heterogeneous Pd catalysts for olefin polymerization prepared by traditional protonolysis methods (top) or recently developed halide abstraction (bottom).

We showed that [^{i}Pr$_3$Si][RSiO–Al(OR^F)$_3$] reacts with (a-diimine)PdMeCl by a halide abstraction route that forms [(α-diimine)PdMe][RSiO–Al(OR^F)$_3$], Figure 1.16.[134] This reaction is very selective (^{i}Pr$_3$SiMe is not detected) because R$_3$Si$^+$ ions have some of the highest halide ion affinities known.[108] In addition virtually all of the Pd–Me$^+$ sites are active in olefin insertion reactions. Halide abstraction is a general methodology to generate ion-pairs in solution,[45,61] and we view this reaction as filling a methodological gap in the surface organometallic community that often relies on reactions of Brønsted acid sites with organometallics to form well-defined species.

Beyond olefin polymerization with supported organometallic cations

Reactive d^0 metal hydrides have a rich history as well-defined heterogenous catalysts supported on SiO_2,[135,136] usually prepared by treating supported organometallics with H_2. Silicasupported late transition metal hydrides on supports are less common,[137–139] but can be prepared by oxidative addition of Pt(0) to generate Pt–H species.[140] Though reactive, –OH groups on SiO_2 nearly always favor formation of type A species containing RSiO–M (Figure 1.3).[141]

Figure 1.9 showed differences in the reactivity of Cp^*ZrMe_3 with SiO_2 and SAO, the latter forming an ion pair that has activity in olefin polymerization reactions. Contacting the $[Cp^*ZrMe_2][SAO]$ forms very reactive $Zr–H^+$ species that hydrogenate arenes, Figure 1.17.[82,83,142,143] The key step in this reaction is the coordination of the arene to the electron deficient $Zr–H^+$, which can be thought of as a surface analog to a solvent separated ion pair. This behavior is analogous to cationic d^0 species that coordinate and exchange arene solvents in solution.[144–146] Successive migratory insertion and hydrogenolysis steps shown in Figure 1.17 form the cyclohexane product. This reaction shows remarkable facial selectivity, giving all cis-substituted products in hydrogenation reactions of substituted arenes.[147]

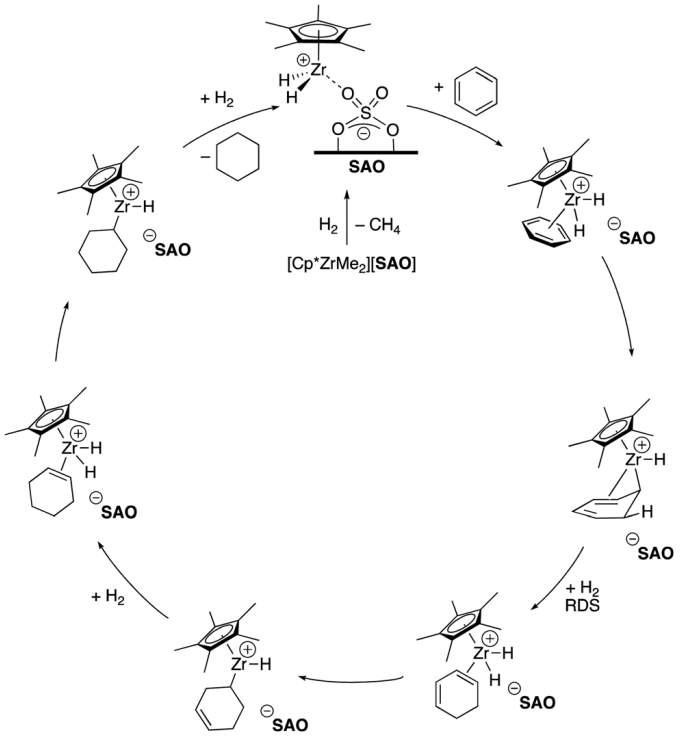

Figure 1.17. Arene hydrogenation of catalyzed by Zr–H+ supported on SAO.

Most of the classic examples of d^0 M–H supported on silica engage in s-bond metathesis reactions.[135,136] Zr–H/SiO_2–Al_2O_3 are promising catalysts for hydrogenolysis of polyethylene,[148] which is attracting increasing attention as a method to degrade polymer waste to useful alkane feedstocks.[149] In alkane hydrogenolysis Zr–H reacts with a C–H bond through s-bond metathesis to form H_2 and M–R that b-alkyl eliminates[150] to form MR(olefin) intermediates that are successively hydrogenated to lower molecular weight products, Figure 1.18. Though the rate limiting step in this reaction is not known, in solution cationic d^0 organometallics react faster in s-bond metathesis reactions than related neutral species,[151] suggesting that d^0 M–H^+ may accelerate alkane rearrangements.[152]

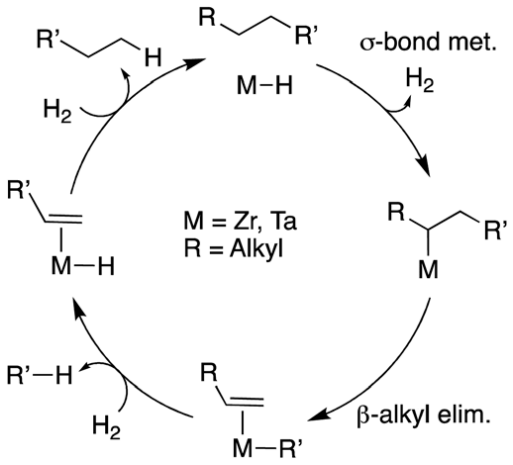

Figure 1.18. Alkane hydrogenolysis by a M-H.

We prepared Ta–H^+ sites on SAO (Figure 1.19(a))[153] and compared their reactivity to Ta–H supported on SiO_2, the latter of which are known to catalyze alkane hydrogenolysis reaction.[154] Ta– H^+ sites on SAO converts 100 equivalents of n-$C_{14}H_{30}$, a liquid surrogate for polyethylene, to a statistical mixture of alkanes in only 2 h, while identical reaction conditions with Ta–H supported on SiO_2 results in only 17% conversion of tetradecane. Ta–H^+ sites on SAO also catalyze hydrogenolysis of low molecular weight HDPE to produce CH_4–C_{26} in ~30% yield. The residual polymer has higher molecular weight than the starting material suggesting that only the more mobile polymer fraction reacts with Ta–H^+ sites on SAO. Finally, Ta–H^+ sites on SAO are also significantly more reactive in alkane metathesis reactions than Ta–H supported on SiO_2.

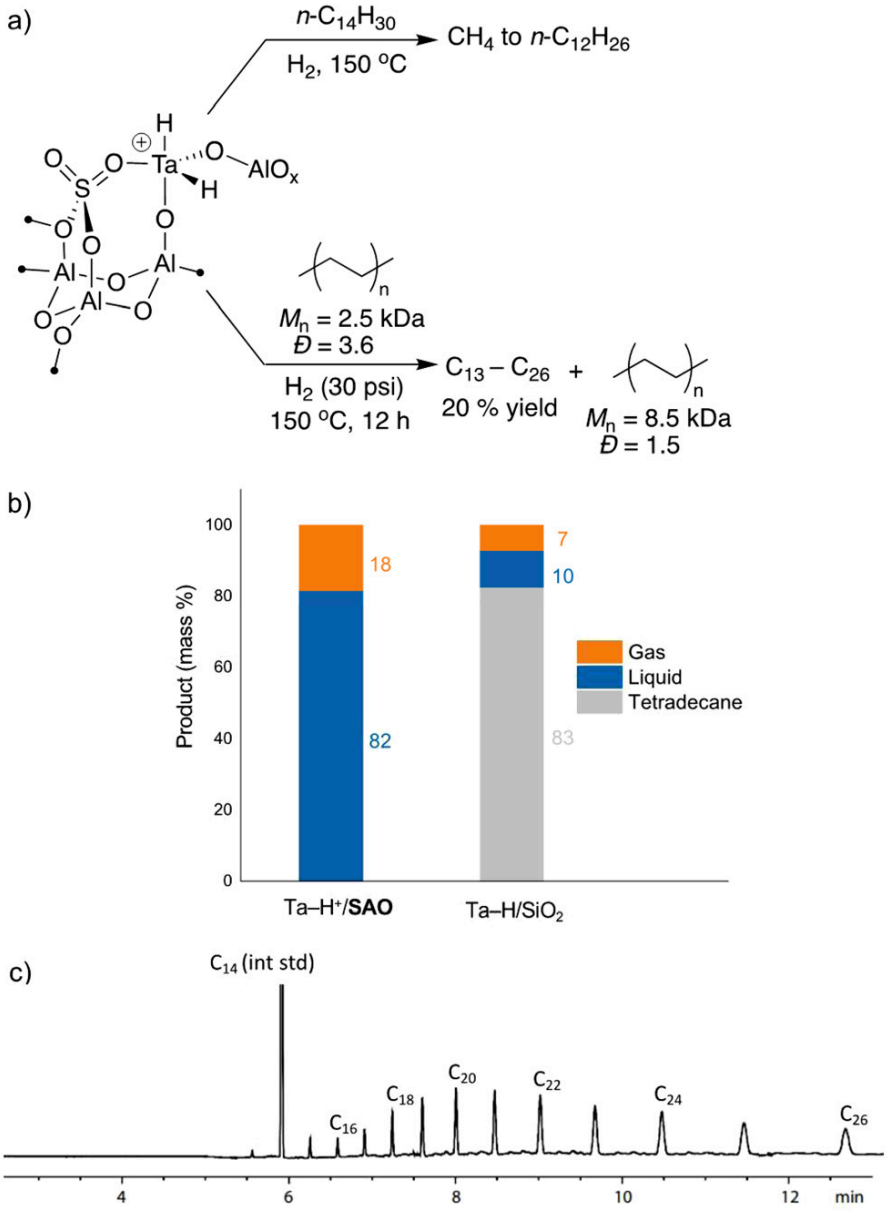

Figure 1.19. Reactivity of Ta–H+ on SAO in hydrogenolysis reactions (a). Direct comparison of Ta–H+/SAO and Ta–H/SiO2 in tetradecane hydrogenolysis after 2 h (b). Gas chromatograph of liquid products produced by Ta–H+/ SAO in hydrogenolysis of polyethylene. Reproduced from ref. 153 with permission from the American Chemical Society, copyright 2023.

Designing cationic metal hydrides on weakly coordinating supports appears to be a promising strategy to increase reactivity in alkane rearrangement reactions. Similar strategies using cationic transition metal complexes in solution to mediate these reactions are unlikely for a simple reason, alkanes are rarely compatible solvents with cations. Indeed, solvation of organometallic cations by polar halogenated solvents usually prevents formation of s-CH alkane intermediates in solution,[155–159] and only recently have these types of compounds become widely available in using in-crystallo[160] organometallic chemistry of cationic Rh(I) olefin complexes with H_2 in porous single crystals in the absence of solvent.[161–166]

This concept extends beyond generation of $M–H^+$ sites on weakly coordinating supports. [Cp*IrMe(PMe_3)][SZO] in Figure 1.20(a) catalyzes H/D exchange reactions of methane and arenes faster than the corresponding Ir species supported on SiO_2.[167] This reaction is mechanistically similar to the σ-bond metathesis reactions discussed above,[168] but shows that trends observed in supported d^0 species also extend to Ir. C–H activation reactions that involve concerted metalation deprotonation (CMD)[169] are also accelerated on weakly coordinating supports. Cationic (^{dm}Phebox)Ir(III) (Figure 1.20(b)) supported on SZO is more active in stoichiometric dehydrogenation reactions than the corresponding neutral complex in solution.[170] DFT studies support experimental observations and show that neutral (^{dm}Phebox)Ir($OAc)_2$ is predicted to activate C–H bonds with higher barrier to produce more stable intermediates than [(^{dm}Phebox)Ir(OAc)][SZO]. This also results in higher barrier for b-H elimination, a key

step in Ir-catalyzed dehydrogenation reactions,[171] for the neutral Ir–R compared to the cationic supported species.

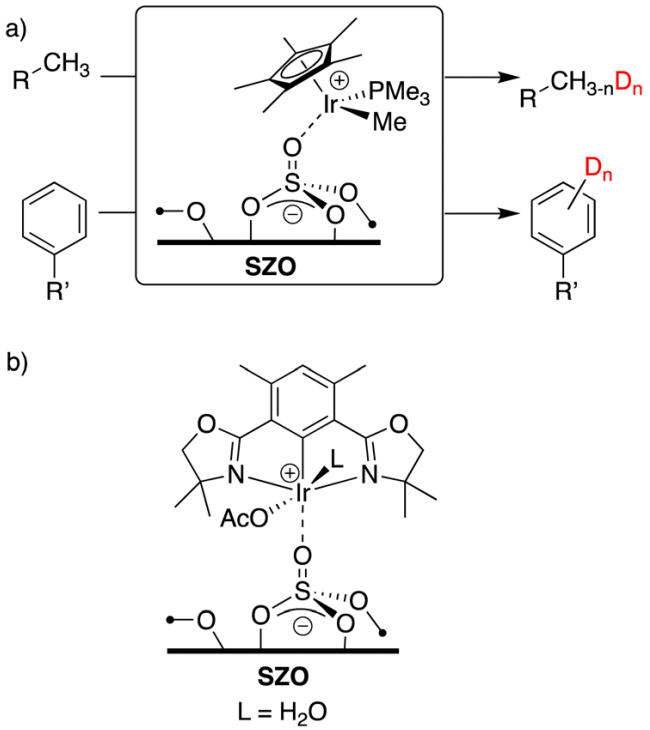

Figure 1.20. H/D exchange of arenes and alkanes catalyzed by [Cp*IrMe(PMe3)][SZO] (a). Cationic [(dmPhebox)Ir(OAc)][SZO] (b).

Outlook

Acidity plays a deciding role in the structure of organometallics on surfaces. Though quantification of Brønsted and Lewis acidity on surfaces cannot directly parallel trends observed in solution, this article showed various methods that can provide key insights to acid strength on surfaces. Titrations of –OH groups on supports are possible, as shown for reactions of PR_3 with SZO, but laborious. We feel that the relationship between ^{29}Si NMR chemical shift and DPE is a more powerful single point measurement

that reports on the ability of an oxide to form an ion-pair. This is because of the broad ^{29}Si NMR chemical shift window between R_3Si–X, $R_3Si^{d+d}X$, and $[R_3Si][X]$. The ^{29}Si NMR chemical shift is predicted to vary ~300 ppm between R_3Si–OMe and free R_3Si^+ (R = alkyl). Though the formation of a free R_3Si^+ on an oxide is unlikely the practical range in ^{29}Si NMR chemical shift scale is closer to ~100 ppm using R_3Si–OMe and $[R_3Si][CH_6B_{11}Cl_6]$ as examples. This spans a wide range of DPE; the acidic end of this range of DPE being significantly lower than RSi–OHAl$(OR^F)_3$, the strongest Brønsted acid on an oxide and the most weakly coordinating oxide from the ^{29}Si NMR chemical shift scale.

Access to more weakly coordinating supports remains a significant challenge. The Lewis activated Brønsted acid strategy is promising, but still in in its infancy on heterogeneous supports. Part of this reason is related to the need for stronger Lewis acids that bind to –OH groups on surfaces with sufficient binding energy to form a bridging RE–OHLA site (E = surface element). Lewis acids stronger than Al$(OR^F)_3$, which are becoming available,[172] would be useful for this purpose. An alternative is to react oxides containing stronger Brønsted acid –OH groups with Al$(OR^F)_3$(PhF) to enhance acidity.

The use of the ^{29}Si NMR chemical shift scale has a hidden benefit. Weakly coordinating oxides form R_3Si^+ capped surfaces that show characteristic reactivity of silylium-like ions. $[R_3Si][SZO]$ activate C–F bonds[118] or abstract chloride from (cod)IrCl(py).[173] R_3Si^+ have exceptionally high halide ion affinities, indicating that R_3Si^+ capped surfaces will selectively abstract a halide from an organometallic complex, as shown for the reaction of (N^N)PdMeCl with $[^iPr_3Si][RSiO–Al(OR^F)_3]$ in Figure 1.16.

As the field of surface organometallic chemistry continues to grow more nuanced methods to evaluate how the support affects structure will likely be necessary. Acidity clearly plays a deciding role in the species described here, but there are supports, such as redox active battery materials,[174] where new metrics will be needed to accurately describe how thermodynamics properties of the surface affects structure of an organometallic or inorganic site active in a catalytic reaction.

References

1. R. H. Morris, *Chem. Rev*., **2016**, 116, 8588–8654.

2. Y. Marcus, M. J. Kamlet and R. W. Taft, *J. Phys. Chem*., **1988**, 92, 3613–3622.

3. Y. Marcus*, Ions in Solution and their Solvation*, **2015**, pp. 107–155, DOI: 10.1002/9781118892336.ch4.

4. W. E. Dasent, *Journal*, **1983**, 96, 194–195.

5. A. Zheng, S.-B. Liu and F. Deng, *Chem. Rev.*, **2017**, 117, 12475–12531.

6. M. I. Zaki, M. A. Hasan, F. A. Al-Sagheer and L. Pasupulety, *Colloids Surf., A*, **2001**, 190, 261–274.

7. C. Morterra and G. Magnacca, *Catal. Today,* **1996,** 27, 497–532.

8. W. E. Farneth and R. J. Gorte, *Chem. Rev.,* **1995**, 95, 615–635.

9. R. J. Gorte, *Catal. Lett.,* **1999**, 62, 1–13.

10. C. A. Reed, *Acc. Chem. Res.,* **2013**, 46, 2567–2575.

11. C. A. Reed, *Acc. Chem. Res*., **2010**, 43, 121–128.

12. G. A. Olah, G. K. S. Prakash, J. Sommer and A. Molnar, *Superacid Chemistry, John Wiley & Sons*, **2009**.

13. E. S. Stoyanov, K.-C. Kim and C. A. Reed*, J. Am. Chem. Soc.,* **2006**, 128, 8500–8508.

14. J. F. Haw, *Phys. Chem. Chem. Phys.,* **2002,** 4, 5431–5441.

15. A. Corma and H. García, *Chem. Rev.,* **2003**, 103, 4307–4366.

16. Y. Román-Leshkov and M. E. Davis, *ACS Catal.,* **2011**, 1, 1566–1580.

17. A. Comas-Vives, M. Valla, C. Copéret and P. Sautet, *ACS Cent. Sci.,* **2015**, 1, 313–319.

18. A. Comas-Vives, M. Schwarzwälder, C. Copéret and P. Sautet, *J. Phys. Chem. C,* **2015**, 119, 7156–7163.

19. M. Valla, R. Wischert, A. Comas-Vives, M. P. Conley, R. Verel, C. Copéret and P. Sautet, *J. Am. Chem. Soc.,* **2016**, 138, 6774–6785.

20. R. Wischert, C. Copéret, F. Delbecq and P. Sautet, *Angew. Chem., Int.* Ed., **2011**, 50, 3202–3205.

21. R. Wischert, C. Copéret, F. Delbecq and P. Sautet, *Chem. Commun.,* **2011**, 47, 4890–4892.

22. C. Copéret, *Chem. Rev.,* **2010**, 110, 656–680.

23. C. Copéret, A. Comas-Vives, M. P. Conley, D. P. Estes, A. Fedorov, V. Mougel, H. Nagae, F. Núñez-Zarur and P. A. Zhizhko, *Chem. Rev.,* **2016**, 116, 323–421.

24. J. D. A. Pelletier and J.-M. Basset, *Acc. Chem. Res.,* **2016**, 49, 664–677.

25. S. L. Wegener, T. J. Marks and P. C. Stair, *Acc. Chem. Res.,* **2011**, 45, 206–214.

26. Y. Liang and R. Anwander, *Dalton Trans.,* **2013**, 42, 12521–12545.

27. J. Guzman and B. C. Gates, *Dalton Trans.,* **2003**, 3303–3318.

28. E. Bekyarova and M. P. Conley, *Dalton Trans.,* **2022**, 51, 8557–8570.

29. P. J. Toscano and T. J. Marks, *J. Am. Chem. Soc.,* **1985,** 107, 653–659.

30. E. Y.-X. Chen and T. J. Marks, *Chem. Rev.,* **2000**, 100, 1391–1434.

31. C. P. Gordon, L. Lätsch and C. Copéret, *J. Phys. Chem. Lett.,* **2021**, 12, 2072–2085.

32. A. J. Rossini, A. Zagdoun, M. Lelli, A. Lesage, C. Copéret and L. Emsley*, Acc. Chem. Res.,* **2013**, 46(9), 1942–1951.

33. A. J. Rossini, *J. Phys. Chem. Lett.,* **2018**, 9, 5150–5159.

34. P. Sautet and F. Delbecq*, Chem. Rev.,* **2010**, 110, 1788–1806.

35. S. Bordiga, E. Groppo, G. Agostini, J. A. van Bokhoven and C. Lamberti, *Chem. Rev.,* **2013,** 113, 1736–1850.

36. D. Trummer, K. Searles, A. Algasov, S. A. Guda, A. V. Soldatov, H. Ramanantoanina, O. V. Safonova, A. A. Guda and C. Copéret*, J. Am. Chem. Soc.,* **2021**, 143, 7326–7341.

37. G. W. Coates, P. D. Hustad and S. Reinartz, Angew. *Chem., Int. Ed.,* **2002**, 41, 2236–2257.

38. G. W. Coates, *Chem. Rev.,* **2000**, 100, 1223–1252.

39. S. L. J. Luckham and K. Nozaki, *Acc. Chem. Res.,* **2021**, 54, 344–355.

40. A. Nakamura, T. M. J. Anselment, J. Claverie, B. Goodall, R. F. Jordan, S. Mecking, B. Rieger, A. Sen, P. W. N. M. van Leeuwen and K. Nozaki, *Acc. Chem. Res.,* **2013**, 46, 1438–1449.

41. Z. Chen and M. Brookhart, *Acc. Chem. Res.,* **2018**, 51, 1831–1839.

42. C. Tan and C. Chen*, Angew. Chem., Int. Ed.,* **2019**, 58, 7192–7200.

43. C. Chen, *Nat. Rev. Chem.,* **2018**, 2, 6–14.

44. M. C. Baier, M. A. Zuideveld and S. Mecking, *Angew. Chem., Int. Ed.,* **2014**, 53, 9722–9744.

45. A. Macchioni, *Chem. Rev.,* **2005**, 105, 2039–2074.

46. P. S. Kulyabin, G. P. Goryunov, M. I. Sharikov, V. V. Izmer, A. Vittoria, P. H. M. Budzelaar, V. Busico, A. Z. Voskoboynikov, C. Ehm, R. Cipullo and D. V. Uborsky, *J. Am. Chem. Soc.,* **2021,** 143, 7641–7647.

47. W. Kaminsky, *J. Polym. Sci., Part A: Polym. Chem.*, **2004**, 42, 3911–3921.

48. P. Jutzi, C. Müller, A. Stammler and H.-G. Stammler, *Organometallics,* **2000**, 19, 1442–1444.

49. M. Brookhart, B. Grant and A. F. Volpe, Jr., *Organometallics,* **1992**, 11, 3920–3922.

50. L. K. Johnson, S. Mecking and M. Brookhart, *J. Am. Chem. Soc.,* **1996**, 118, 267–268.

51. L. Guo, S. Dai, X. Sui and C. Chen, *ACS Catal.*, **2016**, 6, 428–441.

52. W. Zhang, P. M. Waddell, M. A. Tiedemann, C. E. Padilla, J. Mei, L. Chen and B. P. Carrow, *J. Am. Chem. Soc.,* **2018**, 140, 8841–8850.

53. A. Ashuiev, M. Humbert, S. Norsic, J. Blahut, D. Gajan, K. Searles, D. Klose, A. Lesage, G. Pintacuda, J. Raynaud, V. Monteil, C. Copéret and G. Jeschke, *J. Am. Chem. Soc*., **2021**, 143, 9791–9797.

54. M. P. McDaniel, M. D. Jensen, K. Jayaratne, K. S. Collins, E. A. Benham, N. D. Mcdaniel, P. K. Das, J. L. Martin, Q. Yang, M. G. Thorn and A. P. Masino, in *Tailor-Made Polymers*, ed. J. R. Severn and J. C. Chadwick, **2008**, DOI: 10.1002/9783527621668.ch7, pp. 171–210.

55. S. Tsuji, D. C. Swenson and R. F. Jordan, *Organometallics*, **1999**, 18, 4758–4764.

56. D. B. Culver, R. W. Dorn, A. Venkatesh, J. Meeprasert, A. J. Rossini, E. A. Pidko, A. S. Lipton, G. R. Lief and M. P. Conley, *ACS Cent. Sci*., **2021**, 7, 1225–1231.

57. D. B. Culver, J. Corieri, G. Lief and M. P. Conley, *Organometallics*, **2022,** 41, 892–899.

58. J. Joubert, F. Delbecq, P. Sautet, E. L. Roux, M. Taoufik, C. Thieuleux, F. Blanc, C. Copéret, J. Thivolle-Cazat and J.-M. Basset, *J. Am. Chem. Soc.,* **2006,** 128, 9157–9169.

59. A. Kermagoret, R. N. Kerber, M. P. Conley, E. Callens, P. Florian, D. Massiot, C. Copéret, F. Delbecq, X. Rozanska and P. Sautet, *Dalton Trans.,* **2013**, 42, 12681–12687.

60. S. Collins, W. M. Kelly and D. A. Holden, *Macromolecules,* **1992**, 25, 1780–1785.

61. I. M. Riddlestone, A. Kraft, J. Schaefer and I. Krossing, *Angew. Chem., Int. Ed.,* **2018**, 57, 13982–14024.

62. R. N. Kerber, A. Kermagoret, E. Callens, P. Florian, D. Massiot, A. Lesage, C. Copéret, F. Delbecq, X. Rozanska and P. Sautet, *J. Am. Chem. Soc.,* **2012**, 134, 6767–6775.

63. A. Kermagoret, R. N. Kerber, M. P. Conley, E. Callens, P. Florian, D. Massiot, F. . Delbecq, X. Rozanska, C. Copéret and P. Sautet, *J. Catal.,* **2014**, 313, 46–54.

64. J. Pelletier, J. Espinas, N. Vu, S. Norsic, A. Baudouin, L. Delevoye, J. Trébosc, E. Le Roux, C. Santini, J.-M. Basset, R. M. Gauvin and M. Taoufik, *Chem. Commun.,* **2011**, 47, 2979–2981.

65. K. C. Szeto, Z. R. Jones, N. Merle, C. Rios, A. Gallo, F. Le Quemener, L. Delevoye, R. M. Gauvin, S. L. Scott and M. Taoufik, *ACS Catal.,* **2018,** 8, 7566–7577.

66. S. D. Fleischman and S. L. Scott, *J. Am. Chem. Soc.,* **2011**, 133, 4847–4855.

67. Z. A. Taha, E. W. Deguns, S. Chattopadhyay and S. L. Scott, *Organometallics,* **2006**, 25, 1891–1899.

68. J. F. Walzer, US Pat., 5643847, **1995**.

69. N. Millot, C. C. Santini, A. Baudouin and J.-M. Basset, *Chem. Commun*., **2003**, 2034–2035, DOI: 10.1039/b304047j.

70. D. W. Sauter, N. Popoff, M. A. Bashir, K. C. Szeto, R. M. Gauvin, L. Delevoye, M. Taoufik and C. Boisson, *Chem. Commun.,* **2016**, 52, 4776–4779.

71. Y.-J. Wanglee, J. Hu, R. E. White, M.-Y. Lee, S. M. Stewart, P. Perrotin and S. L. Scott, *J. Am. Chem. Soc.,* **2012**, 134, 355–366.

72. L. O. Müller, D. Himmel, J. Stauffer, G. Steinfeld, J. Slattery, G. Santiso-Quiñones, V. Brecht and I. Krossing, *Angew. Chem., Int. Ed.,* **2008,** 47, 7659–7663.

73. K. K. Samudrala, W. Huynh, R. W. Dorn, A. J. Rossini and M. P. Conley, *Angew. Chem., Int. Ed.,* **2022**, 61, e202205745.

74. H. Bohrer, N. Trapp, D. Himmel, M. Schleep and I. Krossing, *Dalton Trans.,* **2015**, 44, 7489–7499.

75. P. Erdmann, J. Leitner, J. Schwarz and L. Greb, *ChemPhysChem*, **2020**, 21, 987–994.

76. D. B. Culver, A. Venkatesh, W. Huynh, A. J. Rossini and M. P. Conley, *Chem. Sci.,* **2020**, 11, 1510–1517.

77. J. B. Miller, J. Schwartz and S. L. Bernasek, *J. Am. Chem. Soc.,* **1993,** 115, 8239–8247.

78. H. Großekappenberg, M. Reißmann, M. Schmidtmann and T. Müller, *Organometallics***, 2015**, 34, 4952–4958.

79. I. Del Rosal, I. C. Gerber, R. Poteau and L. Maron, *J. Phys. Chem*. A, **2010**, 114, 6322–6330.

80. R. J. Witzke, A. Chapovetsky, M. P. Conley, D. M. Kaphan and M. Delferro, *ACS Catal.*, **2020**, 11822–11840, DOI: 10.1021/acscatal.0c03350.

81. M. Jezequel, V. Dufaud, M. J. Ruiz-Garcia, F. Carrillo-Hermosilla, U. Neugebauer, G. P. Niccolai, F. Lefebvre, F. Bayard, J. Corker, S. Fiddy, J. Evans, J.-P. Broyer, J. Malinge and J.-M. Basset, *J. Am. Chem. Soc.,* **2001**, 123, 3520–3540.

82. L. A. Williams, N. Guo, A. Motta, M. Delferro, I. L. Fragalá, J. T. Miller and T. J. Marks, *Proc. Natl. Acad. Sci. U. S. A.,* **2013**, 110, 413–418.

83. C. P. Nicholas, H. Ahn and T. J. Marks, *J. Am. Chem. Soc.,* **2003**, 125, 4325–4331.

84. M. Hino, S. Kobayashi and K. Arata*, J. Am. Chem. Soc.,* **1979**, 101, 6439–6441.

85. M. Hino and K. Arata, *Chem. Commun.,* **1980**, 851–852, DOI: 10.1039/c39800000851.

86. D. Farcasiu, A. Ghenciu and J. Q. Li, *J. Catal.,* **1996**, 158, 116–127.

87. W. Chen, X. Yi, L. Huang, W. Liu, G. Li, D. Acharya, X. Sun and A. Zheng, *Catal. Sci. Technol.*, **2019**, 9, 5045–5057.

88. X. Li, K. Nagaoka, L. J. Simon, R. Olindo, J. A. Lercher, A. Hofmann and J. Sauer, *J. Am. Chem. Soc.,* **2005**, 127, 16159–16166.

89. J. E. Tabora and R. J. Davis, *J. Am. Chem. Soc.,* **1996**, 118, 12240–12241.

90. R. S. Drago and N. Kob, *J. Phys. Chem. B,* **1997**, 101, 3360–3364.

91. J. F. Haw, J. Zhang, K. Shimizu, T. N. Venkatraman, D.-P. Luigi, W. Song, D. H. Barich and J. B. Nicholas, *J. Am. Chem. Soc.,* **2000,** 122, 12561–12570.

92. R. C. Klet, D. M. Kaphan, C. Liu, C. Yang, A. J. Kropf, F. A. Perras, M. Pruski, A. S. Hock and M. Delferro, *J. Am. Chem. Soc.,* **2018,** 140, 6308–6316.

93. J. Rodriguez, D. B. Culver and M. P. Conley, *J. Am. Chem. Soc.,* **2019**, 141, 1484–1488.

94. A. M. Tatyana and I. K. Martin, Russ. *Chem. Rev.,* **1969,** 38, 795.

95. I. Kaljurand, A. Kütt, L. Sooväli, T. Rodima, V. Mäemets, I. Leito and I. A. Koppel, *J. Org. Chem.,* **2005**, 70, 1019–1028.

96. F. Haase and J. Sauer, *J. Am. Chem. Soc.,* **1998,** 120, 13503–13512.

97. I. Krossing and I. Raabe, *Angew. Chem., Int. Ed.,* **2004**, 43, 2066–2090.

98. S. P. Fisher, A. W. Tomich, S. O. Lovera, J. F. Kleinsasser, J. Guo, M. J. Asay, H. M. Nelson and V. Lavallo, *Chem. Rev.,* **2019**, 119, 8262–8290.

99. H. Yamamoto and K. Futatsugi, *Angew. Chem., Int. Ed.,* **2005**, 44, 1924–1942.

100. T. Xu, N. Kob, R. S. Drago, J. B. Nicholas and J. F. Haw, *J. Am. Chem. Soc.,* **1997**, 119, 12231–12239.

101. A. Kraft, J. Beck, G. Steinfeld, H. Scherer, D. Himmel and I. Krossing, *Organometallics,* **2012**, 31, 7485–7491.

102. W. R. Gunther, V. K. Michaelis, R. G. Griffin and Y. Román- Leshkov, *J. Phys. Chem. C,* **2016**, 120, 28533–28544.

103. J. P. Osegovic and R. S. Drago, *J. Phys. Chem. B,* **1999,** 104, 147–154.

104. P. Erdmann and L. Greb, *Angew. Chem., Int. Ed.,* **2022,** 61, e202114550.

105. X. Yi, Y.-K. Peng, W. Chen, Z. Liu and A. Zheng, *Acc. Chem. Res.,* **2021**, 54, 2421–2433.

106. W. Huynh and M. P. Conley, *Dalton Trans.,* **2020**, 49, 16453–16463.

107. C. A. Reed, *Acc. Chem. Res.,* **1998**, 31, 325–332.

108. H. F. T. Klare, L. Albers, L. Süsse, S. Keess, T. Müller and M. Oestreich, *Chem. Rev.,* **2021**, 121, 5889–5985.

109. C. A. Reed, Z. Xie, R. Bau and A. Benesi*, Science*, **1993**, 262, 402–404.

110. C. P. Gordon, C. Raynaud, R. A. Andersen, C. Copéret and O. Eisenstein, *Acc. Chem. Res.,* **2019**, 52, 2278–2289.

111. D. B. Culver, W. Huynh, H. Tafazolian, T.-C. Ong and M. P. Conley, *Angew. Chem., Int. Ed.,* **2018**, 57, 9520–9523.

112. G. Wu, D. Rovnyak, M. J. A. Johnson, N. C. Zanetti, D. G. Musaev, I Morokuma, R. R. Schrock, R. G. Griffin and C. C. Cummins, *Am. Chem. Soc.,* **1996**, 118, 10654–10655.

113. K. B. Wiberg, J. D. Hammer, K. W. Zilm and J. R. Cheeseman, *J. Org. Chem.,* **1999**, 64, 6394–6400.

114. S. Berger, U. Fleischer, C. Geletneky and J. C. W. Lohrenz, *Chem. Ber.,* **1995**, 128, 1183–1186.

115. R. P. Young, C. R. Lewis, C. Yang, L. Wang, J. K. Harper and L. J. Mueller, *Magn. Reson. Chem.,* **2019**, 57, 211–223.

116. R. V. Viesser, L. C. Ducati, C. F. Tormena and J. Autschbach, *Chem. Sci.,* **2017**, 8, 6570–6576.

117. J. Sauer and R. Ahlrichs, *J. Chem. Phys.,* **1990**, 93, 2575–2583.

118. D. B. Culver and M. P. Conley, *Angew. Chem., Int. Ed.,* **2018**, 57, 14902–14905.

119. J. Bluemel, *J. Am. Chem. Soc.,* **1995**, 117, 2112–2113.

120. M. P. Conley, C. Copéret and C. Thieuleux, *ACS Catal*., **2014**, 4, 1458–1469.

121. C. Zapilko, M. Widenmeyer, I. Nagl, F. Estler, R. Anwander, G. Raudaschl-Sieber, O. Groeger and G. Engelhardt, *J. Am. Chem. Soc.,* **2006**, 128, 16266–16276.

122. W. Song, D. M. Marcus, S. M. Abubakar, E. Jani and J. F. Haw, *J. Am. Chem. Soc.,* **2003**, 125, 13964–13965.

123. P. Preishuber-Pflugl and M. Brookhart, *Macromolecules,* **2002**, 35, 6074–6076.

124. A. Dorcier, N. Merle, M. Taoufik, F. Bayard, C. Lucas, A. de Mallmann and J. M. Basset, *Organometallics*, **2009**, 28, 2173–2178.

125. H. Tafazolian, D. B. Culver and M. P. Conley, *Organometallics*, **2017,** 36, 2385–2388.

126. M. Stalzer, M. Delferro and T. Marks, *Catal. Lett.,* **2015**, 145, 3–14.

127. J. Zhang, A. Motta, Y. Gao, M. M. Stalzer, M. Delferro, B. Liu, T. L. Lohr and T. J. Marks, *ACS Catal.,* **2018,** 8, 4893–4901.

128. J. Rodriguez and M. P. Conley, *Inorg. Chem*., **2021**, 60, 6946–6949.

129. S. Dai, X. Sui and C. Chen, *Angew. Chem., Int. Ed.,* **2015**, 54, 9948–9953.

130. J. L. Rhinehart, L. A. Brown and B. K. Long, *J. Am. Chem. Soc.,* **2013**, 135, 16316–16319.

131. D. B. Culver, H. Tafazolian and M. P. Conley, *Organometallics,* **2018**, 37, 1001–1006.

132. P. Wucher, J. B. Schwaderer and S. Mecking, *ACS Catal.,* **2014,** 4, 2672–2679.

133. S. Dai and C. Chen, *Angew. Chem., Int. Ed.,* **2020**, 59, 14884–14890.

134. J. Gao, R. W. Dorn, G. P. Laurent, F. A. Perras, A. J. Rossini and M. P. Conley, *Angew. Chem., Int. Ed.,* **2022**, e202117279.

135. J.-M. Basset, C. Copéret, D. Soulivong, M. Taoufik and J. T. Cazat, *Acc. Chem. Res*., **2009**, 43, 323–334.

136. C. Copéret, D. P. Estes, K. Larmier and K. Searles, *Chem. Rev.,* **2016**, 116, 8463–8505.

137. S. L. Scott, A. Mills, C. Chao, J.-M. Basset, N. Millot and C. C. Santini, *J. Mol. Catal. A: Chem*., **2003**, 204–205, 457–463.

138. Y. S. Choi, E. G. Moschetta, J. T. Miller, M. Fasulo, M. J. McMurdo, R. M. Rioux and T. D. Tilley, *ACS Catal.,* **2011**, 1, 1166–1177.

139. M. Rimoldi, D. Fodor, J. A. van Bokhoven and A. Mezzetti, *Chem. Commun.,* **2013**, 49, 11314–11316.

140. S. Maier, S. P. Cronin, M.-A. Vu Dinh, Z. Li, M. Dyballa, M. Nowakowski, M. Bauer and D. P. Estes, *Organometallics,* **2021**, 40, 1751–1757.

141. D. Gajan, D. Levine, E. Zocher, C. Copéret, A. Lesage and L. Emsley, *Chem. Sci.,* **2011**, 2, 928–931.

142. H. Ahn, C. P. Nicholas and T. J. Marks, *Organometallics*, **2002**, 21, 1788–1806.

143. W. Gu, M. M. Stalzer, C. P. Nicholas, A. Bhattacharyya, A. Motta, J. R. Gallagher, G. Zhang, J. T. Miller, T. Kobayashi, M. Pruski, M. Delferro and T. J. Marks*, J. Am. Chem. Soc.*, **2015**, 137, 6770–6780.

144. P. G. Hayes, W. E. Piers and M. Parvez, *J. Am. Chem. Soc.,* **2003**, 125, 5622–5623.

145. S. J. Lancaster, O. B. Robinson, M. Bochmann, S. J. Coles and M. B. Hursthouse, *Organometallics,* **1995**, 14, 2456–2462.

146. D. J. Gillis, R. Quyoum, M.-J. Tudoret, Q. Wang, D. Jeremic, A. W. Roszak and M. C. Baird, *Organometallics*, **1996**, 15, 3600–3605.

147. M. M. Stalzer, C. P. Nicholas, A. Bhattacharyya, A. Motta, M. Delferro and T. J. Marks, *Angew. Chem., Int. Ed.,* **2016,** 55, 5263–5267.

148. V. Dufaud and J.-M. Basset, *Angew. Chem., Int. Ed.,* **1998**, 37, 806–810.

149. U. Kanbur, G. Zang, A. L. Paterson, P. Chatterjee, R. A. Hackler, M. Delferro, I. I. Slowing, F. A. Perras, P. Sun and A. D. Sadow, *Chem,* **2021**, 7, 1347–1362.

150. M. E. O'Reilly, S. Dutta and A. S. Veige, *Chem. Rev.,* **2016**, 116, 8105–8145.

151. A. D. Sadow and T. D. Tilley, *Organometallics,* **2003**, 22, 3577–3585.

152. Z. Li, Q. Shi, X. Ma, Y. Li, K. Wen, L. Qin, H. Chen, W. Huang, F. Zhang, Y. Lin, T. J. Marks and H. Huang, *Nat. Commun*., **2022**, 13, 144.

153. J. Gao, L. Zhu and M. P. Conley, *J. Am. Chem. Soc.,* **2023**, DOI: 10.1021/jacs.2c13610, In Press.

154. M. Chabanas, V. Vidal, C. Copéret, J. Thivolle-Cazat and J.-M. Basset, *Angew. Chem., Int. Ed.*, **2000,** 39, 1962–1965.

155. W. H. Bernskoetter, C. K. Schauer, K. I. Goldberg and M. Brookhart, *Science*, **2009**, 326, 553–556.

156. H. M. Yau, A. I. McKay, H. Hesse, R. Xu, M. He, C. E. Holt and G. E. Ball, *J. Am. Chem. Soc.,* **2016**, 138, 281–288.

157. J. D. Watson, L. D. Field and G. E. Ball, *J. Am. Chem. Soc.,* **2022**, 144 17622–17629.

158. S. A. Bartlett, N. A. Besley, A. J. Dent, S. Diaz-Moreno, J. Evans, M. L. Hamilton, M. W. D. Hanson-Heine, R. Horvath, V. Manici, X.-Z. Sun, M. Towrie, L. Wu, X. Zhang and M. W. George, *J. Am. Chem. Soc.,* **2019**, 141, 11471–11480.

159. J. A. Calladine, S. B. Duckett, M. W. George, S. L. Matthews, R. N. Perutz, O. Torres and K. Q. Vuong, *J. Am. Chem. Soc.,* **2011**, 133, 2303–2310.

160. K. A. Reid and D. C. Powers, *Chem. Commun.,* **2021**, 57, 4993–5003.

161. A. J. Martínez-Martínez, B. E. Tegner, A. I. McKay, A. J. Bukvic, N. H. Rees, G. J. Tizzard, S. J. Coles, M. R. Warren, S. A. Macgregor and A. S. Weller, *J. Am. Chem. Soc.,* **2018**, 140, 14958–14970.

162. T. M. Boyd, B. E. Tegner, G. J. Tizzard, A. J. Martínez-Martínez, S. E. Neale, M. A. Hayward, S. J. Coles, S. A. Macgregor and A. S. Weller, *Angew. Chem., Int. Ed.,* **2020**, 59, 6177–6181.

163. A. I. McKay, A. J. Bukvic, B. E. Tegner, A. L. Burnage, A. J. Martínez- Martínez, N. H. Rees, S. A. Macgregor and A. S. Weller, *J. Am. Chem. Soc.,* **2019**, 141, 11700–11712.

164. A. J. Bukvic, A. L. Burnage, G. J. Tizzard, A. J. Martínez-Martínez, A. I. McKay, N. H. Rees, B. E. Tegner, T. Krämer, H. Fish, M. R. Warren, S. J. Coles, S. A. Macgregor and A. S. Weller, *J. Am. Chem. Soc.,* **2021**, 143, 5106–5120.

165. L. R. Doyle, M. R. Galpin, S. K. Furfari, B. E. Tegner, A. J. Martínez-Martínez, A. C. Whitwood, S. A. Hicks, G. C. Lloyd-Jones, S. A. Macgregor and A. S. Weller, *Organometallics*, **2022**, 41, 284–292.

166. C. G. Royle, L. Sotorrios, M. R. Gyton, C. N. Brodie, A. L. Burnage, S. K. Furfari, A. Marini, M. R. Warren, S. A. Macgregor and A. S. Weller, *Organometallics*, **2022**, 41, 3270–3280.

167. D. M. Kaphan, R. C. Klet, F. A. Perras, M. Pruski, C. Yang, A. J. Kropf and M. Delferro, *ACS Catal*., **2018**, 8, 5363–5373.

168. C. P. Gordon, D. B. Culver, M. P. Conley, O. Eisenstein, R. A. Andersen and C. Copéret, *J. Am. Chem. Soc.,* **2019,** 141, 648–656.

169. D. Lapointe and K. Fagnou, *Chem. Lett.,* **2010,** 39, 1118–1126.

170. Z. H. Syed, D. M. Kaphan, F. A. Perras, M. Pruski, M. S. Ferrandon, E. C. Wegener, G. Celik, J. Wen, C. Liu, F. Dogan, K. I. Goldberg and M. Delferro, *J. Am. Chem. Soc.,* **2019**, 141, 6325–6337.

171. J. Choi, A. H. R. MacArthur, M. Brookhart and A. S. Goldman, *Chem. Rev.,* **2011**, 111, 1761–1779.

172. M. O. Akram, J. R. Tidwell, J. L. Dutton and C. D. Martin, *Angew. Chem., Int. Ed.,* **2022**, 61, e202212073.

173. J. Rodriguez and M. P. Conley, *Org. Lett.,* **2022**, 24, 4680–4683.

174. A. Chapovetsky, R. M. Kennedy, R. Witzke, E. C. Wegener, F. Dogan, I. Patel, M. Ferrandon, J. Niklas, O. G. Poluektov, N. Rui, S. D. Senanayake, J. A. Rodriguez, N. J. Zaluzec, L. Yu, J. Wen, C. Johnson, C. J. Jenks, A. J. Kropf, C. Liu, M. Delferro and D.M. Kaphan, *ACS Catal.,* **2022**, 12, 7233–7242.

Chapter 2. Formation of a Strong Heterogeneous Aluminum Lewis Acid on Silica

Abstract

$Al(OC(CF_3)_3)(PhF)$ reacts with silanols present on partially dehydroxylated silica to form well-defined $\equiv SiOAl(OC(CF_3)_3)_2(O(Si\equiv)_2)$ (**1**). The aluminum in **1** adopts a distorted trigonal bipyramidal coordination geometry. Fluoride ion affinity (FIA) calculations follow experimental trends and show that **1** is a stronger Lewis acid than $B(C_6F_5)_3$ and $Al(OC(CF_3)_3)(PhF)$ but is weaker than $Al(OC(CF_3)_3)$ and $^{i}Pr_3Si^{+}$. $Cp_2Zr(CH_3)_2$ reacts with **1** to form $[Cp_2ZrCH_3]$ $[\equiv SiOAl(OC(CF_3)_3)_2(CH_3)]$ (**3**) by methide abstraction. This reactivity pattern is similar to reactions of organometallics with the proposed strong Lewis acid sites present on Al_2O_3.

Introduction

Reactions between organometallics and oxide surfaces provide mechanistic insights about the structure and function of active sites in heterogeneous catalysts.[1] Aluminum oxide (Al_2O_3) shows interesting reactivity towards organometallics that distinguishes this support from other common oxides (Figure 2.1a). At very high dehydroxylation temperatures (1000°C) the Al_2O_3 surface lacks a significant quantity of OH groups and reacts with $Cp^*_2Th(CH_3)_2$ to generate ion-pairs formed by methide abstraction by Lewis acidic Al-sites.[2] At lower dehydroxylation temperatures (500–700°C) γ-Al_2O_3 contains a significant surface coverage of OH groups that promotes protonolysis reactions of M R groups, but a small quantity of the supported

organometallic also forms ion-pairs by alkyl abstraction from Lewis sites.[3] This reactivity pattern plays an important role in generating catalytically active sites in common heterogeneous mixtures for the polymerization of olefins. For example, $Al^{i}Bu_3$, $Cp^{b}{}_2ZrCl_2$ (Cp^{b} =1-butylcyclopentadienyl) and γ-Al_2O_3 self-assemble in a network of reactions to form small quantities of $[Cp^{b}{}_2Zr\ H][H\ AlO_X]$ ion-pairs that are the active sites for the polymerization of ethylene.[4]

Both experiment[5] and theory[5b,6] predict that Lewis sites responsible for the reactivity shown in Figure 2.1a are present at very low surface coverage, which limits experimental strategies to assess the structure and function of these apparently strong Lewis acids present on Al_2O_3. More broadly, generation of oxides containing strong well-defined Lewis sites is limited. Reactions of alkylaluminum[7,8] or alkylgallium[9] with silica tend to form mixtures of surface species. The common strong Lewis acid $B(C_6F_5)_3$ forms adducts with silanols present on SiO_2 partially dehydroxylated at 700°C ($SiO_{2\text{-}700}$), which can be deprotonated with weak aniline bases to form ion-pairs, Figure 2.1b.[10,11] Silica partially dehydroxylated at 500°C ($SiO_{2\text{-}500}$) contains a high surface coverage of silanols and reacts with $B(C_6F_5)_3$ through a dehydration-reorganization-protonolysis cascade to form pairs of Lewis sites (Figure 2.1b).[12] However, this well defined heterogeneous Lewis acid does not participate in the characteristic reactivity shown in Figure 2.1a.

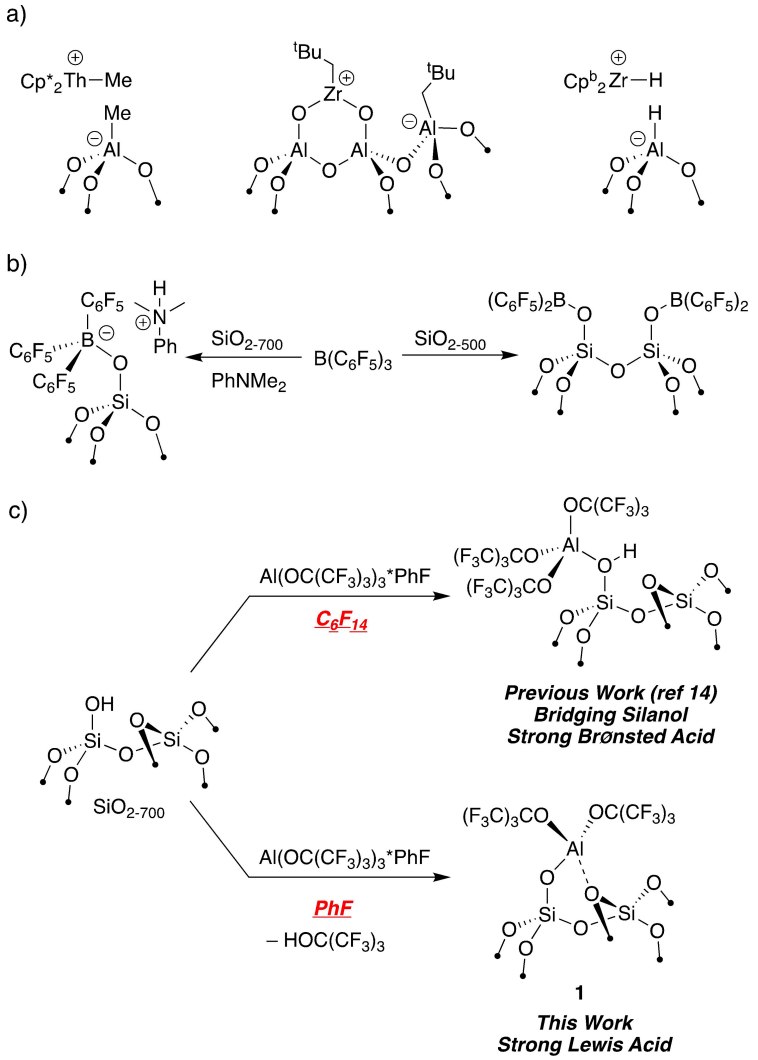

Figure 2.1. Representative examples of ion-pairs formed on Al_2O_3 (a, Cp*= pentamethylcyclopentadienyl; Cp^b=1-butylcyclopentadienyl). Reactivity of $B(C_6F_5)_3$ with SiO_2 (b). Well-defined Lewis acid sites formed in this study (c).

$Al(OC(CF_3)_3)(PhF)$[13] is a stronger Lewis acid than $B(C_6F_5)_3$. $Al(OC(CF_3)_3)(PhF)$ reacts with $SiO_{2\text{-}700}$ in perfluorohexane to form bridging silanols that, when deprotonated, form weakly coordinated ion-pairs with silylium-like ions[14] or (α-diimine)Pd Me^+ organometallics.[15] This study describes the reaction of $Al(OC(CF_3)_3)(PhF)$ with partially dehydroxylated SiO_2 in *fluorobenzene* solvent, which induces proton transfer to form

[SiOAl(OC(CF_3)$_3$)$_2$(O(Si)$_2$) (**1**), Figure 2.1c. Experimental and theoretical studies show that the aluminum sites in **1** are very strong Lewis acids, and these Lewis sites participate in alkyl abstraction reactions typical of reactions between organometallics and Al_2O_3 surfaces shown in Figure 2.1a.

Results and Discussion

The reaction of Aerosil $SiO_{2\text{-}700}$ (0.26 ± 0.01 mmol SiOH g $^{1}{}_{SiO2}$) with Al(OC(CF_3)$_3$)$_3$(PhF) at 45°C forms **1** and 0.22± 0.01 mmol nonafluoro-*tert*-butyl alcohol g $^{-1}{}_{SiO2}$ (Figure 2.1c, bottom reaction). This result indicates that most silanols present on this silica react to form **1**. ICP-OES analysis of **1** gives 0.21 ±0.01 mmol$_{Al}$ g ^{1}, indicating that 1.0 equiv of nonafluoro-*tert*-butyl alcohol is released per aluminum grafted onto the silica surface in this reaction. Suspending **1** in CD_3CN results in desorption of fluorobenzene (0.23 ± 0.01 mmolg^{-1}). The FTIR of **1** contains *sp*^{2} C H stretches at 3081 cm $^{-1}$ and *sp*^{2} C=C stretches at 1480 cm^{-1} from adsorbed PhF (Figure 2.6). This spectrum also contains a complex ν_{OH} region with signals assigned to unreacted silanols (3724 cm ^{1}) and hydrogen bonded silanols (3668 and 3548 cm $^{-1}$). The ^{1}H MAS NMR spectrum of **1** contains signals at 7.1 (PhF), 4.6 (hydrogen bonded SiOH) and 2.3 ppm (free SiOH), Figure 2.8. The hydrogen bonded silanols present in this material are probably a result of the unreacted silanols interacting with the OC(CF_3)$_3$ fragments in **1**. This behavior is common in well-defined species generated on silica.[16] The bridging silanol in Si OH Al(OC(CF_3)$_3$) appears at 3542 cm ^{1} in the FTIR spectra and 5.0 ppm in ^{1}H NMR spectra, indicating that this species is not present to an appreciable extent in **1**.[14]

The $^{27}Al\{^{1}H\}$ magic angle spinning (MAS) NMR spectrum of **1** recorded at 18.8T contains a single signal that simulates as an isotropic chemical shift (δ_{iso}) of 74 ppm and a quadrupolar coupling constant (C_Q) of 18.0 MHz (Figure 2.2a). These values are similar to those obtained from static ^{27}Al NMR measurements at 14.1 and 9.4T that give δ_{iso} of 4820 ppm and C_Q values of 17.71.0 MHz (Figure 2.9).

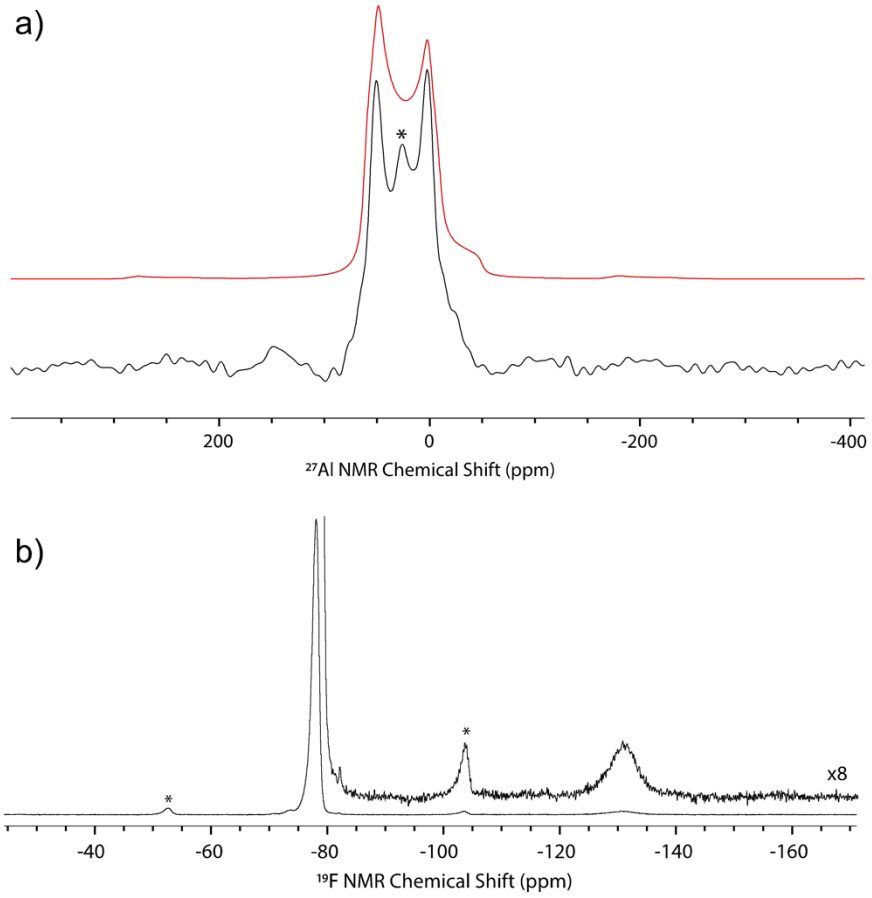

Figure 2.2. 27Al{1H} MAS NMR spectrum of 1 at 18.8 T (a, experimental in black simulation in red, νrot=18.87 kHz, *=probe background); 19F MAS NMR spectrum of 1 (b, νrot=13 kHz, *=spinning side bands).

Uncertainties in δ_{iso} and C_Q were estimated by varying these parameters in simulations (Figure 2.9c). The ^{19}F MAS NMR spectrum of **1** is shown in Figure 2.2b and

contains signals at 78 and 132 ppm assigned to the $OC(CF_3)_3$ groups and physisorbed PhF, respectively. The ratio of these signals is 27:1, in agreement with the 1:1 stoichiometry suggested from desorption experiments (Figure 2.7). However, the diagnostic ^{1}H and ^{19}F NMR chemical shifts indicate that PhF is not close to the Al sites in **1**.[14] The ^{19}F MAS NMR spectrum does not contain signals from Si $OC(CF_3)_3$ expected at 74 ppm,[17] indicating that opening of strained siloxane bridges by $HOC(CF_3)_3$ or $Al(OC(CF_3)_3)_3(PhF)$ does not occur during generation of **1**. The 1:1 Al:R^FOH ratio obtained from elemental analysis and mass balance, and the lack of siloxane bridge reactivity, indicate that aluminum dimers are not present in **1**.

The NMR parameters of the SiH_3-capped silsesquioxane models of **1** shown in Figure 2.3 were calculated using the B3LYP/6-31G++(d,p) level of theory. This silsesquioxane cluster is a simplified model for the complex amorphous silica surface, but contains an isolated silanol and unstrained Si O Si bridges that approximate the coordination environment for an isolated silanol on $SiO_{2\text{-}700}$.[18] The calculated C_Q is given below each structure. The distorted trigonal bipyramidal structure shown in Figure 2.3a contains an Al OSi (1.693 Å), two Al $OC(CF_3)_3$ (1.755 Å), and two long Al F (2.101 Å and 2.125 Å). The sum of the Al O bond angles is 360.0°, and the F Al F bond angle is 163.7° (τ=0.73). This structure is expected to have a C_Q of 26.0 MHz, which is larger than obtained experimentally for **1**. Replacing one Al F with a siloxane bridge forms the distorted trigonal bipyramidal structure (τ=0.63) shown in Figure 2.3b predicted to have a smaller C_Q of 18.7 MHz, which is close to experimental values. This structure contains Al X distances of 1.775 Å (Al OSi), 1.724 Å and 1.752 Å (Al $OC(CF_3)_3$), 1.974 Å (Al

$O(Si)_2$), and 2.381 Å (Al F). The sum of Al O angles is 353.03° and the F Al $O(Si)_2$ angle is 162.7°. The PhF adduct of **1** results in an Al site predicted to have a C_Q value of 20.1 MHz, larger than the experimental ^{27}Al NMR data (Figure 2.3c).

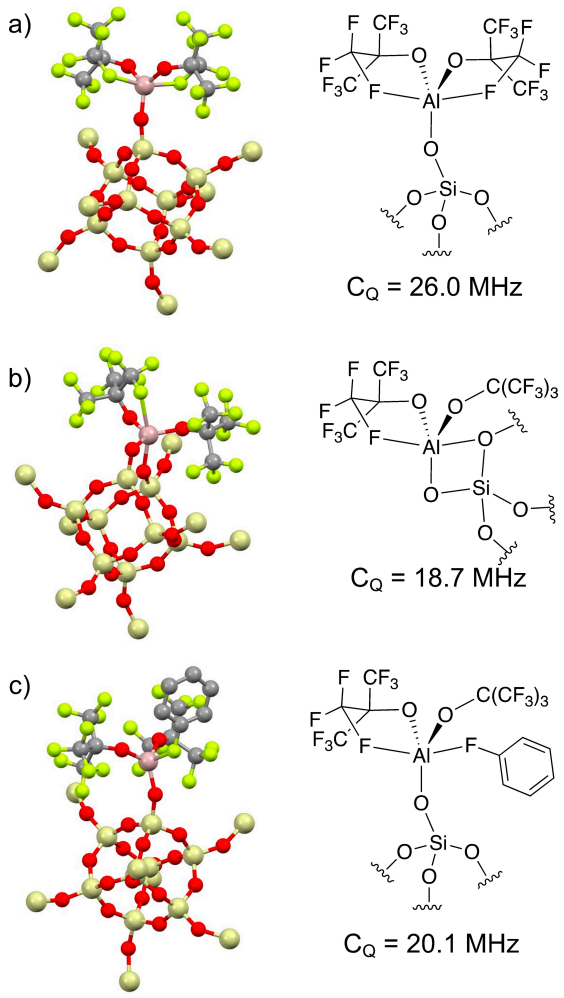

Figure 2.3. Calculated structures approximating 1 using the silsesquioxane cluster to simulate the SiO2 surface. The calculated 27Al NMR parameters of each structure are given below each structure.

1 is a very strong Lewis acid. Table 1 contains the calculated fluoride ion affinity (FIA) for **1** and related Lewis acids calculated using the BP86/SV(P) level of theory.[19,20]

1 has a FIA of 528 kJmol ^{1}. This value is significantly larger than the calculated FIA for $B(C_6F_5)_3$ (448 kJmol ^{1}) and slightly larger than isolable $Al(OC(CF_3)_3)(PhF)$ (514 kJmol ^{1}). **1** is a weaker Lewis acid than $Al(OC(CF_3)_3)_3$ and $^{i}Pr_3Si^{+}$.

The ^{31}P NMR chemical shift of Lewis adducts containing $O{=}PEt_3$ are also diagnostic of the strength of a Lewis acids in solution[21] or on solid surfaces.[22] The reaction of **1** with 1.1 equiv $O{=}PEt_3$ forms **2** [Eq. (1)]. The $^{31}P\{^{1}H\}$ MAS NMR spectrum of **2** contains signals at 78 ppm (change in ^{31}P NMR chemical shift=$\Delta\delta$=28 ppm, 92%) and 82 ppm ($\Delta\delta$=32 ppm, 8%) as well as a signal for physisorbed $O{=}PEt_3$ (54 ppm, $\Delta\delta$=4 ppm, Figure 2.11). For comparison, the $^{31}P\{^{1}H\}$ NMR spectrum of $O{=}PEt_3$ contacted with $B(C_6F_5)_3$ contains a signal at 77.8 ppm ($\Delta\delta$=26.6 ppm) in CD_2Cl_2.[23] Similar to the FIA data presented in Table 1, the experimental $^{31}P\{^{1}H\}$ NMR data indicate that the aluminum sites in **1** are weaker Lewis acids than typical silylium-like species generated in solution ($\Delta\delta$=42.2 ppm)[24] or supported on sulfated zirconium oxide ($\Delta\delta$=43 ppm).[25] The 31

P NMR parameters of **2** were calculated using the small cluster model of **1** shown in Figure 2.3b containing a molecule of $O{=}PEt_3$ coordinated to aluminum (Figure 2.28), which results in distortion of the originally trigonal bipyramidal aluminum to the more common tetrahedral geometry. The calculated $\Delta\delta^{31}P$ is 31 ppm. This value is close to the experimental results, suggesting both $^{31}P\{^{1}H\}$ NMR signals in **2** correspond to tetrahedral aluminum sites.[26]

Table 2.1: Fluoride Ion Affinity (FIA) of Selected Lewis Acids and 1 in kJmol ^{1}.

Compound	FIA
B(C6F5)3	448
$Al(OC(CF_3)_3)_3(PhF)$	514
1	528
$Al(OC(CF_3)_3)_3$	540
iPr_3Si+	1073

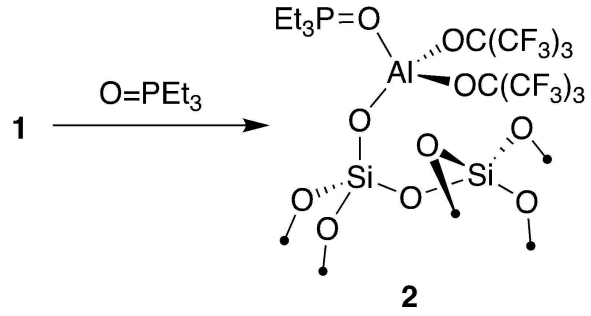

The reaction of **1** with $Cp_2Zr(^{13}CH_3)_2$ is complex, which is expected in cases where $Cp_2Zr\ CH_3{}^{+}$ fragments are generated on silica.[27] A $^{13}C\{^{1}H\}$ Cross Polarization Magic Angle Spinning (CPMAS) NMR spectrum of $Cp_2Zr(CH_3)_2$/**1** recorded at 298 K is shown in Figure 2.4a and contains four carbon-13 enriched signals at 38, 23, 3, and 11 ppm. A reaction scheme accounting for these signals is shown in Figure 2.4b. The signal at 23 ppm is assigned to $Cp_2Zr(^{13}CH_3)(OSi)$ (**4**).[28] Consistent with this result methane forms in this reaction (0.060.01 mmolg ^{1}), indicating that **4** forms by the reaction of $Cp_2Zr(CH_3)_2$ with residual silanols present on **1**. The signal at 3 ppm is assigned to Si $^{13}CH_3$, which occurs by reactions of Zr $^{13}CH_3{}^{+}$ with nearby siloxane bridges to form $[Cp_2Zr(OSi)]$ $[SiOAl(OC(CF_3)_3)_2(CH_3)]$ (**5**) and Si 13CH3.[27]

The signals corresponding to the ion-pair $[Cp_2ZrCH_3][\ SiOAl(OC(CF_3)_3)_2(CH_3)]$ (**3**) appear at 38 ppm for the $[Cp_2Zr\ ^{13}CH_3]^+$ and at 11 ppm for the $[SiOAl(OC(CF_3)_3)_2(^{13}CH_3)]$. A 2D ^1H-^{13}C CP heteronuclear correlation (HETCOR) NMR spectrum of **3** shows that the Zr-$^{13}CH_3$ 13C NMR signal at 38 ppm correlates with H NMR signals at 2.0 ppm, and the Al $^{13}CH_3$ ^{13}C NMR signal at -11 ppm correlates with ^1H NMR signals at 0.6 ppm (Figure 2.19). The ^{27}Al MAS NMR spectrum of **3** contains a signal with δ_{iso} =77 ppm and a C_Q =11.2 MHz (Figure 2.17). The reduced C_Q value is consistent with a more symmetrical tetrahedral aluminum environment in **3** as compared to **1**.

A $^{13}C\{^{27}Al\}$ Phase-Modulated Resonance-Echo Saturation-Pulse Double-Resonance (PM-RESPDOR)[29,30] experiment was recorded to confirm the ^{13}C NMR signal assignment of the Al $^{13}CH_3$ group in **3**. This experiment was performed in a zirconia rotor sealed with a silicone plug at 110 K with cooled nitrogen gas to prevent the decomposition of samples that could occur with conventional room temperature MAS setups. The RESPDOR experiment re-introduces the ^{13}C ^{27}Al dipolar couplings under MAS, and the application of a saturation pulse to the ^{27}Al spins results in 13C NMR signal dephasing for carbons close to aluminum.[29,30] The rate of signal dephasing is dependent on the C Al internuclear distance; short durations of dipolar recoupling selectively dephase ^{13}C ^{27}Al spin pairs that are close to one another. The $^{13}C\{^{27}Al\}$ RESPDOR spectra recorded with a short duration of dipolar recoupling (τ_{rec} = 0.4 ms) and the difference spectrum are shown in Figure 2.4c. These spectra show that only the ^{13}C NMR signal at -11 ppm dephases in the RESPDOR experiment. This result

unambiguously assigns this ^{13}C NMR signal to the Al $^{13}CH_3$ group from the $[SiOAl(OC(CF_3)_3)_2(^{13}CH_3)]$ anion that forms as a result of methide abstraction between $Cp_2Zr(^{13}CH_3)_2$ and **1**. Fitting the $^{13}C\{^{27}Al\}$ RESPDOR dephasing curve gives an Al C internuclear distance of 1.8 0.2 Å with a relatively large error in the measurement (Figure 2,20a). However, comparison of the RESPDOR curve of **3** with that of aluminum acetylacetonate shows that the rate of dipolar dephasing is much faster for **3**, confirming a C Al covalent bond (Figure 2.20b). The ^{13}C NMR signals for the Zr CH_3 fragments in **3** and **4** did not exhibit signal dephasing in the $^{13}C\{^{27}Al\}$ PM-RESPDOR experiment, indicating that these carbons are far (>5 Å) from the aluminum, consistent with the proposed structure discussed below.

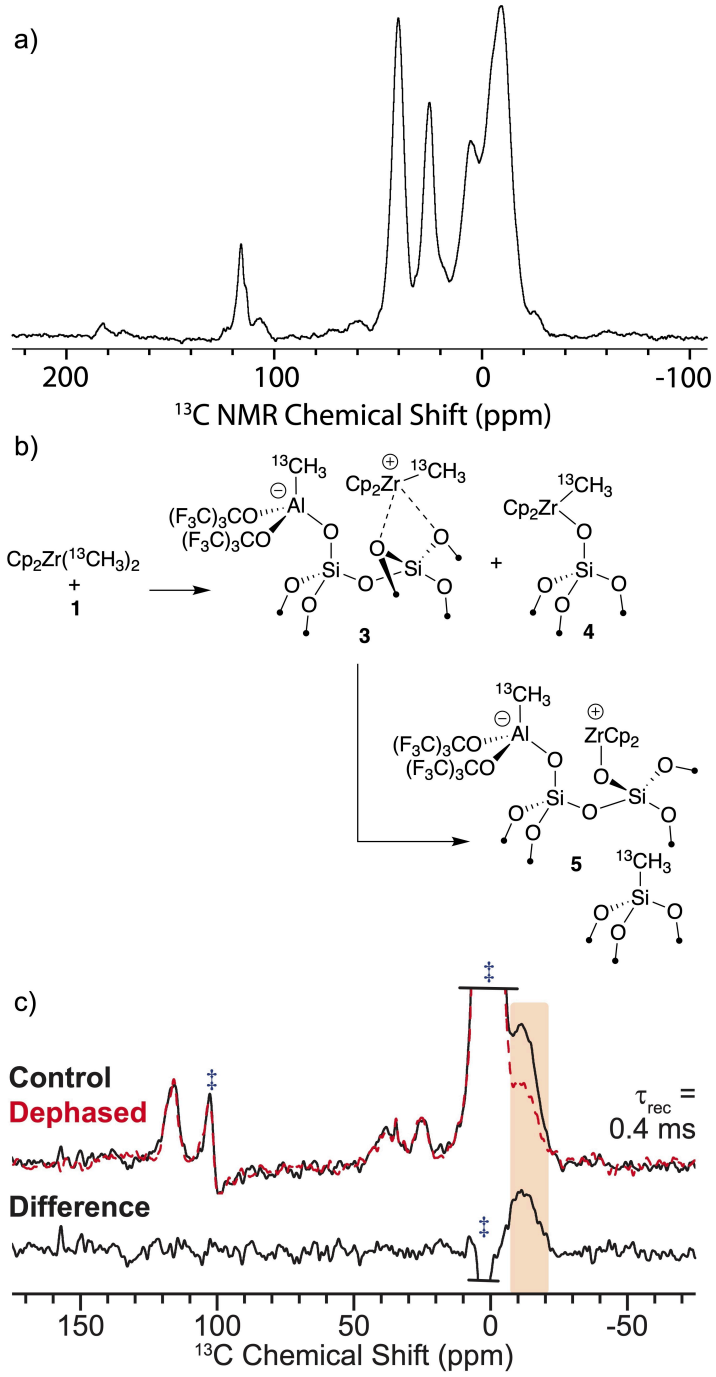

Figure 2.4. Room temperature $^{13}C\{^1H\}$ CPMAS NMR spectrum of Cp_2Zr-$(^{13}CH_3)_2$/**1** (a). Reaction of **1** to form **3**, **4** and **5** (b). $^{13}C\{^{27}Al\}$ PMRESPDOR NMR spectra of **3** recorded with 0.4 ms of dipolar recoupling and either with (red, dashed) or without (black, solid) a PM saturation pulse applied to the ^{27}Al spins (c). A difference spectrum is shown below these NMR spectra. The daggers originate from the silicone plug ^{13}C NMR signals.

DFT calculations of the small cluster shown in Figure 2.5 reproduces many experimental observations. At the B3LYP/ 6-31++G(d,p) level of theory $[Cp_2ZrCH_3][SiOAl(OC(CF_3)_3)_2(CH_3)]$ is predicted to exhibit ^{13}C chemical shifts of 10 for $[SiOAl(OC(CF_3)_3)_2(\mathbf{C}H_3)]$ and 35 ppm for $[Cp_2Zr\ \mathbf{C}H_3]^+$, respectively. The calculated ^{27}Al C_Q is 11.6 MHz, close to experimental C_Q of 11.2 MHz. A small C_Q for $[SiOAl(OC(CF_3)_3)_2(\mathbf{C}H_3)]$ is a result of the near ideal tetrahedral geometry of the anion (C Al O=109.9°, 117.4° and 117.4°). The Al C distance is 1.96 Å, within the range of extracted values from $^{13}C\{^{27}Al\}$ PM-RESPDOR experiments. The methide abstraction reaction from $Cp_2Zr\text{-}(CH_3)_2$ by **1** results in a $Cp_2Zr(CH_3)^+$ fragment that coordinates to nearby siloxane bridges to form a formally saturated 18-electron zirconocenium. The Zr $(OSi\equiv)_2$ distances are 2.497 Å and 2.532 Å, longer than the Zr O distance in $Cp_2ZrMe(thf)^+$ (2.122(14) Å).[31]

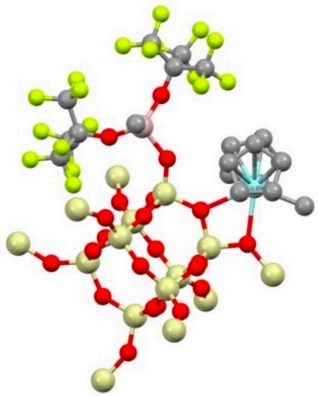

Figure 2.5. Structure of $[Cp_2ZrCH_3][SiOAl(OC(CF_3)_3)_2(CH_3)]$ calculated at the B3LYP/6-31++G(d,p) level of theory.

Generation of an 18-electron metallocenium in [Cp_2ZrCH_3][$SiOAl(OC(CF_3)_3)_2(CH_3)$] does not prohibit typical reaction chemistry of d^0 $Cp_2Zr–Me^+$ ions. Pressurizing C_6H_{12} slurries of $Cp_2Zr(^{13}CH_3)_2$/**1** with 20.6 bar ethylene results in rapid formation of polyethylene ($78.6 g_{PE}\ g_{cat}^{-1}\ h^{-1}$), showing that the siloxane bridges are weakly coordinated to the $Cp_2Zr\ CH_3^+$ fragment in **3**. Contacting $Cp_2Zr(^{13}CH_3)_2$/**1** with excess vinyl chloride generates 0.0730.004 mmol 3-^{13}C-propene,[32] indicating that 33% of total zirconium in $Cp_2Zr(^{13}CH_3)_2$/**1** inserts olefins. This result is consistent with the complex speciation observed in the ^{13}C CPMAS NMR spectrum because **4** and **5** are not expected to insert olefins. The percentage of $Zr–Me^+$ sites that insert olefins in $Cp_2Zr(^{13}CH_3)_2$/**1** is slightly higher than obtained in mixtures of Al^iBu_3, $Cp^b{}_2ZrCl_2$ (Cp^b =1-butylcyclopentadienyl) and γAl_2O_3;[4] but lower than obtained for well-defined organometallic olefin polymerization catalysts supported on weakly coordinating supports.[15,33]

Conclusion

$Al(OC(CF_3)_3)(PhF)$ shows interesting reaction chemistry with $SiO_{2\text{-}700}$. When mixed in perfluorohexane bridging silanol adducts form.[14] When mixed in fluorobenzene proton transfer occurs to release nonafluoro-*tert*-butyl alcohol and forms **1**. The $^{31}P\{^1H\}$ MAS NMR chemical shift of **2** and FIA of **1** indicate that the aluminum is more Lewis acidic than $B(C_6F_5)_3$. The slightly higher FIA for **1** compared to $Al(OC(CF_3)_3)(PhF)$ is not totally surprising; OSi ligands on partially dehydroxylated silica are known to be electron withdrawing.[34] The strong Lewis acidity in **1** promotes

methide abstraction from $Cp_2Zr(CH_3)_2$ to form metallocenium ion-pairs that were elusive with well-defined Lewis sites on oxide supports. **1** may provide a platform to evaluate how strong Lewis sites on oxides affect catalytic properties of well-defined heterogeneous catalysts, which we are currently exploring.

Materials and Methods

General Considerations

All manipulations were performed under an inert atmosphere of dinitrogen or argon using standard Schlenk or glovebox techniques. Benzene-d6 was purchased from Cambridge Isotope Laboratories, dried over sodium/benzophenone, degassed by freeze-pump-thaw cycles, distilled under vacuum, and stored in an inert atmosphere glovebox. Pentane was degassed by purging Ar through the solvent and dried by passing through a solvent system containing two activated alumina columns. Pentane was stored over sodium/benzophenone, degassed, and distilled under vacuum prior to use. Fluorobenzene was dried over CaH2, degassed, and vacuum distilled prior to use. Al(OC(CF3)3)3(PhF) was prepared by literature methods.1 Aerosil-200 silica was partially dehydroxylated at 700 ˚C as previously described.2 Vinyl chloride was stored over activated Cu/mol sieves for at least 24h to remove O_2 and H_2O. FTIR spectra were recorded in transmission mode as pressed pellets using a Bruker Alpha IR spectrometer in an argon-filled glovebox. Elemental analysis of Al and Zr were carried out by digesting solid samples in 2% nitric acid for 12 hours at room temperature and measuring samples at the University

of California, Riverside Environmental Sciences Research Laboratory (ESRL) on a Perkin-Elmer Optima 7300DV ICP-OES.

Solution NMR spectra at 7.05T were acquired on an Avance Bruker 300 NMR spectrometer. 1H NMR spectra were referenced to the NMR solvent residual peak. Solution 19F{1H} spectra were referenced to an external standard of C6F6. All room temperature solid-state NMR samples were packed in 4 mm zirconia rotors and sealed with a Kel-F cap under an argon or dinitrogen atmosphere in a glovebox. Solid state NMR spectra at the University of California, Riverside were recorded under magic angle spinning or under static conditions at 14.1 T using Bruker NEO600 spectrometer. All solid-state NMR processing used Bruker Topspin.

1H-13C CP-HETCOR and 13C{27Al} PM-RESPDOR solid-state NMR spectroscopy experiments were performed at Iowa State University and Ames Laboratory on a 9.4 T Bruker wide-bore magnet equipped with a AVANCE III console and a 3.2 mm HXY dynamic nuclear polarization (DNP) NMR probe configured in double resonance mode. A REDOR box radio frequency (RF) splitter (NMR Service GmbH) was applied to the X-channel of the NMR probe to tune the X channel simultaneously to 13C and 27Al.3 Both the X- and Y-preamplifiers were used and assigned to 13C and 27Al, respectively, and connected to the REDOR box RF splitter via a T-joint adapter. Bandpass filters were applied to both 13C and 27Al to isolate the two resonance frequencies. The sample was packed into a 3.2 mm sapphire NMR rotor inside an Ar filled glovebox and capped with a silicone plug in front of the zirconium drive cap to minimize air exposure. The transfer time from the glovebox to the NMR probe was less than 10 seconds. NMR experiments

were performed at ca. 110 K under a N2 atmosphere (cooled with N2 gas used for spinning). All NMR experiments were performed with a 10 kHz MAS frequency. 1H $\pi/2$ and π pulses were 2.5 and 5 μs in duration, corresponding to a 100 kHz RF field. 13C $\pi/2$ and π pulses were 5 and 10 μs in duration, corresponding to a 50 kHz RF field. 1H→13C CP was performed during the CP-HETCOR experiment and at the beginning of the 13C{27Al} PMRESPDOR experiment. 1H→13C CP was achieved with simultaneous 1H and 13C spin-lock pulses (1H spin-lock pulse exhibited a 90-100 % ramp) with RF fields of ~ 69 (ramped from ~ 62 to 69 kHz) or 46 kHz, respectively. The 2D 1H-13C CP-HETCOR NMR spectrum was recorded with 100 kHz 1H RF field eDUMBO$_{1\text{-}22}$ homonuclear dipolar decoupling during the indirect acquisition of ^{1}H,[4] a 1 ms CP contact time, a 0.35 s recycle delay, 384 scans, a 32 μs t1 dwell and 160 t1 TD points (total t1 acquisition = 2.56 ms; total experimental time ~ 6 h). 13C{27Al} PMRESPDOR experiments5 were performed with a 27Al phase-modulated (PM) saturation pulse that was 1 ms in duration with an ~ 15 kHz 27Al RF field (CT nutation frequency = 45 kHz). Rotational-Resonance Double-Resonance (REDOR) recoupling with a 50 kHz RF field was applied to the 13C spins to re-introduce the 13C-27Al dipolar interaction under MAS. The 13C{27Al} PM-RESPDOR experiment was acquired with a 1 ms 1H→13C CP contact time, a 0.35s recycle delay, 5120 scans and 8 total TD points (4 control and 4 dephased; total experimental time ~ 4 h). 100 kHz 1H RF field SPINAL-64 heteronuclear decoupling was applied during the acquisition of 13C and throughout the entire 13C{27Al} RESPDOR experiment.6

Numerical solid-state NMR simulations of the 13C{27Al} PM-RESPDOR experiment was performed using SIMPSON v4.2.1.7 All numerical simulations were performed with the rep168 crystal file, 10 γ angles and a maximum time duration of 1.0 μs where the Hamiltonian was considered time independent. 13C{27Al} PM-RESPDOR numerical simulations were performed on a two-spin 13C-27Al spins system with a 27Al CQ = 11 MHz (determined experimentally), a 10 kHz MAS frequency, 50 kHz RF field REDOR recoupling applied to the 13C spin, and a 15 kHz RF field PM saturation pulse applied to the 27Al spin (1 ms in duration). All 13C and 27Al pulses were on-resonance with the center of gravity of the NMR signals (QIS calculated for 27Al CQ = 11 MHz, ca. 67 ppm).

Synthesis and Characterization of 1

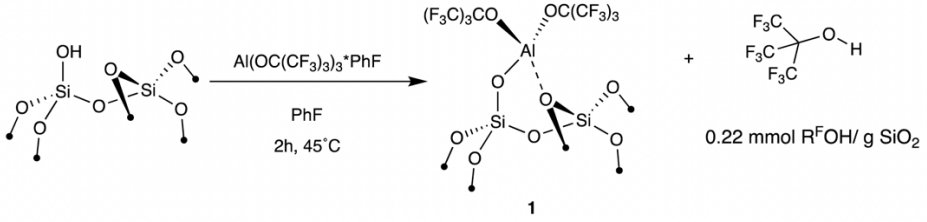

A double-schlenk flask containing two arms separated by a medium porosity frit was charged with $SiO_{2\text{-}700}$ (1g, 0.26 mmol OH) and $Al(OC(CF_3)_3)_3(PhF)$ (240 mg, 0.29 mmol, 1.1 mol eq) in one arm of the flask inside an argon-filled glovebox. The flask was removed from the glovebox, connected to a vacuum line equipped with a diffusion pump, and evacuated for 5 min. Fluorobenzene (~ 6 mL) was condensed onto the solids at 77K. The mixture was warmed to room temperature and heated to 45 ˚C for 2h. During this

time the mixture was stirred gently to promote mixing and prevent the compacted silica from breaking into smaller fragments. After 2h at 45 °C the clear colorless solution was filtered away from the functionalized silica to the other arm of the double Schlenk. The arm of the double Schlenk containing the functionalized silica was cooled to 77K, causing PhF on the other side of the flask to condense onto the solid. The PhF was warmed to 25 °C, stirred for 5 min, and filtered back to the other side of the double Schlenk. This procedure was repeated two more times to wash residual $Al(OC(CF_3)_3)_3(PhF)$ away from the silica material. The volatiles were vacuum transferred to a new flask and R^FOH released in this reaction (0.22 ± 0.01 mmol g^{-1}_{SiO2}) was quantified using solution $^{19}F\{^1H\}$ NMR spectroscopy using C_6F_6 as an internal standard. The functionalized silica was dried under vacuum for 40 minutes. **1** is a white solid, which was stored in an Ar glovebox freezer at -20˚C. Suspending **1** in a CD_3CN containing C_6Me_6 standard results in desorption of 0.23 ± 0.01 mmol g^{-1} PhF. ICP-OES confirms 0.21 ± 0.011 $mmol_{Al}$ g^{-1}_{SiO2}. Elemental analysis gives 2.71% C (2.3 $mmol_C$ g^{-1}).

FTIR: ν_{O-H} = 3724 (≡Si-**OH**), 3668 and 3548 (H-bonded (≡Si-**OH**) cm^{-1} as well as ν_{C-H} = 3081 and sp^2 $\nu_{C=C}$ = 1480 (PhF physisorbed to surface) cm^{-1}.

Solid State NMR: ^1H MAS NMR (600MHz, 10 kHz): 7.1 (PhF), 4.6 (hydrogen bonded ≡SiOH), 2.3 (≡Si-**OH**) ppm

$^{13}C\{1H\}$ MAS NMR (151 MHz, 10 kHz): 122 ppm (q, $^1J_{CF}$ = 279 Hz, ≡Si-O-$Al(OC(\mathbf{C}F_3)_3)_2$) 131 and 114 ppm (PhF) 78 ppm (≡Si-O-$Al(O\mathbf{C}(CF_3)_3)_2$)

^{19}F MAS NMR (470MHz, 13 kHz): -78 ppm (≡Si-O-$Al(OC(C\mathbf{F_3})_3)_2$), -132 ppm (Ph**F**)

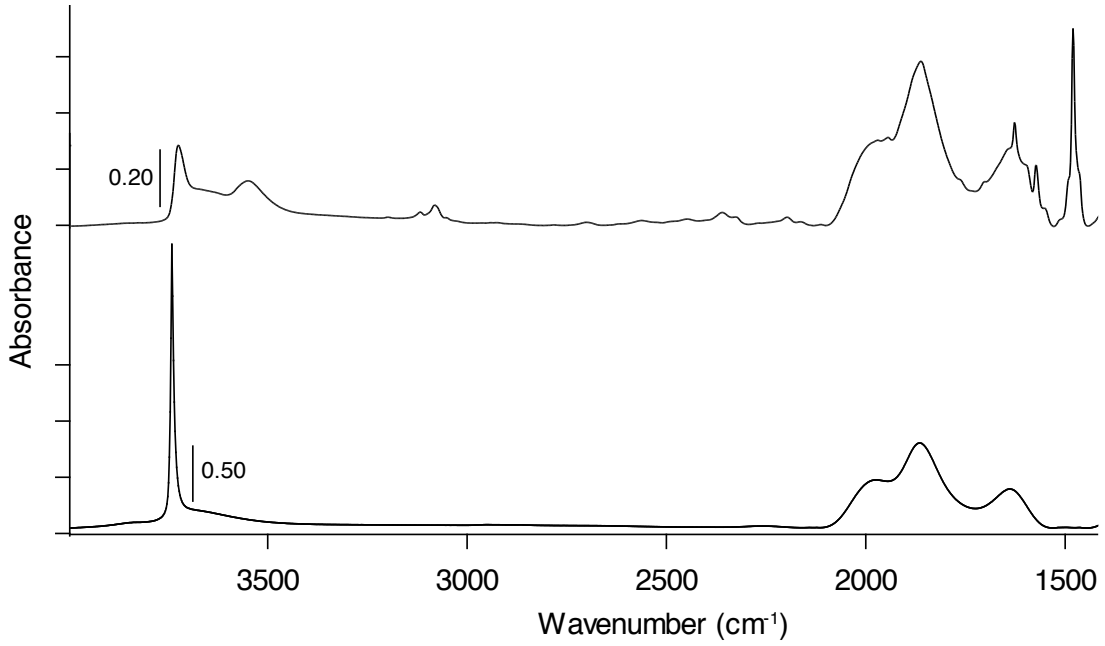

Figure 2.6. FT-IR spectrum of **1** (top) stacked with $SiO_{2\text{-}700}$ (bottom), wavenumbers (cm^{-1}).

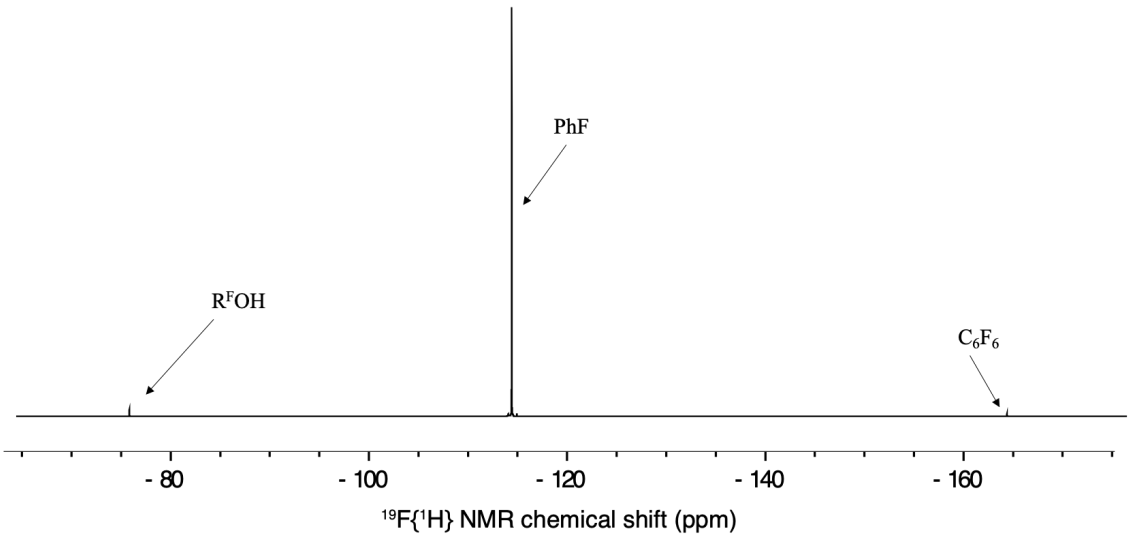

Figure 2.7. $^{19}F\{^{1}H\}$ NMR spectrum of the volatiles after the grafting of **1** in PhF, NMR taken in C_6D_6 with an internal standard of C_6F_6.

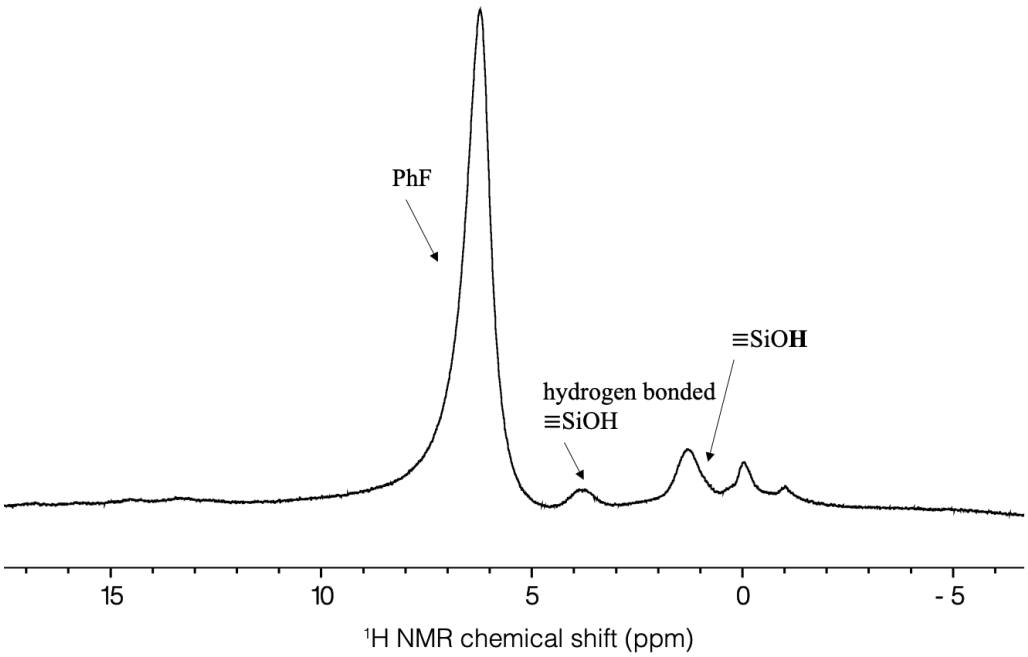

Figure 2.8. 10 kHz MAS ^{1}H NMR of **1**, 7.1 (PhF), 4.6 (hydrogen bonded ≡SiOH), 2.3 (≡Si-**OH**) ppm

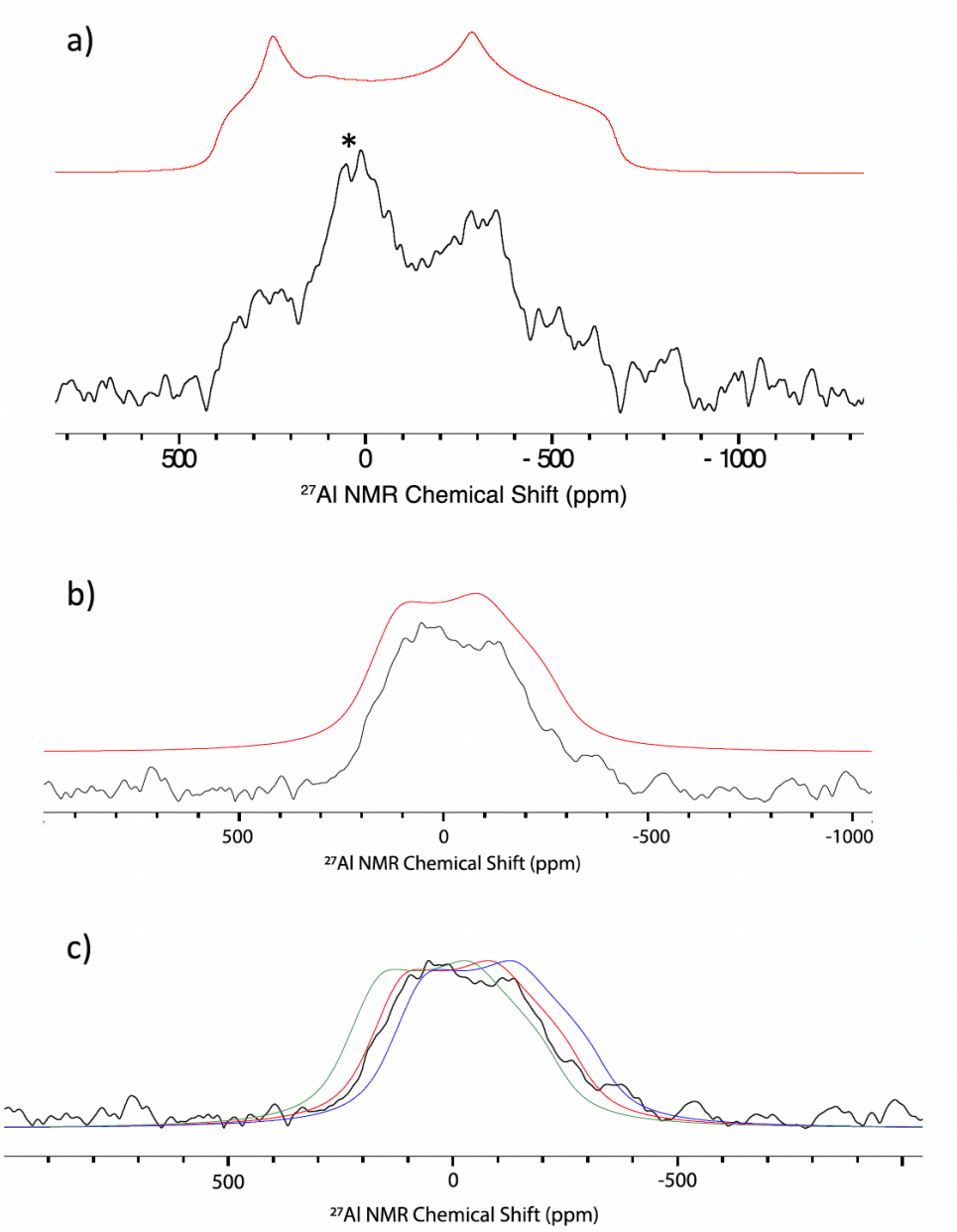

Figure 2.9. (a) Static 27Al NMR of 1 recorded at room temperature in a 4mm zirconia rotor at 9.4 T, top = simulation, bottom = experimental spectrum, probe background denoted by asterisk (*). (b) Static 27Al NMR of 1 recorded at room temperature in a 4mm zirconia rotor at 14.1 T, top = simulation, bottom = experimental spectrum. (c) simulations of static 27Al NMR data at 14.1 T with CQ = 17.9 MHz, $\eta = 0.35$, and $\delta = 0$ (blue), 48.3 (red), and 100 (green) ppm. These data show that the 27Al NMR simulations are sensitive to chemical shift, and these differences in chemical shift are resolvable in this experiment. From these simulations, and the subtle changes in line shapes using these parameters, we estimate the error to be ± 20 ppm for δ and ± 1 MHz for CQ.

Table 2.2. NMR simulations of 27Al NMR parameters for 1. These values are averages of simulations performed at 14.1T and 9.4T. The 27Al NMR spectrum acquired at 9.4T is shown in Figure 2.10.

	δ_{iso} (ppm)	Ω (ppm)	κ	C_q (MHz)	η
14.1 T	48.2	117	-0.99	17.9	0.36
9.4 T	48.4	116	-0.99	17.4	0.35

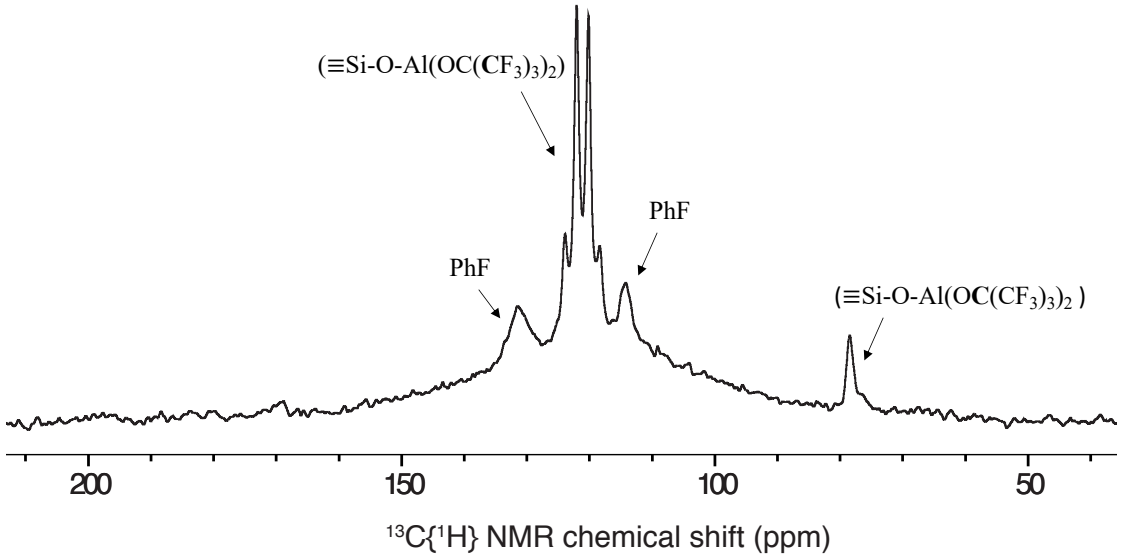

Figure 2.10. $^{13}C\{^{1}H\}$ MAS NMR of 1 acquired at 10 kHz spinning speed. The broad feature centered at 120 ppm is probe background.

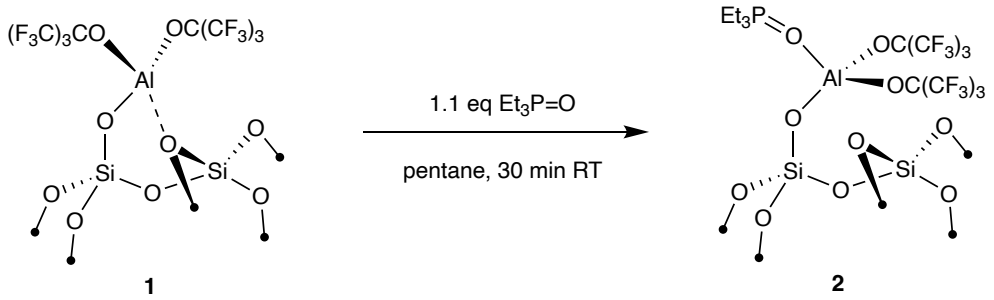

Synthesis of 2: 1 (0.500 g, 0.110 mmol Al) and TEPO (0.016g, 1.1 eq, 0.121 mmol) were transferred to separate arms of a double-Schlenk flask inside an argon-filled glovebox. The flask was removed from the glovebox, connected to a high vacuum line, and evacuated for 5 min. Pentane (~ 5 mL) was condensed into the side of the flask containing TEPO at 77K, and the clear colorless solution was filtered to the other side of the double-Schlenk onto 1. The mixture was warmed to room temperature and gently stirred for 30 minutes to promote mixing and prevent the silica from further breaking down. After this time, the clear colorless solution was filtered to the other side of the double-Schlenk. The arm of the double Schlenk containing the functionalized silica was cooled to 77K, causing the pentane on the other side of the flask to condense onto the functionalized silica. The pentane was warmed to 25˚C, stirred for 5 min, and filtered back to the other side of the double Schlenk. This procedure was repeated two more times to remove unreacted TEPO from the functionalized silica surface. The volatiles were removed under vacuum and the solid was dried under diffusion pump vacuum for 45 minutes. 2 was collected as a white solid and was stored in an Ar glovebox freezer at -20˚C. Analysis of the solution phase shows that PhF (0.211 mmol g^{-1}) desorb from the surface during this reaction. ICP-OES 0.209 $mmol_{Al}\ g^{-1}{}_{SiO2}$ and 0.221 $mmol_{P}\ g^{-1}{}_{SiO2}$. Elemental analysis gives 4.87 %C (4 $mmol_{C}\ g^{-1}$).

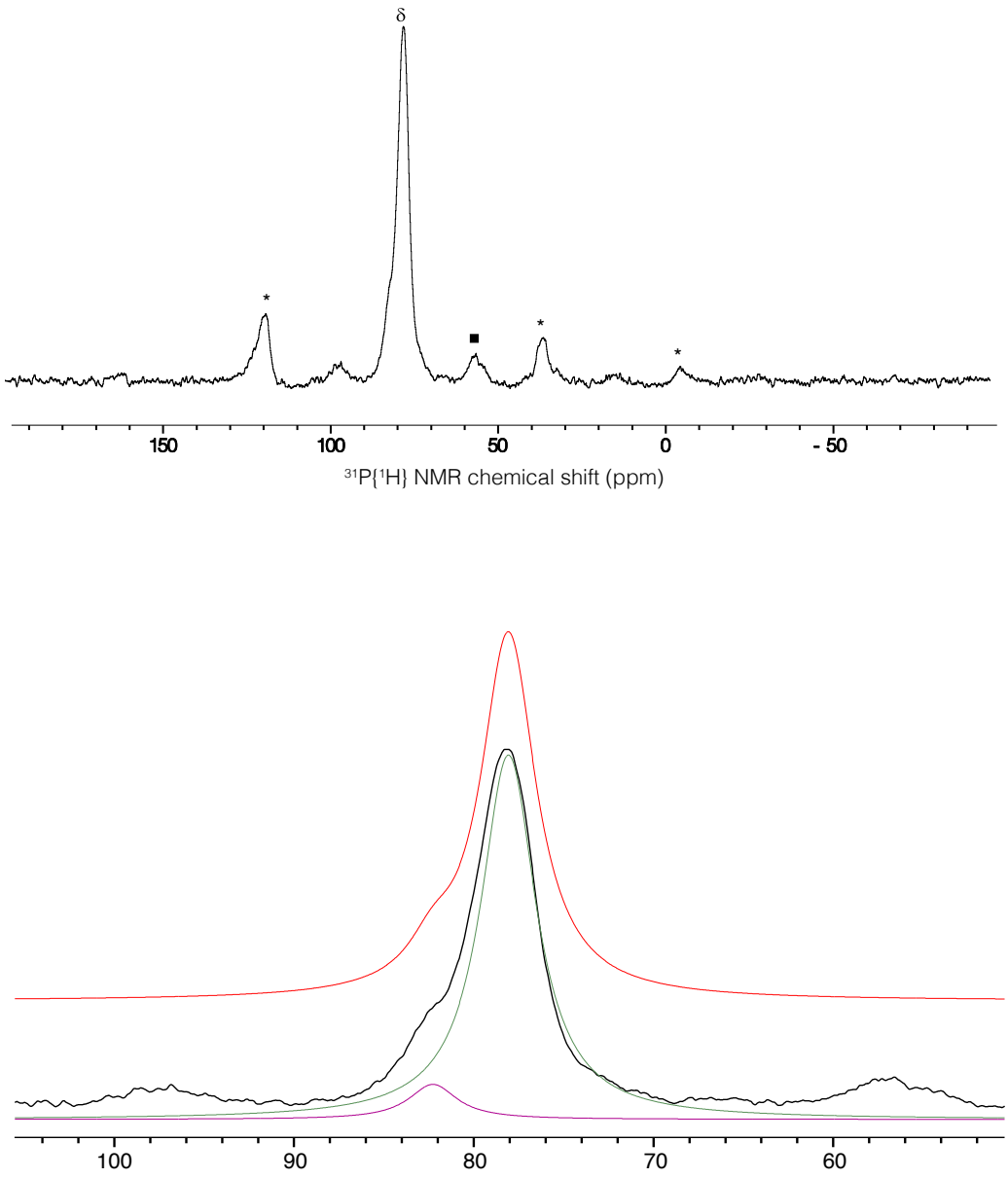

Figure 2.11. 10kHz $^{31}P\{^{1}H\}$ MAS NMR of 2 (top spectrum). Expansion of the isotropic chemical shift region of the $^{31}P\{^{1}H\}$ MAS NMR of 2 with a quantitative deconvolution of the two signals present in this material (bottom spectrum). The isotropic shift at 78 ppm (~92% from deconvolution), with a shoulder on the main peak at 82 ppm (~8% from deconvolution). Spinning sidebands are denoted by the asterisk (*) and TEPO physisorbed to the surface is denoted by the black square at 54 ppm (ssb of physisorbed TEPO at 97 ppm and 18 ppm).

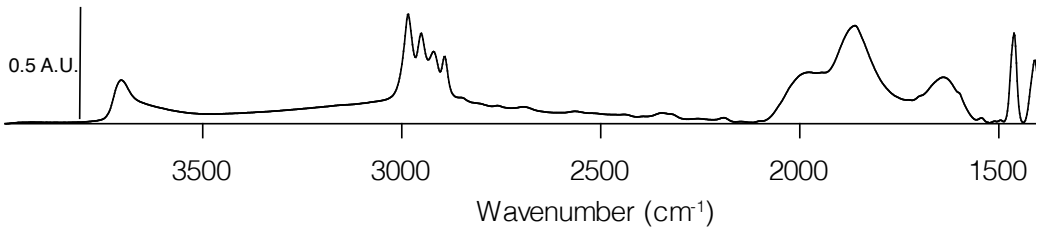

Figure 2.12. FT-IR spectrum of **2**: $\nu_{O\text{-}H}$ = 3709 cm^{-1} (Hydrogen bonded silanols) and $\nu_{C\text{-}H}$ = 2984-2918 cm^{-1}.

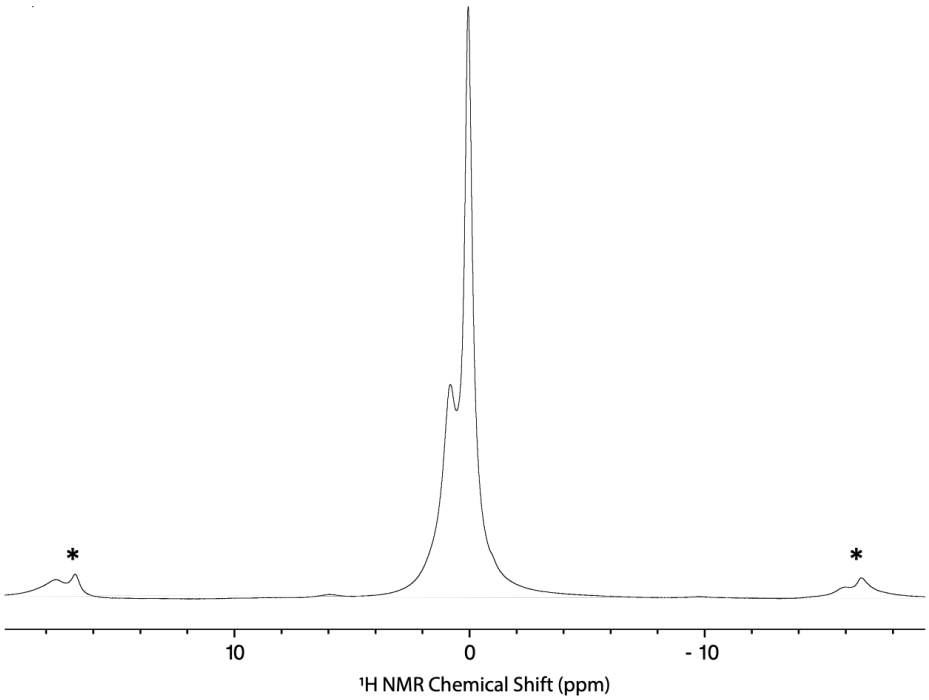

Figure 2.13. 10 kHz MAS ^{1}H NMR of **2** acquired at -20˚C. 0.1 ppm ($C\mathbf{H_3}CH_2)_3P{=}O$) 0.7 ppm ($CH_3C\mathbf{H_2})_3P{=}O$) with spinning sidebands (*) at 17 and -17 ppm.

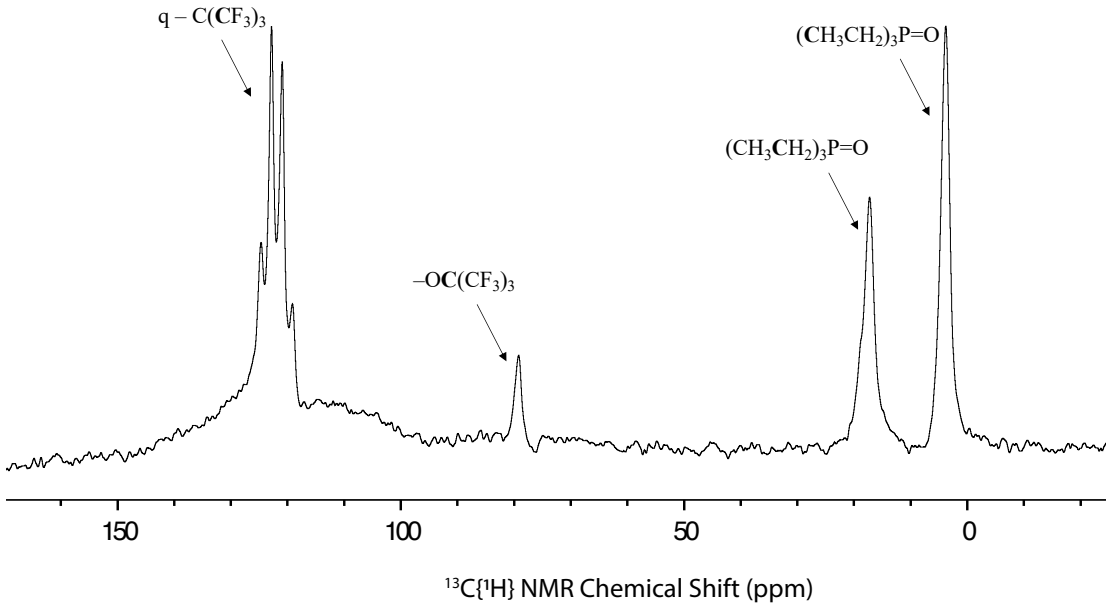

Figure 2.14. 10 kHz MAS $^{13}C\{^{1}H\}$ NMR of 2 acquired at -20˚C.

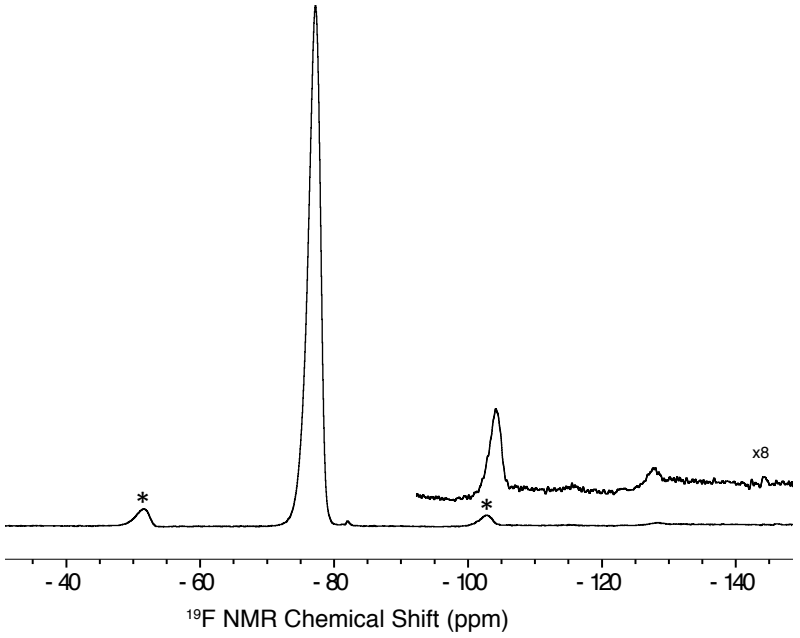

Figure 2.15. 12 kHz MAS ^{19}F NMR of 2. The ×8 zoom shows that the signal intensity for PhF decreases significantly compared to 1.

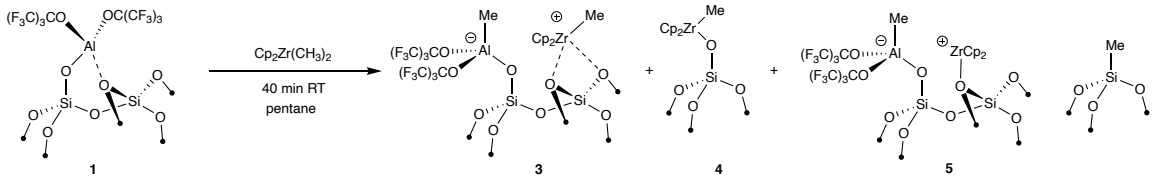

Synthesis of Cp_2ZrMe_2/1: 1 (0.400 g, 0.088 mmol Al LA site) and Cp_2ZrMe_2 (1.5 eq, 0.132 mmol, 0.033 g) were transferred to one arm of a double-Schlenk flask inside an argon-filled glovebox. The flask was removed from the glovebox, connected to a high vacuum line, and evacuated for 5 min. Pentane (~ 8 mL) was condensed onto the solids under vacuum at 77 K, and the mixture was warmed to room temperature and then stirred gently for 40 minutes. The clear, colorless solution was then filtered away from the functionalized silica to the other side of the double-Schlenk. The arm of the double Schlenk containing the functionalized silica was cooled to 77K, causing the pentane on the other side of the flask to condense onto the functionalized silica. The pentane was warmed to 25˚C, stirred for 5 min, and filtered back to the other side of the double Schlenk. This procedure was repeated two more times to wash the silica of residual Cp_2ZrMe_2. The volatiles were collected and isolated in a separate Schlenk storage tube fitted with a Teflon-tap and set aside to be analyzed by ^1H and $^{19}F\{^1H\}$ solution NMR. The surface was then dried under diffusion pump vacuum for 45 minutes. Cp_2ZrMe_2/1 was collected as a pale yellow solid and was stored in an Ar glovebox freezer at -20˚C. ICP-OES analysis of this material gives 0.210 mmol Al/g SiO_2 and 0.212 mmol Zr/g SiO_2. Elemental analysis gives 4.80 %C (4 $mmol_C\ g^{-1}$). An identical procedure was used to generate $Cp_2Zr(^{13}CH_3)_2$/1

FT-IR: $\nu_{C\text{-}H}$ = 3081 and 2935 (C-H from Cp_2ZrMe) cm^{-1}.

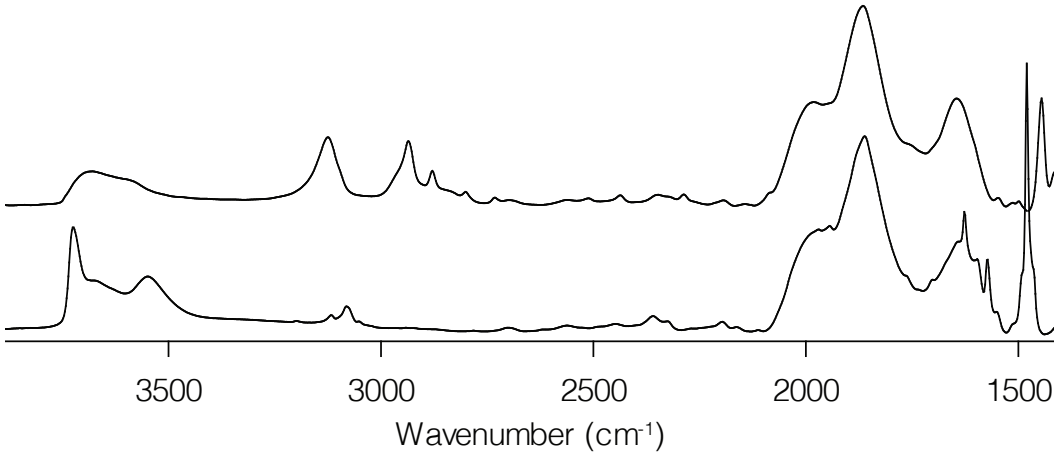

Figure 2.16. FT-IR spectrum of 1 (bottom) stacked with Cp_2ZrMe_2/1 (top), wavenumbers (cm^{-1}).

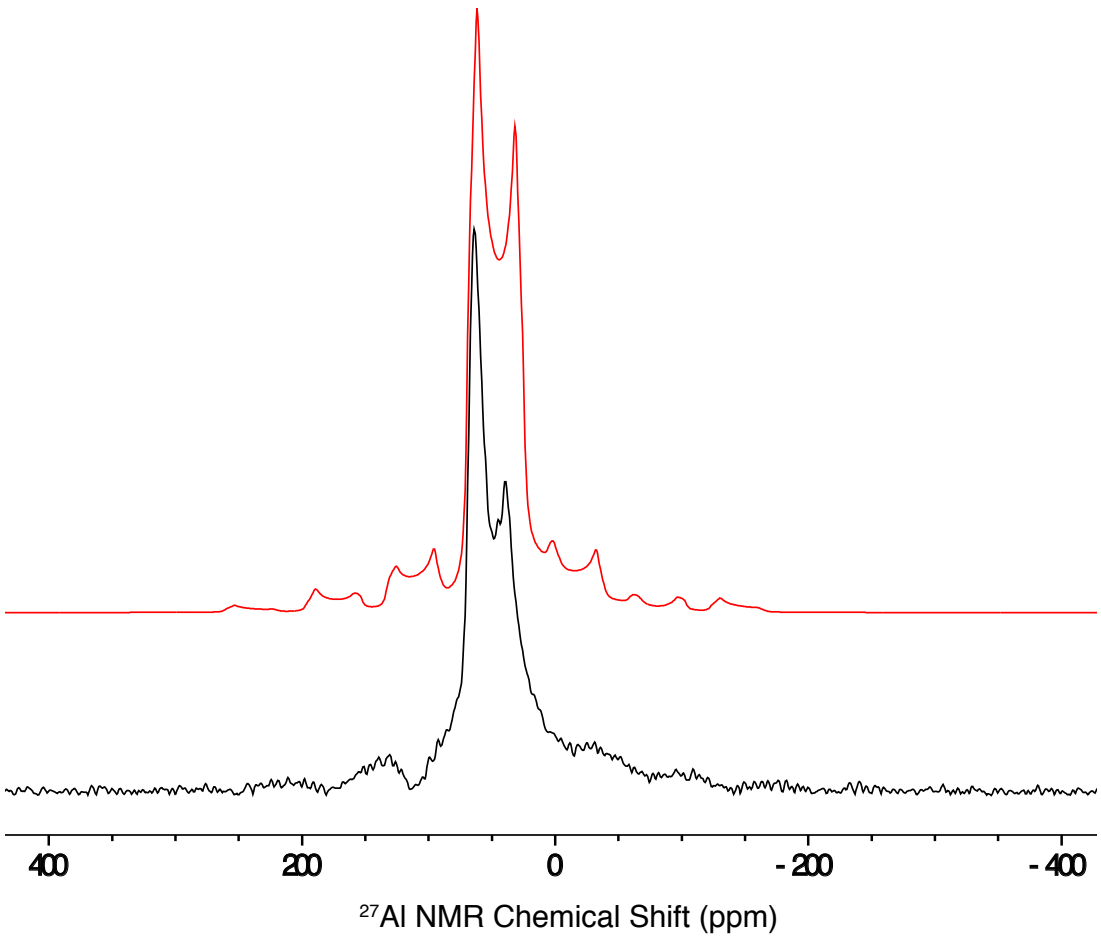

Figure 2.17. 10 kHz MAS $^{27}Al\{^{1}H\}$ Hahn Echo NMR of $Cp_2Zr(^{13}CH_3)_2$/1, top = simulation, bottom = experimental spectrum.

δ_{iso} (ppm)	δ CSA	η CSA	C_q (MHz)	η	α	β	γ
77.1	93.9	0.23	11.2	0.18	254	24	69

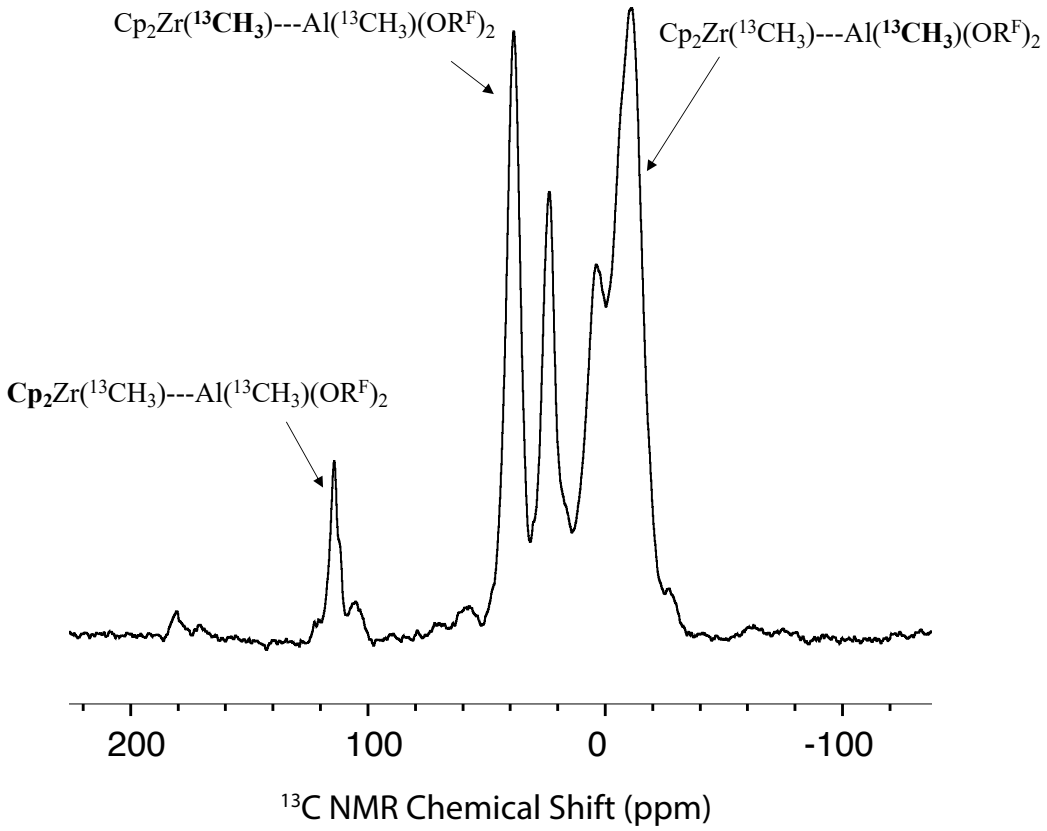

Figure 2.18. 10 kHz ^{13}C CPMAS NMR of $Cp_2Zr(^{13}CH_3)_2$/1. The signal at 23 ppm is assigned to $Cp_2Zr(^{13}CH_3)(OSi\equiv)$ (4).[8] The signal at 3 ppm is from $\equiv Si–^{13}CH_3$; this signal is a signature of decomposition of $Zr–CH_3^+$ sites by alkyl transfer to the silica surface.[9]

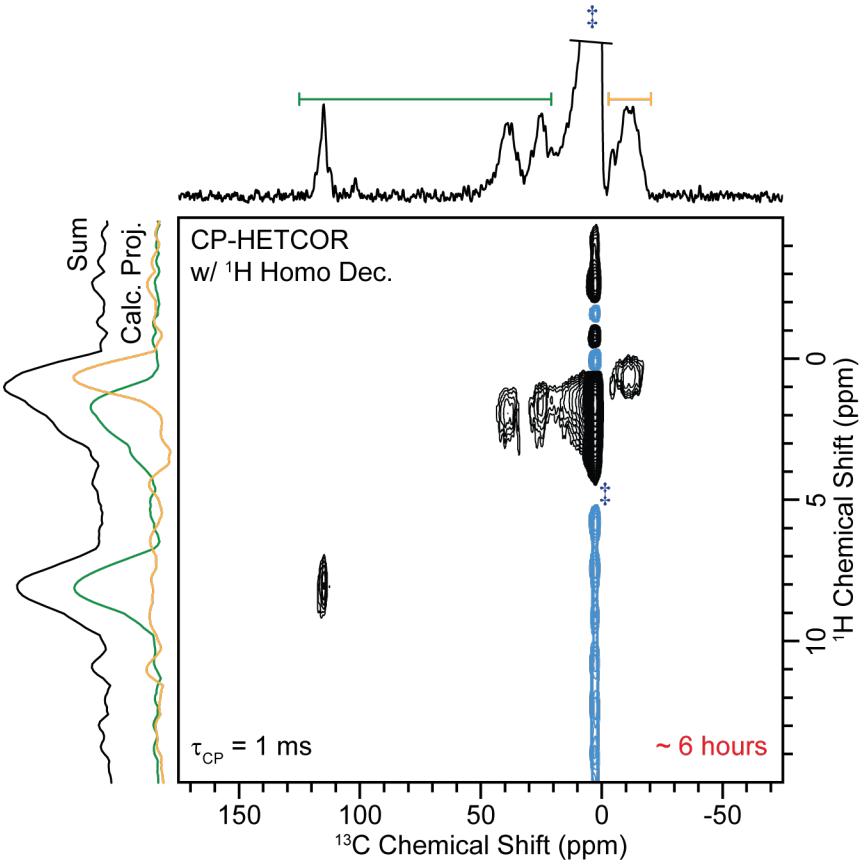

Figure 2.19. 2D ^{1}H-^{13}C CP-HETCOR NMR spectrum of **3** recorded with a 1 ms CP contact time, a 10 kHz MAS frequency, 100 kHz ^{1}H RF field of eDUMBO$_{1\text{-}22}$ homonuclear dipolar decoupling during ^{1}H chemical shift evolution[4] and a sample temperature of ca. 110 K. The blue dagger indicates the silicone plug to ensure the sample was air-free. The ^{1}H dimension was reconstructed by summing over the ^{13}C NMR signals indicated by the green and orange lines within the figure.

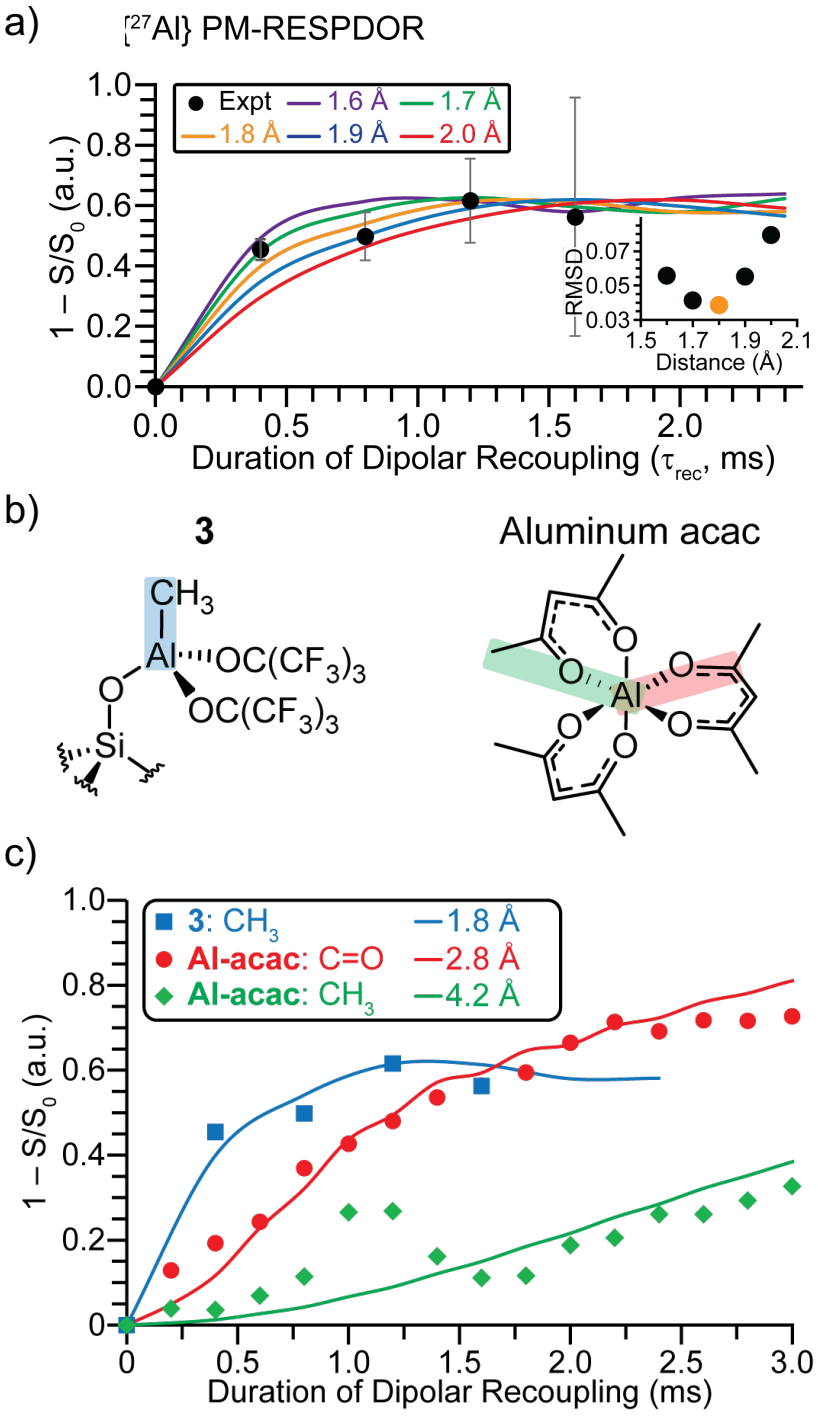

Figure 2.20. (A) $^{13}C\{^{27}Al\}$ PM-RESPDOR curve of **3** for the ^{13}C NMR signal at –11 ppm recorded at 110 K. (B) Structural models of **3** and aluminum acetylacetonate (Al-acac) highlighting the (left, blue) **Al**-**C**H_3 group of **3** and the (right, red) **Al**-O=**C** and (right, green) **Al**-O=C-**C**H_3 groups of Al-acac. (C) $^{13}C\{^{27}Al\}$ PM-RESPDOR curves for the

(blue, squares) **Al**-**C**H_3 group of **3**, (red, circles) **Al**-O=**C** group of Al-acac and (green, diamonds) **Al**-O=C-**C**H_3 group of Al-acac. The solid lines correspond to numerical simulations with the given Al-C internuclear distances. All RESPDOR experiments we performed with a sample temperature of *ca.* 100 K and a 10 kHz MAS frequency.

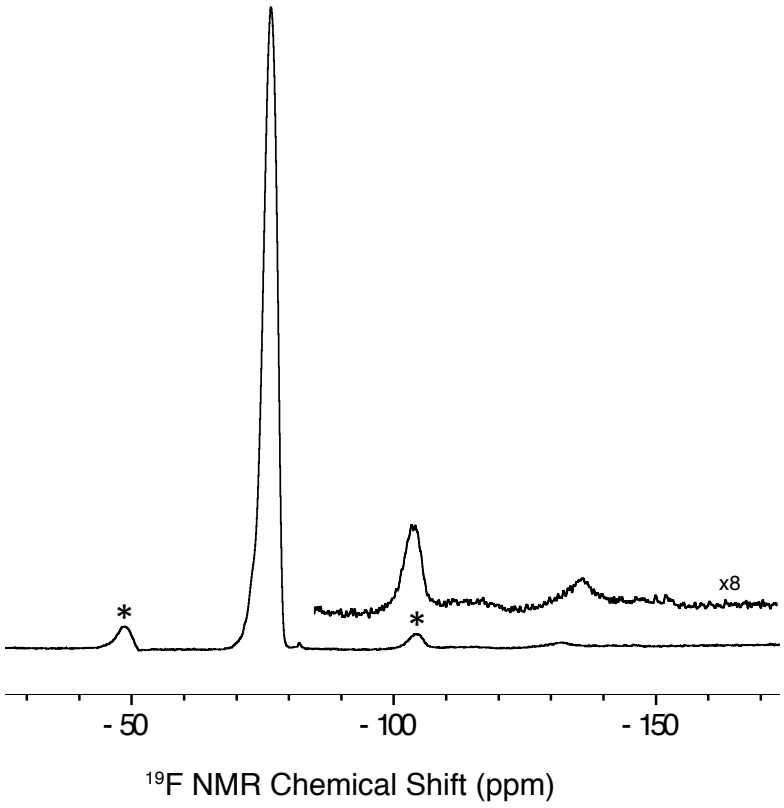

Figure 2.21. 13 kHz MAS ^{19}F NMR of **$Cp_2Zr(^{13}CH_3)_2$/1**. The ×8 zoom shows that the signal intensity for PhF decreases significantly compared to **1**.

Polymerization of Ethylene by Cp_2ZrMe_2/1: In a N_2 filled glovebox, a 12 mL glass liner was charged with 15 mg of **Cp_2ZrMe_2/1** (0.0033 mmol Zr) and 5mL cyclohexane. The liner was placed in the well of a Biotage Endeavor high-pressure reactor, and the reactor was pressurized with 300 psi (20 atm) ethylene at 45˚C for 20 minutes. The reactor was then vented and purged with nitrogen to remove ethylene from the system.

The liner containing spent catalyst and polymer was removed, and the resulting polymer was isolated, washed with EtOH, filtered, and dried under vacuum to constant weight. The reaction produced 415 mg of polyethylene. Polymerizations were repeated in triplicate to determine an average activity of 78.6 g_{PE}/g_{cat}^{-1} h^{-1}.

Reaction of Vinyl Chloride with Cp_2ZrMe_2/1: In an Ar glovebox, a 100mL round bottom flask was charged with 25 mg of **by Cp_2ZrMe_2/1** or **$Cp_2Zr(^{13}CH_3)_2$/1** and fitted with a Teflon tap fitted high vacuum adapter. The flask was removed from the glovebox, connected to a high vacuum line, and evacuated for 5 minutes. 1 atm of vinyl chloride was added to the flask. The flask was heated to 50 ˚C for 7 hours. The volatiles were quantified by GC-FID. Triplicate runs of this experiment show that 0.073 ± 0.004 mmol propylene/g SiO_2 and 0.033 mmol methane/ g SiO_2 form in this reaction. Analysis of the volatiles by NMR by transfer into a Teflon valved NMR tube containing C_6D_6 using **$Cp_2Zr(^{13}CH_3)_2$/1** showed that ^{13}C-C3-propene is the only isomer formed in this reaction.

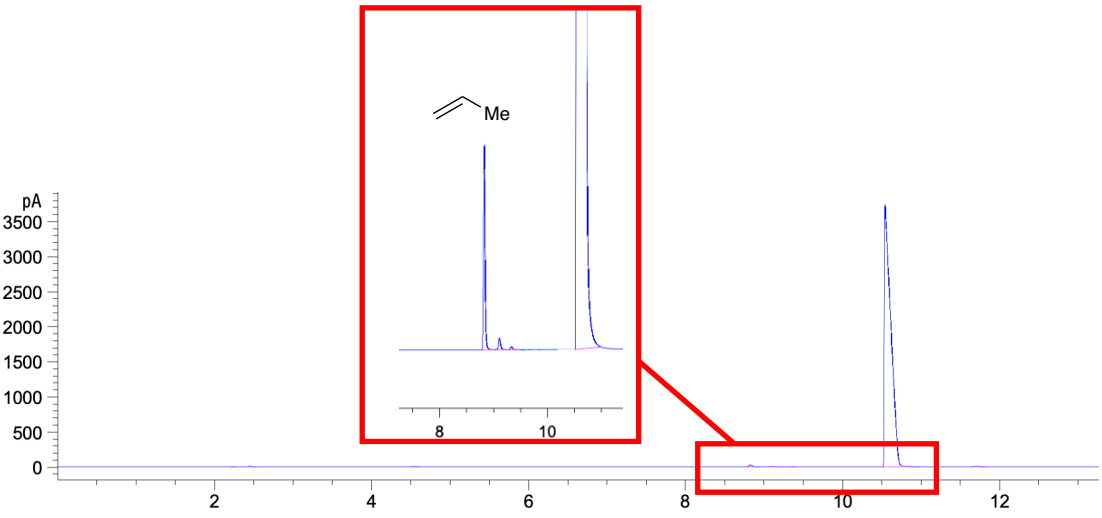

Figure 2.22. Gas chromatogram of volatiles from vinyl chloride contacted Cp_2ZrMe_2 on Al LA SiO_2, retention time of 8.7 minutes for propylene on HPPLOT-Q, quantified 0.078 mmol Zr-Me cation/ g Al LA SiO_2.

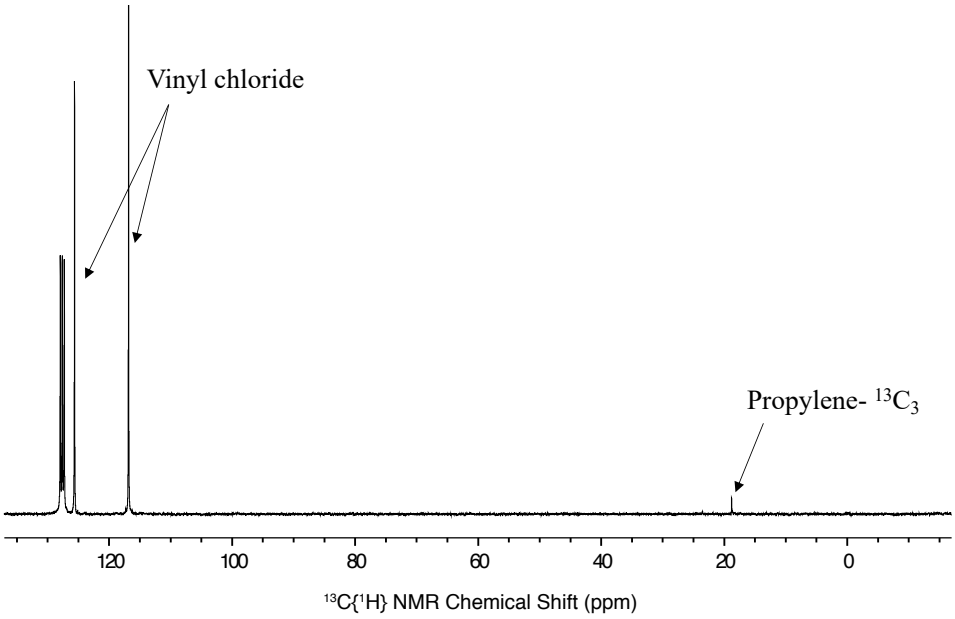

Figure 2.23. $^{13}C\{^1H\}$ NMR of volatiles from vinyl chloride contacted **$Cp_2Zr(^{13}CH_3)_2$/1.**

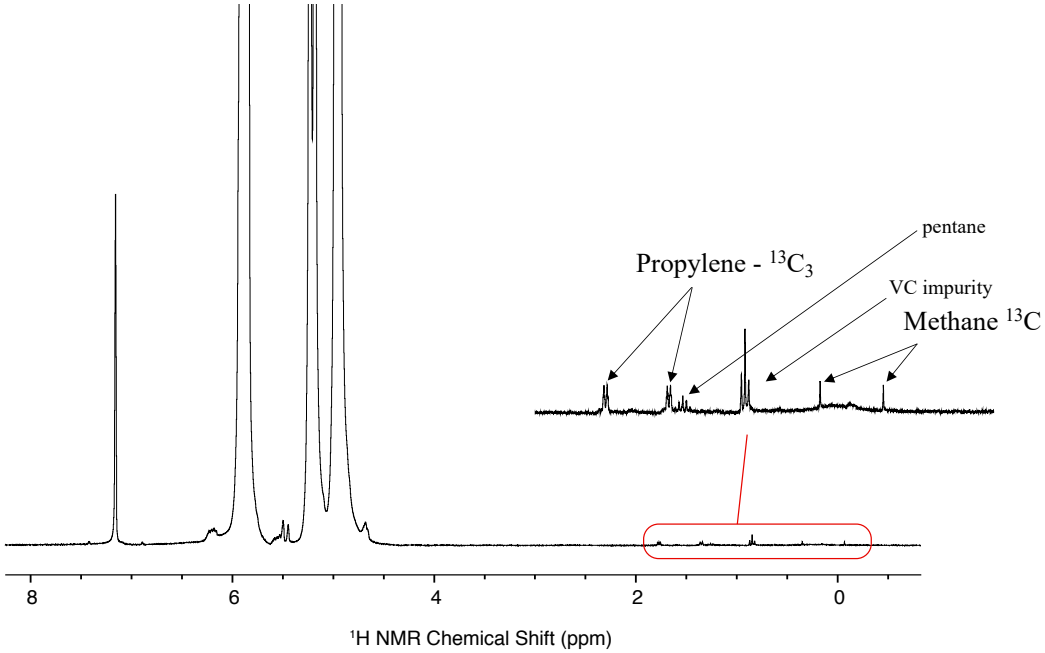

Figure 2.24. ^1H NMR of volatiles from vinyl chloride contacted **$Cp_2Zr(^{13}CH_3)_2$/1.**

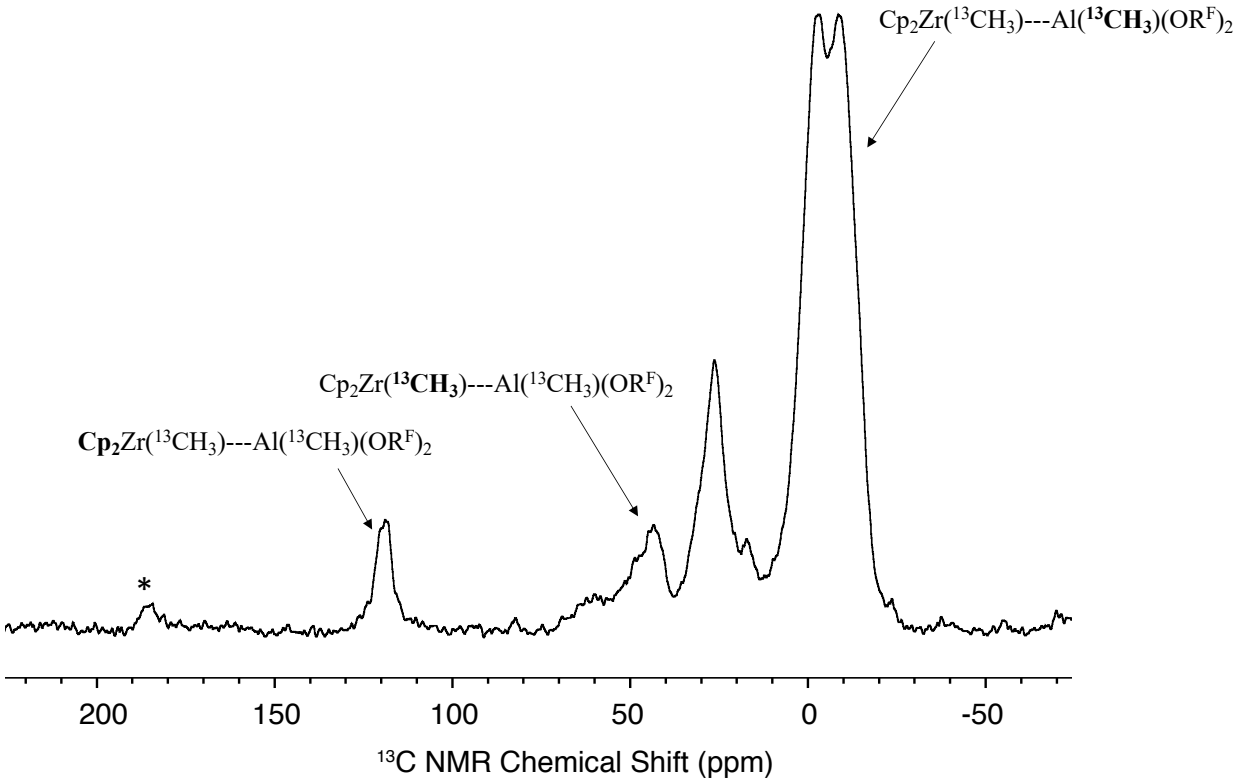

Figure 2.25. 10 kHz ^{13}C CPMAS NMR of vinyl chloride contacted **$Cp_2Zr(^{13}CH_3)_2$/1**. The signals at 23 ppm and 3 ppm show that $Cp_2Zr(^{13}CH_3)(OSi\equiv)$ and $\equiv Si-^{13}CH_3$ do not react with vinyl chloride under these conditions.

References

1.
   a. C. Copéret, F. Allouche, K. W. Chang, M. Conley, M. F. Delley, A. Fedorov, I. Moroz, V. Mougel, M. Pucino, K. Searles, K. Yamamoto, P. Zhizhko, Angew. Chem. Int. Ed. 2018, 57, 6398–6440; *Angew. Chem.* **2018**, 130, 6506–6551.

   b. C. Copéret, A. Comas-Vives, M. P. Conley, D. P. Estes, A. Fedorov, V. Mougel, H. Nagae, F. Núñez-Zarur, P. A. Zhizhko, *Chem. Rev.* **2016,** 116, 323–421.

   c. S. L. Wegener, T. J. Marks, P. C. Stair, *Acc. Chem. Res.* **2012**, 45, 206–214.

   d. M. Stalzer, M. Delferro, T. Marks, *Catal. Lett.* **2015,** 145, 3–14.

   e. J. D. A. Pelletier, J.-M. Basset, *Acc. Chem. Res.* **2016**, 49, 664–677.

   f. M. K. Samantaray, V. D'Elia, E. Pump, L. Falivene, M. Harb, S. Ould Chikh, L. Cavallo, J.-M. Basset, *Chem. Rev.* **2020,** 120, 734–813.

   g. R. J. Witzke, A. Chapovetsky, M. P. Conley, D. M. Kaphan, M. Delferro, *ACS Catal.* **2020**, 10, 11822–11840.

   h. E. Bekyarova, M. P. Conley, *Dalton Trans.* **2022**, 51, 8557–8570.

2.
   a. T. J. Marks, *Acc. Chem. Res.* **1992**, 25, 57–65.

   b. P. J. Toscano, T. J. Marks, *J. Am. Chem. Soc.* **1985,** 107, 653–659.

3. J. Joubert, F. Delbecq, P. Sautet, E. L. Roux, M. Taoufik, C. Thieuleux, F. Blanc, C. Copéret, J. Thivolle-Cazat, J.-M. Basset, *J. Am. Chem. Soc.* **2006**, 128, 9157–9169.

4. D. B. Culver, R. W. Dorn, A. Venkatesh, J. Meeprasert, A. J. Rossini, E. A. Pidko, A. S. Lipton, G. R. Lief, M. P. Conley, *ACS Cent. Sci.* **2021**, 7, 1225–1231.

5.
   a. K. Khivantsev, N. R. Jaegers, J.-H. Kwak, J. Szanyi, L. Kovarik, *Angew. Chem. Int. Ed.* 2021, 60, 17522–17530; *Angew. Chem.* **2021**, 133, 17663–17671.

   b. R. Wischert, C. Copéret, F. Delbecq, P. Sautet, *Angew. Chem. Int. Ed.* 2011, 50, 3202–3205; Angew. Chem. **2011**, 123, 3260–3263.

6.

a. R. Wischert, P. Laurent, C. Copéret, F. Delbecq, P. Sautet, *J. Am. Chem. Soc.* **2012**, 134, 14430–14449.

b. M. Valla, R. Wischert, A. Comas-Vives, M. P. Conley, R. Verel, C. Copéret, P. Sautet, *J. Am. Chem. Soc.* **2016**, 138, 6774–6785.

c. A. Motta, L. Fragalà, T. J. Marks, *J. Am. Chem. Soc.* **2008**, 130, 16533–16546.

7.

a. R. N. Kerber, A. Kermagoret, E. Callens, P. Florian, D. Massiot, A. Lesage, C. Copéret, F. ß. Delbecq, X. Rozanska, P. Sautet, *J. Am. Chem. Soc.* **2012**, 134, 6767–6775.

b. A. Kermagoret, R. N. Kerber, M. P. Conley, E. Callens, P. Florian, D. Massiot, C. Coperet, F. Delbecq, X. Rozanska, P. Sautet, *Dalton Trans.* **2013,** 42, 12681–12687.

c. A. Kermagoret, R. N. Kerber, M. P. Conley, E. Callens, P. Florian, D. Massiot, F. Delbecq, X. Rozanska, C. Coperet, P. Sautet, *J. Catal.* **2014,** 313, 46–54.

8. A notable exception to this trend is the reaction of AliBu3 with SiO2 in Et2O, which forms a well-defined alkylaluminum site. However, the Lewis acidity of this organoaluminum site was not reported. See: J. Pelletier, J. Espinas, N. Vu, S. Norsic, A. Baudouin, L. Delevoye, J. Trébosc, E. Le Roux, C. Santini, J. M. Basset, R. M. Gauvin, M. Taoufik, *Chem. Commun.* **2011**, 47, 2979–2981.

9.

a. K. C. Szeto, Z. R. Jones, N. Merle, C. Rios, A. Gallo, F. Le Quemener, L. Delevoye, R. M. Gauvin, S. L. Scott, M. Taoufik, *ACS Catal.* **2018**, 8, 7566–7577.

b. S. D. Fleischman, S. L. Scott, *J. Am. Chem. Soc.* **2011**, 133, 4847–4855.

c. Z. A. Taha, E. W. Deguns, S. Chattopadhyay, S. L. Scott, *Organometallics* **2006**, 25, 1891–1899.

10. J. F. Walzer, US Patent 5643847, 1995; b) N. Millot, C. C. Santini, A. Baudouin, J.-M. Basset, *Chem. Commun.* **2003**, 2034–2035.

11. D. W. Sauter, N. Popoff, M. A. Bashir, K. C. Szeto, R. M. Gauvin, L. Delevoye, M. Taoufik, C. Boisson, *Chem. Commun.* **2016,** 52, 4776–4779.

12. Y.-J. Wanglee, J. Hu, R. E. White, M.-Y. Lee, S. M. Stewart, P. Perrotin, S. L. Scott, *J. Am. Chem. Soc.* **2012**, 134, 355–366.

13. L. O. Müller, D. Himmel, J. Stauffer, G. Steinfeld, J. Slattery, G. Santiso-Quiñones, V. Brecht, I. Krossing, *Angew. Chem. Int. Ed.* 2008, 47, 7659–7663; *Angew. Chem.* **2008**, 120, 7772–7776.

14. D. B. Culver, A. Venkatesh, W. Huynh, A. J. Rossini, M. P. Conley, *Chem. Sci.* **2020**, 11, 1510–1517.

15. J. Gao, R. W. Dorn, G. P. Laurent, F. A. Perras, A. J. Rossini, M. P. Conley, *Angew. Chem. Int. Ed.* 2022, 61, e202117279; *Angew. Chem.* **2022,** 134, e202117279.

16.
    a. C. Nedez, A. Theolier, F. Lefebvre, A. Choplin, J. M. Basset, J. F. Joly, *J. Am. Chem. Soc.* **1993**, 115, 722–729.

    b. B. Rhers, A. Salameh, A. Baudouin, E. A. Quadrelli, M. Taoufik, C. Copéret, F. Lefebvre, J.-M. Basset, X. Solans-Monfort, O. Eisenstein, W. W. Lukens, L. P. H. Lopez, A. Sinha, R. R. Schrock, *Organometallics* **2006**, 25, 3554–3557.

17.
    a. F. Zhai, R. R. Schrock, A. H. Hoveyda, P. Müller, *Organometallics 2***020**, 39, 2486–2492.

    b. F. Feige, J. Al-Issa, J. F. Kögel, E. Lork, E. Rychagova, S. Ketkov, J. Beckmann, *Eur. J. Inorg. Chem.* **2021**, 4402–4405.

18. I. Del Rosal, I. C. Gerber, R. Poteau, L. Maron, *J. Phys. Chem. A* **2010**, 114, 6322–6330.

19. See the Supporting Information for details. This level of theory was previously used for FIA calculations of several Lewis acids, see: H. Böhrer, N. Trapp, D. Himmel, M. Schleep, I. Krossing, *Dalton Trans.* **2015**, 44, 7489–7499.

20. For a detailed discussion about the computations of FIA see: P. Erdmann, J. Leitner, J. Schwarz, L. Greb, *ChemPhysChem* **2020**, 21, 987–994.

21. P. Erdmann, L. Greb, *Angew. Chem. Int. Ed.* **2022**, 61, e202114550; Angew. Chem. 2022, 134, e202114550.

22. J. P. Osegovic, R. S. Drago, *J. Phys. Chem. B* **2000**, 104, 147–154.

23. M. M. Morgan, A. J. V. Marwitz, W. E. Piers, M. Parvez, *Organometallics* **2013**, 32, 317–322.

24. H. Großekappenberg, M. Reißmann, M. Schmidtmann, T. Müller, *Organometallics* **2015**, 34, 4952–4958.

25. D. B. Culver, M. P. Conley, *Angew. Chem. Int. Ed.* **2018**, 57, 14902–14905; *Angew. Chem.* 2018, 130, 15118–15121.

26. This model does not provide insights about why two 31P-{1H} NMR signals are present in this spectrum. This may be related to heterogeneities on the silica surface that result in slightly different structures of the O=PEt3 adducts on silica. For a perspective on heterogeneities encountered in well defined species supported on silica see: D. Gajan, C. Coperet, *New J. Chem.* **2011**, 35, 2403–2408.

27. N. Popoff, R. M. Gauvin, M. A. De, M. Taoufik, *Organometallics* **2012**, 31, 4763–4768.

28. M. Jezequel, V. Dufaud, M. J. Ruiz-Garcia, F. Carrillo-Hermosilla, U. Neugebauer, G. P. Niccolai, F. Lefebvre, F. Bayard, J. Corker, S. Fiddy, J. Evans, J.-P. Broyer, J. Malinge, J.-M. Basset, *J. Am. Chem. Soc.* **2001**, 123, 3520–3540.

29.
    a. Z. Gan, *Chem. Commun.* **2006**, 4712–4714.

    b. L. Chen, Q. Wang, B. Hu, O. Lafon, J. Trébosc, F. Deng, J.-P. Amoureux, *Phys. Chem. Chem. Phys.* **2010**, 12, 9395–9405.

    c. E. Nimerovsky, R. Gupta, J. Yehl, M. Li, T. Polenova, A. Goldbourt, *J. Magn. Reson.* **2014**, 244, 107–113.

30. In this experiment we used Rotational-Echo DOuble-Resonance (REDOR) recoupling (two 180° pulses per rotor cycle) on the 13C channel instead of more typical rotary resonance recoupling (R3), symmetry-based SR421, or phase or amplitude modulated SFAM sequences. REDOR recoupling is tolerant to experimental imperfections (MAS fluctuations, RF inhomogeneity, etc.) and is simple to implement. For more details on 13C{27Al} RESPDOR experiments see: F. Pourpoint, J. Trébosc, R. M. Gauvin, Q. Wang, O. Lafon, F. Deng, J.-P. Amoureux, *ChemPhysChem* **2012,** 13, 3605–3615.

31. R. F. Jordan, C. S. Bajgur, R. Willett, B. Scott, *J. Am. Chem. Soc.* **1986**, 108, 7410–7411.

32. For reactions of organometallic zirconium cations and vinyl chloride see: R. A. Stockland, S. R. Foley, R. F. Jordan, *J. Am. Chem. Soc.* **2003,** 125, 796–809.

33.
    a. C. P. Nicholas, H. Ahn, T. J. Marks, *J. Am. Chem. Soc.* **2003**, 125, 4325–4331.

    b. L. A. Williams, N. Guo, A. Motta, M. Delferro, I. L. Fragala, J. T. Miller, T. J. Marks, *Proc. Natl. Acad. Sci. USA* **2013**, 110, 413–418.

c. H. Tafazolian, D. B. Culver, M. P. Conley, *Organometallics* **2017**, 36, 2385–2388.

34.

a. M. P. Conley, G. Lapadula, K. Sanders, D. Gajan, A. Lesage, I. Del Rosal, L. Maron, W. W. Lukens, C. Copéret, R. A. Andersen, *J. Am. Chem. Soc.* **2016**, 138, 3831–3843.

b. V. Mougel, C. Coperet, *Chem. Sci.* **2014**, 5, 2475–2481.

Chapter 3. A Supported Ziegler-Type Organohafnium Site Metabolizes Polypropylene

Abstract

$Cp_2Hf(CH_3)_2$ reacts with silica containing strong aluminum Lewis sites to form $Cp_2Hf–^{13}CH_3^+$ paired with aluminate anions. $Cp_2Hf–^{13}CH_3^+$ reacts with isotatic polypropylene and H_2 to form oils with moderate molecular weights (M_n = 290–1200 Da) in good yields. The aliphatic oils show characteristic $^{13}C\{^1H\}$ NMR properties consistent with complete loss of diastereoselectivity and formation of regioirregular errors under 1 atm H_2. These results show that a Ziegler–Natta-type active site is compatible in a common reaction used to digest waste plastic into smaller aliphatic fragments.

Introduction

Ziegler−Natta olefin polymerization reactions are the foundation of the plastics economy and produce millions of tons of highly versatile polyethylene or polypropylene products per year. Most polyolefins reach end-of-life as unrecyclable waste.[1] Treating plastic waste with H_2 and a catalyst forms low molecular weight alkanes that could be processed back to the monomer, which is a plausible strategy to a circular plastics economy. These hydrogenolysis reactions are usually catalyzed by supported nanoparticles[2] or the heterogeneous "single-site" d0 metal hydrides shown in Figure 3.1.[3] The well-defined catalysts activate a C−H bond in the polymer by σ-bond metathesis[4] and β-alkyl eliminate[5] to form MR(olefin) intermediates that are hydrogenated under the reaction conditions, Figure 3.1b.

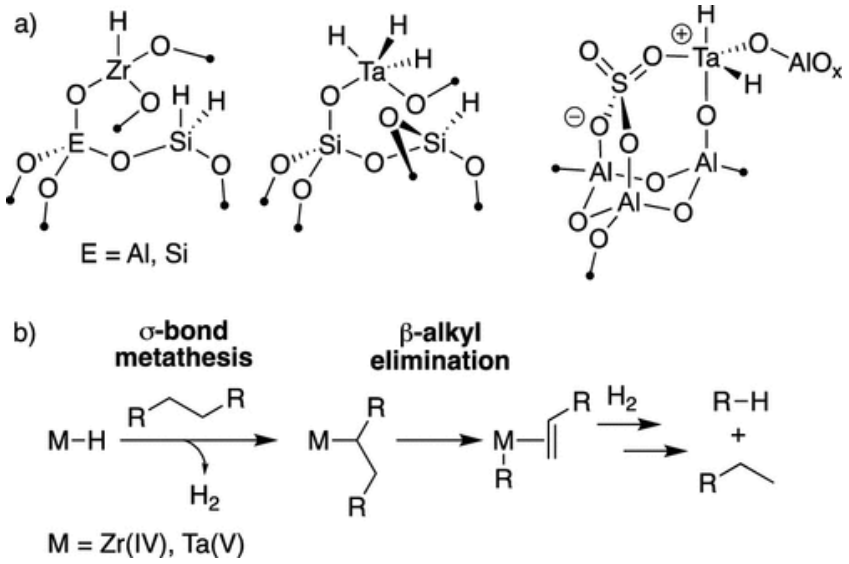

Figure 3.1. Supported d0 metal hydrides (a). Key steps in C−C hydrogenolysis (b).

Our hypothesis is that cationic organometallics used as olefin polymerization catalysts could engage in the reactions shown in Figure 3.1b. Modern olefin polymerization catalysts contain a Group IV metallocene[6] or postmetallocene[7] precatalyst that is activated[8] to form LnM−R+ (M = Ti, Zr, Hf; R = H, alkyl) that coordinate and insert[9] olefins to grow the polymer chain. These steps are shown in Figure 3.2 for the formation of isotactic polypropylene (iPP)[10] through the common 1,2-insertion of propylene into LnM−R$^+$.[11]

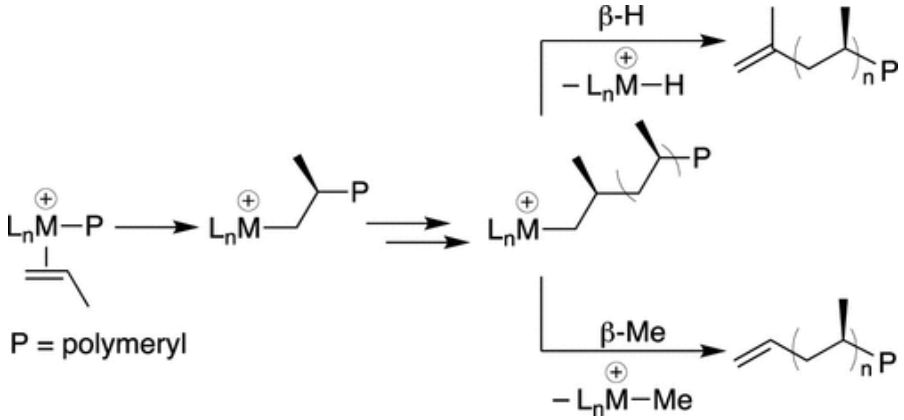

Figure 3.2. Abbreviated key steps in iPP synthesis.

Chain transfer releases the polymer from the metal to regenerate catalytically active $LnM-R^+$.[12] In the absence of alkylaluminum, the most common chain transfer pathways are β-H elimination to generate $LnM-H^+$ and iPP with vinylidene end groups or β-Me elimination to generate $LnM-Me^+$ and iPP with vinyl end groups. The outcome of this reaction depends on sterics. $Cp_2Hf-CH_3^+$ terminates propylene polymerization by β-H elimination, but bulkier $Cp^*_2Hf- CH_3^+$ favors chain termination by β-methyl elimination.[13]

The β-Me elimination shown in Figure 3.2 is a signature of β- alkyl elimination required for C−C hydrogenolysis shown in Figure 3.1b. Cationic hafnocenes generated in solution are known to engage in σ-bond metathesis reactions,[14] analogous to the d0 metal hydrides shown in Figure 3.1a.[3] Therefore, cationic metallocenes formed during olefin polymerization reactions would be expected to show activity in reactions that digest polyolefins in the presence of H_2. Catalysts of this type are more desirable than those shown in Figure 3.1. $LnM-R^+$ forms readily in solution[8] or on solid supports in common

industrial compositions used for ethylene polymerization.[15] This paper describes $Cp_2Hf{-}CH_3^+$ sites on a weakly coordinating oxide[16] that catalyze hydrogenolysis of iPP.

Silica functionalized with $Al(OC(CF_3)_3)(PhF)$[17] forms $SiOAl(OC(CF_3)_3)_2(O(Si\ \ )_2)$ containing 0.21 mmolAl g^{-1} and residual unreacted SiOH.[18] $Cp_2Hf(^{13}CH_3)_2$ reacts with this support to form the mixture of species shown in Figure 3.3a (0.21 mmolHf g^{-1}). The $^{13}C\{^1H\}$ cross-polarization magic angle spinning (CPMAS) NMR spectrum of this material is shown in Figure 3.3b and contains signals at 38 ($Hf{-}^{13}CH_3\ ^+$), 24 ($Hf{-}^{13}CH_3$), 2 ($Si{-}^{13}CH_3$), and −11 ppm ($Al{-}^{13}CH_3$), respectively. The reactivity shown in Figure 3.3a can be rationalized by the following chemical steps. $[Cp_2Hf{-}^{13}CH_3]$ $[SiOAl(OC(CF_3)_3)_2(CH_3)]$ (1) forms by methide abstraction from $Cp_2Hf(^{13}CH_3)_2$ by the strong aluminum Lewis sites, analogous to reactions of $B(C_6F_5)_3$ with d0 organometallics in solution.[19] Residual −OH sites present on the support react with $Cp_2Hf(^{13}CH_3)_2$ to form CH_4 (0.07 ± 0.01 $mmol_{CH4}$ g^{-1}) and $Cp_2Hf(^{13}CH_3)OSi{\equiv})$ (2). This result indicates that ∼30% of the Lewis sites in $SiOAl(OC(CF_3)_3)_2(O(Si{\equiv})_2)$ do not react with Cp_2Hf- $(^{13}CH_3)_2$. 3 forms when Hf−Me+ in 1 reacts with a nearby siloxane bridge to generate [Cp2Hf(OSi≡)][SiOAl(OC-$(CF_3)_3)_2(CH_3)$] and $Si{-}^{13}CH_3$, which is also observed when $Cp_2Zr{-}CH_3$ + fragments are generated on silica.[20]

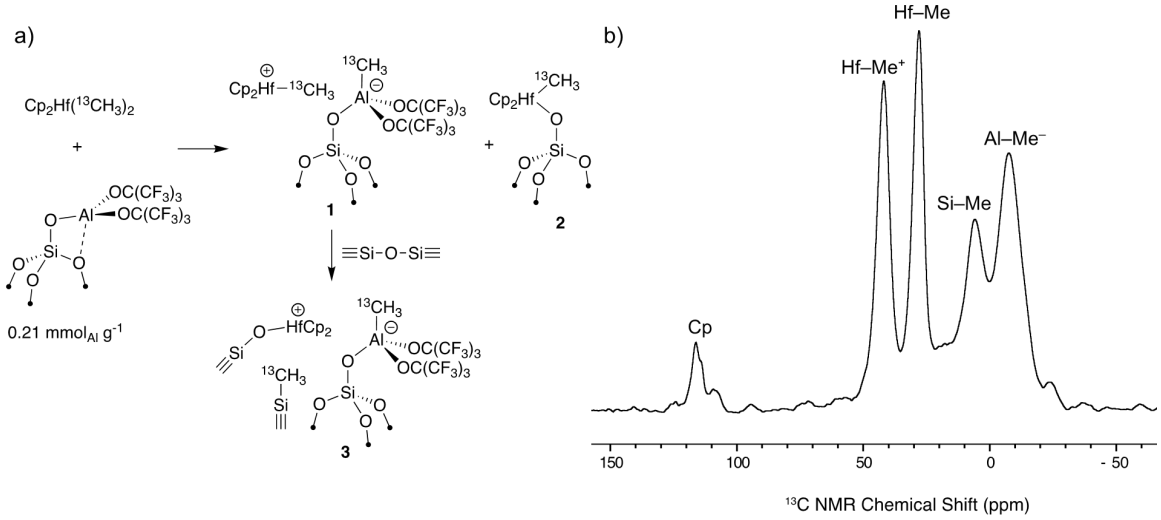

Figure 3.3: Reaction of $Cp_2Hf(CH_3)_2$ and $SiOAl(OC\text{-}(CF_3)_3)_2(O(Si\equiv)_2)$ to form 1, 2, and 3 (a). $^{13}C\{^1H\}$ CPMAS NMR spectrum of the reaction products (b). νrot = 10 kHz.

The catalytic properties of $Cp_2Hf(CH_3)_2$/ $SiOAl(OC\text{-}(CF_3)_3)_2(O(Si\equiv)_2)$ in a melt of iPP (Mn = 13.3 kDa; Đ = 2.4; mmmm = 94%; ∼110 C3H6/Hf) with H_2 are given in Table 1. These reactions form a complex mixture of saturated alkane products lacking diastereopurity, as shown in eq 1. Similar to previous studies,[3g] high temperature $^{13}C\{^1H\}$ NMR analysis of the recovered unreacted polymer maintains high mmmm purity.

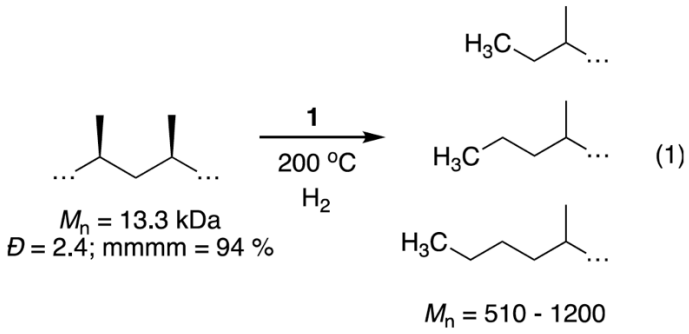

Table 3.1: Catalytic Activity of 1 in PP Hydrogenolysis[a]

Entry	Pressure (atm)	Yield C_1−C_5 (%)	Yield Oil[b] (%)	M_n[c] (g/mol)
1	1*d*	2	62	390
2	1*e*	12	83	290
3*f*	1*e*	7	38	350
4	5	4	62	220
5	10	8	88	240
6	2*g*	n.d.	29	1100
7	5*g*	n.d.	20	1200

a Reactions run with 200 mg of iPP and 200 mg of $Cp_2Hf(CH_3)_2$/ $SiOAl(OC(CF_3)_3)_2(O(Si)_2)$ (0.042 mmol of Hf) at 200 °C for 24 h at the pressure given in the table. [b]$(mg_{oil})/(mg_{iPP})$. [c]Determined from quantitative $^{13}C\{^1H\}$ NMR of extracted oils. [d]H_2:Hf ~ 100. [e] ~ 1500. [f]Zr derivative of 1, reported in ref 17. H_2:Hf (or Zr) *g* Performed with H_2 fed to the reactor on demand (see the Materials and Methods section for details). n.d. = not determined.

Available data suggest that a Hf−CH3 + is the catalytically active site in $Cp_2Hf(CH_3)_2$/ $SiOAl(OC\text{-}(CF_3)_3)_2(O(Si\equiv)_2)$. Native $SiOAl(OC\text{-}(CF_3)_3)_2(O(Si\equiv)_2)$ sluggishly converts iPP to extractable oils in the presence of 1 atm H_2 (15% yield), suggesting that unreactive Lewis sites play a minimal role in the catalytic chemistry involving 1. Reacting $Cp_2Hf(CH_3)_2$/ $SiOAl(OC\text{-}(CF_3)_3)_2(O(Si\equiv)_2)$ with H_2 at 150 ˚C for 12 h in the absence of iPP forms methane (0.09 mmol g−1), and the FTIR of this material contains a broad signal at 1650 cm−1 tentatively assigned to a hafnium hydride. This reactivity pattern is expected from extensive precedent in the homogeneous and heterogeneous literature showing that M− R species react with H2 to form M−H and RH.3a Under identical conditions, independently synthesized 2 forms only 0.001 mmol

CHd4 g−1. In addition, 2 does not react with iPP under hydrogenolysis conditions to form extractable oils nor incorporate deuterium into residual iPP in the presence of D2 (see the Materials and Methods section for details).

After 24 h at 200 ˚C under 1 atm H2, 1 forms an oil in 62% yield, Entry 1. Analysis of the gas phase before extraction of the oil shows that only 2% of the polymer is converted to light gases (1.5 CH_4 Hf^{-1}, 0.01 C2H6 Hf^{-1} , 0.11 C3H6 Hf^{-1}, and 1.1 C4H10 Hf^{-1} , 1.2 C5H10 Hf^{-1}). Increasing the H2:Hf ratio to ∼1500 results in near complete conversion of iPP to oil (83%) and light gas (12%), Entry 2. The zirconium derivative of 118 is also active in this reaction but produces less oil (38%) and light gas (7%) than hafnium, Entry 3. A closed Parr reactor charged with 5 or 10 atm H2 also results in a good yield of oils with minimal volatile gas formation (Entries 4 and 5). However, at 2 or 5 atm with H2 supplied on demand, conditions that prevent recovery of volatile gases, yields of extracted oils drop (Table 1, Entries 6 and 7). The 1H NMR data for the extracted oils are largely uninformative, but these spectra contain signals for internal olefins ranging from ∼1:50 to ∼1:2000 olefin:C3H6 unit, depending on the conditions (see Materials and Methods).

Quantitative 13C{1H} NMR spectra of the oils in C_6D_6 are shown in Figure 3.4. Most spectra in Figure 3.4 contain signals that are characteristic of regioirregular errors encountered in polypropylene synthesis,11 or copolymerization reactions of ethylene and propylene.[21] These results indicate that some degree of chain straightening occurs during hydrogenolysis with 1. All 13C{1H} NMR spectra contain signals for ethyl, propyl, and butyl end groups. Integration of the end groups relative to the rest of the 13C{1H} NMR

signals gives the Mn values of the oils reported in Table 1. The matrix assisted laser desorption ionization (MALDI) mass spectrum of extracted oil from Entry 1 contains a broad distribution of products centered at a m/z of 538 (~10 C3H6 units *Ag+) that is close to Mn obtained from integration of 13C{1H} NMR signals. GCMS data of the oil is complex but also supports the formation of a distribution of branched alkanes. These trends hold for all oils isolated in Table 1.

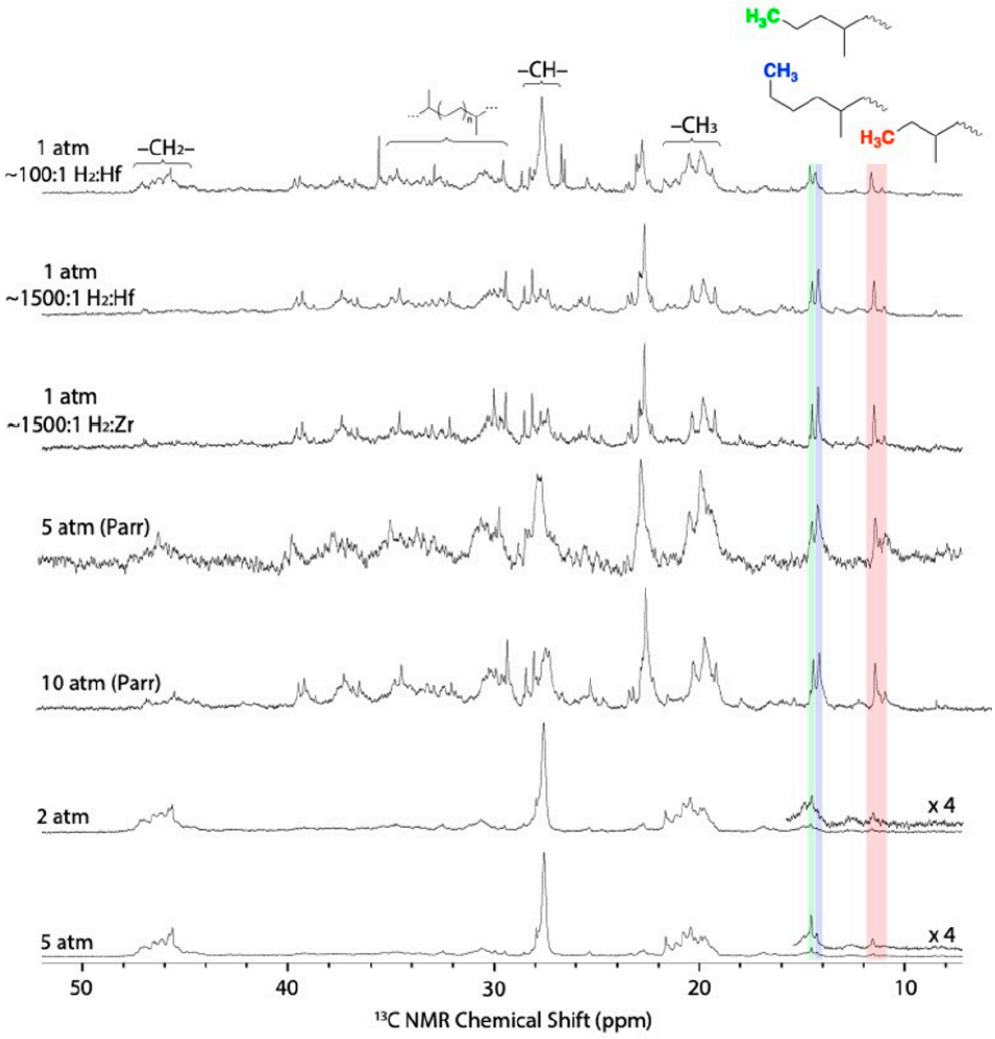

Figure 3.4. Quantitative 13C{1H} NMR spectra shown from 10 to 50 ppm for oils produced in hydrogenolysis reactions. End groups are highlighted for clarity.

Reactions of iPP with 1 and D2 (1 atm, D2:Hf ~ 100) at 200 ˚C also result in formation of oils and small amounts of light gas in similar yields as those performed with H2. The 2H NMR spectrum of unreacted iPP at 120 ˚C in C2H2Cl4 contains signals for −CD−, −CHD−, and −CHxD3−x in a ~1:1:2 ratio, eq 2. This spectrum also contains signals for CH3CH2CD2CD C(CH3)P (P = polymeryl). The oils formed in this reaction also contained deuterium at all possible positions (−CD−:−CHD−:−CHxD3−x ~ 1:4:10).

These data suggest that Hf−H+ reacts with a primary or secondary C−H bond in iPP by σ-bond metathesis to form Hf−R+, Scheme 1.[22] β-Alkyl elimination forms Hf(R)(olefin)+ intermediates that are hydrogenated by H2. Hf(R)(olefin)+ probably dissociates olefin to allow the hydrogenolysis of Hf− R+ by a σ-bond metathesis reaction prior to olefin hydrogenation. This process forms propyl (observed) and isopropyl (not observed) end groups. Deuterium incorporation into recovered iPP suggests that the σ-bond metathesis reactions shown in Scheme 3.1 are reversible and accounts for the −CHD− and −CDxH3−x in recovered iPP and atactic oils.

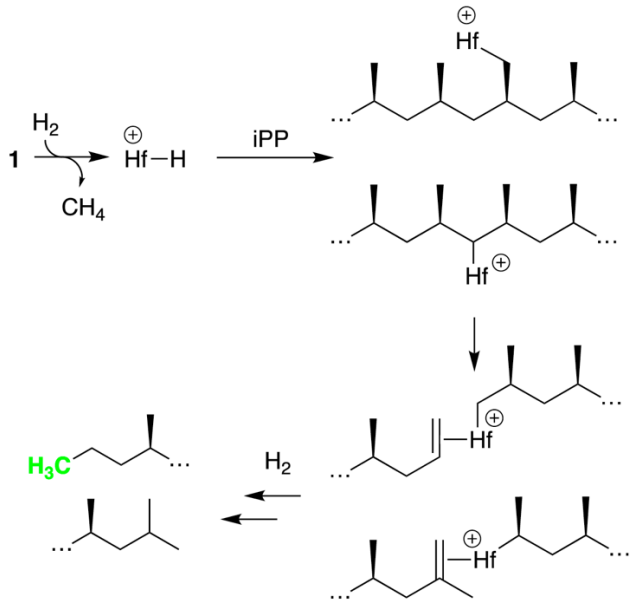

Scheme 3.1: Cleavage of an iPP Chain by 1

The atactic oils must lose diastereoselectivity. Epimerization can occur by β-H elimination, nondissociative alkene flipping,[23] and unselective olefin insertion,[24] shown in Scheme 2. This process incorporates deuterium at the −CD− position in the oils or iPP. Deuteration of −CH− positions can also occur by reactions of 3˚ Hf−R+ with D2. Residual Lewis acidic aluminum in Cp2Hf(CH3)2/ SiOAl(OC(CF3)3)2(O(Si ≡)2) could also promote isomerization reactions, resulting in loss of tacticity.[25] Why the oils are atactic and the recovered iPP maintains high isotacticity is currently unclear but could imply that unreacted iPP chains are the dominant species in the recovered polymer.

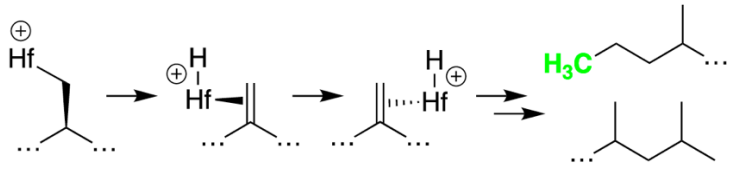

Scheme 3.2: Epimerization of a Methyl Group Mediated by Hf-H+

The atactic oils also incorporate regioirregular "errors" into the chain. Quantitative 13C{1H} NMR data of extracted oils suggest that regioirregular errors occur throughout the alkyl chain and not solely at chain ends. In propylene polymerization reactions the regioirregular errors, formally 3,1 insertion products, arise from 1,2 insertion of propylene to form a 2˚ M−R that eliminates β-H and reinserts to form a 1˚ M−R, Figure 3.5a.[11] This pathway is not plausible under the hydrogenolysis conditions. Instead, C−H bond activation by Hf−H+ generates a Hf−R+ that undergoes β-alkyl elimination, and 2,1-reinsertion gives the chain-straightened product after hydrogenolysis, Figure 3.5b. Reactions from a terminal isopropyl position generate the butyl end group. If the chain-straightened intermediate β-alkyl eliminates, the ethyl end group forms after hydrogenation.

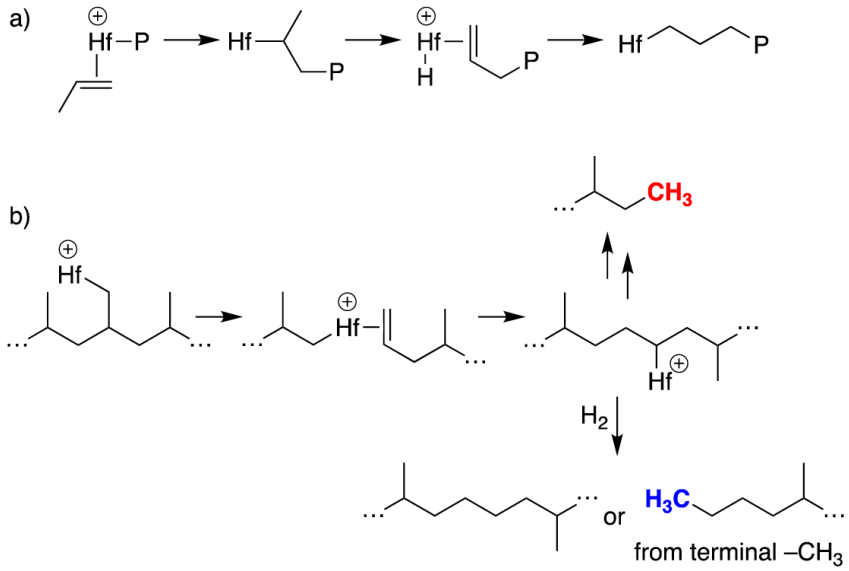

Figure 3.5: Steps involved in a formal 3,1- insertion of propylene during polymerization reaction (a). Regioirregular error formation under hydrogenolysis conditions (b).

Until this report the most common catalysts for hydrogenolysis of polyolefins were supported noble metal nanoparticles[2] or supported d0 metal hydrides (Figure 3.1a).[3] Comparisons between these disparate classes of catalysts are difficult, but 1 does appear to offer some advantage. 1 selectively produces long chain hydrocarbons and avoids significant formation of light gases at prolonged reaction times. We suspect that the selectivity rests on the moderate activity of 1 in the reactions involved in hydrogenolysis of iPP. For example, under essentially identical reaction conditions Ta−H+ sites supported on sulfated aluminum oxide converts the same iPP to shorter liquid hydrocarbon fragments and more light gas, indicating that Ta−H+ facilitates more chain cleavage than 1.[3g]

Metallocene catalysts that polymerize olefins have been overlooked as catalysts for degradation of aliphatic polyolefin plastics.[26] The reactivity of 1, and the inactivity of 2, in iPP hydrogenolysis show the critical role of forming an organometallic ion-pair in this reaction. Many modern Ziegler−Natta catalysts for olefin polymerization contain mixtures of metallocene, aluminum alkyl (or methaluminoxane), and an oxide support; and these mixtures likely self-assemble to form ion pairs similar to the Hf−H+ derived from 1.[15] A plausible implication of the results shown here is that the broad portfolio of modern Ziegler−Natta catalysts available for olefin polymerization may also catalyze reactions that degrade the polymers that these catalysts produce.

Materials and Methods

General Considerations

All manipulations were performed under an inert atmosphere of dinitrogen or argon using standard Schlenk or glovebox techniques. C_6D_6 was purchased from Cambridge Isotope Laboratories, dried over sodium/benzophenone, degassed by three successive freeze-pump-thaw cycles, distilled under vacuum, and stored in an inert atmosphere glovebox. $C_2D_2Cl_4$ was purchased from Cambridge Isotope Laboratories and used as received. Pentane was dried by passing through a J.C. Meyer solvent system containing two activated alumina columns, stored over sodium/benzophenone, degassed, and distilled under vacuum. Hydrogen (UHP grade) was purchased from Airgas and was passed through oxygen/water trap (CRS, ZPure H_2O/O_2) immediately before use. Isotactic polypropylene (M_n =13.3 kDa) was purchased from Sigma Aldrich and used without further purification. Deuterium was purchased from CIL and was dried/ deoxygenated using activated 4Å molecular sieves and regenerated BASF Cu catalyst. ≡ $SiOAl(OC(CF_3)_3)_2(O(Si\equiv)_2)$ was prepared as previously described.[18] Cp_2HfMe_2 and $Cp_2Hf(^{13}CH_3)_2$ were prepared as reported.[27] FTIR spectra were recorded in transmission mode as pressed pellets using a Bruker Alpha IR spectrometer in an argon-filled glovebox. Elemental analysis of Al and Hf were carried out by digesting solid samples in 2% nitric acid for 12 hours at room temperature and measuring samples at the University of California, Riverside Environmental Sciences Research Laboratory (ESRL) on a Perkin-Elmer Optima 7300DV ICP-OES.

Solution NMR data (^{1}H, ^{2}H, and $^{13}C\{^{1}H\}$) was acquired at 14.1T on an Avance Bruker 600 MHz NMR spectrometer. ^{1}H and ^{13}C NMR spectra were referenced to the residual proton signal from the NMR solvent. Quantitative $^{13}C\{^{1}H\}$ NMR experiments were acquired using an inverse-gated decoupling pulse sequence using a 90° pulse of 9.0 μs, a relaxation time of 5 s and an acquisition time of 2 s. Samples for this measurement were prepared at 10% weight solution of polymers in 0.05 M $Cr(acac)_3$ dissolved in 1,1,2,2-tetrachloroethane-d_2 solution at 120 °C. Analogous procedures were used to analyze oils in C_6D_6 solution at ambient temperature. Solid state NMR spectra were recorded under magic angle spinning at 14.1 T using Bruker NEO600 spectrometer. All solid-state NMR samples were packed in 4 mm zirconia rotors and sealed with a Kel-F cap in an argon filled glovebox.

Matrix assisted laser desorption ionization (MALDI) mass spectrometry were recorded on an ABSCIEX 5800 MALDI TOF/TOF mass spectrometer. Samples were prepared by dissolving extracted oil (5 mg) in THF (5 mL). Prior to spotting on the sample plate, an aliquot of this solution (0.1 mL) was mixed with a saturated solution of $AgNO_3$ in MeCN (0.1 mL). ~ 0.5 μL of the solution was placed on the sample plate, followed by 0.5 μL of the matrix solution (2,5 dihydroxybenzoic acid (DHB) solution prepared in a 3:2 (*v*:*v*) mixture of tetrahydrofuran and methanol at a 10 mg/mL concentration). The solvents were removed by gently heating the stainless-steel sample plate under air.

Synthesis of Cp_2HfMe_2/≡SiOAl$(OC(CF_3)_3)_2(O(Si≡)_2)$: ≡SiOAl$(OC(CF_3)_3)_2(O(Si≡)_2)$ (0.500 g, 0.11 $mmol_{Al}$ g^{-1}) and Cp_2HfMe_2 (1 eq, 0.11 mmol, 0.037 g) were transferred to one arm of a double-Schlenk flask inside an argon-filled glovebox. The flask was removed from the glovebox, connected to a high vacuum line, and evacuated for 5 min. Pentane (~8 mL) was condensed onto the solids under vacuum at 77 K. The mixture was warmed to room temperature and stirred gently for 40 minutes. The clear, colorless solution was then filtered away from the solids to the other side of the double-Schlenk. The arm of the double-Schlenk containing the functionalized silica was cooled to 77K, causing the pentane on the other side of the flask to condense onto the solids. The mixture was warmed to 25˚C, stirred for 5 min, and filtered back to the other side of the double Schlenk. This procedure was repeated two more times to wash the functionalized silica of unreacted Cp_2HfMe_2. The volatiles were distilled into a separate large volume Schlenk flask (2 L) fitted with a Teflon-tap cooled to 77K under vacuum. Warming the flask to room temperature places all solvent and any CH_4 formed in this reaction into the gas phase. Analysis of the gas phase by GC-FID shows 0.07 ± 0.001 $mmol_{CH4}$ g^{-1} released during the grafting. The double-Schleck flask was dried under diffusion pump vacuum for 45 minutes.

Cp_2HfMe_2/≡SiOAl$(OC(CF_3)_3)_2(O(Si≡)_2)$ is a white solid. This material was stored in an Ar glovebox freezer at -20˚C. An identical procedure was used to prepare ^{13}C labeled $Cp_2Hf(^{13}CH_3)_2$/≡SiOAl$(OC(CF_3)_3)_2(O(Si≡)_2)$. The white solid was stored in an Ar glovebox freezer at -20˚C. Digestion of this material in 2% nitric acid for 12 hours at room temperature gives 0.21 $mmol_{Hf}$ g^{-1} by ICP-EOS analysis. FT-IR: $\nu_{C\text{-}H}$ = 3120 and

2924 (C-H from Cp_2HfMe) cm^{-1}. ^1H MAS NMR (10 kHz, -20 °C): d 5.7 ppm (Cp), 0.2 ppm (Hf-Me/Al-Me) ; $^{13}C\{^1H\}$ CPMAS NMR (10 kHz, -20 °C): d 112 (Cp), 38 (Hf-Me^+), 24 (Hf-Me), 2 Si-Me, -11 (Al-Me^-) ppm.

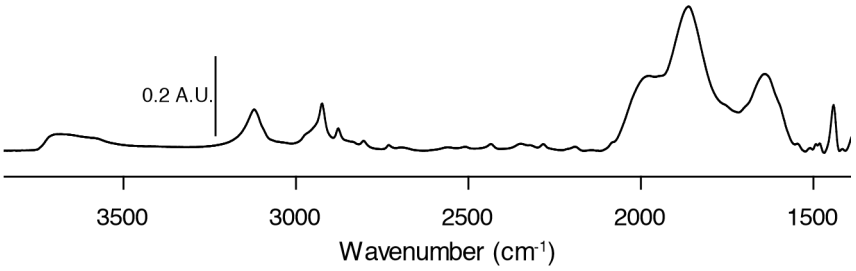

Figure 3.6. FT-IR spectrum of $Cp_2HfMe_2/{\equiv}SiOAl(OC(CF_3)_3)_2(O(Si{\equiv})_2)$.

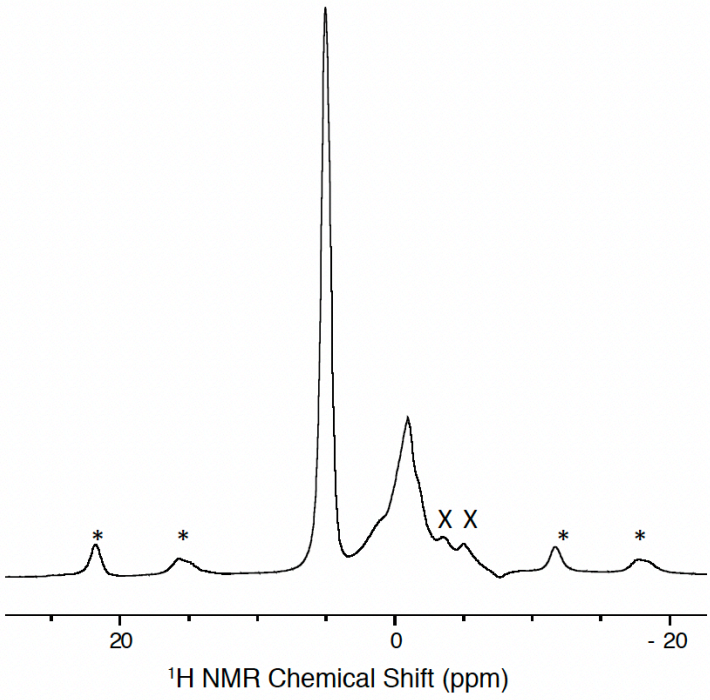

Figure 3.7. 10kHz MAS ^1H NMR of $Cp_2HfMe_2/{\equiv}SiOAl(OC(CF_3)_3)_2(O(Si{\equiv})_2)$ acquired at -20˚C. Probe background signals are labeled with an "x," spinning sidebands are labeled with a *.

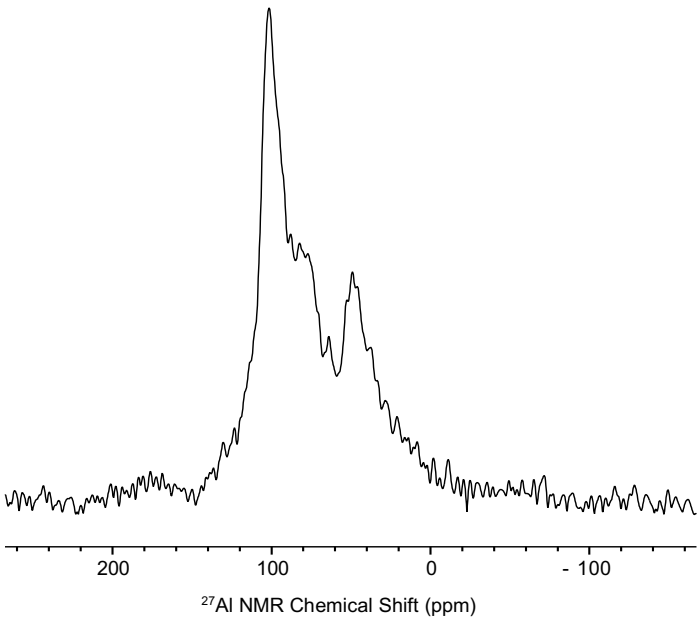

Figure 3.8. $^{27}Al\{^{1}H\}$ MAS NMR spectrum of $Cp_2HfMe_2/\equiv SiOAl(OC(CF_3)_3)_2(O(Si\equiv)_2)$ recorded at 10 kHz spinning speed.

Synthesis of $Cp_2Hf(^{13}CH_3)(OSi\equiv)$ (2): Silica partially dehydroxylated at 700 ºC ($SiO_{2\text{-}700}$, 0.500 g, 0.13 mmol -OH) and Cp_2HfMe_2 (1 eq, 0.13 mmol, 0.044 g) were transferred to one arm of a double-Schlenk flask inside an argon-filled glovebox. The flask was removed from the glovebox, connected to a high vacuum line, and evacuated for 5 min. Pentane (~ 8 mL) was condensed onto the solids under vacuum at 77 K. The mixture was warmed to room temperature and stirred gently for 40 minutes. The clear, colorless solution was then filtered away from the solids to the other side of the double-Schlenk. The arm of the double Schlenk containing the functionalized silica was cooled to 77K, causing the pentane on the other side of the flask to condense onto the solids. The mixture was warmed to 25˚C, stirred for 5 min, and filtered back to the other side of the

double Schlenk. This procedure was repeated two more times to wash the functionalized silica of unreacted Cp_2HfMe_2. The volatiles were distilled into a separate large volume Schlenk flask (2 L) fitted with a Teflon-tap cooled to 77K under vacuum. Warming the flask to room temperature places all solvent and any CH_4 formed in this reaction into the gas phase. Analysis of the gas phase by GC-FID shows 0.25 $mmol_{CH4}$ g^{-1} released during the grafting. The double-Schleck flask was dried under diffusion pump vacuum for 45 minutes. The white solid was stored in an Ar glovebox freezer at -20˚C. FT-IR: $\nu_{C\text{-}H}$ = 3115 and 2915 (C-H from Cp_2HfMe) cm^{-1}. ^1H MAS NMR (10 kHz, -20 ºC): d 5.5 (CpH), 0.18 (Hf–CH_3); $^{13}C\{^1H\}$ CPMAS NMR (10 kHz, -20 ºC): d 110 (Cp), 23 (Hf-Me) ppm.

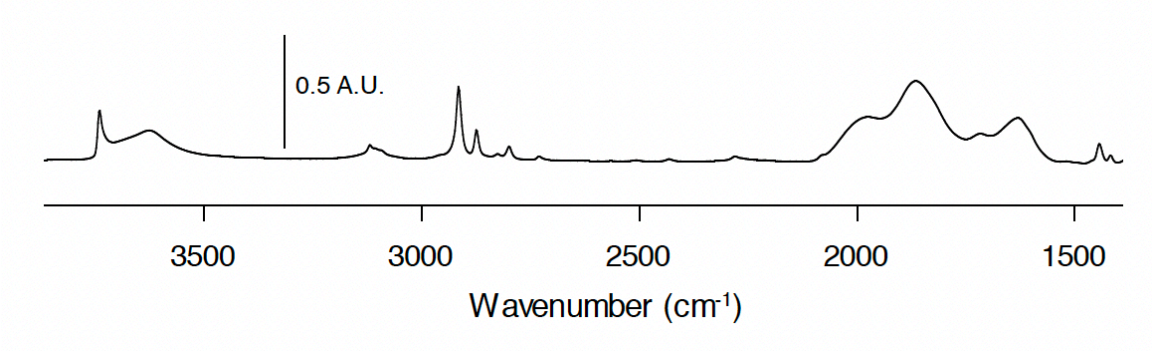

Figure 3.9. FT-IR spectrum of **2** wavenumbers (cm^{-1}).

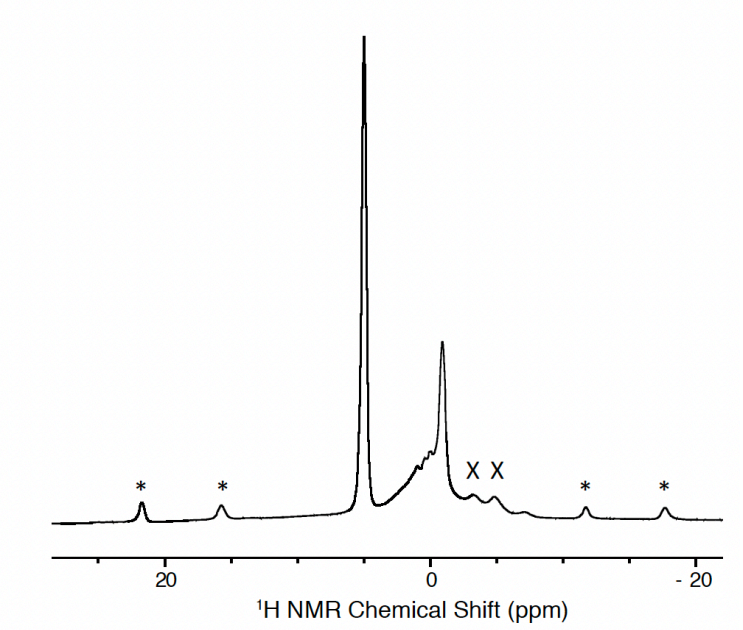

Figure 3.10. ^{1}H NMR of **2** acquired at -20˚C and 10 kHz spinning speed. Probe background signals are labeled with an "x," spinning sidebands are labeled with a *.

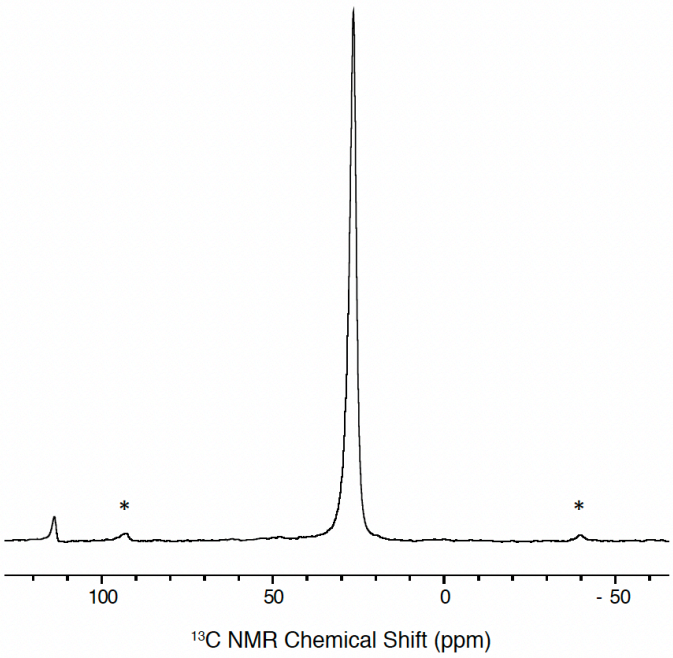

Figure 3.11. ^{13}C{^{1}H} CPMAS NMR of **2** acquired at -20˚C at 10 kHz spinning speed. Spinning sidebands are labeled with a *.

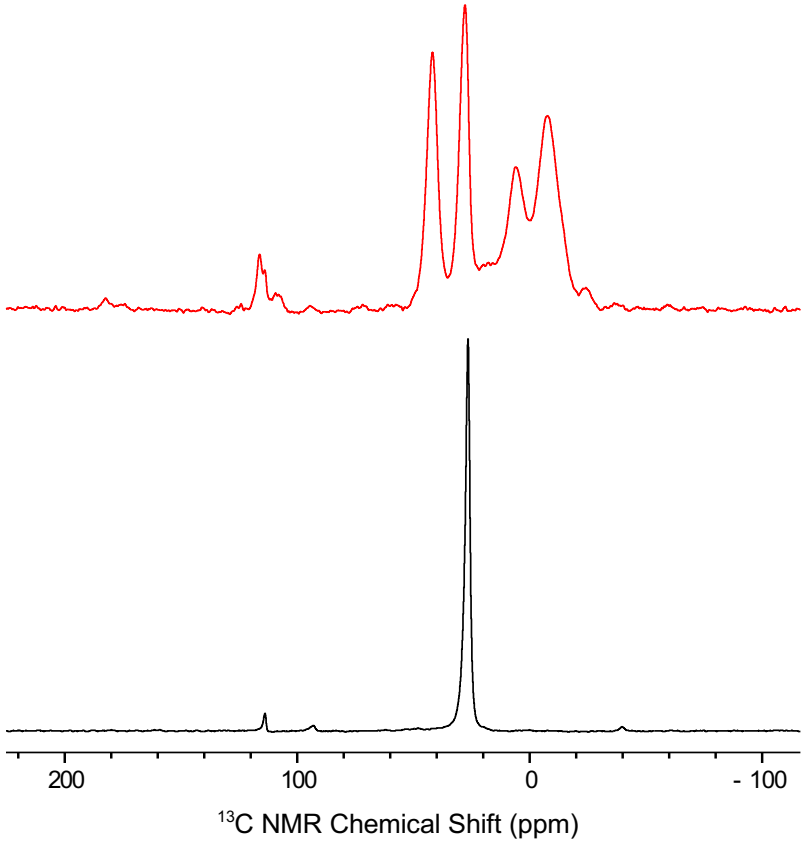

Figure 3.12. Stacked plot of the $^{13}C\{^{1}H\}$ CPMAS NMR spectrum of Cp_2HfMe_2/≡ $SiOAl(OC(CF_3)_3)_2(O(Si≡)_2)$ (top, red) and **2** (bottom, black).

Reaction of Cp_2HfMe_2/≡$SiOAl(OC(CF_3)_3)_2(O(Si≡)_2)$ or $Cp_2Hf(CH_3)(OSi≡)$ with H_2. In an argon-filled glovebox, a 100mL Schlenk flask fitted with a Teflon-tap was loaded with 200 mg $Cp_2Hf(CH_3)_2$/≡$SiOAl(OC(CF_3)_3)_2(O(Si≡)_2)$ (0.042 mmol Hf). The flask was removed from the glovebox, connected to a high vacuum line, and evacuated for 5 min. The flask was filled with 1atm of H_2 (4.16 mmol), sealed, disconnected from the line, and heated at 150 ˚C for 12h. Volatiles were sampled directly from the flask and analyzed by GC FID (0.09 mmol CH_4/g). The flask was evacuated and the material was stored in an

argon-filled glovebox freezer. An identical procedure was used for reaction of $Cp_2Hf(CH_3)(OSi\equiv)$ (0.052 mmol Hf) with 1atm of H_2 (4.16 mmol). The flask was filled with 1atm of H_2 (4.16 mmol), sealed, disconnected from the line, and heated at 150 ˚C for 12h. Volatiles were sampled directly from the flask and analyzed by GC FID (0.001 mmol CH_4/g).

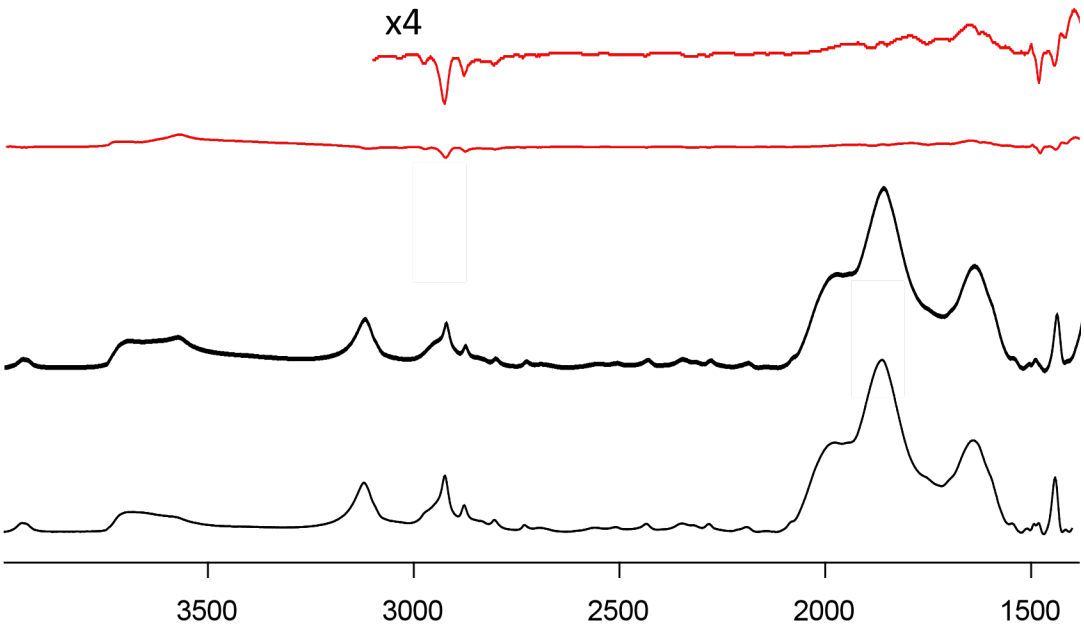

Figure 3.13. FTIR of $Cp_2HfMe_2/\equiv SiOAl(OC(CF_3)_3)_2(O(Si\equiv)_2)$ treated with H_2 at 150 °C (middle, black), FTIR of $Cp_2HfMe_2/\equiv SiOAl(OC(CF_3)_3)_2(O(Si\equiv)_2)$ (bottom), and the difference spectrum showing which FTIR signals disappear and appear in this reaction (top, red trace and close up).

Procedure for the hydrogenolysis of iPP with $Cp_2HfMe_2/\equiv SiOAl(OC(CF_3)_3)_2(O(Si\equiv)_2)$.

At 1 atm:

In an argon-filled glovebox, a 100mL Schlenk flask fitted with a Teflon-tap was loaded with 200 mg iPP and 200 mg $Cp_2Hf(CH_3)_2/\equiv SiOAl(OC(CF_3)_3)_2(O(Si\equiv)_2)$ (0.042 mmol

Hf). The flask was removed from the glovebox, connected to a high vacuum line, and evacuated for 5 min. The flask was filled with 1atm of H_2 (4.16 mmol), sealed, disconnected from the line, and heated at 200 ˚C for 24h. Volatiles were sampled directly from the flask and analyzed by GC FID. Following analysis of volatile gases, the flask was opened to ambient atmosphere to proceed with the extraction of oils and remaining solids. Dichloromethane (~10 mL) was added to the flask at room temperature, and the solution was decanted from the residual polymer melt and spent catalyst mixture. This was repeated two more times. The combined dichloromethane extract was concentrated by heating gently to remove the solvent.

An identical procedure was used for reactions of iPP with D_2, except purified D_2 was used in place of H_2. An essentially identical procedure was used in experiments with H_2:Hf(Zr) ~ 1500, but a 1.5L glass bottle as shown below was used. The polymer and the catalyst were placed in the nub on the bottom of the flask and heated under 1 atm H2.

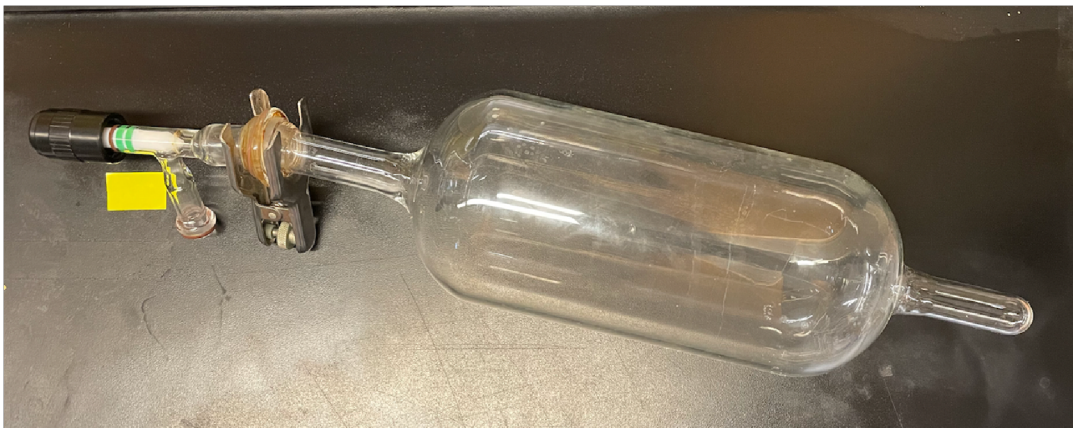

At 5 or 10atm Pressure in a Parr Reactor:

A 100 mL glass reaction liner was charged with 200 mg of $Cp_2Hf(CH_3)_2$/≡

$SiOAl(OC(CF_3)_3)_2(O(Si\equiv)_2)$ and 200 mg iPP in an argon filled glovebox. The reactor was sealed and pressurized with desired pressure of hydrogen (passed through a CRS ZPure O_2/H_2O filter) on demand and heated at 300 °C for 24h. The higher temperature is necessary because the thermocouple is not measuring temperature in the glass sleave. Control experiments showed that 300 °C is required to melt iPP; 200 °C to 250 °C was not hot enough to melt the polymer. After the reaction, the reactor was cooled to ambient temperature and the volatile gases were transferred into a 2L flask. Gas samples were aliquoted to determine volatile gas yields. CH_2Cl_2 (10 mL) was added to each glass liner under ambient atmosphere, and the solution was decanted from the remaining solid. This procedure was repeated three more times. The combined CH_2Cl_2 extract was concentrated by heating gently to remove the solvent and yields were calculated by weighing the amount of oil isolated.

At 2 or 5atm Pressure fed on Demand in a Parallel High Pressure Reactor:

Hydrogenolysis of iPP reactions at elevated H_2 pressures on demand were performed in a Biotage Endeavor parallel reactor in a N_2 filled glovebox. A 15 mL glass reaction liner was charged with 200 mg of $Cp_2Hf(CH_3)_2/\equiv SiOAl(OC(CF_3)_3)_2(O(Si\equiv)_2)$ and 200 mg iPP. The reactor was sealed and pressurized with desired pressure of hydrogen on demand and heated at 200 °C for 24h. After the reaction the reactor was vented with N_2 and cooled to ambient temperature inside the glovebox. CH_2Cl_2 (10 mL) was added to each glass liner under ambient atmosphere, and the solution was decanted from the remaining solid. This procedure was repeated three more times. The combined CH_2Cl_2 extract was

concentrated by heating gently to remove the solvent and yields were calculated by weighing the amount of oil isolated.

Quantification of Gas Phase Products from the hydrogenolysis of iPP with Cp_2HfMe_2/≡ $SiOAl(OC(CF_3)_3)_2(O(Si≡)_2)$

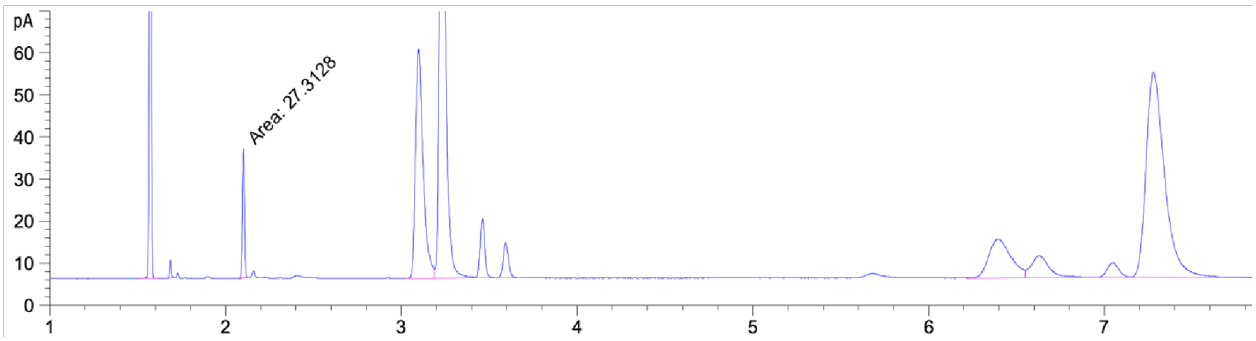

Figure 3.14. GC of the gas phase of iPP hydrogenolysis reactions with Cp_2HfMe_2/≡ $SiOAl(OC(CF_3)_3)_2(O(Si≡)_2)$ under 1 atm H_2 (H_2:Hf ~ 100). The amounts gases are reported in the main text.

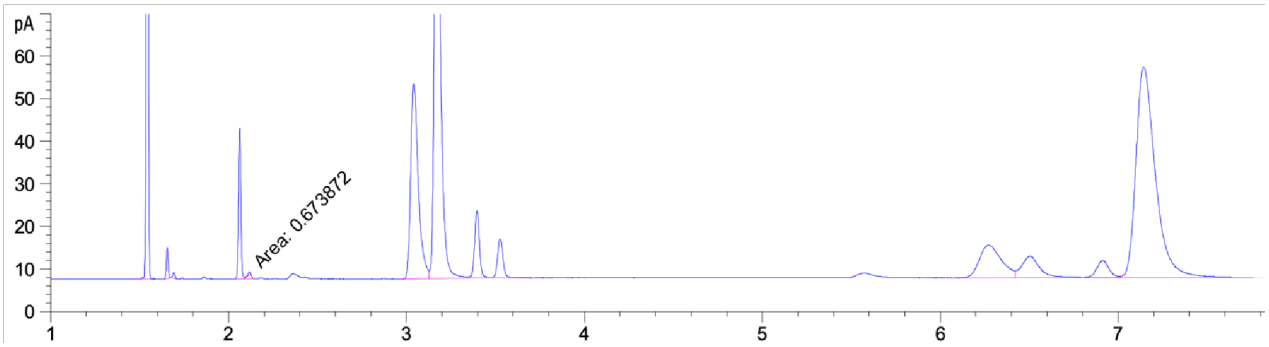

Figure 3.15. GC of the gas phase of iPP hydrogenolysis reactions with Cp_2HfMe_2/≡ $SiOAl(OC(CF_3)_3)_2(O(Si≡)_2)$ under 1 atm D_2 (D_2:Hf ~ 100). The amounts gases generated in this reaction are essentially identical to those reported in the main text.

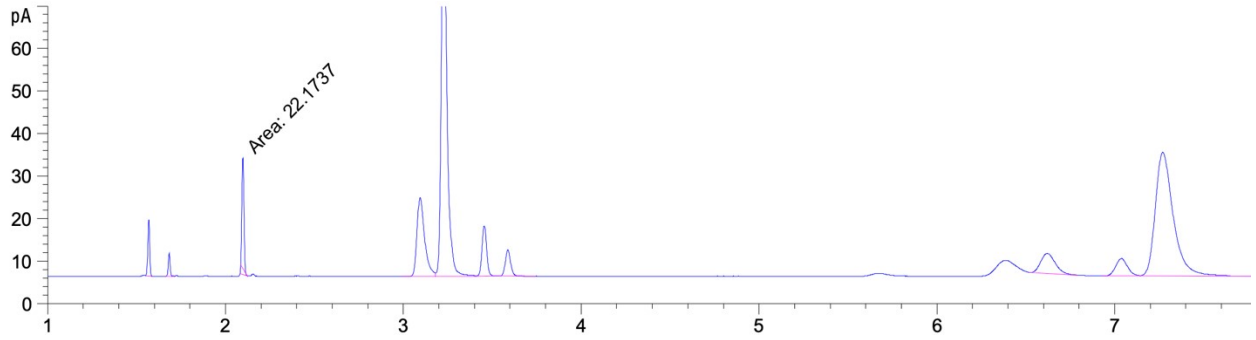

Figure 3.16. GC of the gas phase of iPP hydrogenolysis reactions with Cp_2HfMe_2/≡ $SiOAl(OC(CF_3)_3)_2(O(Si≡)_2)$ under 1 atm H_2 (H_2:Hf ~ 1500). The amounts of gas evolved are 1.8 CH_4 Hf^{-1}, 0.4 C_2H_6 Hf^{-1}, 1.35 C_3H_6 Hf^{-1} and 9.9 C_4H_{10} Hf^{-1}, and 9.3 C_5H_{10} Hf^{-1}. The total yield of light gases are 11.5 % (23 mg) based on this data.

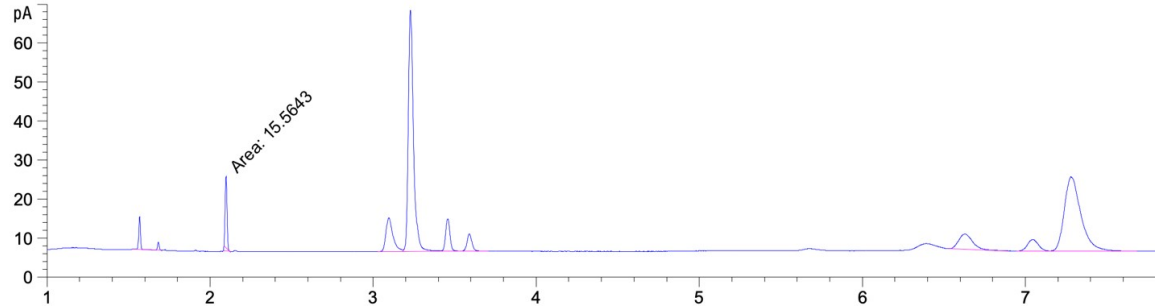

Figure 3.17. GC of the gas phase of iPP hydrogenolysis reactions with Cp_2ZrMe_2/≡ $SiOAl(OC(CF_3)_3)_2(O(Si≡)_2)$ under 1 atm H_2 (H_2:Zr ~ 1500). The amounts of gas evolved are 1.1 CH_4 Hf^{-1}, 1.6 C_2H_6 Zr^{-1}, 1.0 C_3H_6 Zr^{-1} and 6.7 C_4H_{10} Zr^{-1}, and 4.9 C_5H_{10} Zr^{-1}. The total yield of light gases are 7 % (14 mg) based on this data.

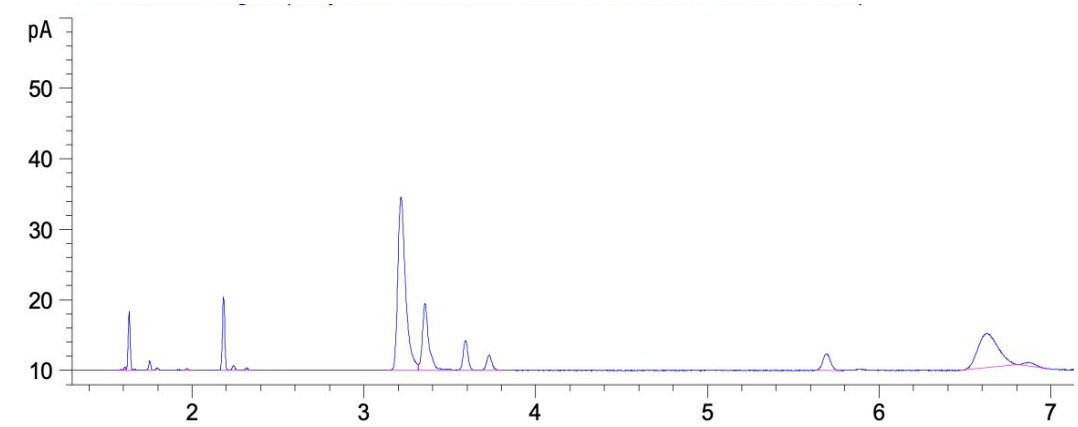

Figure 3.18. GC of the gas phase of iPP hydrogenolysis reactions with Cp_2HfMe_2/≡

$SiOAl(OC(CF_3)_3)_2(O(Si\equiv)_2)$ under 5 atm H_2. The amounts of gas evolved are 1.55 CH_4 Hf^{-1}, 0.12 C_2H_6 Hf^{-1}, 0.76 C_3H_6 Hf^{-1}, 6.62 C_4H_{10} Hf^{-1}, and 1.81 C_5H_{10} Hf^{-1}. The total yield of light gases are 4 % (8 mg) based on this data.

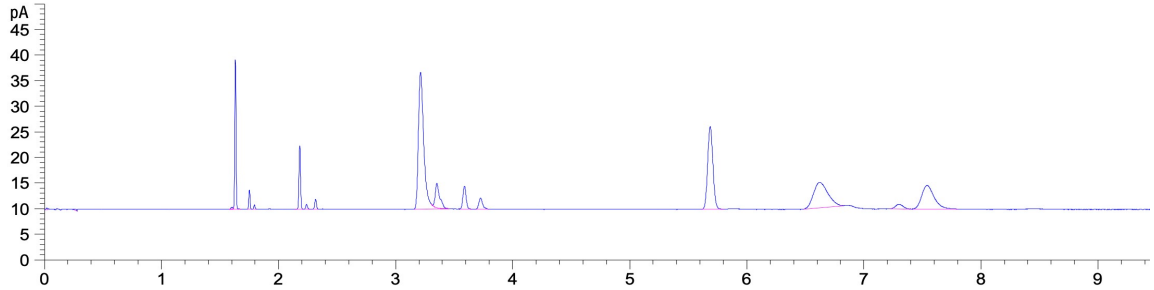

Figure 3.19. GC of the gas phase of iPP hydrogenolysis reactions with Cp_2HfMe_2/≡ $SiOAl(OC(CF_3)_3)_2(O(Si\equiv)_2)$ under 10 atm H_2. The amounts of gas evolved are 5.4 CH_4 Hf^{-1}, 0.37 C_2H_6 Hf^{-1}, 1.1 C_3H_6 Hf^{-1}, 6.83 C_4H_{10} Hf^{-1}, and 6.53 C_5H_{10} Hf^{-1}. The total yield of light gases are 7.3 % (14.6 mg) based on this data.

MALDI MS of oils from the hydrogenolysis of iPP with Cp_2HfMe_2/≡SiOAl(OC $(CF_3)_3)_2(O(Si\equiv)_2)$.

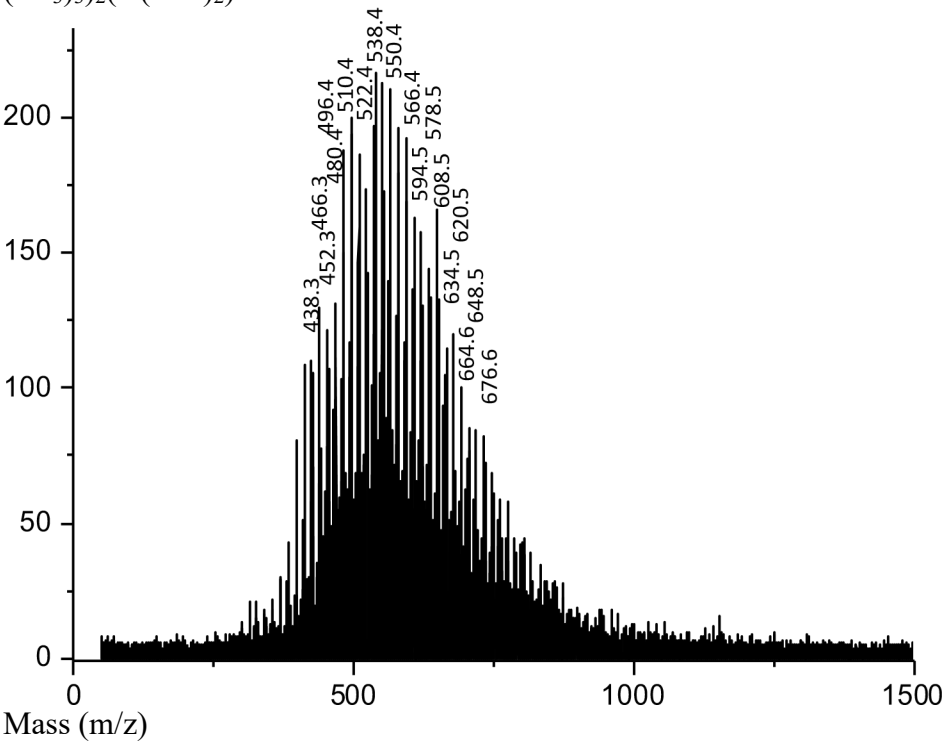

Figure 3.20. Representative MALDI MS of the oils obtained from hydrogenolysis of iPP with H_2:Hf ~ 100.

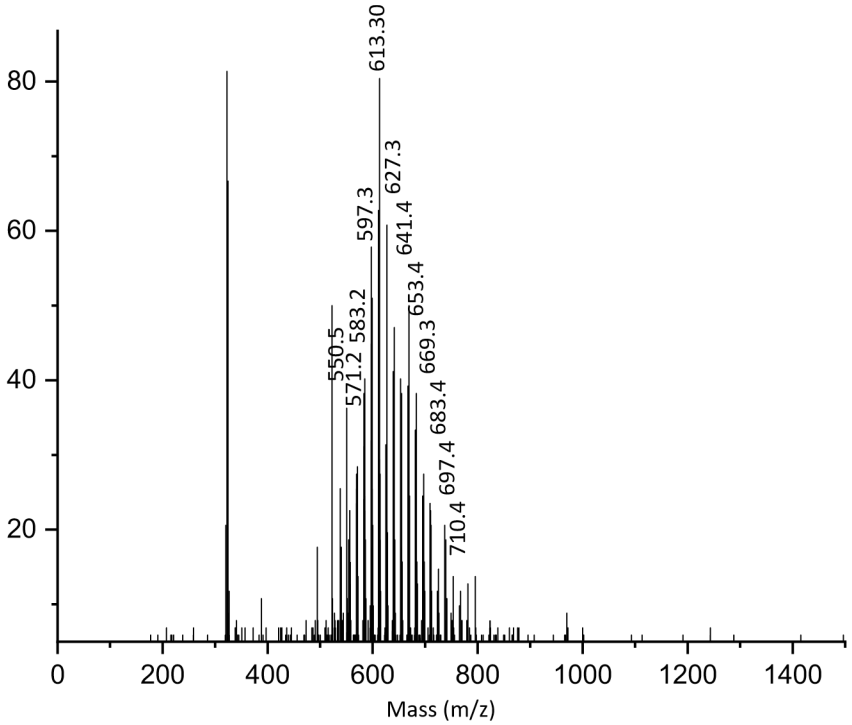

Figure 3.21. Representative MALDI MS of the oils obtained from hydrogenolysis of iPP with D_2:Hf ~ 100.

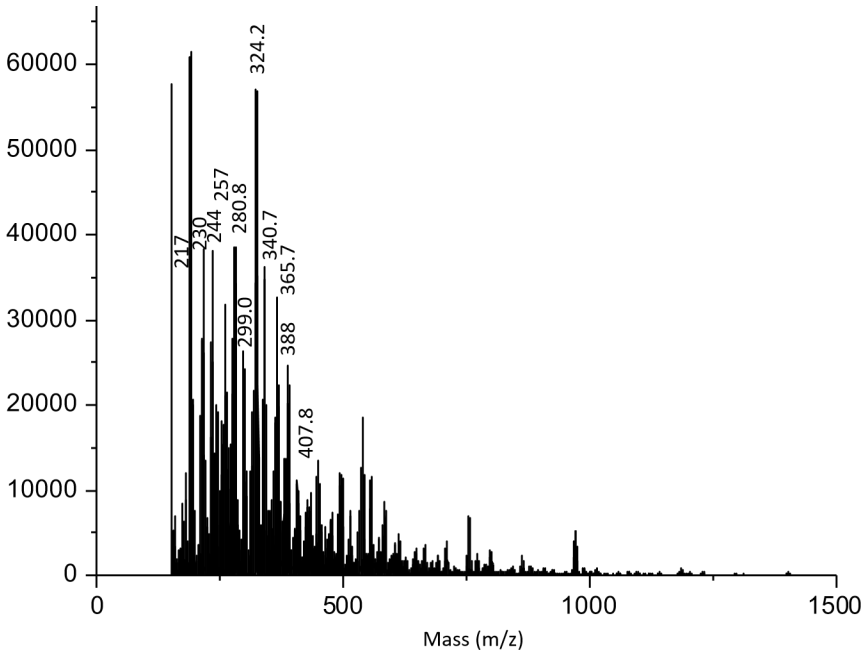

Figure 3.22. Representative MALDI MS of the oils obtained from hydrogenolysis of iPP with H_2:Hf ~ 1500.

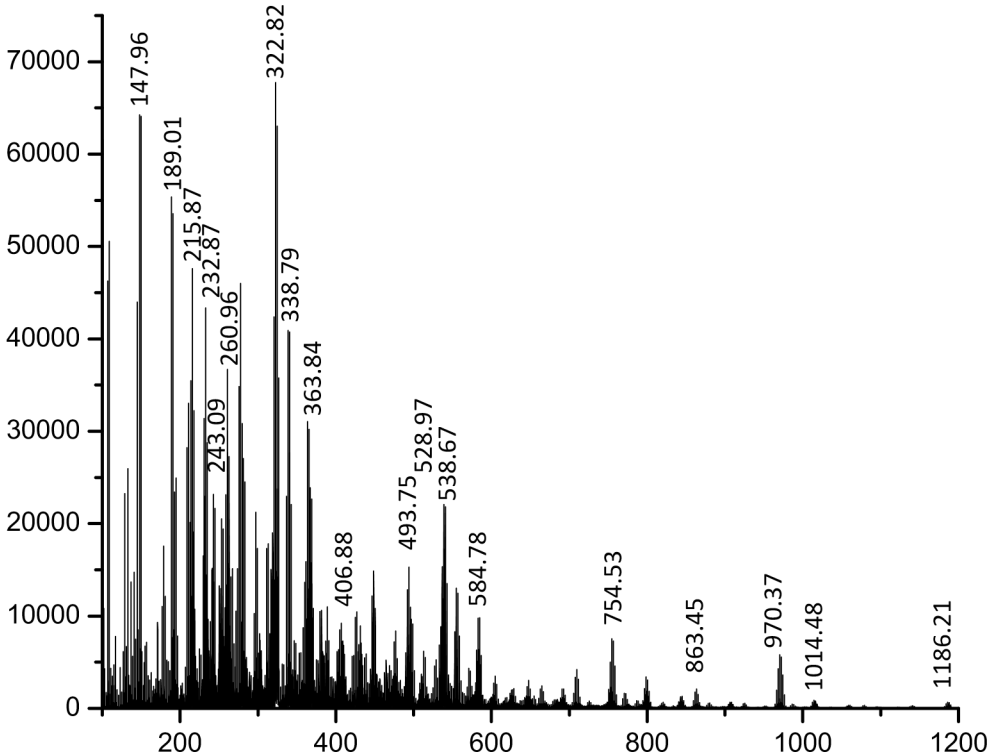

Figure 3.23. Representative MALDI MS of the oils obtained from hydrogenolysis of iPP under 5 atm H_2.

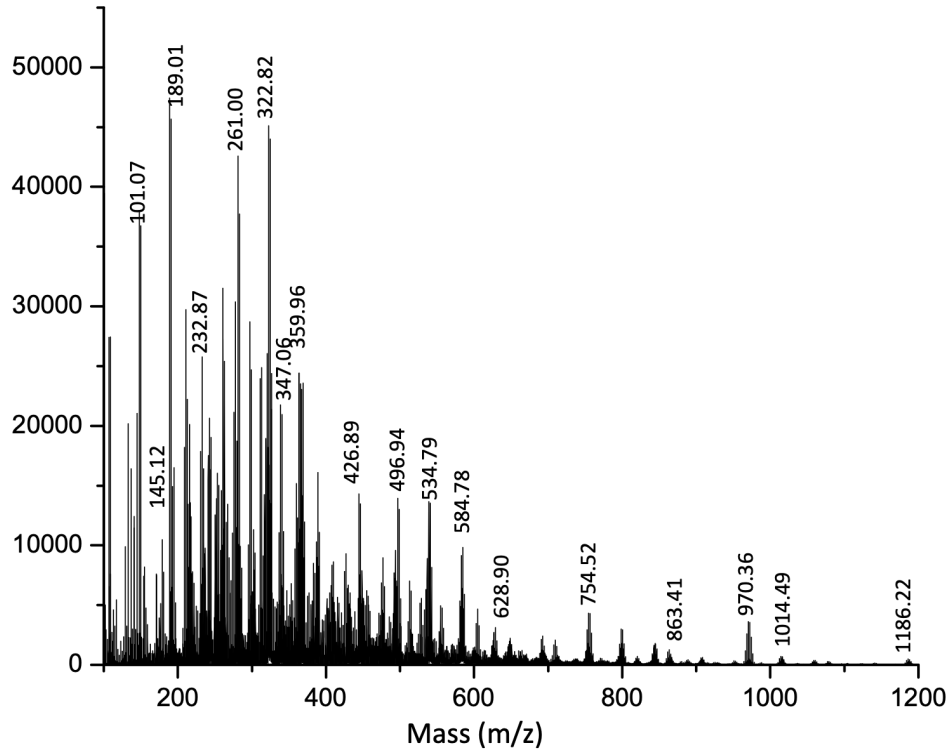

Figure 3.24. Representative MALDI MS of the oils obtained from hydrogenolysis of iPP under 10 atm H_2.

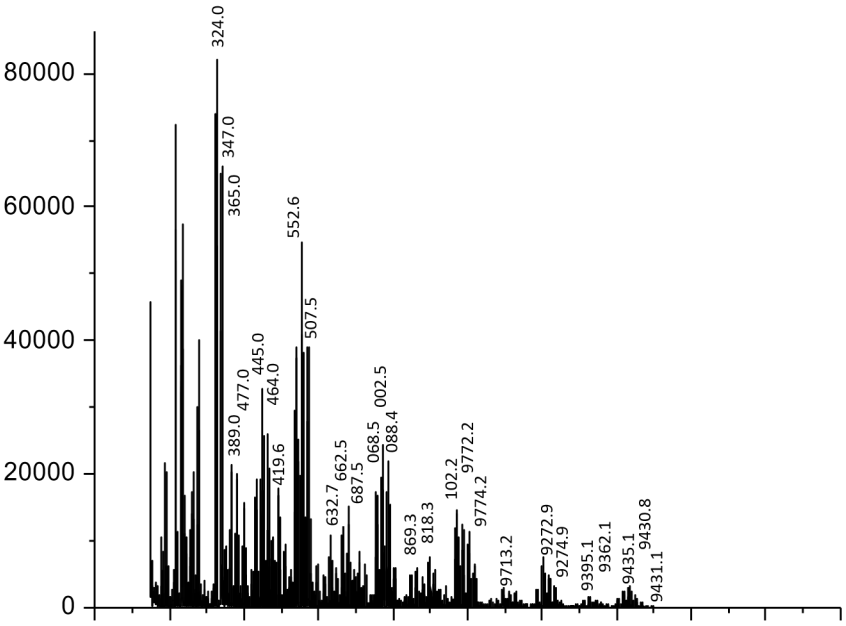

Figure 3.25. Representative MALDI MS of the oils obtained from hydrogenolysis of iPP under 2 atm H_2 fed on demand.

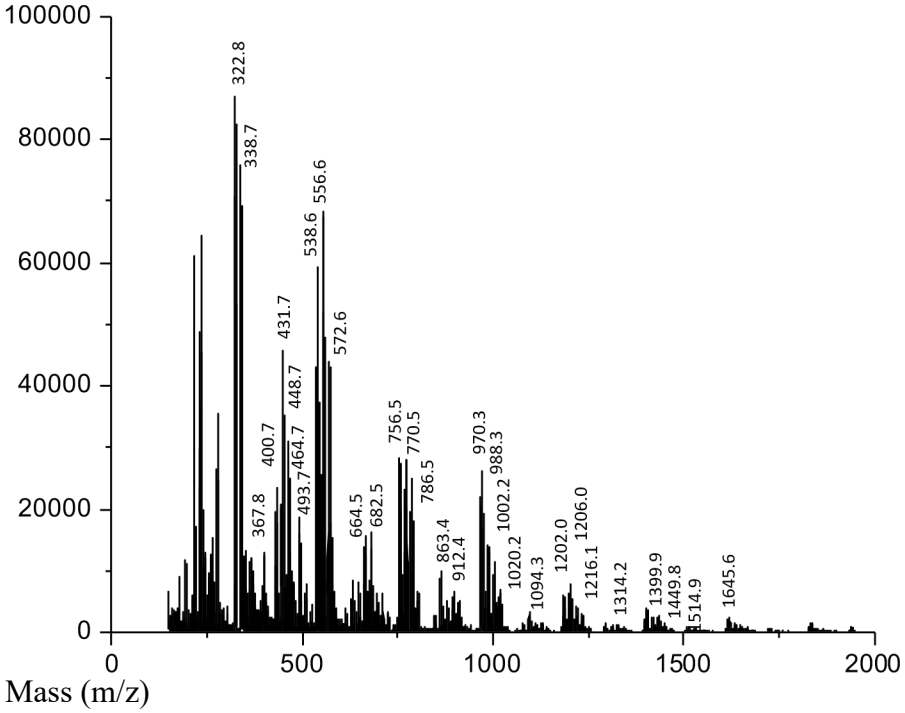

Figure 3.26. Representative MALDI MS of the oils obtained from hydrogenolysis of iPP under 5 atm H_2 fed on demand.

GCMS of oils from the hydrogenolysis of iPP with Cp_2HfMe_2/ ≡SiOAl $(OC(CF_3)_3)_2$ $(O(Si≡)_2)$.

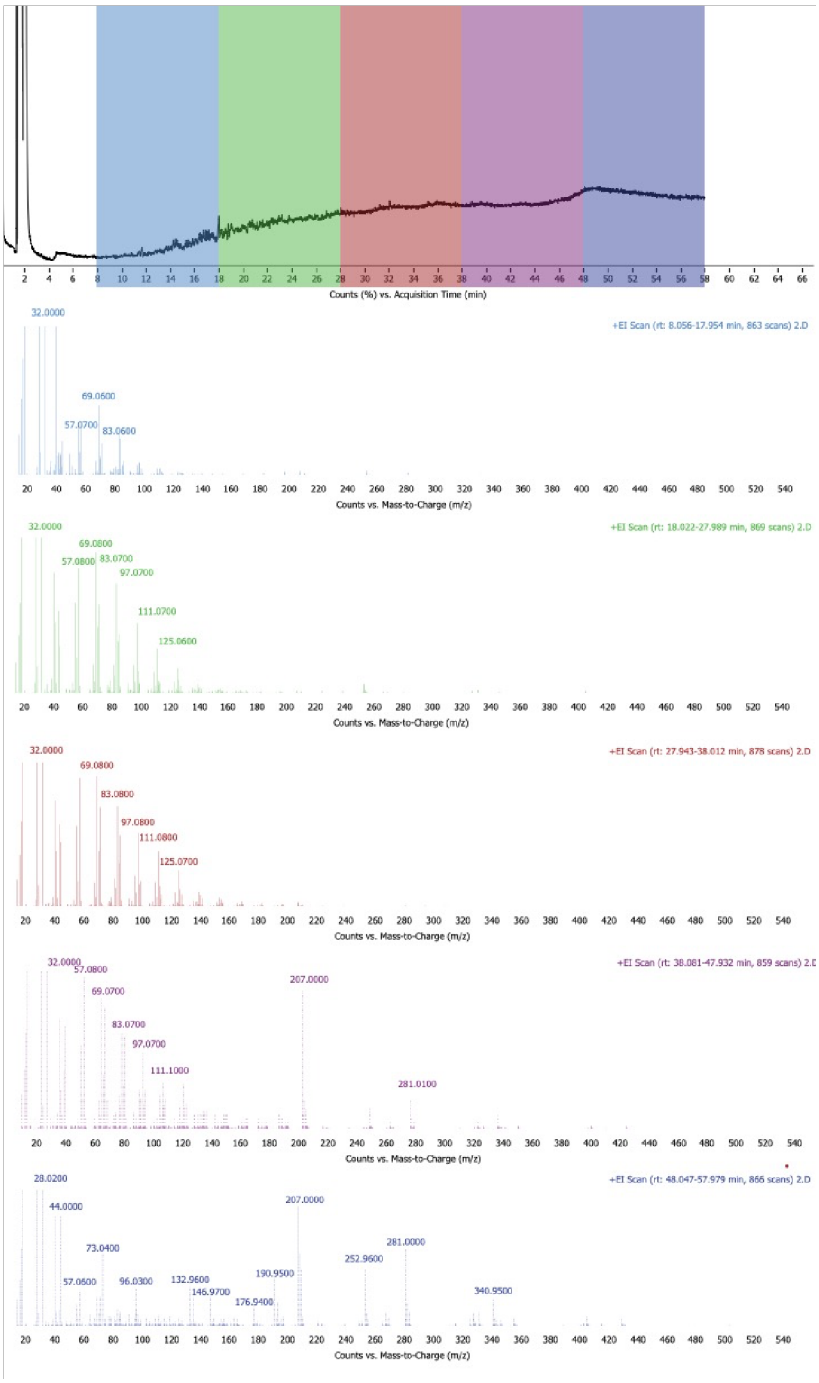

Figure 3.27. GCMS of oil produced with Cp_2HfMe_2/≡SiOAl$(OC(CF_3)_3)_2(O(Si≡)_2)$ under 1 atm H_2 (H_2:Hf ~ 100). The data is too complex to integrate a single peak. The GC and MS data is color coded to give representative fractions showing how higher MW ions form at higher retention times.

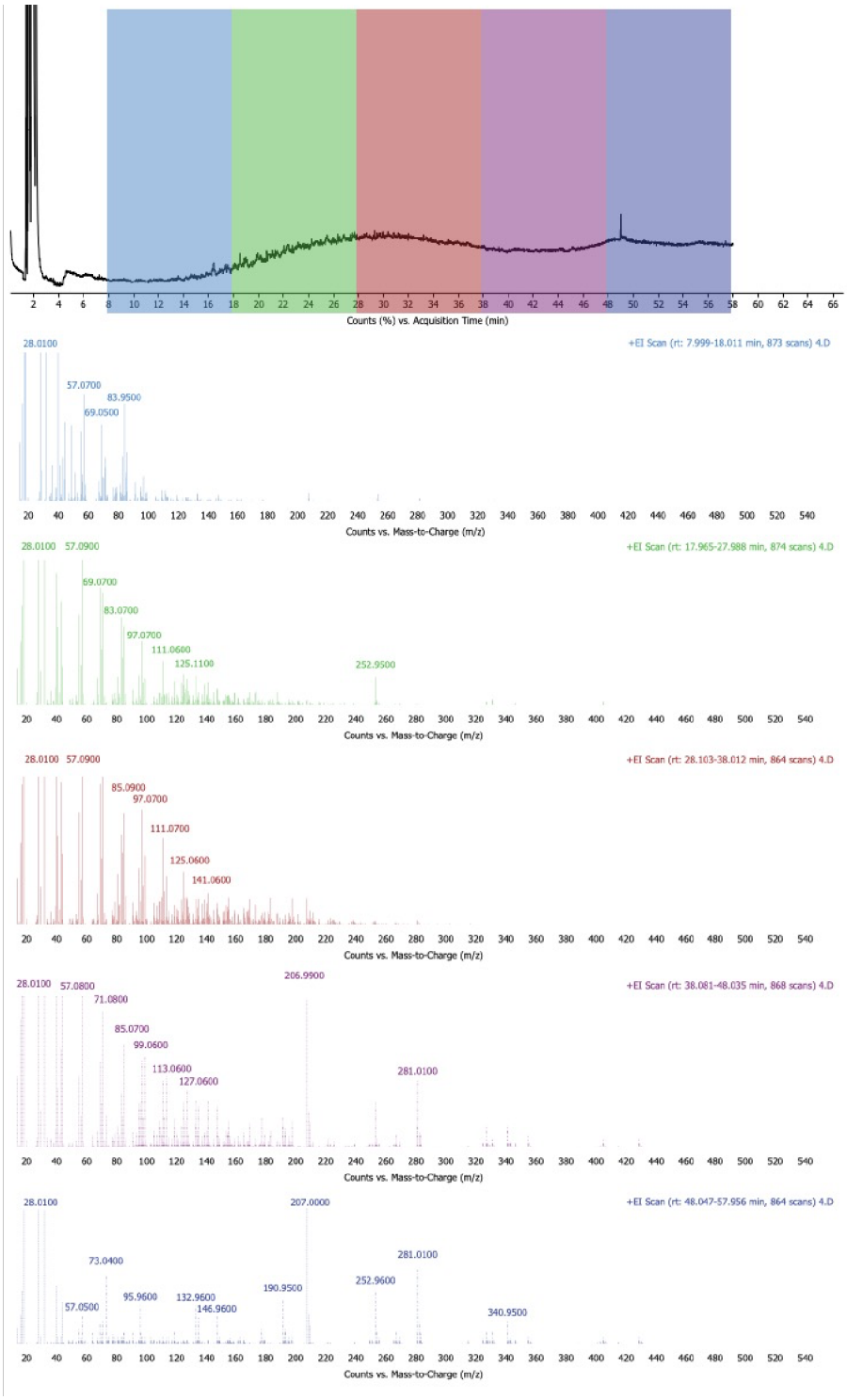

Figure 3.28. GCMS of oil produced with Cp_2HfMe_2/≡SiOAl(OC(CF_3)$_3$)$_2$(O(Si≡)$_2$) under 5 atm H_2. The data is too complex to integrate a single peak. The GC and MS data is color coded to give representative fractions showing how higher MW ions form at higher retention times.

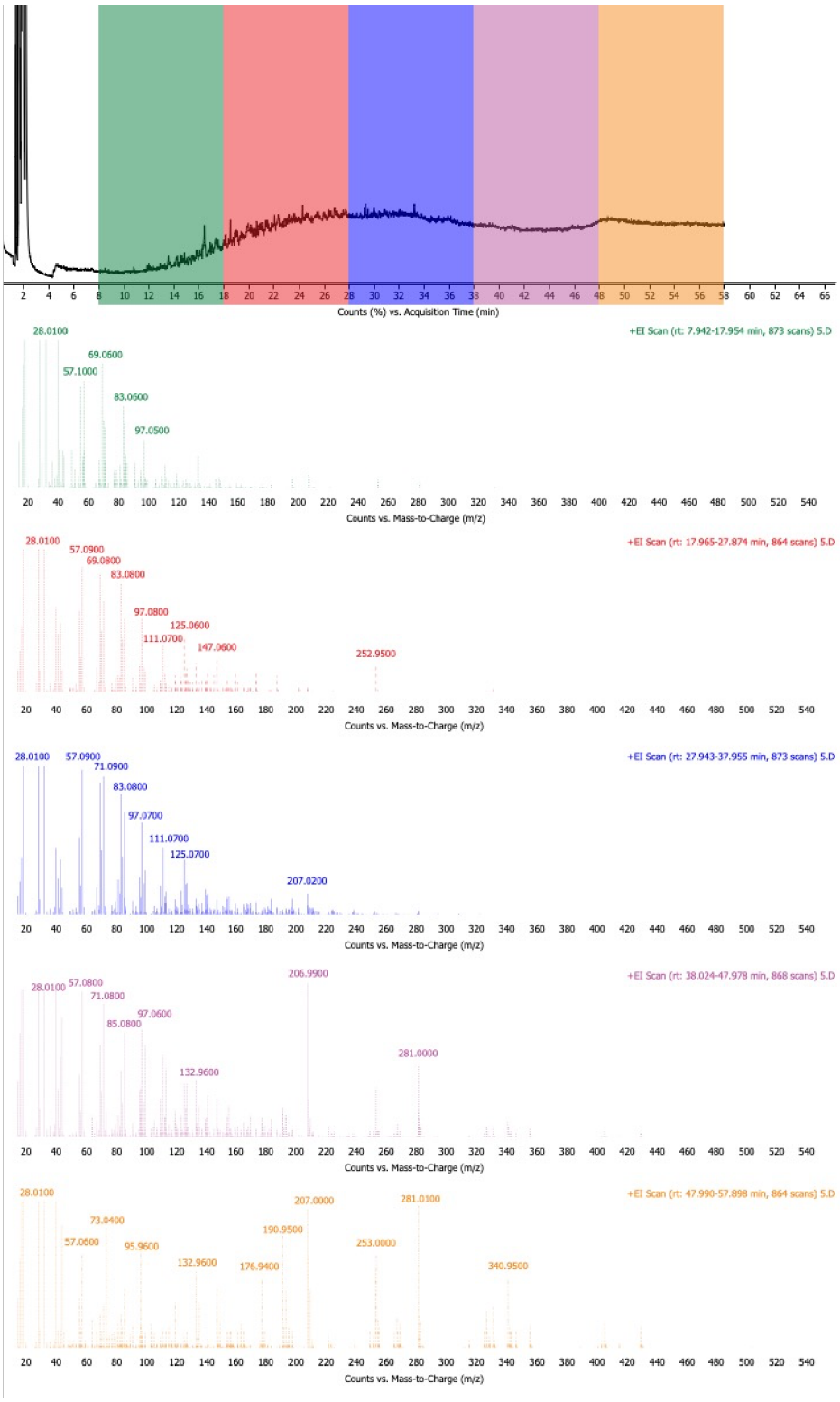

Figure 3.29. GCMS of oil produced with Cp_2HfMe_2/≡SiOAl(OC(CF_3)$_3$)$_2$(O(Si≡)$_2$) under 10 atm H_2. The data is too complex to integrate a single peak. The GC and MS data is

color coded to give representative fractions showing how higher MW ions form at higher retention times.

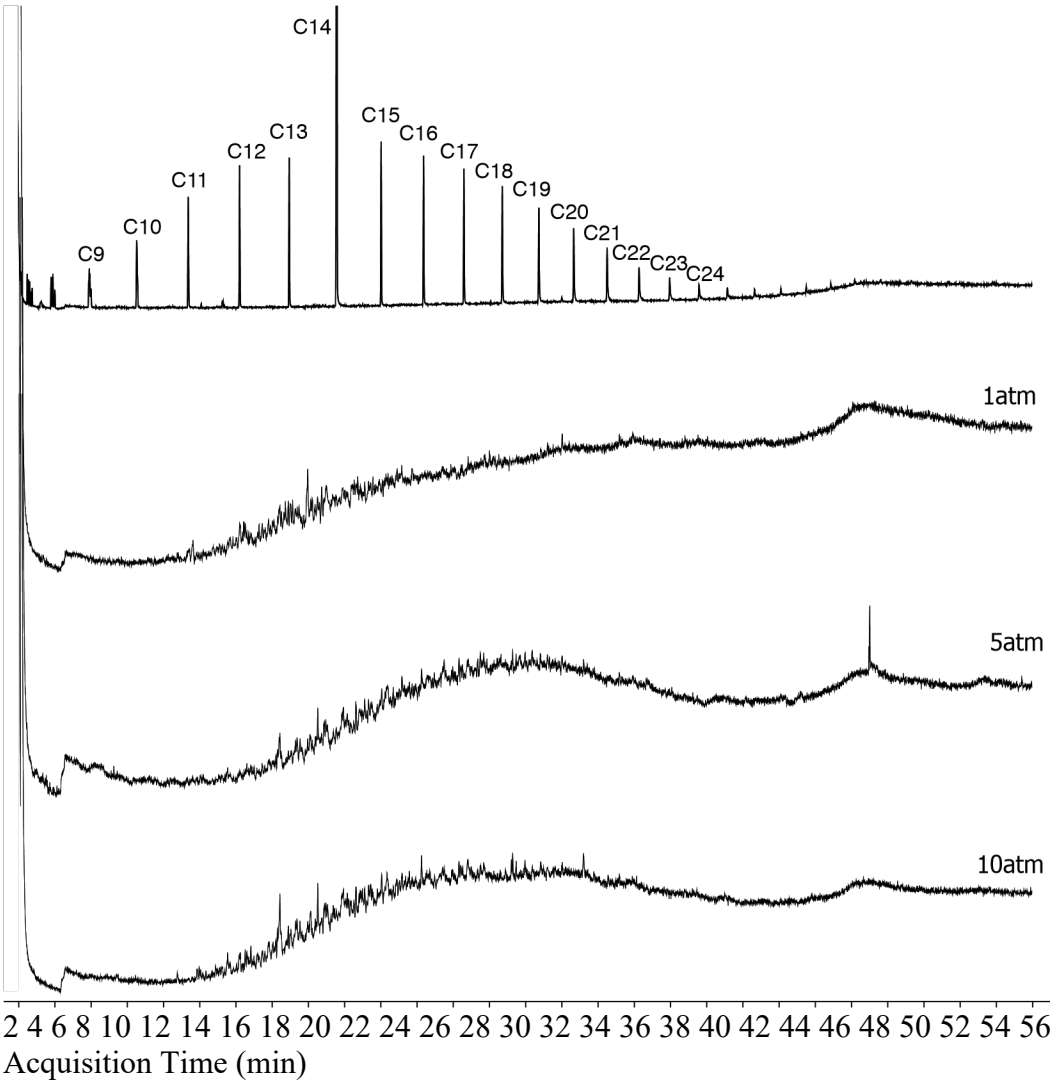

Figure 3.30. GC data of oils produced with Cp_2HfMe_2/≡SiOAl(OC(CF_3)$_3$)$_2$(O(Si≡)$_2$) under the pressures given in the figure (bottom three chromatograms). The top chromatogram is a mixture of alkanes produced from alkane metathesis reactions of tetradecane with a different catalyst (see: Gao, J.; Zhu, L.; Conley, M. P. Cationic Tantalum Hydrides Catalyze Hydrogenolysis and Alkane Metathesis Reactions of Paraffins and Polyethylene. *J. Am. Chem. Soc.* 2023, *145*, 4964-4968). The top chromatogram contains linear the C_n listed in the figure to show the reader where linear alkanes appear with this method. Also apparent in this top chromatogram is the flat base line throughout the GC method, indicating the complexity of the oils produced in iPP hydrogenolysis reactions using this catalyst.

^{1}H NMR data for oils produced from the hydrogenolysis of iPP with Cp_2HfMe_2/≡ $SiOAl(OC(CF_3)_3)_2(O(Si≡)_2)$.

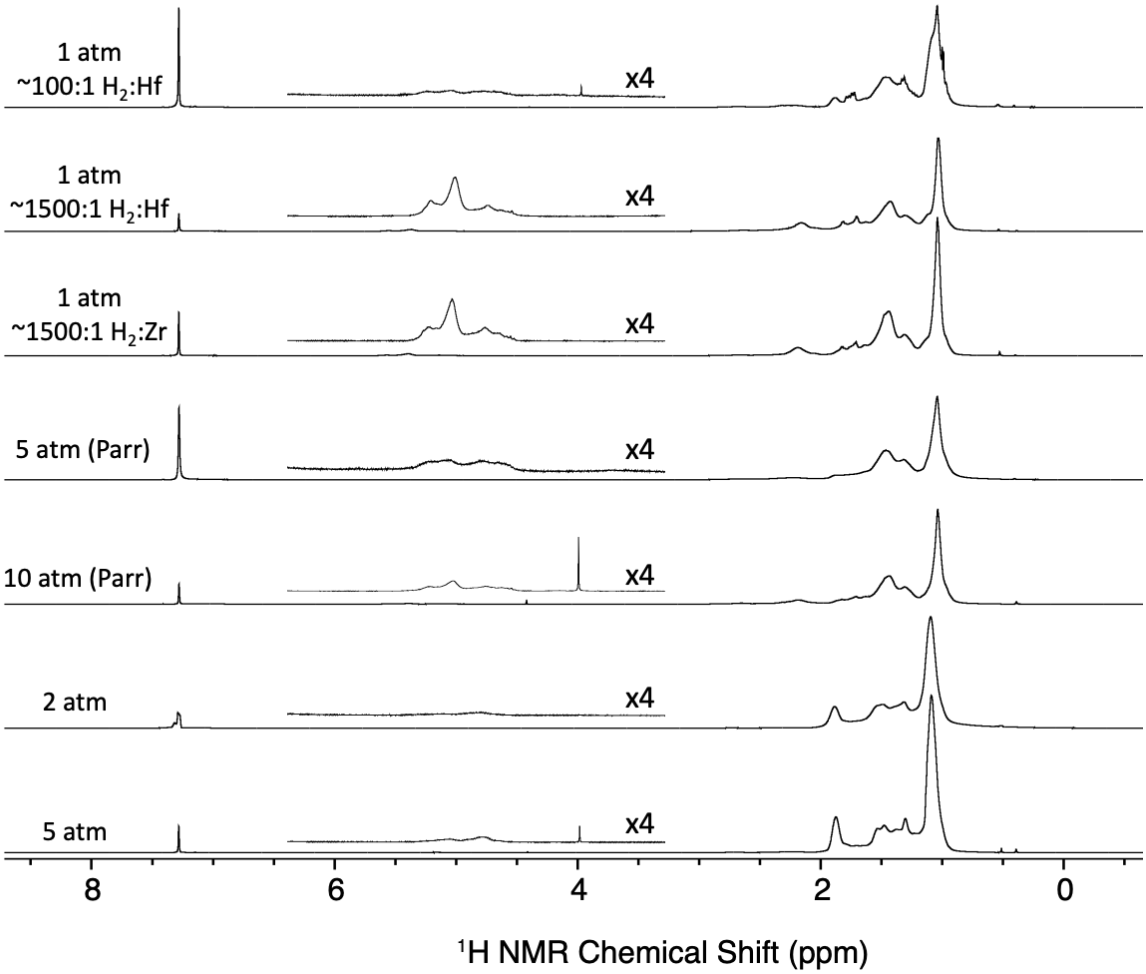

Figure 3.31. ^{1}H NMR spectra of extracted oils recorded in C_6D_6 at ambient temperature. The pressures in the figure correspond to the H_2 pressure used for the hydrogenolysis reaction.

Table 3.2. Integral values obtained from ^{1}H NMR data shown in Figure 3.31.

Conditions	Olefin:C_3H_6
1 atm (~100:1 H_2:Hf)	1:294
1 atm (~1500:1 H_2:Hf)	1:54
1 atm (~1500:1 H_2:Zr)	1:58

5 atm Parr	1:200
10 atm Parr	1:82
2 atm	1:1768
5 atm	1:533

^{2}H NMR data for using D_2 in iPP degradation reactions $Cp_2HfMe_2/{\equiv}SiOAl(OC(CF_3)_3)_2(O(Si{\equiv})_2)$.

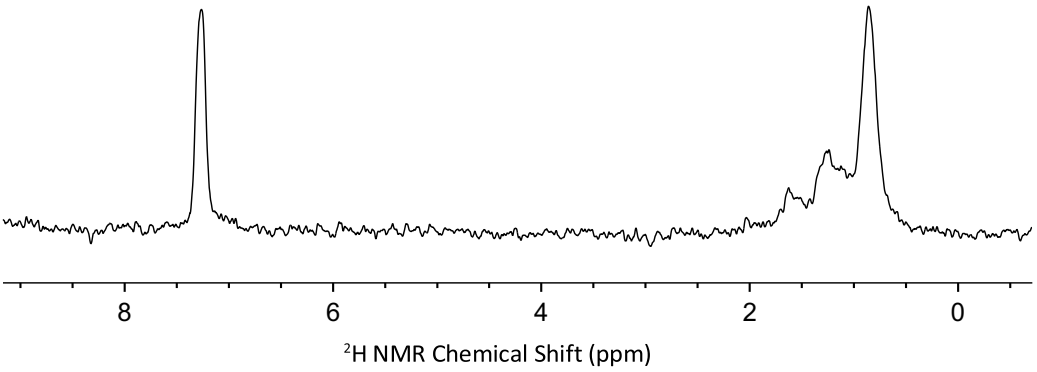

Figure 3.32. ^{2}H NMR of extracted oil recorded in $CHCl_3$ at ambient temperature. The oil in this spectrum was generated at D_2:Hf ~ 100.

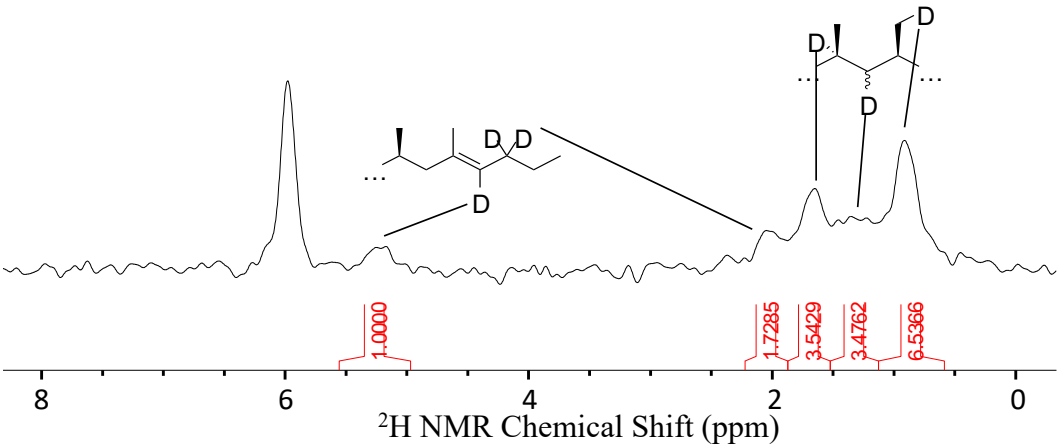

Figure 3.33. ^{2}H NMR spectrum of residual iPP after reaction with 1 and D_2. Signals for each C– D are given in the figure. The chemical shifts for $CH_3CH_2CD_2{=}CDC(CH_3)P$ are from *J. Am. Chem. Soc.* 1998, *120,* 2308-2321.

Representative high temperature NMR data of residual iPP after reactions with H_2 and $Cp_2HfMe_2/{\equiv}SiOAl(OC(CF_3)_3)_2(O(Si{\equiv})_2)$.

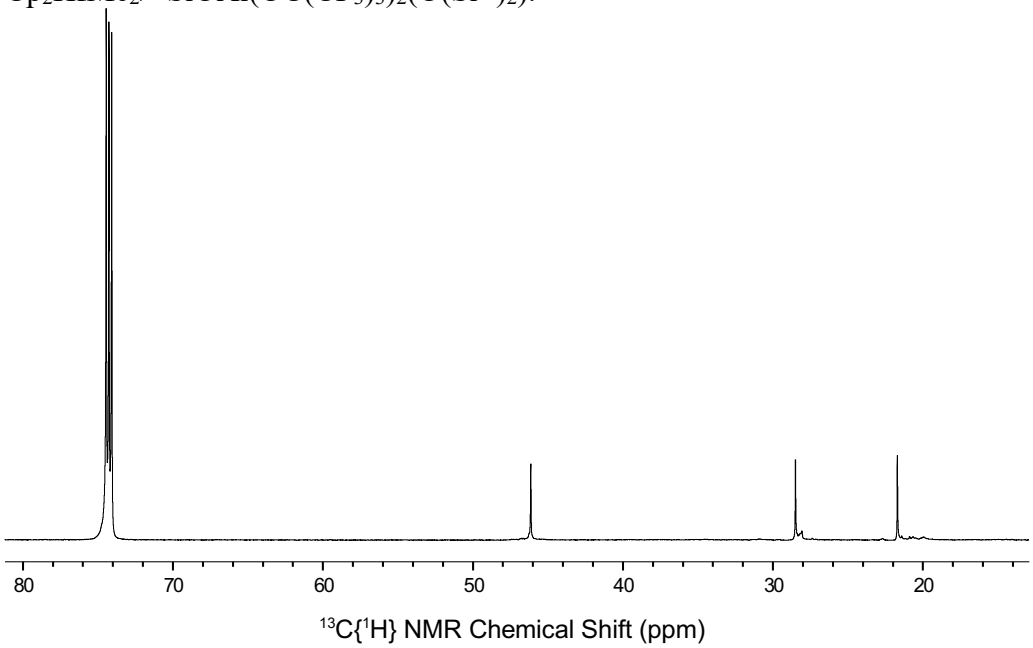

Figure 3.34. Quantitative $^{13}C\{^1H\}$ NMR spectrum of the residual polymer melt from the hydrogenolysis of iPP with $Cp_2HfMe_2/{\equiv}SiOAl(OC(CF_3)_3)_2(O(Si{\equiv})_2)$ at 1atm, collected at 120˚C in $C_2D_2Cl_4$.

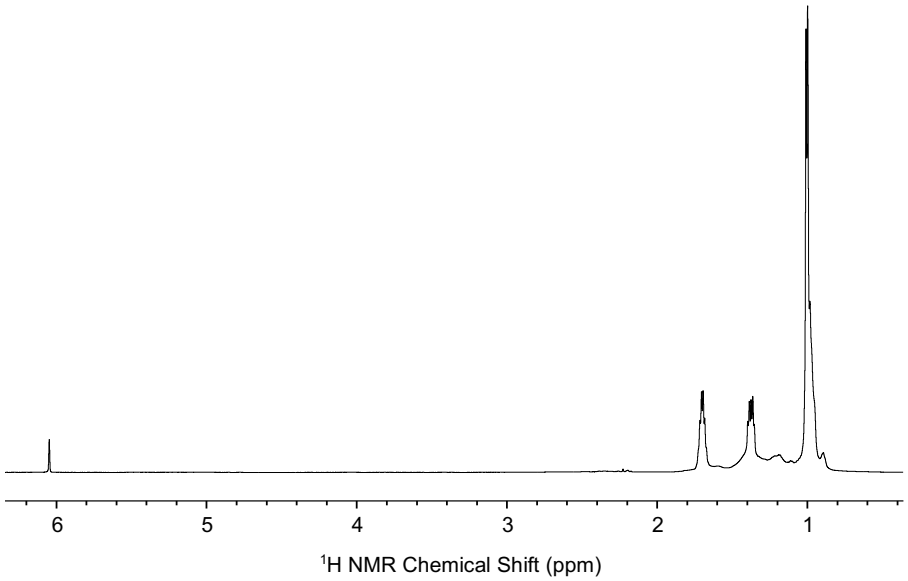

Figure 3.35. ^1H NMR spectrum of the residual polymer melt from the hydrogenolysis of iPP with $Cp_2HfMe_2/{\equiv}SiOAl(OC(CF_3)_3)_2(O(Si{\equiv})_2)$ at 1atm, collected at 120˚C in $C_2D_2Cl_4$.

Table 3.3. Integral values obtained from quantitative $^{13}C\{^{1}H\}$ NMR data shown in Figure 3.4.

	Sum of Integrals for end groups	Sum of Integrals for all other carbons	Ratio of end group integral to C_3H_6 units	Calculated M_n[a] (g/mol)
1atm (H_2:Hf ~ 100)	1.46	35	8.1	388
1atm (H_2:Hf ~ 1500)	4.19	72.1	5.7	290
1atm (H_2:Zr ~ 1500)	3.74	79.3	7.06	347
5atm (Parr)	1	14.00	4.67	238
10atm (Parr)	1	12.84	4.28	221
2atm (on demand)	7.5	572	25.4	1136
5atm (on demand)	4.62	355.73	25.6	1146

[a] – All M_n values also include a propyl end group in the molecular weight.

iPP degradation reactions using ≡SiOAl(OC(CF$_3$)$_3$)$_2$(O(Si≡)$_2$).

In an argon-filled glovebox, a 100mL Schlenk flask fitted with a Teflon-tap was loaded with 200 mg iPP and 200 mg ≡SiOAl(OC(CF$_3$)$_3$)$_2$(O(Si≡)$_2$) (0.044 mmol Al). The flask was removed from the glovebox, connected to a high vacuum line, and evacuated for 5 min. The flask was filled with 1atm of H_2 (4.16 mmol), sealed, disconnected from the line, and heated at 200 ˚C for 24h. Volatiles were sampled directly from the flask and analyzed by GC FID. Following analysis of volatile gases, the flask was opened to ambient atmosphere to proceed with the extraction of oils and remaining solids. Dichloromethane (~10 mL) was added to the flask at room temperature, and the solution was decanted from the residual polymer melt and spent catalyst mixture. This was repeated two more times. The combined dichloromethane extract was concentrated by heating gently to remove the solvent. The yield of oil from this reaction was 30 mg (15 % from initial iPP mass).

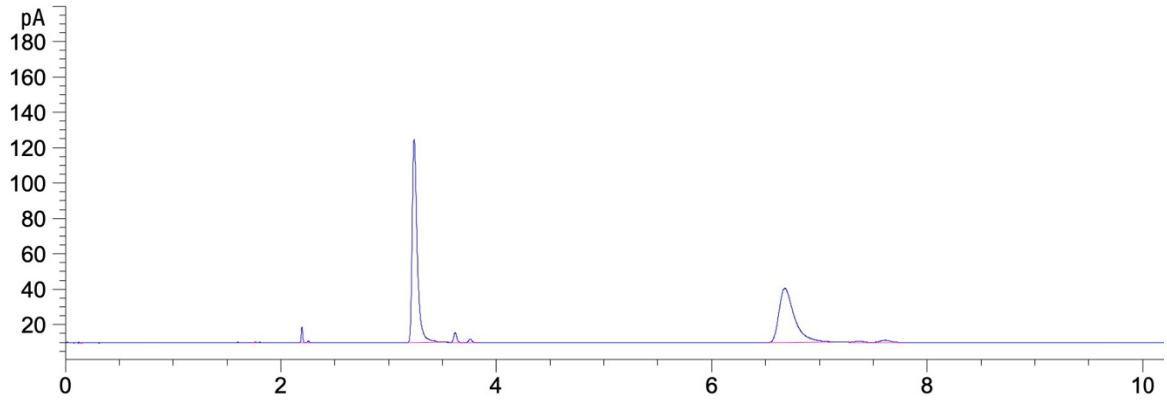

Figure 3.36. GC of the gas phase of iPP hydrogenolysis reactions with 200 mg ≡ $SiOAl(OC(CF_3)_3)_2(O(Si\equiv)_2)$. The amounts of gas evolved are 0 CH_4 Hf^{-1}, 0 C_2H_6 Zr^{-1}, 0.01 C_3H_6 Zr^{-1} and 0.4 C_4H_{10} Zr^{-1}, and 0.2 C_5H_{10} Zr^{-1}. The total yield of light gases are 0.01% (2 mg) based on this data.

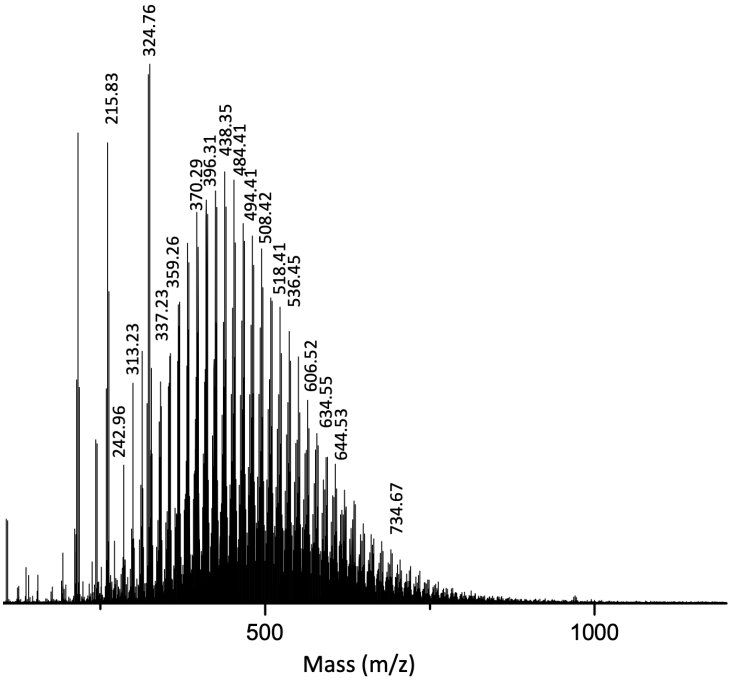

Figure 3.37. Representative MALDI MS of the oils using ≡$SiOAl(OC(CF_3)_3)_2(O(Si\equiv)_2)$.

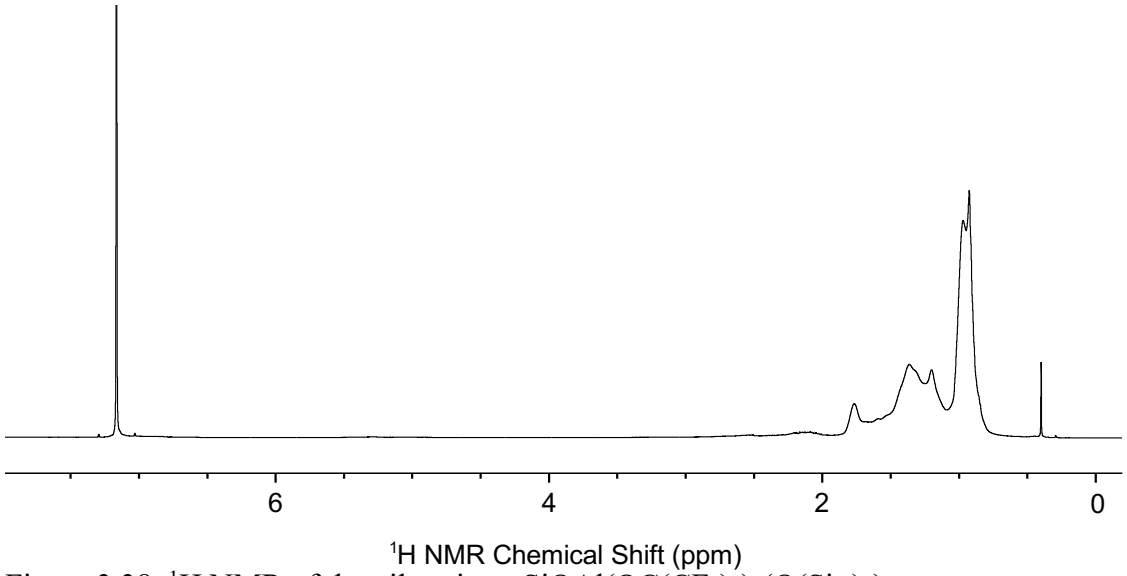

Figure 3.38. ^{1}H NMR of the oils using ≡SiOAl(OC(CF$_3$)$_3$)$_2$(O(Si≡)$_2$).

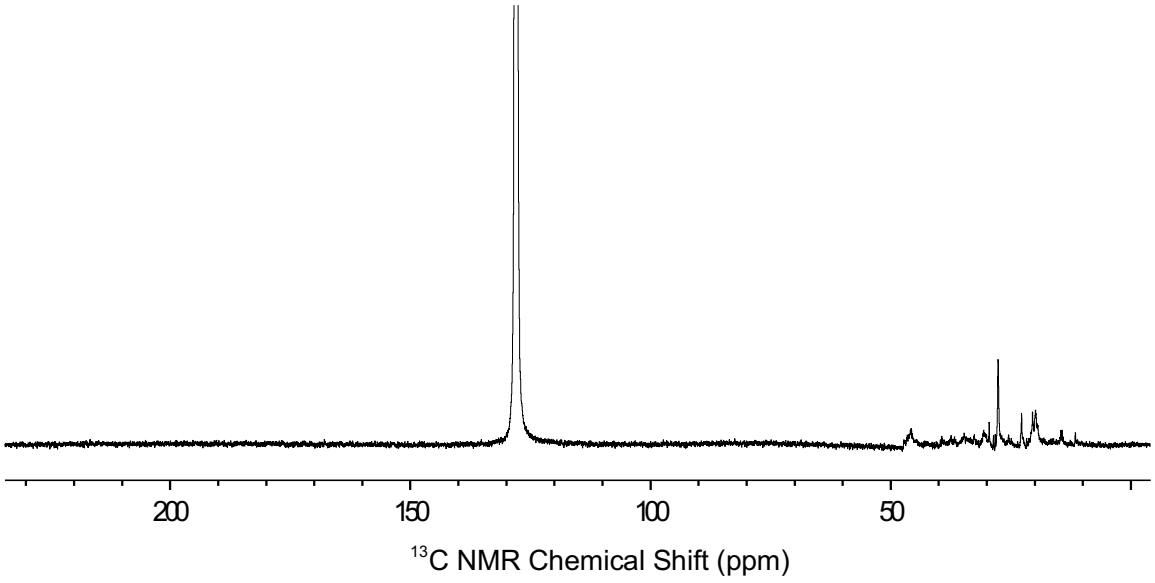

Figure 3.39. ^{13}C{^{1}H} NMR of the oils using ≡SiOAl(OC(CF$_3$)$_3$)$_2$(O(Si≡)$_2$).

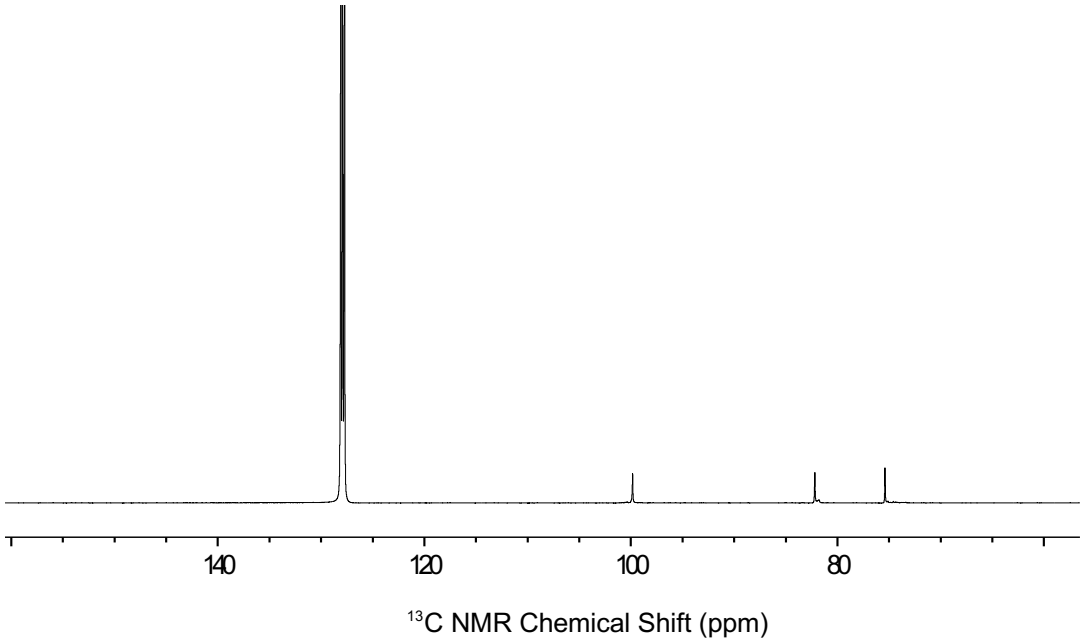

Figure 3.40. Quantitative $^{13}C\{^{1}H\}$ NMR of the residual iPP using $\equiv SiOAl(OC(CF_3)_3)_2(O(Si\equiv)_2)$ showing highly isotactic iPP remains after the reaction. Recorded at 120 ºC in $C_2D_2Cl_4$

iPP degradation reactions using $Cp_2Hf(CH_3)(OSi\equiv)$ (2).

In an argon-filled glovebox, a 100mL Schlenk flask fitted with a Teflon-tap was loaded with 200 mg iPP and 200 mg $Cp_2Hf(CH_3)(OSi\equiv)$ (0.052 mmol Hf). The flask was removed from the glovebox, connected to a high vacuum line, and evacuated for 5 min. The flask was filled with 1atm of purified D_2 (4.16 mmol), sealed, disconnected from the line, and heated at 200 ˚C for 24h. Volatiles were sampled directly from the flask and analyzed by GC FID. Following analysis of volatile gases, the flask was opened to ambient atmosphere to proceed with the extraction of oils and remaining solids. Attempts to isolate oil using the procedures with other materials described here (successive dichloromethane (~10 mL) extracts), resulted in no isolable oil.

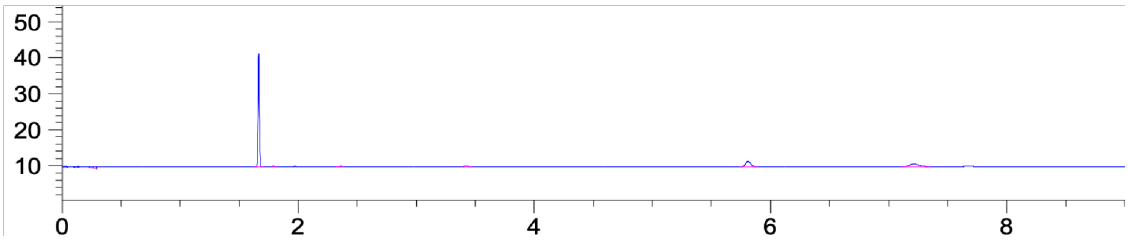

Figure 3.41. GC of the gas phase of iPP hydrogenolysis reactions with 200mg Hf/SiO2 1atm D2 control. The amounts of gas evolved are 0.08 CH_4 Hf^{-1}, 0 C_2H_6 Zr^{-1}, 0 C_3H_6 Zr^{-1} and 0 C_4H_{10} Zr^{1}, and 0.003 C_5H_{10} Zr^{-1}.

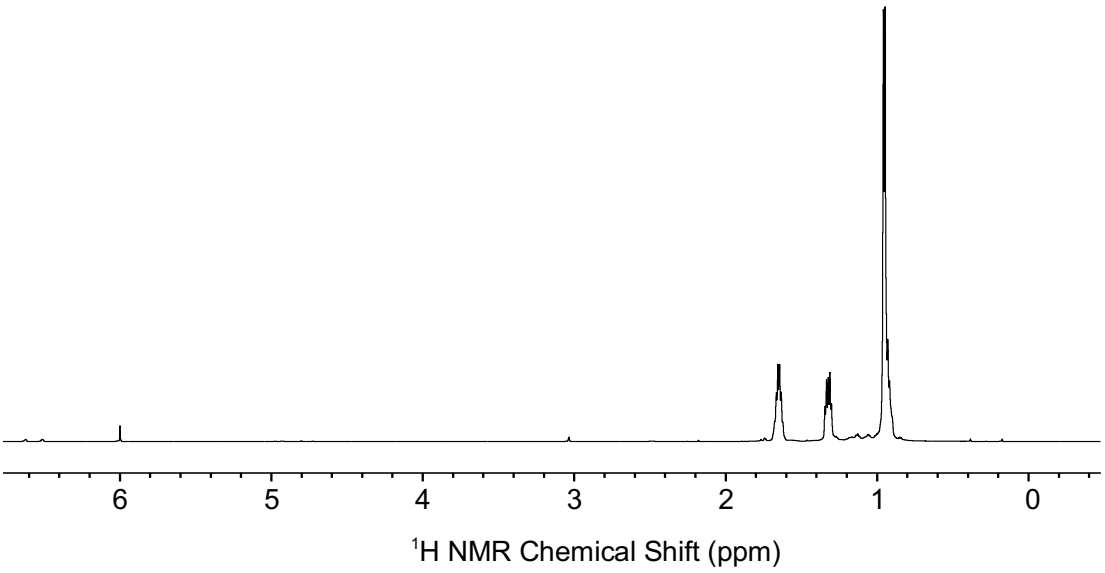

Figure 3.42. ^{1}H NMR of the residual iPP using 2. Recorded at 120 °C in $C_2D_2Cl_4$.

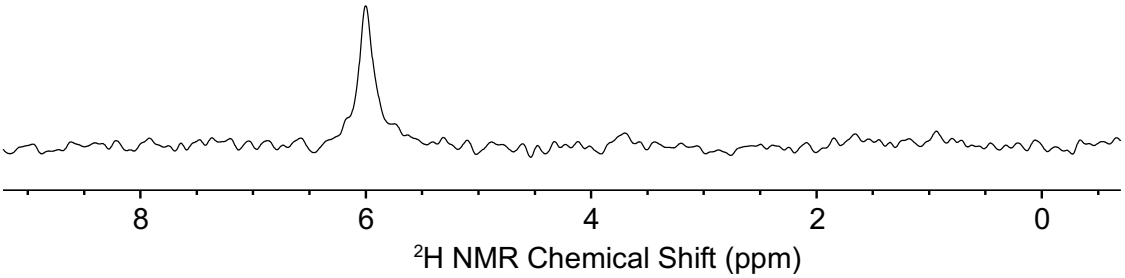

Figure 3.43. ^{2}H NMR of the residual iPP using 2. Recorded at 120 °C in $C_2D_2Cl_4$. A ^{2}H NMR signal for any of the sites in iPP is not observed under these conditions (ns = 13590, d1 = 0.5 s, total experiment time = 6.5 h)

References

1. Peczak, I. L.; Kennedy, R. M.; Hackler, R. A.; Lee, B.; Meirow, M.; Luijten, E.; Poeppelmeier, K. R.; Delferro, M. Treasuring trash: Pt/SrTiO3 catalysts process plastic waste into high-value materials. Matter 2023, 6, 3296–3321.

2.

    a. Celik, G.; Kennedy, R. M.; Hackler, R. A.; Ferrandon, M.; Tennakoon, A.; Patnaik, S.; LaPointe, A. M.; Ammal, S. C.; Heyden, A.; Perras, F. A.; Pruski, M.; Scott, S. L.; Poeppelmeier, K. R.; Sadow, A. D.; Delferro, M. Upcycling Single-Use Polyethylene into HighQuality Liquid Products. ACS Cent. Sci. 2019, 5, 1795–1803.

    b. Rorrer, J. E.; Beckham, G. T.; Román-Leshkov, Y. Conversion of Polyolefin Waste to Liquid Alkanes with Ru-Based Catalysts under Mild Conditions. JACS Au 2021, 1, 8–12.

    c. Wang, C.; Xie, T.; Kots, P. A.; Vance, B. C.; Yu, K.; Kumar, P.; Fu, J.; Liu, S.; Tsilomelekis, G.; Stach, E. A.; Zheng, W.; Vlachos, D. G. Polyethylene Hydrogenolysis at Mild Conditions over Ruthenium on Tungstated Zirconia. JACS Au 2021, 1, 1422–1434.

    d. Hackler, R. A.; Lamb, J. V.; Peczak, I. L.; Kennedy, R. M.; Kanbur, U.; LaPointe, A. M.; Poeppelmeier, K. R.; Sadow, A. D.; Delferro, M. Effect of Macro- and Microstructures on Catalytic Hydrogenolysis of Polyolefins. Macromolecules 2022, 55, 6801–6810.

    e. Kots, P. A.; Liu, S.; Vance, B. C.; Wang, C.; Sheehan, J. D.; Vlachos, D. G. Polypropylene Plastic Waste Conversion to Lubricants over Ru/TiO2 Catalysts. ACS Catal. 2021, 11, 8104–8115.

    f. Rorrer, J. E.; Troyano-Valls, C.; Beckham, G. T.; Román-Leshkov, Y. Hydrogenolysis of Polypropylene and Mixed Polyolefin Plastic Waste over Ru/C to Produce Liquid Alkanes. ACS Sustainable Chem. Eng. 2021, 9, 11661–11666.

3. Review:

    a. Copéret, C.; Estes, D. P.; Larmier, K.; Searles, K. Isolated Surface Hydrides: Formation, Structure, and Reactivity. Chem. Rev. 2016, 116, 8463–8505. Supported Zr–H:

    b. Dufaud, V.; Basset, J.-M. Catalytic Hydrogenolysis at Low Temperature and Pressure of Polyethylene and Polypropylene to Diesels or Lower Alkanes by a

Zirconium Hydride Supported on Silica-Alumina: A Step Toward Polyolefin Degradation by the Microscopic Reverse of Ziegler–Natta Polymerization. Angew. Chem., Int. Ed. 1998, 37, 806– 810.

c. Mason, A. H.; Motta, A.; Das, A.; Ma, Q.; Bedzyk, M. J.; Kratish, Y.; Marks, T. J. Rapid atom-efficient polyolefin plastics hydrogenolysis mediated by a well-defined single-site electrophilic/ cationic organo-zirconium catalyst. Nat. Commun. 2022, 13, 7187. Supported Zr species that react with polymers and AlR3:

d. Kanbur, U.; Zang, G.; Paterson, A. L.; Chatterjee, P.; Hackler, R. A.; Delferro, M.; Slowing, I. I.; Perras, F. A.; Sun, P.; Sadow, A. D. Catalytic carbon-carbon bond cleavage and carbon-element bond formation give new life for polyolefins as biodegradable surfactants. Chem. 2021, 7, 1347–1362. Perspective on supported Ta–H:

e. Basset, J.-M.; Coperet, C.; Soulivong, D.; Taoufik, M.; Cazat, J. T. Metathesis of Alkanes and Related Reactions. Acc. Chem. Res. 2010, 43, 323–334. Ta–H+ supported on sulfated alumina:

f. Gao, J.; Zhu, L.; Conley, M. P. Cationic Tantalum Hydrides Catalyze Hydrogenolysis and Alkane Metathesis Reactions of Paraffins and Polyethylene. J. Am. Chem. Soc. 2023, 145, 4964–4968.

g. Gao, J.; Zhu, L.; Conley, M. P. Polypropylene Degradation Catalyzed by Tantalum Hydrides Supported on Sulfated Alumina. ACS Catal. 2023, 13, 10765–10769.

4. Waterman, R. σ-Bond Metathesis: A 30-Year Retrospective. Organometallics 2013, 32, 7249–7263.

5. O'Reilly, M. E.; Dutta, S.; Veige, A. S. β-Alkyl Elimination: Fundamental Principles and Some Applications. Chem. Rev. 2016, 116, 8105–8145.

6. Alt, H. G.; Köppl, A. Effect of the Nature of Metallocene Complexes of Group IV Metals on Their Performance in Catalytic Ethylene and Propylene Polymerization. Chem. Rev. 2000, 100, 1205–1222.

7. Baier, M. C.; Zuideveld, M. A.; Mecking, S. Post-Metallocenes in the Industrial Production of Polyolefins. Angew. Chem., Int. Ed. 2014, 53, 9722–9744.

8. Bochmann, M. The Chemistry of Catalyst Activation: The Case of Group 4 Polymerization Catalysts. Organometallics 2010, 29, 4711–4740.

9. Grubbs, R. H.; Coates, G. W. α-Agostic Interactions and Olefin Insertion in Metallocene Polymerization Catalysts. Acc. Chem. Res. 1996, 29, 85–93.

10. Coates, G. W. Precise control of polyolefin stereochemistry using single-site metal catalysts. Chem. Rev. 2000, 100, 1223–1252.

11. Resconi, L.; Cavallo, L.; Fait, A.; Piemontesi, F. Selectivity in Propene Polymerization with Metallocene Catalysts. Chem. Rev. 2000, 100, 1253–1346.

12. Amin, S. B.; Marks, T. J. Versatile Pathways for In Situ Polyolefin Functionalization with Heteroatoms: Catalytic Chain Transfer. Angew. Chem., Int. Ed. 2008, 47, 2006–2025.

13. Resconi, L.; Piemontesi, F.; Franciscono, G.; Abis, L.; Fiorani, T. Olefin polymerization at bis(pentamethylcyclopentadienyl)zirconium and -hafnium centers: chain-transfer mechanisms. J. Am. Chem. Soc. 1992, 114, 1025–1032.

14. Sadow, A. D.; Tilley, T. D. Enhanced Reactivity of Cationic Hafnocene Complexes toward σ-Bond Metathesis Reactions. Si–H and Si–C Bond Activations in Stoichiometric and Catalytic Organosilane Conversions. Organometallics 2003, 22, 3577–3585.

15. Culver, D. B.; Dorn, R. W.; Venkatesh, A.; Meeprasert, J.; Rossini, A. J.; Pidko, E. A.; Lipton, A. S.; Lief, G. R.; Conley, M. P. Active Sites in a Heterogeneous Organometallic Catalyst for the Polymerization of Ethylene. ACS Cent. Sci. 2021, 7, 1225–1231.

16.

    a. Witzke, R. J.; Chapovetsky, A.; Conley, M. P.; Kaphan, D. M.; Delferro, M. Non-Traditional Catalyst Supports in Surface Organometallic Chemistry. ACS Catal. 2020, 10, 11822–11840.

    b. Samudrala, K. K.; Conley, M. P. Effects of surface acidity on the structure of organometallics supported on oxide surfaces. Chem. Commun. 2023, 59, 4115–4127.

17. Mu¨ller, L. O.; Himmel, D.; Stauffer, J.; Steinfeld, G.; Slattery, J.; Santiso-Quiñones, G.; Brecht, V.; Krossing, I. Simple Access to the Non-Oxidizing Lewis Superacid PhF→Al(ORF)3 (RF = C(CF3)3). Angew. Chem., Int. Ed. 2008, 47, 7659–7663.

18. Samudrala, K. K.; Huynh, W.; Dorn, R. W.; Rossini, A. J.; Conley, M. P. Formation of a Strong Heterogeneous Aluminum Lewis Acid on Silica. Angew. Chem., Int. Ed. 2022, 61, No. e202205745.

19. Chen, E. Y.-X.; Marks, T. J. Cocatalysts for Metal-Catalyzed Olefin Polymerization: Activators, Activation Processes, and Structure-Activity Relationships. Chem. Rev. 2000, 100, 1391−1434.

20. Popoff, N.; Gauvin, R. M.; De Mallmann, A.; Taoufik, M. On the Fate of Silica-Supported Half-Metallocene Cations: Elucidating a Catalyst's Deactivation Pathways. Organometallics 2012, 31, 4763− 4768.

21.

    a. Tynys, A.; Fonseca, I.; Parkinson, M.; Resconi, L. Quantitative 13C NMR Analysis of Isotactic Ethylene−Propylene Copolymers Prepared with Metallocene Catalyst: Effect of Ethylene on Polymerization Mechanisms. Macromolecules 2012, 45, 7704− 7710.

    b. Cheng, H. N.; Smith, D. A. Carbon-13 NMR studies of lowmolecular-weight ethylene-propylene copolymers and characterization of polymer chain ends. Macromolecules 1986, 19, 2065−2072.

22. Based on reactivity trends of d0 organometallics with H2 in solution this reaction should be suppressed as the pH2 increases. The data shown in Table 1 (Entries 4 and 5) do not show an obvious effect of pH2 in terms of yield of isolated oil. Speciation of well defined d0 M−R or M−H (Figure 3.1a) under hydrogenolysis reaction conditions has not been determined experimentally, but data presented in ref 3c show that hydrogenolysis of hexadecane is zero order in H2. Studies to determine how 1 evolves under alkane hydrogenolysis conditions are ongoing.

23.

    a. Stoebenau, E. J.; Jordan, R. F. Alkyne and Alkene Complexes of a d0 Zirconocene Aryl Cation. J. Am. Chem. Soc. 2004, 126, 11170−11171.

    b. Peng, T. S.; Gladysz, J. A. Mechanism of equilibration of diastereomeric chiral rhenium alkene complexes of the formula [(C5H5)Re(NO)(PPh3)(H2C=CHR)]+ BF4 - . The metal traverses between alkene enantiofaces without dissociation! J. Am. Chem. Soc. 1992, 114, 4174−4181.

24.

    a. Yoder, J. C.; Bercaw, J. E. Chain Epimerization during Propylene Polymerization with Metallocene Catalysts: Mechanistic Studies Using a Doubly Labeled Propylene. J. Am. Chem. Soc. 2002, 124, 2548−2555.

    b. Sillars, D. R.; Landis, C. R. Catalytic Propene Polymerization: Determination of Propagation, Termination, and Epimerization Kinetics by Direct NMR

Observation of the (EBI)Zr- (MeB(C6F5)3)propenyl Catalyst Species. J. Am. Chem. Soc. 2003, 125, 9894–9895.

25. Sun, J.; Lee, Y.-H.; Yappert, R. D.; LaPointe, A. M.; Coates, G. W.; Peters, B.; Abu-Omar, M. M.; Scott, S. L. Bifunctional tandem catalytic upcycling of polyethylene to surfactant-range alkylaromatics. Chem. 2023, 9, 2318–2336.

26. Zirconocene dichlorides react with Ali Bu3 to form organozirconium species that mediate chain scission in cis-1,4-polybutadiene: Cannavacciuolo, F. D.; Yadav, R.; Esper, A.; Vittoria, A.; Antinucci, G.; Zaccaria, F.; Cipullo, R.; Budzelaar, P. H. M.; Busico, V.; Goryunov, G. P.; Uborsky, D. V.; Voskoboynikov, A. Z.; Searles, K.; Ehm, C.; Veige, A. S. A High-Throughput Approach to Repurposing Olefin Polymerization Catalysts for Polymer Upcycling. Angew. Chem., Int. Ed. 2022, 61, No. e202202258.

27. Jantunen, K. C.; Scott, B. L.; Kiplinger, J. L. A Comparative Study of the Reactivity of Zr(IV), Hf(IV) and Th(IV) Metallocene Complexes: Thorium Is Not a Group IV Metal after All. *J. Alloys Compd.* 2007, *444–445* (SPEC. ISS.), 363–368. https://doi.org/10.1016/j.jallcom.2007.03.138.

Chapter 4. Formation of Strong Boron Lewis Acid Sites on Silica

Abstract

Bis(1-methyl-*ortho*-carboranyl)borane is a strong Lewis acid that reacts with the isolated silanols present on silica to form the well-defined Lewis site (^{Me}oCb$_2$B)(OSi≡) (**1**) and H_2. $^{11}B\{^1H\}$ MAS NMR data of **1** is consistent with a three-coordinate boron site. Contacting **1** with O=PEt$_3$ (TEPO), and measuring $^{31}P\{^1H\}$ MAS NMR spectra, show that **1** preserves the strong Lewis acidity of HB^{Me}oCb$_2$. Reactions of **1** with Cp$_2$Hf(^{13}CH$_3$)$_2$ show that the Lewis sites are capable of abstracting methide groups from Hf to form [Cp$_2$Hf–^{13}CH$_3$][H$_3{}^{13}$C–B(^{Me}oCb$_2$)OSi≡], but with low efficiency.

Introduction

The interface of materials science and organometallic chemistry is a rich landscape for the development and application of well-defined heterogeneous catalysts for a variety of chemical transformations.[1] This field depends on the discrete understanding of surface sites present on a material, typically a high surface area oxide, and how those sites react with an organometallic. Nearly all oxides are terminated with –OH sites that react with organometallics through protonolysis reactions, shown in eq 1 between a generic organometallic and surface hydroxyl to generate either $L_nM–O_X$ or L_nM---O_X ion-pairs (O_X = surface oxygen). The type of surface site formed in this reaction usually depends on the acidity of the surface hydroxyl,[2] which is dependent on the type of oxide used and is often encountered when using less common oxide supports.[3]

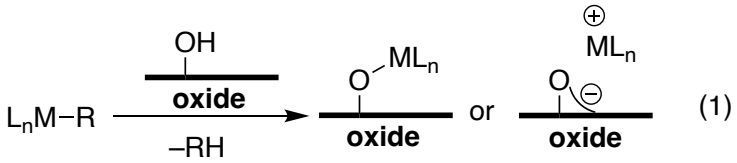

(1)

Alumina (Al_2O_3) is a classic example where the oversimplification shown in eq 1 breaks down. Typical g-Al_2O_3 materials are also terminated with –OH groups, but a small quantity of strong Lewis sites persist on these materials.[4] The Lewis sites play an important role in the formation of catalytically active sites on aluminas, Figure 4.1a. For example, Al_2O_3 dehydrated at 1000 °C reacts with $Cp^*_2Th(CH_3)_2$ (Cp^* = pentamethylcyclopentadienyl) to generate $[Cp^*_2Th–CH_3][H_3C–AlO_X]$ formed by methide abstraction by Lewis acidic Al-sites.[5] Lower dehydroxylation temperatures also preserve this type of reactivity, exemplified by the reaction of Al_2O_3 partially dehydroxylated at 500 °C with $Zr(CH_2{}^tBu)_4$ to form $[Zr(CH_2{}^tBu)(O_X)_2][{}^tBuH_2C–AlO_X]$.[6] Both results are related to the reactivity of common olefin polymerization compositions containing metallocenes, AlR_3, and Al_2O_3 that form $[Cp^b_2Zr–H][H–AlO_X]$ ion-pairs (Cp^b = 1-butylcyclopentadienyl).[7]

Each of the examples in Figure 4.1a rely on the exceedingly low surface coverage of the Lewis site present on dehydrated aluminas.[4b] Generating strong Lewis sites on oxides using the reaction shown in eq 1 with alkylaluminum[8,9] or alkylgallium[10] tends to form mixtures of surface species. $Al(OC(CF_3)_3)(PhF)$,[11] a very strong Lewis acid, shows solvent dependent reactivity with silica partially dehydroxylated at 700 °C ($SiO_{2\text{-}700}$) shown in Figure 4.1b. In *perfluorohexane* $Al(OC(CF_3)_3)(PhF)$ reacts with the isolated silanols present on $SiO_{2\text{-}700}$ to form Brønsted acidic bridging silanols that behave as

weakly coordination anions when deprotonated.[12] In *fluorobenzene* $Al(OC(CF_3)_3)(PhF)$ reacts with $SiO_{2\text{-}700}$ in the more traditional manner shown in eq 1.[13] These aluminum sites participate in similar alkyl abstraction reactions as those shown in Figure 4.1.[13-14]

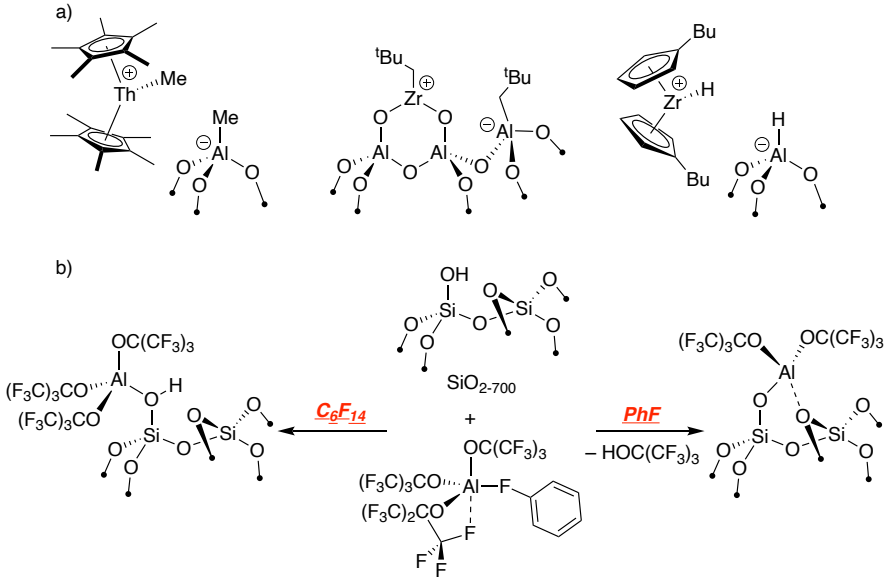

Figure 4.1. Representative examples of ion-pairs formed on Al_2O_3.

Access to oxides containing boron Lewis sites continues to be challenging. Common boric acid impregnation methods followed by heat treatment tend to form networks containing mixtures of 3- or 4-coordinate boron from solid-state NMR studies.[15,16] Though lacking strong Lewis acidity many of these materials show interesting reactivity in oxidative dehydrogenation reactions.[17] BCl_3 or BF_3 also react with silica and probably forms poorly defined Lewis sites.[18]

Reactions of trialkylboranes to generate Lewis sites are limited to the examples shown in Figure 4.2a. BEt_3 reacts with partially dehydroxylated silicas and is claimed to

form $Et_2B–OSi\equiv$ from FTIR studies.[19] $B(C_6F_5)_3$, a common strong Lewis acid,[20] forms adducts with $SiO_{2\text{-}700}$ that can be trapped in presence of *N*,*N*-dimethylaniline to form supported anilinium sites,[21,22] but direct protonation by surface silanols to form the Lewis acidic $(C_6F_5)_2B–OSi\equiv$ and C_6F_5H were not observed. Silica dehydrated at 500 °C ($SiO_{2\text{-}500}$) results in the formation of pairs of Lewis sites that involves the adsorbed water on $SiO_{2\text{-}500}$ and forms pairs of $(C_6F_5)_2B–OSi\equiv$.[23] However, these Lewis sites are not sufficiently acidic to abstract methide from $Cp_2Zr(CH_3)_2$. Related species were studied in solution using isolable silsesquioxanes as models for silica surfaces.[24]

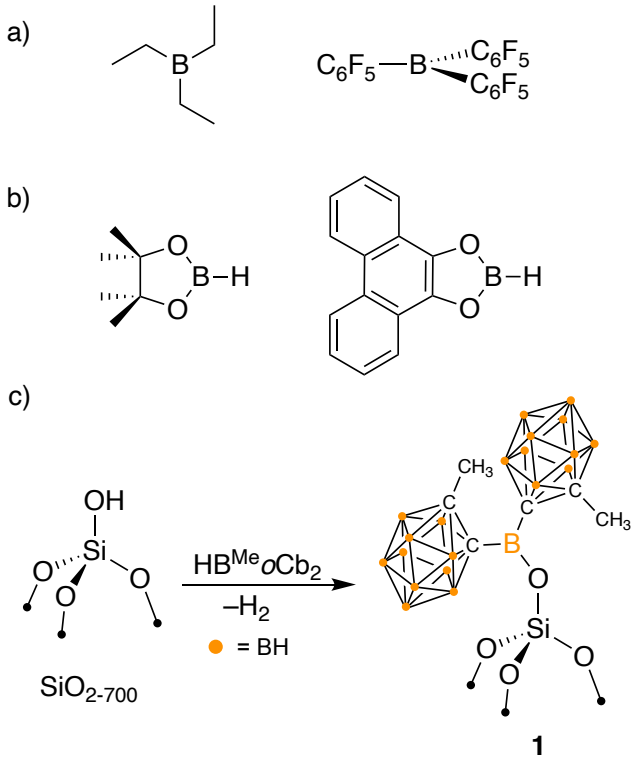

Figure 4.2. BR_3 (a) or HBR_2 (b) reagents used in silica functionalization reactions. The reaction of Bis(1-methyl-*ortho*-carboranyl)borane ($HB^{Me}oCb_2$) with $SiO_{2\text{-}700}$ described in this study (c).

HBR_2 tend to be more reactive towards silica.[25,26] Pinacolborane reacts with silica to form well-defined pinacolborate species that were studied in detail by solid-state NMR spectroscopy.[27] Phenantro[9,10-d][1,3,2]dioxaborole reacts with $SiO_{2\text{-}700}$ either by elimination of H_2 or by protonolysis of a B–O group to form well-defined surface borates.[28] Lewis acidity was not studied in these examples, but $B(OR)_3$ species, even when containing perfluorinated alkoxy groups, are mild Lewis acids.[29]

This paper describes the reaction of Bis(1-methyl-*ortho*-carboranyl)borane ($HB^{Me}oCb_2$)[30] with $SiO_{2\text{-}700}$, Figure 4.2c. $HB^{Me}oCb_2$ is a Lewis superacid, defined as Lewis acids having higher fluoride ion affinity than SbF_5.[29,31] The *ortho*-carboranyl functionalities attached to the central boron act as strong electron withdrawing groups and provide a more congested steric environment around the Lewis acidic boron compared to $–C_6F_5$.[32] In addition, the Lewis acidic p-orbital on boron is highly localized on the central boron atom,[33] which is in contrast to the more delocalized LUMO in $B(C_6F_5)_3$. The data described below shows that the boron sites formed in reactions with silica are very Lewis acidic.

Results and Discussion

In benzene solution $HB^{Me}oCb_2$ reacts with $SiO_{2\text{-}700}$ to form $^{Me}oCb_2B(OSi\equiv)$ (**1**) and H_2 (0.23 mmol g^{-1}). ICP-OES of digested **1** gives 4.77 $mmol_B$ g^{-1} (20.7 B/H_2), which is close to the expected 21:1 ratio from the amount of H_2 evolved in this reaction. Figure 4.3

shows the FTIR of native $SiO_{2\text{-}700}$ and **1**. The n_{OH} for isolated silanols in $SiO_{2\text{-}700}$ decrease significantly in **1**, consistent with the reaction in Figure 4.2c, but unreacted silanols are present. The FTIR of **1** also contains broad n_{OH} at 3686 cm^{-1} suggesting some type of hydrogen bonding interaction with residual silanols and the carborane groups. The spectrum for **1** also contains n_{CH} at 2948 and 2878 cm^{-1} as well as n_{BH} at 2649 and 2589 cm^{-1}.

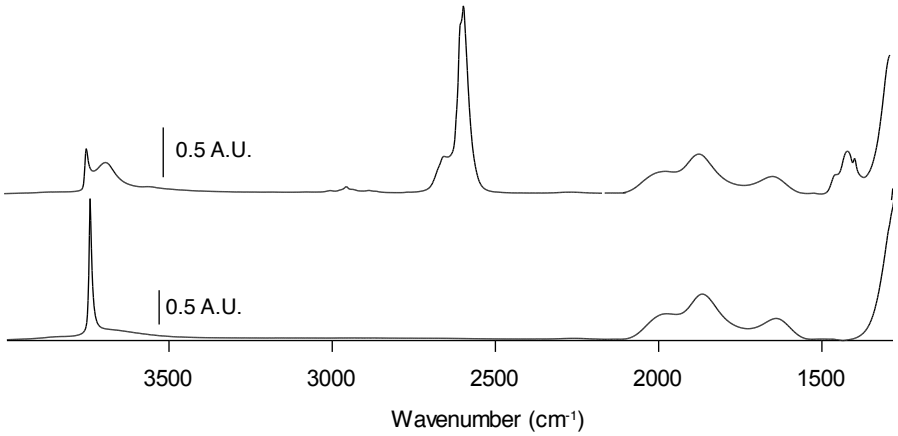

Figure 4.3. FTIR spectra of $SiO_{2\text{-}700}$ (bottom) and **1** (top).

The $^{11}B\{^1H\}$ magic angle spinning (MAS) NMR spectrum of **1** is shown in Figure 4.4. A broad signal centered at 27 ppm is assigned to the central tricoordinate boron. Formation of tricoordinate boron sites is relatively common in boron oxide type materials,[15] and these signals are typically broad due to the larger quadrupolar coupling (C_Q) for tricoordinate boron compared to four-coordinate boron.[34] Available $^{11}B\{^1H\}$ MAS NMR data suggests that supported $B(C_6F_5)_3$ also adopts a tricoordinate structure.[23,35] This is in contrast to the well-defined aluminum Lewis acid supported on silica

mentioned above that forms a tetrahedral aluminum site.[13] The $^{11}B\{^{1}H\}$ MAS NMR spectrum also contains signals at 2, -6, -8, and -11 ppm for the borons that are part of the carborane dodecahedron. The $^{13}C\{^{1}H\}$ cross polarization magic angle spinning (CPMAS) NMR spectrum of **1** contains the expected three signals at 25 ($-CH_3$), 71, and 78 ppm (see the Supporting Information).

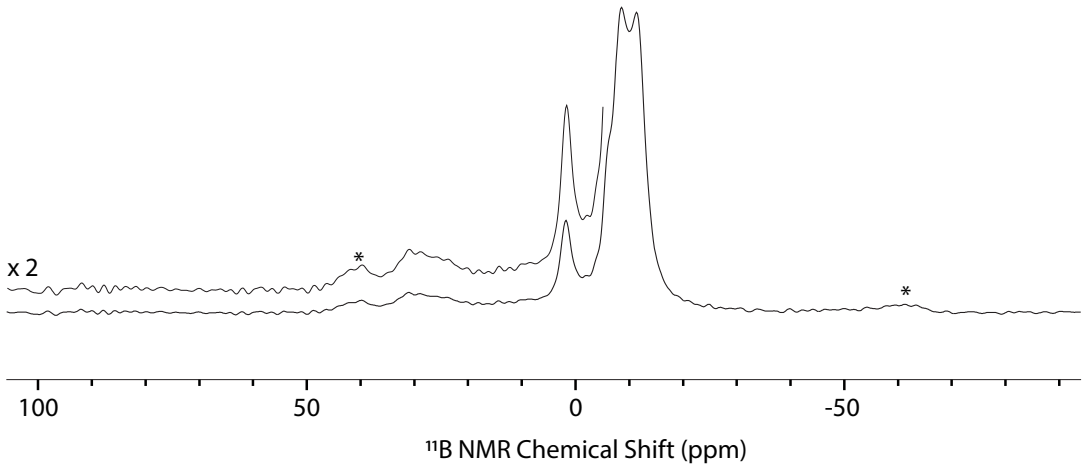

Figure 4.4. $^{11}B\{^{1}H\}$ MAS NMR spectra of **1**. n_{rot} = 10 kHz; * = spinning side band.

The change in $^{31}P\{^{1}H\}$ NMR chemical shift of triethylphosphineoxide (TEPO) is used as a diagnostic probe to determine Lewis acidity in solution[36] or on solids containing Lewis acid sites.[37] Contacting **1** with TEPO (1 equiv/B in **1**) results in formation of the phosphine oxide adduct **1*TEPO**, eq 2. The $^{11}B\{^{1}H\}$ MAS NMR of **1*TEPO** contains a new signal at -1.5 ppm assigned to the tetrahedral central boron. Resonances for the boron atoms of the carborane groups appear at identical positions as in **1**. However, this spectrum also contains the characteristic broad tricoordinate boron signal from **1** at 27 ppm, indicating that some Lewis acidic borons in **1** do not coordinate TEPO. The $^{31}P\{^{1}H\}$

MAS NMR data is consistent with this observation, which contains a signal at 78 (Dd = 28 ppm) and 54 ppm (Dd = 4 ppm), assigned to the adduct and physisorbed TEPO respectively.

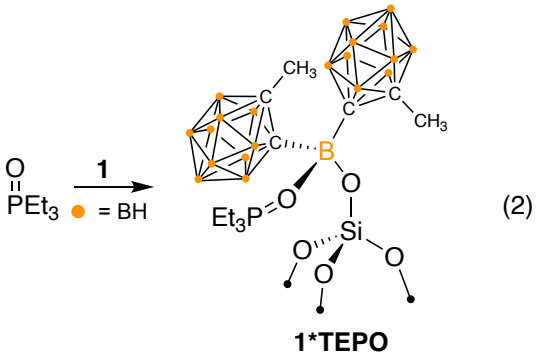

(2)

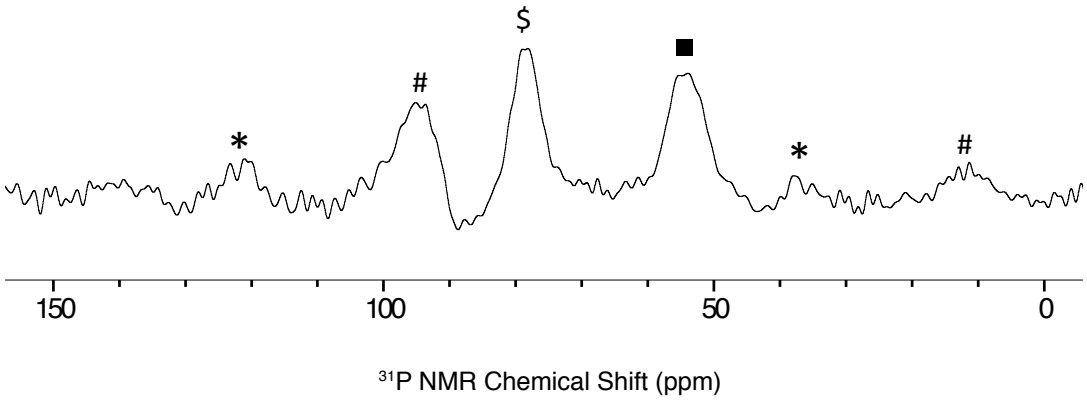

Figure 4.5. $^{31}P\{^{1}H\}$ MAS NMR spectra of **1*TEPO**. n_{rot} = 10 kHz; $ = **1*TEPO**; * = spinning side band for **1*TEPO**; black square = physisorbed TEPO; # = spinning side bands for physisorbed TEPO.

Selected $^{31}P\{^{1}H\}$ NMR data for TEPO adducts are given in Table 1. The $\Delta\delta$ values obtained for **1*TEPO** are similar to those obtained in solution for TEPO adducts of $HB^{Me}oCb_2$ and $B(C_6F_5)_3$, indicating that the accessible boron in **1** is quite Lewis acidic.

These values are identical to that obtained from the TEPO adduct of $[\equiv SiOAl(OR^F)_2(O(Si\equiv)_2)]$ but lower than the $\Delta\delta^{31}P$ for the $[Et_3Si][\mathbf{SZO}]$. The latter surface species is a silylium-like ion, which are very strong Lewis acids that generally have large $\Delta\delta^{31}P$ values.[38] In solution, it is noteworthy that the Gutmann-Beckett method also is unreliable for carboranyl boranes, exemplified with B*o*Cb_3 being measured as less Lewis acidic than $HB^{Me}oCb_2$ with ion affinities and other metrics indicating the opposite.[32] This is due to the steric effects of the carborane groups.

Table 4.1. Selected Δδ 31P{1H} NMR data for TEPO adducts of Lewis acids in solution or supported on oxides.

Compound	Δδ	ref
1	28	This work
$HB^{Me}oCb_2$	35.8 (C_6D_6) 30.0 ($CDCl_3$)	[30]
$B(C_6F_5)_3$	26.6 (CD_2Cl_2)	[39]
$[\equiv SiOAl(OR^F)_2(O(Si\equiv)_2)]$	28	[13]
$[Et_3Si][\mathbf{SZO}]$[a]	43	[40]

[a] – **SZO** = sulfated zirconium oxide.

Methide or hydride abstraction from an organometallic is a quintessential reaction of strong Lewis acid sites on oxides (Figure 4.1). To test if **1** is capable of any degree of methide abstraction we treated the material with $Cp_2Hf(^{13}CH_3)_2$ (Cp = cyclopentadienyl), an organometallic known to react with well-defined aluminum Lewis acid as shown in Figure 4.1b.[14] This reaction results in the formation of CH_4 (0.07 mmol g^{-1}) indicating that $Cp_2Hf(^{13}CH_3)_2$ reacts with the residual silanols present on **1**. Indeed, FTIR data of

$Cp_2Hf(^{13}CH_3)_2$/**1** shown in Figure 4.6a contains a reduced ν_{OH} band for silanols, consistent with their consumption. Also consistent with a surface reaction are the new sp^3 C-H bands in this spectrum. The ν_{BH} band in this material is unperturbed with respect to **1**. ICP-OES analysis of digested material gives 0.076 $mmol_{Hf}$ g^{-1}. This loading is surprisingly close to the amount of CH_4 formed in this reaction, indicating that the major reaction pathway between **1** and $Cp_2Hf(CH_3)_2$ involves silanols that do not react with $HB^{Me}oCb_2$ on $SiO_{2\text{-}700}$ resulting in the common protonolysis reaction shown in eq 1.

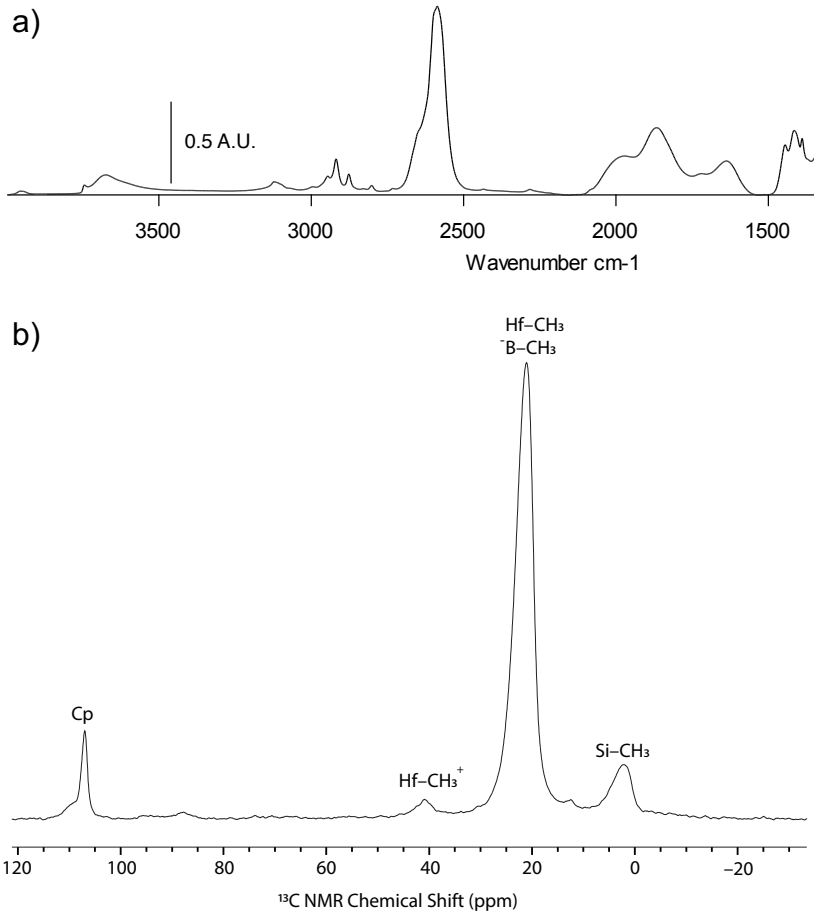

Figure 4.6. FTIR of $Cp_2Hf(^{13}CH_3)_2$/**1** (a). $^{13}C\{^1H\}$ CPMAS NMR spectrum of $Cp_2Hf(^{13}CH_3)_2$/**1**. n_{rot} = 10 kHz (b).

However, the $^{13}C\{^{1}H\}$ CPMAS NMR spectrum of $Cp_2Hf(^{13}CH_3)_2$/**1** shown in Figure 4.5 does lend some support for ionization by Lewis sites. Unsurprisingly, this spectrum contains an intense signal at 21 ppm for a neutral Hf–$^{13}CH_3$ and a major Cp signal at 110 ppm. These results are consistent with formation of $Cp_2Hf(^{13}CH_3)(OSi\equiv)$. This spectrum also contains a minor Cp signal at 113 ppm as well as a signal at 41 ppm for Hf–$^{13}CH_3^+$, consistent with the formation of small amounts of $[Cp_2Hf–^{13}CH_3][H_3{}^{13}C–B(^{Me}oCb_2)OSi\equiv]$. A signal for the $[H_3{}^{13}C–B(^{Me}oCb_2)OSi\equiv]$ was not observed, which could be due to overlap with the Hf–CH_3 signal in $Cp_2Hf(^{13}CH_3)(OSi\equiv)$.[41] The signal at 2 ppm is from ≡Si–$^{13}CH_3$ sites.

The spectral data are consistent with the reactions in Scheme 1. $Cp_2Hf(^{13}CH_3)_2$ preferentially reacts with residual silanols present in **1** to form $Cp_2Hf(^{13}CH_3)(OSi\equiv)$ and methane. $Cp_2Hf(^{13}CH_3)_2$ also reacts with the boron Lewis sites in **1** to form $[Cp_2Hf–^{13}CH_3][H_3{}^{13}C–B(^{Me}oCb_2)OSi\equiv]$. Reactive d^0 organometallic cations are known to react with silica surfaces by opening of Si–O–Si bridges by transferring alkyl groups and forming ≡Si–$^{13}CH_3$,[42] which is consistent with the formation of **3**.

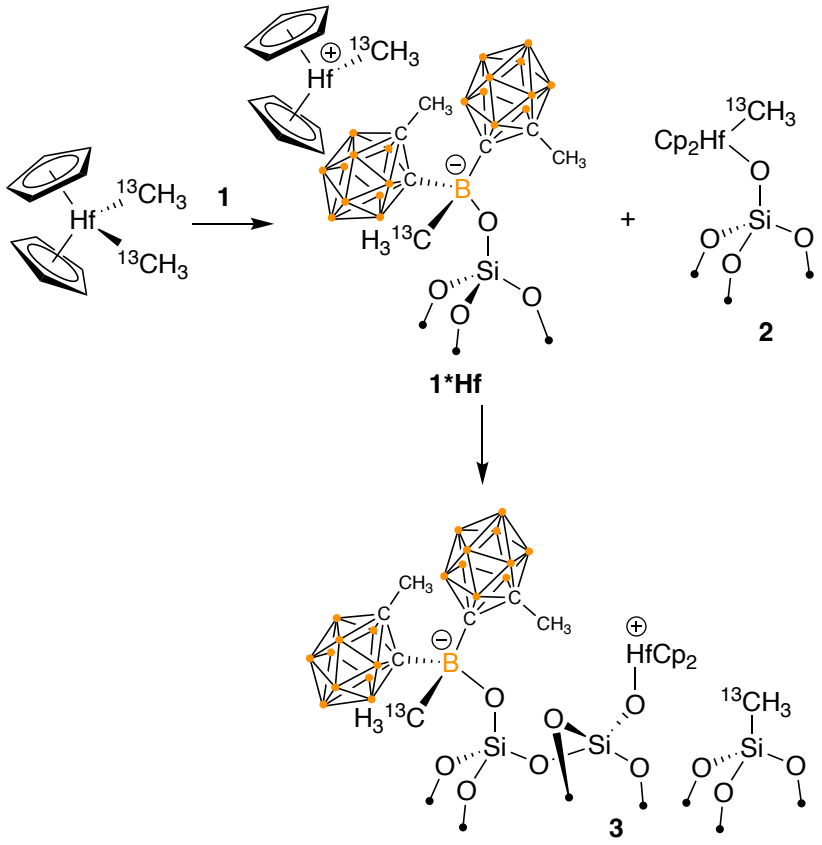

Scheme 4.1. Reaction **1** with $Cp_2Hf(^{13}CH_3)_2$.

In a qualitative sense, the reactivity in Scheme 1 is remarkably similar to that obtained previously between $Al(OC(CF_3)_3)(PhF)$/silica and either $Cp_2Zr(CH_3)_2$[13] or $Cp_2Hf(CH_3)_2$.[14] However, **1** clearly forms less $Hf–CH_3^+$ than $Al(OC(CF_3)_3)(PhF)$/silica. Attempts to quantify the amount of $[Cp_2Hf–^{13}CH_3][H_3C^{13}–B(^{Me}oCb_2)OSi\equiv]$ formed on **1** using vinyl chloride as an active site probe by quantification of evolved propylene[43] were consistent with very low surface coverage of the ion-pair (~0.002 mmol g^{-1}, see the materials and methods section for details). The data provided in Table 1 show that both **1** and $Al(OC(CF_3)_3)(PhF)$/silica have similar Lewis acidity, based on $\Delta\delta$ ^{31}P NMR

measurements of TEPO adducts. This suggests that the sterically bulky carborane groups may be restricting access to the central boron site in **1**, which results in low $Hf–CH_3^+$ surface coverage.

Conclusions

There are limited examples showing that reactions of boranes and silica (or other oxides) form well-defined products, and even fewer examples that form strong Lewis sites. Monomeric $HB^{Me}oCb_2$ is a rare example where a well-defined three-coordinate boron site forms when contacted with silica and the strong Lewis acidity is preserved. This promising result suggests that other bulky secondary boranes may also react with oxides to form well-defined Lewis acid sites on oxides. Tuning the steric environment in related boranes should result in more efficient methide abstraction chemistry. However, this comes with the caveat that Lewis acidic boranes that would produce a more sterically open boron site often engage in monomer-dimer equilibria,[44] which may affect the products obtained during surface functionalization chemistry.

Materials and Methods

General Considerations

All manipulations were performed under an inert atmosphere of dinitrogen or argon using standard Schlenk or glovebox techniques. Benzene-d_6 was purchased from Cambridge Isotope Laboratories, dried over sodium/benzophenone, degassed by freeze-

pump-thaw cycles, distilled under vacuum, and stored in an inert atmosphere glovebox. FTIR spectra were recorded in transmission mode as pressed pellets using a Bruker Alpha IR spectrometer in an argon-filled glovebox. $HB^{Me}oCb_2$ was prepared according to literature procedures.[30] All solid-state NMR samples were packed in 4 mm zirconia rotors and sealed with a Kel-F cap under an argon or dinitrogen atmosphere in a glovebox. Solid state NMR spectra were recorded under magic angle spinning or under static conditions at 14.1 T using Bruker NEO600 spectrometer. All solid-state NMR processing used Bruker Topspin.

*Synthesis of **1**.* $SiO_{2\text{-}700}$ (0.5g, 0.13 mmol OH) and $HB^{Me}oCb_2$ (0.040 g, 0.13 mmol, 1.0 mol eq) were transferred to one arm of a double-Schlenk flask inside an argon-filled glovebox. The flask was removed from the glovebox, connected to a high vacuum line, and evacuated for 5 min. Benzene (~ 6 mL) was condensed onto the solids at 77 K. The mixture warmed to room temperature and stirred for 30 min. During this time the mixture was stirred gently to promote mixing and prevent the compacted silica from breaking into smaller fragments. After this time the clear colorless solution was filtered away from **1** to the other side of the double Schlenk. The arm of the double Schlenk containing **1** was cooled to 0˚C, causing benzene on the other side of the flask to condense onto the solid. The benzene was warmed to 25˚C, stirred for 5 min, and filtered back to the other side of the double Schlenk. This procedure was repeated two more times to wash any residual $HB^{Me}oCb_2$ away from **1**. The volatiles from the reaction mixture were analyzed by GC-TCD (Figure 7) resulting in 0.23 mmol H_2/g SiO_2. **1** was dried under vacuum for 40 minutes. The white H-BSO solid was stored in an Ar glovebox freezer at -20˚C. ICP-OES

of **1** after digestion in 5% nitric acid solution gives 4.77 $mmol_B$ g^{-1}. $^{13}C\{^1H\}$ CPMAS NMR data: 25 (≡Si-O–B(**Me***o*Cb)$_2$), 71 and 78 ppm (≡Si-O–B(Me*o***Cb**)$_2$). $^{11}B\{^1H\}$ MAS NMR data: 27, 2, -6, -8, and -11 ppm, respectively.

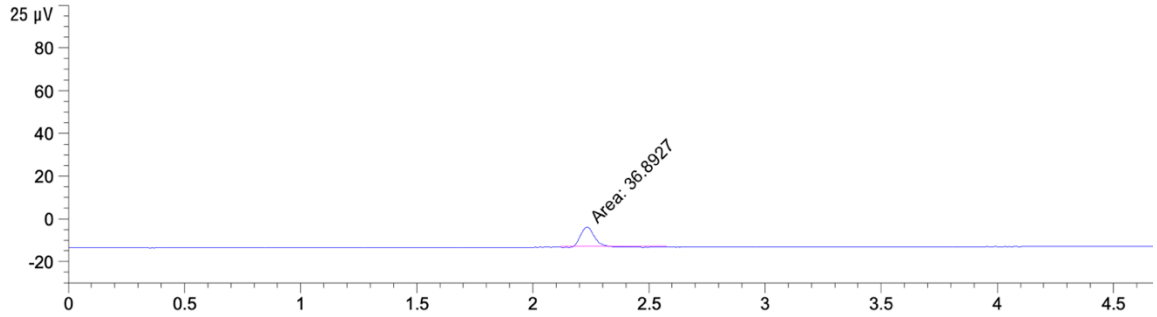

Figure 4.7. GC-TCD of grafting volatiles from **H-BSO**, 0.23 mmol H_2/g SiO_2.

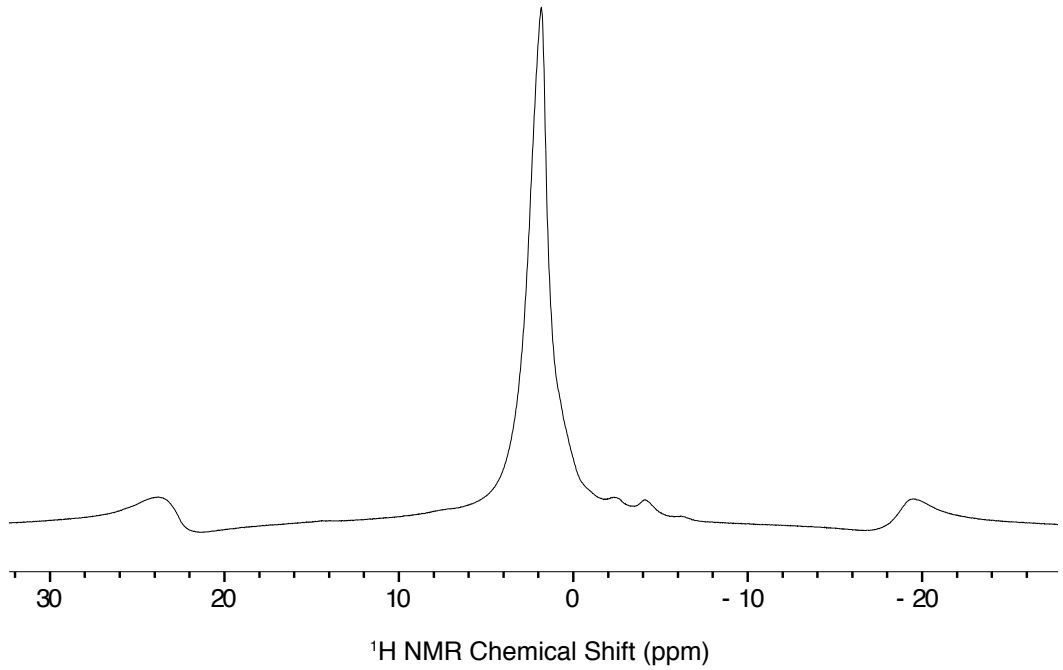

Figure 4.8. 12.5kHz ^1H MAS NMR of **1** acquired at room temperature, 1.86 ppm (≡Si-O–B(**Me***o*Cb)$_2$). Signals at -2.4 ppm and -4.1 ppm are from probe background.

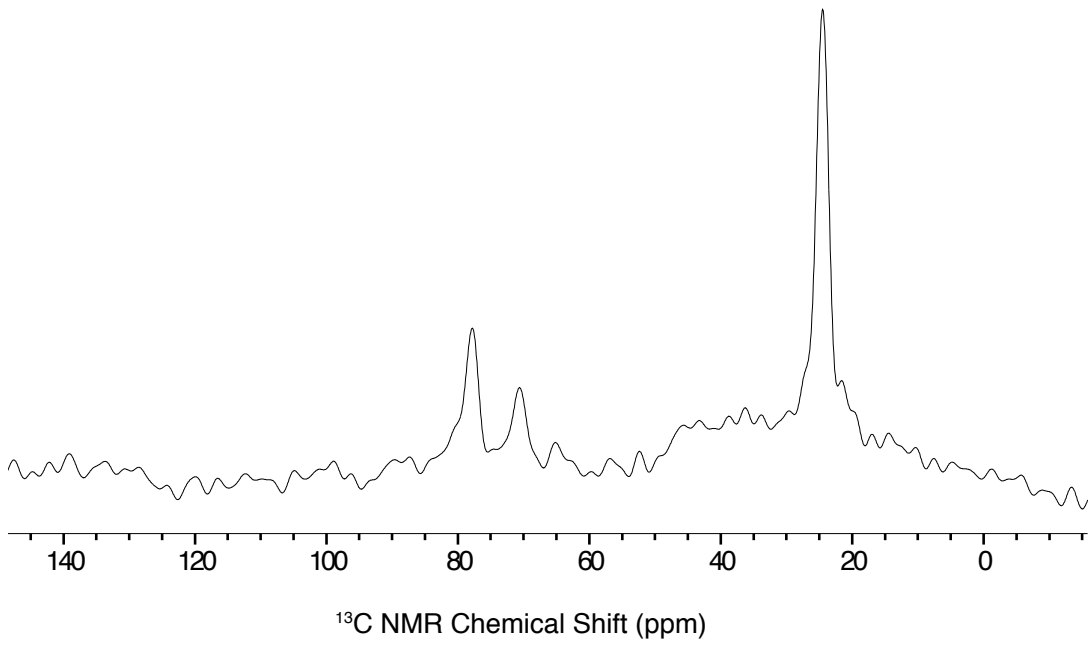

Figure 4.9. 10 kHz ^{13}C CPMAS NMR of **1** acquired at room temperature containing signals at 24.6 ppm (≡Si-O-B(**Me***o*Cb)$_2$), 70.8 and 77.8 ppm (≡Si-O-B(Me*o***Cb**)$_2$).

*Synthesis of **1*TEPO.*** An essentially identical procedure for **1** was used to generate **1*TEPO**. **1** (0.2 g, 0.046 mmol Lewis acidic B) and triethylphosphine oxide (TEPO) (0.005 g, 0.9 eq, 0.041 mmol) and pentane (~ 5 mL) were used in this procedure. **1*TEPO** was collected as a white solid and was stored in an Ar glovebox freezer at -20 ˚C. $^{31}P\{^1H\}$ MAS NMR data: 78 ppm (1*TEPO and 54 ppm (physisorbed TEPO).$^{11}B\{^1H\}$ MAS NMR data: 30.6 ppm (≡Si-O-B(MeoCb)$_2$), -1.5 ppm ((≡Si-O-**B**(MeoCb)$_2$(TEPO)) -11‾-6 ppm and 1.9 ppm (≡Si-O-B(MeoCb)$_2$).

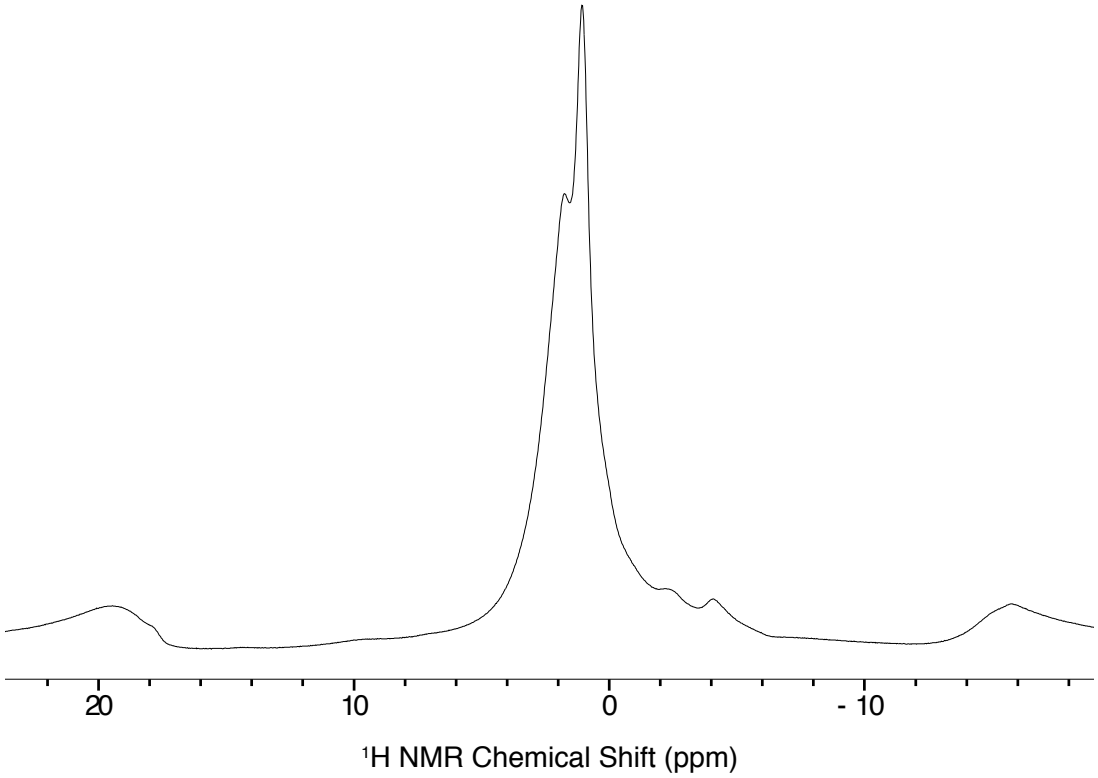

Figure 4.10. 10kHz 1H MAS NMR of 1*TEPO acquired at room temperature containing signals at 1.1 ppm (CH3CH2)3P=O) 1.7 ppm (CH3CH2)3P=O). Signals at -2.4 ppm and -4.1 ppm are from probe background.

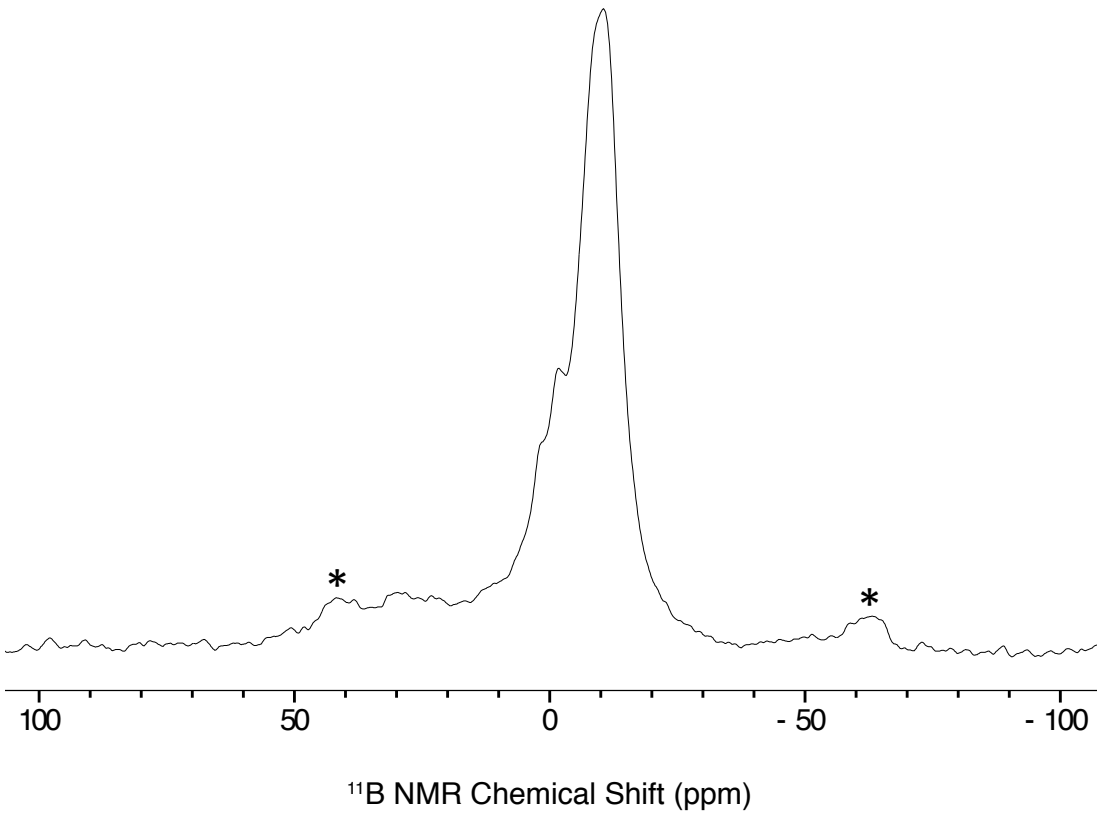

Figure 4.11. 10kHz MAS Hahn echo ^{11}B NMR of **1*TEPO** acquired at room temperature containing sigals at 27 ppm (≡Si-O-**B**(Me*o*Cb)$_2$), -1.5 ppm (**1*TEPO**). The signals from -11 to -6 ppm are from the carborane. Spinning sidebands labeled with an asterisk (*)

*Synthesis of **1*Hf.*** An essentially identical procedure for **1** was used to generate **1*Hf**. **1** (0.100 g, 0.023 mmol Lewis acidic B) and $Cp_2Hf(^{13}CH_3)_2$ (0.009 g, 1.1 eq, 0.025 mmol) and pentane (~ 5 mL) were used in this procedure. **1*Hf** was collected as a white solid and was stored in an Ar glovebox freezer at -20 ˚C. The volatiles from the reaction mixture were analyzed by GC resulting in 0.07 mmol CH_4/g SiO_2. ICP-OES of 1 after digestion in 5% nitric acid solution gives 0.076 $mmol_{Hf}$ g^{-1} and 5.03 $mmol_B$ g^{-1}. $^{13}C\{^1H\}$ CPMAS NMR data: 107.2 ppm (Cp), 40.8 ppm (Hf-$^{13}CH_3$ cation), 21.4 ppm (Hf-$^{13}CH_3$

neutral), 2.2 ppm (Si-$^{13}CH_3$). $^{11}B\{^1H\}$ MAS NMR data: 32 ppm (≡Si-O-**B**(Me*o*Cb)$_2$), 3.0 ppm (≡Si-O-**B**(CH_3)(Me*o*Cb)$_2$), -11 – -6 ppm (≡Si-O-B(Me*o***Cb**)$_2$),

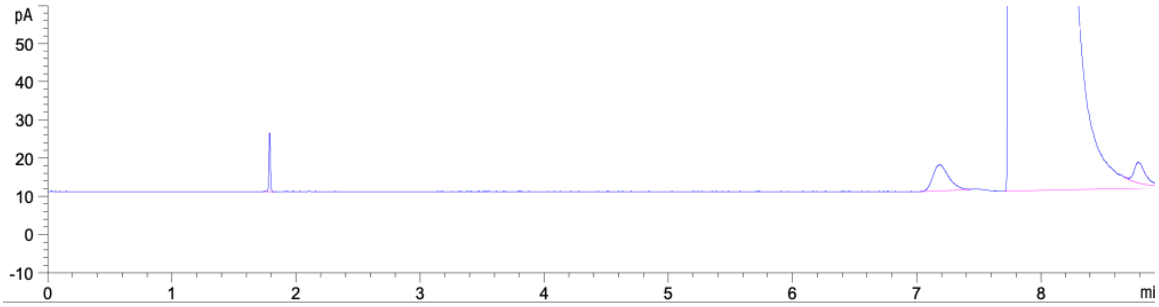

Figure 4.12. GC-FID of volatiles released during grafting of Cp2HfMe2 on **1**, 0.07 mmol CH4/g SiO2

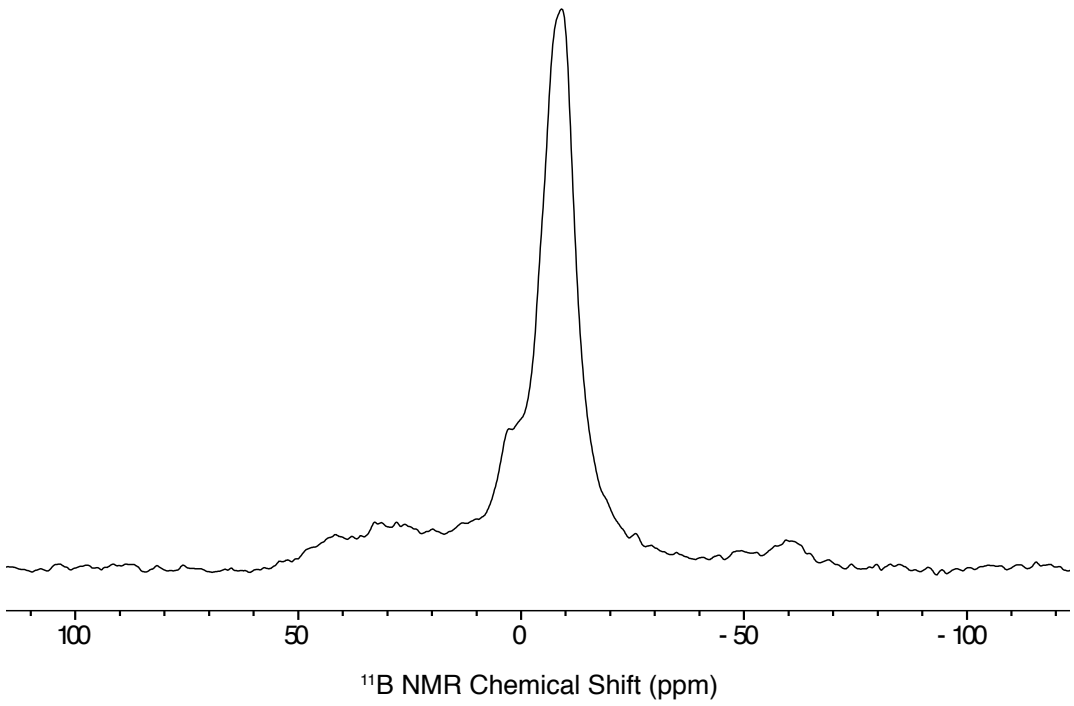

Figure 4.13. 10kHz MAS Hahn echo ^{11}B NMR of **1*Hf.** Spinning sidebands denoted by the asterisk (*)

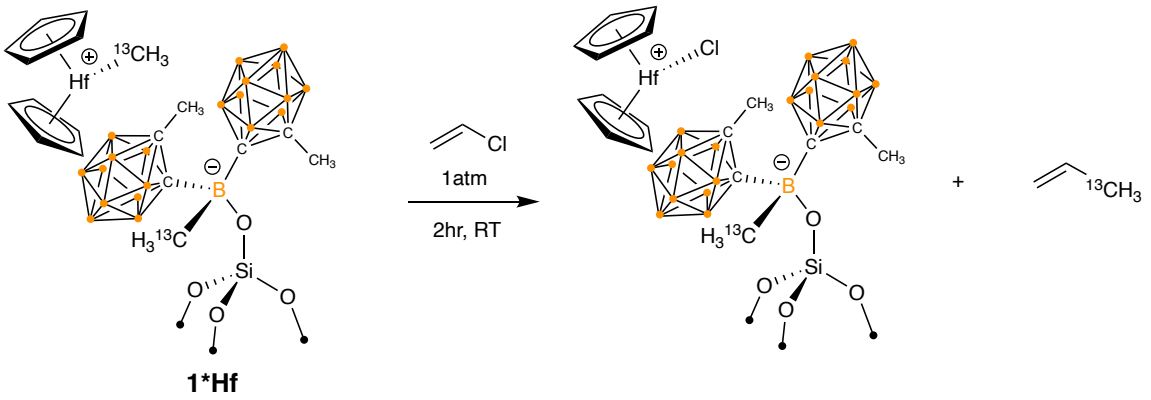

Reaction of Vinyl Chloride with 1*Hf: 0.100 g **1*Hf** was transferred into a 100mL round bottom flask fitted with a Teflon tap fitted high vacuum adapter an argon-filled glovebox. The flask was removed from the glovebox, connected to a high vacuum line, and evacuated for 5 min. 1 atm of vinyl chloride, dried rigorously over molecular sieves and freshly generated BASF copper catalysts to remove water and oxygen, was added to the flask. The flask was left at room temperature for 2 hours. The volatiles were quantified by GC-FID, showing that 0.002 mmol propylene/g SiO_2 are released during this reaction.

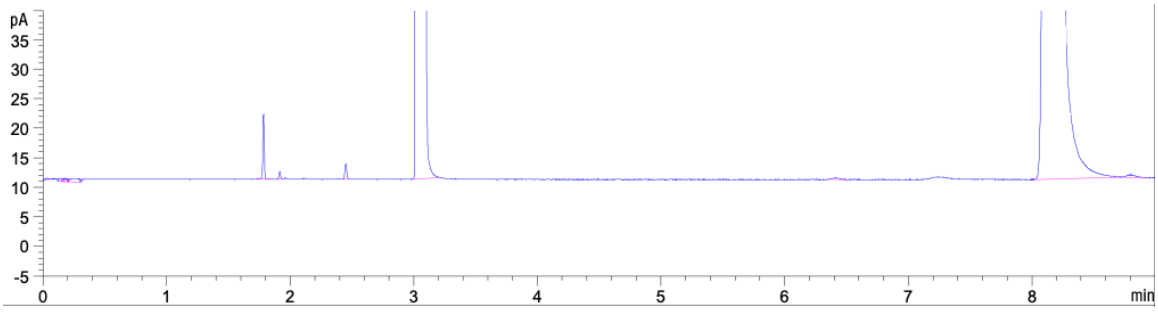

Figure 4.14. GC-FID of volatiles released after contacting vinyl chloride with Hf/H-BSO, 0.002 mmol propylene/g SiO_2

References

1.

   a. Copéret, C.; Allouche, F.; Chan, K. W.; Conley, M. P.; Delley, M. F.; Fedorov, A.; Moroz, I. B.; Mougel, V.; Pucino, M.; Searles, K.; Yamamoto, K.; Zhizhko, P. A. Bridging the Gap between Industrial and Well-Defined Supported Catalysts. *Angew. Chem., Int. Ed.* **2018**, *57*, 6398-6440.

   b. Copéret, C.; Comas-Vives, A.; Conley, M. P.; Estes, D. P.; Fedorov, A.; Mougel, V.; Nagae, H.; Núñez-Zarur, F.; Zhizhko, P. A. Surface Organometallic and Coordination Chemistry toward Single-Site Heterogeneous Catalysts: Strategies, Methods, Structures, and Activities. *Chem. Rev.* **2016**, *116*, 323-421.

   c. Zaera, F. Designing Sites in Heterogeneous Catalysis: Are We Reaching Selectivities Competitive With Those of Homogeneous Catalysts? *Chem. Rev.* **2022**, *122*, 8594-8757; d) Stalzer, M.; Delferro, M.; Marks, T. Supported Single-Site Organometallic Catalysts for the Synthesis of High-Performance Polyolefins. *Catal. Lett.* **2015**, *145*, 3-14.

2. Samudrala, K. K.; Conley, M. P. Effects of surface acidity on the structure of organometallics supported on oxide surfaces. *Chem. Commun.* **2023**, *59*, 4115-4127.

3. Witzke, R. J.; Chapovetsky, A.; Conley, M. P.; Kaphan, D. M.; Delferro, M. Non-Traditional Catalyst Supports in Surface Organometallic Chemistry. *ACS Catal.* **2020**, 11822-11840.

4.

   a. Khivantsev, K.; Jaegers, N. R.; Kwak, J.-H.; Szanyi, J.; Kovarik, L. Precise Identification and Characterization of Catalytically Active Sites on the Surface of γ-Alumina. *Angew. Chem., Int. Ed.* **2021**, *60*, 17522-17530.

   b. Wischert, R.; Copéret, C.; Delbecq, F.; Sautet, P. Optimal Water Coverage on Alumina: A Key to Generate Lewis Acid–Base Pairs that are Reactive Towards the C-H Bond Activation of Methane. *Angew. Chem., Int. Ed.* **2011**, *50*, 3202-3205.

5.

   a. Marks, T. J. Surface-bound metal hydrocarbyls. Organometallic connections between heterogeneous and homogeneous catalysis. *Acc. Chem. Res.* **1992**, *25*, 57-65.

   b. Toscano, P. J.; Marks, T. J. Supported organoactinides. High-resolution solid-state carbon-13 NMR studies of catalytically active, alumina-bound

pentamethylcyclopentadienyl)thorium methyl and hydride complexes. *J. Am. Chem. Soc.* **1985**, *107*, 653-659.

6. Joubert, J.; Delbecq, F.; Sautet, P.; Roux, E. L.; Taoufik, M.; Thieuleux, C.; Blanc, F.; Copéret, C.; Thivolle-Cazat, J.; Basset, J.-M. Molecular Understanding of Alumina Supported Single-Site Catalysts by a Combination of Experiment and Theory. *J. Am. Chem. Soc.* **2006**, *128*, 9157-9169.

7. Culver, D. B.; Dorn, R. W.; Venkatesh, A.; Meeprasert, J.; Rossini, A. J.; Pidko, E. A.; Lipton, A. S.; Lief, G. R.; Conley, M. P. Active Sites in a Heterogeneous Organometallic Catalyst for the Polymerization of Ethylene. *ACS Cent. Sci.* **2021**, *7*, 1225-1231.

8.
    a. Kerber, R. N.; Kermagoret, A.; Callens, E.; Florian, P.; Massiot, D.; Lesage, A.; Copéret, C.; Delbecq, F. ß.; Rozanska, X.; Sautet, P. Nature and Structure of Aluminum Surface Sites Grafted on Silica from a Combination of High-Field Aluminum-27 Solid-State NMR Spectroscopy and First-Principles Calculations. *J. Am. Chem. Soc.* **2012**, *134*, 6767-6775.

    b. Kermagoret, A.; Kerber, R. N.; Conley, M. P.; Callens, E.; Florian, P.; Massiot, D.; Coperet, C.; Delbecq, F.; Rozanska, X.; Sautet, P. Triisobutylaluminum: bulkier and yet more reactive towards silica surfaces than triethyl or trimethylaluminum. *Dalton Trans.* **2013**, *42*, 12681-12687.

    c. Kermagoret, A.; Kerber, R. N.; Conley, M. P.; Callens, E.; Florian, P.; Massiot, D.; Delbecq, F. ß.; Rozanska, X.; Coperet, C.; Sautet, P. Chlorodiethylaluminum supported on silica: A dinuclear aluminum surface species with bridging Œº2-Cl-ligand as a highly efficient co-catalyst for the Ni-catalyzed dimerization of ethene. *J. Catal.* **2014**, *313*, 46-54.

9. An exception to this trend is the reaction of $Al^{i}Bu_3$ with SiO_2 in Et_2O, which forms a well-defined alkylaluminum site. However, the Lewis acidity of this organoaluminum site was not reported. See: Pelletier, J.; Espinas, J.; Vu, N.; Norsic, S.; Baudouin, A.; Delevoye, L.; Trébosc, J.; Le Roux, E.; Santini, C.; Basset, J.-M.; Gauvin, R. M.; Taoufik, M. A well-defined silica-supported aluminium alkyl through an unprecedented, consecutive two-step protonolysis–alkyl transfer mechanism. *Chem. Commun.* **2011**, *47*, 2979-2981.

10.
    a. Szeto, K. C.; Jones, Z. R.; Merle, N.; Rios, C.; Gallo, A.; Le Quemener, F.; Delevoye, L.; Gauvin, R. M.; Scott, S. L.; Taoufik, M. A Strong Support Effect in Selective Propane Dehydrogenation Catalyzed by Ga(i-Bu)3 Grafted onto γ-Alumina and Silica. *ACS Catal.* **2018**, *8*, 7566-7577.

b. Fleischman, S. D.; Scott, S. L. Evidence for the Pairwise Disposition of Grafting Sites on Highly Dehydroxylated Silicas via Their Reactions with Ga(CH3)3. *J. Am. Chem. Soc.* **2011**, *133*, 4847-4855.

c. Taha, Z. A.; Deguns, E. W.; Chattopadhyay, S.; Scott, S. L. Formation of Digallium Sites in the Reaction of Trimethylgallium with Silica. *Organometallics* **2006**, *25*, 1891-1899.

11. Müller, L. O.; Himmel, D.; Stauffer, J.; Steinfeld, G.; Slattery, J.; Santiso-Quiñones, G.; Brecht, V.; Krossing, I. Simple Access to the Non-Oxidizing Lewis Superacid PhF→Al(ORF)3 (RF=C(CF3)3). *Angew. Chem., Int. Ed.* **2008**, *47*, 7659-7663.

12. Culver, D. B.; Venkatesh, A.; Huynh, W.; Rossini, A. J.; Conley, M. P. Al(ORF)3 (RF = C(CF3)3) activated silica: a well-defined weakly coordinating surface anion. *Chem. Sci.* **2020**, *11*, 1510 - 1517.

13. Samudrala, K. K.; Huynh, W.; Dorn, R. W.; Rossini, A. J.; Conley, M. P. Formation of a Strong Heterogeneous Aluminum Lewis Acid on Silica. *Angew. Chem., Int. Ed.* **2022**, *61*, e202205745.

14. Samudrala, K. K.; Conley, M. P. A Supported Ziegler-Type Organohafnium Site Metabolizes Polypropylene. *J. Am. Chem. Soc.* **2023**.

15.

a. Sato, S.; Kuroki, M.; Sodesawa, T.; Nozaki, F.; Maciel, G. E. Surface structure and acidity of alumina-boria catalysts. *J. Mol. Catal. A: Chem.* **1995**, *104*, 171-177.

b. Altvater, N. R.; Dorn, R. W.; Cendejas, M. C.; McDermott, W. P.; Thomas, B.; Rossini, A. J.; Hermans, I. B-MWW Zeolite: The Case Against Single-Site Catalysis. *Angew. Chem., Int. Ed.* **2020**, *59*, 6546-6550.

c. Lu, W.-D.; Wang, D.; Zhao, Z.; Song, W.; Li, W.-C.; Lu, A.-H. Supported Boron Oxide Catalysts for Selective and Low-Temperature Oxidative Dehydrogenation of Propane. *ACS Catal.* **2019**, *9*, 8263-8270.

d. Love, A. M.; Thomas, B.; Specht, S. E.; Hanrahan, M. P.; Venegas, J. M.; Burt, S. P.; Grant, J. T.; Cendejas, M. C.; McDermott, W. P.; Rossini, A. J.; Hermans, I. Probing the Transformation of Boron Nitride Catalysts under Oxidative Dehydrogenation Conditions. *J. Am. Chem. Soc.* **2019**, *141*, 182-190.

16. B-OMe site on silica are proposed to decompose to B-H species, see: Morterra, C.; Low, M. J. D. Surface boranes on boria–silica. A method for producing surface

hydride species. *Journal of the Chemical Society D: Chemical Communications* **1969**, 862a-862a.

17.

a. Grant, J. T.; Carrero, C. A.; Goeltl, F.; Venegas, J.; Mueller, P.; Burt, S. P.; Specht, S. E.; McDermott, W. P.; Chieregato, A.; Hermans, I. Selective oxidative dehydrogenation of propane to propene using boron nitride catalysts. *Science* **2016**, *354*, 1570-1573.

b. Venegas, J. M.; Zhang, Z.; Agbi, T. O.; McDermott, W. P.; Alexandrova, A.; Hermans, I. Why Boron Nitride is such a Selective Catalyst for the Oxidative Dehydrogenation of Propane. *Angew. Chem., Int. Ed.* **2020**, *59*, 16527-16535.

18.

a. Bermudez, V. M. Infrared study of boron trichloride chemisorbed on silica gel. *J. Phys. Chem.* **1971**, *75*, 3249-3257.

b. Morrow, B. A.; Devi, A. Reactions of silica surfaces with boron halides. *Journal of the Chemical Society D: Chemical Communications* **1971**, 1237-1238.

19. Blitz, J. P.; Christensen, J. M.; Deakyne, C. A.; Gun'ko, V. M. Silica Surface Modification Reactions with Aluminum and Boron Alkyls and (Alkyl)Chlorides: Reactivities and Surface Nanostructures. *J. Nanosci. Nanotechnol.* **2008**, *8*, 660-666.

20.

a. Stephan, D. W.; Erker, G. Frustrated Lewis Pair Chemistry: Development and Perspectives. *Angew. Chem., Int. Ed.* **2015**, *54*, 6400-6441.

b. Chen, E. Y.-X.; Marks, T. J. Cocatalysts for Metal-Catalyzed Olefin Polymerization: Activators, Activation Processes, and Structure-Activity Relationships. *Chem. Rev.* **2000**, *100*, 1391-1434.

c. Piers, W. E.; Chivers, T. Pentafluorophenylboranes: from obscurity to applications. *Chem. Soc. Rev.* **1997**, *26*, 345-354.

d. Lawson, J. R.; Melen, R. L. Tris(pentafluorophenyl)borane and Beyond: Modern Advances in Borylation Chemistry. *Inorg. Chem.* **2017**, *56*, 8627-8643.

21.

a. Walzer, J. F. Supported Ionic Catalyst Composition US Patent 5,643,847.

b. Millot, N.; Santini, C. C.; Baudouin, A.; Basset, J.-M. Supported cationic complexes: selective preparation and characterization of the well-defined

electrophilic metallocenium cation [[triple bond, length as m-dash]SiO-B(C6F5)3]-[Cp*ZrMe2(Et2NPh)]+ supported on silica. *Chem. Commun.* **2003**, 2034-2035.

22. Sauter, D. W.; Popoff, N.; Bashir, M. A.; Szeto, K. C.; Gauvin, R. M.; Delevoye, L.; Taoufik, M.; Boisson, C. The design of a bipodal bis(pentafluorophenoxy)aluminate supported on silica as an activator for ethylene polymerization using surface organometallic chemistry. *Chem. Commun.* **2016**, *52*, 4776-4779.

23. Wanglee, Y.-J.; Hu, J.; White, R. E.; Lee, M.-Y.; Stewart, S. M.; Perrotin, P.; Scott, S. L. Borane-Induced Dehydration of Silica and the Ensuing Water-Catalyzed Grafting of B(C6F5)3 To Give a Supported, Single-Site Lewis Acid, SiOB(C6F5)2. *J. Am. Chem. Soc.* **2012**, *134*, 355-366.

24.

a. Starr, H. E.; Gagné, M. R. Probing the Source of Enhanced Activity in Multiborylated Silsesquioxane Catalysts for C–O Bond Reduction. *Organometallics* **2022**, *41*, 3152-3160.

b. Starr, H. E. A Complex Molecular Symmetry Analysis of Silsesquioxane Catalysts for Inorganic Students. *J. Chem. Educ.* **2022**, *99*, 2204-2207.

c. Duchateau, R.; van Santen, R. A.; Yap, G. P. A. Silica-Grafted Borato Cocatalysts for Olefin Polymerization Modeled by Silsesquioxane–Borato Complexes. *Organometallics* **2000**, *19*, 809-816.

d. Metcalfe, R. A.; Kreller, D. I.; Tian, J.; Kim, H.; Taylor, N. J.; Corrigan, J. F.; Collins, S. Organoborane-Modified Silica Supports for Olefin Polymerization: Soluble Models for Metallocene Catalyst Deactivation. *Organometallics* **2002**, *21*, 1719-1726.

25. Matsuda, T.; Kawashima, H. An infrared study of hydroboration of lower olefins with diborane on γ-Al2O3. *J. Catal.* **1977**, *49*, 141-149.

26. *N*-heterocyclic carbene adducts of NH3 react with silica forming uncharacterized species that reduce ketones or aldehydes, see: Taniguchi, T.; Curran, D. P. Silica Gel Promotes Reductions of Aldehydes and Ketones by N-Heterocyclic Carbene Boranes. *Org. Lett.* **2012**, *14*, 4540-4543.

27. Cendejas, M. C.; Dorn, R. W.; McDermott, W. P.; Lebrón-Rodríguez, E. A.; Mark, L. O.; Rossini, A. J.; Hermans, I. Controlled Grafting Synthesis of Silica-Supported Boron for Oxidative Dehydrogenation Catalysis. *J. Phys. Chem. C* **2021**, *125*, 12636-12649.

28. Mathey, L.; Alphazan, T.; Valla, M.; Veyre, L.; Fontaine, H.; Enyedi, V.; Yckache, K.; Danielou, M.; Kerdiles, S.; Guerrero, J.; Barnes, J.-P.; Veillerot, M.; Chevalier, N.; Mariolle, D.; Bertin, F.; Durand, C.; Berthe, M.; Dendooven, J.; Martin, F.; Thieuleux, C.; Grandidier, B.; Copéret, C. Functionalization of Silica Nanoparticles and Native Silicon Oxide with Tailored Boron-Molecular Precursors for Efficient and Predictive p-Doping of Silicon. *J. Phys. Chem. C* **2015**, *119*, 13750-13757.

29. Bohrer, H.; Trapp, N.; Himmel, D.; Schleep, M.; Krossing, I. From unsuccessful H2-activation with FLPs containing B(Ohfip)3 to a systematic evaluation of the Lewis acidity of 33 Lewis acids based on fluoride, chloride, hydride and methyl ion affinities. *Dalton Trans.* **2015**, *44*, 7489-7499.

30. Akram, M. O.; Tidwell, J. R.; Dutton, J. L.; Martin, C. D. Bis(1-Methyl-ortho-Carboranyl)Borane. *Angew. Chem., Int. Ed.* **2023**, *62*, e202307040.

31. Erdmann, P.; Leitner, J.; Schwarz, J.; Greb, L. An Extensive Set of Accurate Fluoride Ion Affinities for p-Block Element Lewis Acids and Basic Design Principles for Strong Fluoride Ion Acceptors. *ChemPhysChem* **2020**, *21*, 987-994.

32. Akram, M. O.; Martin, C. D.; Dutton, J. L. The Effect of Carborane Substituents on the Lewis Acidity of Boranes. *Inorg. Chem.* **2023**, *62*, 13495-13504.

33. Akram, M. O.; Tidwell, J. R.; Dutton, J. L.; Martin, C. D. Tris(ortho-carboranyl)borane: An Isolable, Halogen-Free, Lewis Superacid. *Angew. Chem., Int. Ed.* **2022**, *61*, e202212073.

34. Hermanek, S. Boron-11 NMR spectra of boranes, main-group heteroboranes, and substituted derivatives. Factors influencing chemical shifts of skeletal atoms. *Chem. Rev.* **1992**, *92*, 325-362.

35. Other examples of tricoordinate boron on a support, see:
    a. Correa, S. A.; Diaz-Droguett, D. E.; Galland, G. B.; Maraschin, T. G.; De Sousa Basso, N.; Dogan, F.; Rojas, R. S. Modification of rGO by B(C6F5)3 to generated single-site Lewis Acid rGO-O-B(C6F5)2 as co activator of nickel complex, to produce highly disperse rGO-PE nanocomposite. *Appl. Catal., A* **2019**, *580*, 149-157.

    b. Mentoor, K.; Twigge, L.; Niemantsverdriet, J. W. H.; Swarts, J. C.; Erasmus, E. Silica Nanopowder Supported Frustrated Lewis Pairs for CO2 Capture and Conversion to Formic Acid. *Inorg. Chem.* **2021**, *60*, 55-69.

36. Erdmann, P.; Greb, L. What Distinguishes the Strength and the Effect of a Lewis Acid: Analysis of the Gutmann–Beckett Method. *Angew. Chem., Int. Ed.* **2022**, *61*, e202114550.

37. Osegovic, J. P.; Drago, R. S. Measurement of the Global Acidity of Solid Acids by 31P MAS NMR of Chemisorbed Triethylphosphine Oxide. *J. Phys. Chem. B* **1999**, *104*, 147-154.

38. Großekappenberg, H.; Reißmann, M.; Schmidtmann, M.; Müller, T. Quantitative Assessment of the Lewis Acidity of Silylium Ions. *Organometallics* **2015**, *34*, 4952-4958.

39. Morgan, M. M.; Marwitz, A. J. V.; Piers, W. E.; Parvez, M. Comparative Lewis Acidity in Fluoroarylboranes: B(o-HC6F4)3, B(p-HC6F4)3, and B(C6F5)3. *Organometallics* **2013**, *32*, 317-322.

40. Culver, D. B.; Conley, M. P. Activation of C–F Bonds by Electrophilic Organosilicon Sites Supported on Sulfated Zirconia. *Angew. Chem., Int. Ed.* **2018**, *57*, 14902-14905.

41. In borate salts of metallocenium ions the B-CH3 signal often appears in this region, see: Yang, X.; Stern, C. L.; Marks, T. J. Cationic Zirconocene Olefin Polymerization Catalysts Based on the Organo-Lewis Acid Tris(pentafluorophenyl)borane. A Synthetic,Structural, Solution Dynamic, and Polymerization Catalytic Study. *J. Am. Chem. Soc.* **1994**, *116*, 10015-10031.

42. Popoff, N.; Gauvin, R. M.; De, M. A.; Taoufik, M. On the Fate of Silica-Supported Half-Metallocene Cations: Elucidating a Catalyst's Deactivation Pathways. *Organometallics* **2012**, *31*, 4763-4768.

43. Gao, J.; Dorn, R. W.; Laurent, G. P.; Perras, F. A.; Rossini, A. J.; Conley, M. P. A Heterogeneous Palladium Catalyst for the Polymerization of Olefins Prepared by Halide Abstraction Using Surface R3Si+ Species. *Angew. Chem., Int. Ed.* **2022**, *n/a*, e202117279.

44. Parks, D. J.; von H. Spence, R. E.; Piers, W. E. Bis(pentafluorophenyl)borane: Synthesis, Properties, and Hydroboration Chemistry of a Highly Electrophilic Borane Reagent. *Angewandte Chemie International Edition in English* **1995**, *34*, 809-811.

Chapter 5. Conclusions

Discussion

This thesis explores the synthesis and characterization of several novel heterogeneous Lewis acidic catalysts. Lewis acidic sites are implicated in various industrially-relevant heterogeneous catalysts, including the Ziegler-Natta olefin polymerization catalyst. The novel catalysts described in this thesis are characterized using the Gutmann-Beckett method to assess Lewis acidity, in addition to other surface organometallic chemistry techniques including FT-IR, elemental analysis, and solid state NMR. Applying these materials towards characteristic Lewis acid catalyzed reactions such as early metal activation illustrate the promise in some of them as mirrors to industrial catalysts. Well-defined $\equiv SiOAl(OC(CF_3)_3)_2(O(Si\equiv)_2)$ reacts with $Cp_2Zr(CH_3)_2$ to form $[Cp_2ZrCH_3]$ $[\equiv SiOAl(OC(CF_3)_3)_2(CH_3)]$. Solid state NMR spectroscopy confirms the assignment of a ^{13}C-^{27}Al bond, unambiguously assigning the aluminum anion, as well as a methyl cation at 37 ppm. Additional speciation on the surface is observed, with the presence of a neutral Zr-Me and quantitative methane and a Si-Me formed by alkyl abstraction and siloxane bridge opening on the support. Analogously, supporting a strong Lewis superacid bis(1-methyl-*ortho*-carboranyl)borane on silica forms the well-defined Lewis site $(^{Me}oCb_2B)(OSi\equiv)$. This material is characterized by solid state NMR, confirming a tricoordinate boron center. Methide abstraction of $Cp_2Hf(CH_3)_2$ occurs with low efficiency on the support, resulting in minimal formation of the ion-pair and a majority of the surface hafnium composed of the

neutral Hf-Me site. This is suggestive of the bulky carborane groups restricting access to the central boron, limiting formation of the B-Me anion. The use of probe molecules such as triethylphosphine oxide (TEPO) to assess Lewis acidity on the aluminum and boron supports demonstrate the two materials have similar acid strength, both materials showing $\Delta\delta$ values of 28. However, both materials are observed to have different activity towards distinguishing reactivity for Lewis acids, where the pseudo tetracoordinate aluminum support clearly generates ion pairs that are active for ethylene polymerization and the tricoordinate boron support does not. Further exploration of novel derivatized supports can add to the understanding of structure-property relationships discussed in this work.

The synthesis and characterization of these novel materials works towards expanding the library of well-defined solid Lewis acids. Exploring different reactivity patterns on these catalysts, especially with methide abstraction of early metallocenes, provides valuable insight towards structure-property relationships. Given the relevance of Lewis acids across industrial catalysis, where Lewis sites are implicated in a variety of critical syntheses, further studies pursuing the development of other classes of supported Lewis acids may be informative, especially as the library of available molecular Lewis superacids continues to expand. Applying these materials towards fundamental reactions such as olefin polymerization, with the catalyst $[Cp_2ZrCH_3]$ $[\equiv SiOAl(OC(CF_3)_3)_2(CH_3)]$, establishes that these materials are indeed forming stable ion-pairs and can demonstrate characteristic reactivity patterns. The surface coverage concentration of these sites on well-defined supports far outpaces the industrial analogs, affording a material that can be

studied more easily. Prior work[1] has shown the industrial comparisons for Ziegler-Natta type catalysts supported on alumina have surface active site coverage in the micromole range, and the 0.07 mmol concentration of Zr cation active for polymerization observed on the support [Cp_2ZrCH_3] [$\equiv SiOAl(OC(CF_3)_3)_2(CH_3)$] exceeds the concentration observed on industrial comparisons by several orders of magnitude. This afforded the opportunity to study these ion pairs through labeling studies, ^{13}C CPMAS experiments, and RESPDOR experiments, to confirm the formation of cationic Zr-Me and anionic Al-Me species on this support.

Additionally, turning to fundamental ideas in chemistry such as the principle of microscopic reversibility and applying well-defined supports can serve as a powerful method to address challenges in chemical industry. Polyolefins are typically single-use waste products, and are produced globally at a scale of millions of tons annually. These materials are typically synthesized using the Ziegler-Natta or Phillips catalysts industrially.

The Ziegler-Natta system has undergone much development in the 70 years since its discovery, where the first generations of the catalyst were composed of a mixture of $TiCl_3/AlR_3/MgCl_2$ and modern iterations of the catalyst are typically comprised of a metallocene dichloride (Cp_2ZrCl_2), AlR_3 or MAO, and a high surface area metal oxide support such as alumina (Al_2O_3). Contacting the well-defined Lewis acidic support $\equiv SiOAl(OC(CF_3)_3)_2(O(Si\equiv)_2)$ with a standard metallocene, Cp_2HfMe_2, can generate an active catalyst that parallels the structure of modern Ziegler-Natta catalysts with a high surface coverage of active sites. This material can be applied towards the hydrogenolysis

of polypropylene with high yields of paraffinic oil product and minimal formation of low molecular weight hydrocarbon gas. This reaction occurs at modest conditions by industrial and academic standards, at 1 atm of H_2 and 200˚C over 24 hours.

The existing literature for polyolefin hydrogenolysis catalysts typically involve the use of noble metal nanoparticles supported on a high surface area metal oxide or the use of d0 metal hydrides. These suffer from practical drawbacks, such as the cost limitation of applying noble metals at large scales or the synthetic challenges in isolating d0 metal hydrides. These catalysts also typically form large proportions of gaseous products like methane, which are typically considered to be waste products industrially. These catalysts typically activate a C-H bond in the polymer by σ-bond metathesis and β-alkyl elimination to form MR(olefin) intermediates that are hydrogenated to form shorter hydrocarbon chains. Cationic metallocenes can engage in σ-bond metathesis, and cationic metallocenes that are active olefin polymerization catalysts may be expected to show activity towards the hydrogenolysis of polyolefins in the presence of H_2.

Studying the products formed from the hydrogenolysis of polypropylene by $[Cp_2HfCH_3]$ $[\equiv SiOAl(OC(CF_3)_3)_2(CH_3)]$ reveal key mechanistic insights. The presence of regioirregular errors that occur throughout the alkyl chain in most of the oil products is indicative of chain straightening occurring throughout the hydrogenolysis. During hydrogenolysis, the Hf-R appears to undergo β-alkyl elimination and 2,1 reinsertion to yield chain straightened products. This is parallels the 3,1 insertion that can occur during propylene polymerization, where 1,2 insertion can form a 2˚ M-alkyl, which β-H eliminates and reinserts to form 1˚ M-R chains. The deuterolysis experiments confirm

incorporation of deuterium into 1˚, 2˚, and 3˚ positions along the alkyl chain of the oil product. Additionally, the incorporation of deuterium into the residual polymer suggests that the σ-bond metathesis is reversible.

The exploration of novel well-defined supports can serve as a powerful technique to explore the activity of industrial catalysts. Parsing structure-property relationships of these supports and applying techniques such as solid state NMR, FT-IR, and elemental analysis can provide a robust understanding of these materials. This can, in turn, allow for novel developments using well-understood chemistry. Adopting a catalytic system that is already widely used in industry, such as the Ziegler-Natta polyolefin catalyst, and applying it towards a fundamental problem that academic and industrial scholars are studying, can prove to be a powerful strategy towards a solution to the polyolefin waste problem.

References

1. Culver, D. B.; Dorn, R. W.; Venkatesh, A.; Meeprasert, J.; Rossini, A. J.; Pidko, E. A.; Lipton, A. S.; Lief, G. R.; Conley, M. P. Active Sites in a Heterogeneous Organometallic Catalyst for the Polymerization of Ethylene. ACS Cent. Sci. 2021, 7, 1225−1231.